Resolving earthquake source complexities in the heterogeneous Earth

Thesis by

Zhe Jia

In Partial Fulfillment of the Requirements for
the degree of
Doctor of Philosophy

CALIFORNIA INSTITUTE OF TECHNOLOGY
Pasadena, California

2022
Defended May 10th, 2022

Zhe Jia
ORCID: 0000-0003-0652-2646

ACKNOWLEDGEMENTS

The 6-year PhD journey at Caltech, which shaped me as a researcher comes to an end. The influences on me will continue all through my life. I have been really fortunate to have had many wonderful people going through my PhD journey with me, many more than listed here. I owe you my sincere gratitude.

I feel truly fortunate and thankful to my primary advisor Zhongwen Zhan, as he is always enthusiastic, optimistic, constructive, and supportive. Zhongwen has a highly enterprising spirit and exploratory enthusiasm for science, which always infects me when I am tired. He is always optimistic about the future, from which I learned to have the courage to imagine big and overcome whatever difficulties are in front of me. He is always constructive, so no matter how different our perceptions are, it always ends with building a good direction and working towards it. He is always kind and supportive, which allows me to explore science and my career without limiting myself. From him, I learned not only the knowledge, but how to think big yet work critically. I feel genuinely grateful to him for the training and support, and will surely miss these encouraging and mind-opening working experiences.

I am truly thankful to my secondary advisor Robert Clayton, not only for the structure-related knowledge gained from him, but for the free environment of research experience he provided. Rob is always casual and supportive, which helped me get through my stressful years smoothly. My thanks also to my academic advisor Jennifer Jackson for being supportive whenever I need advice or help, and whenever I need to sign the “blue cards”. Thanks to Zach Ross for his kind assistance in my various research items, as well as his advices from a friend’s standpoint. Thanks to Mark Simons for his all-around advisements in my first year, and the funny sailings in his ocean of knowledge. Thanks to Hiroo Kanamori for assisting my research items, and advising me how to understand large earthquakes. I want to express my thanks and commemorate Don Helmberger for helping my research projects, and advising me how to understand the beauty of waveforms. Thanks to Mike Gurnis for helping my research project and teaching me how to macroscopically view Earth dynamics. Thanks to Jean-Philippe Avouac for helping my research project and hosting the active tectonics seminar class, from which I learned a lot. Thanks to Victor, Joann, Nadia, Egill, and all other faculty members at SeismoLab and GPS, from whom I learned so much from their classes and research.

I owe special thanks to Sidao Ni, my first advisor at USTC. Sidao brought me into the field of seismology, settled the fundamentals of my skills and geophysical sense, and continuously supports me through my seismology career. I may not have accomplished a PhD here without him along the journey.

I benefit tremendously from many outstanding professors, postdocs, and graduate students. Thank Wenyuan, Peter, Zhigang, Zhichao, Xin, and Wenbo much for their help during my research and seeking of job opportunities. Thank Chunquan, Zefeng, Lingling, Minyan, Weiqiang, Sunny, Valere, Jack, Jorge, Voon, Ethan, Yan, Yida, Jiaxuan, Ettore, and all others from Zhongwen's and Rob's group for the beneficial and intriguing discussions. Also, I want to thank Donna, Priscilla, Rosemary, Kim, and many other staff at SeismoLab, for their persistent help and support.

I sincerely thank all my friends at Caltech, who are truly important through my PhD life. I want to thank my current and former roommates at South Mudd 370: Minyan, Xiaolin, Ollie, Vish, Vasilije, Pond, Erin, and Ojashvi, for building this office into a place of entertainment and happiness, I'm surely going to miss you guys. I want to thank my friends Zhichao, Wei, Wenbo, Xin, Jorge, Voon, Stacy, Valere, Kangchen, Zefeng, Han, Jiashun, Yida, Yan, and many others in SeismoLab, as well as Cheng, Junyi, Wenlong, Peida, Hongrui, Lei, Yifang, Yan, Xuecheng, Hao, Liyang, Xiaoyi, and many others out of the SeismoLab, for all the joyful and memorable moments. Special thanks to everyone in the SeismoFam for all the good times together.

I can never thank my parents and my grandmother enough for their unconditional love and support, for their sacrifice to provide me with a blissful childhood and the best education possible to them, and for their long-lasting blessing and trust.

Finally, my very special thanks to Zhaoxin Ban, for her love and support. She fills my life with happiness, and keeps motivating my growth. I am very fortunate to have her as a sincere critic, a trustworthy friend, and an adventurous partner.

ABSTRACT

While the commonly used simple assumptions of sources and structures allows useful first-order approximation of earthquakes, they are increasingly insufficient in characterizing the complex earthquake ruptures and the seismic wave propagations. In this thesis, I present studies that address both the source and structural complexities, as well as their interactions, using flexible parameterizations and ideas.

For large earthquakes, I develop a subevent inversion framework to determine their spatiotemporal rupture complexities, and applied it to multiple significant earthquakes. Our method does not assume a fault geometry and kinematic history, and incorporates Bayesian analysis for uncertainty assessments. In Chapter 2, I discovered that the 2018 Fiji Magnitude 8 deep earthquake doublet actually ruptured two slabs, which demonstrates local slab temperature as the critical factor for deep earthquakes, and reveals complex interactions between slabs. In Chapter 3, I determined that the 2019 Ridgecrest Magnitude 7 sequence coseismically ruptured orthogonal faults, and has superficially complex but in-depth simple fault geometries, which illustrates the fault geometrical control of the rupture behaviors which challenges traditional seismic hazard mapping. In Chapter 4, I found the 2021 South Sandwich Island Magnitude 8 earthquake consists of deep regular ruptures connected by a slow tsunamigenic event, which highlights the tsunami potential for deep initiations of megathrust earthquakes.

For smaller earthquakes, I develop a Bayesian differential moment tensor inversion (diffMT) algorithm to remove the common earth structural effects, thus improving the earthquake focal mechanism resolvability. In Chapter 5, I demonstrated that diffMT reduces the moment tensor uncertainties substantially than traditional direct-inversion methods, and found that the North Korea nuclear tests in 2013-2016 are more dominated by explosive mechanism than previous understandings.

Towards high resolution mapping of the Earth structure, I expand the seismic tomography for high resolution basin structure by combining the wide aperture of seismic stations and high density of industrial arrays. In Chapter 6, I applied this approach on the densely populated Los Angeles Basin, and found improved mapping of small scale heterogeneities, which can potentially promote earthquake ground motion assessments.

In summary, I have developed research tools and applied novel ideas on complex seismic events and heterogeneous earth environments. The results illustrate the diverse controlling factors of complex earthquake ruptures, and reveal the complex interactions between earthquakes and earth structure.

PUBLISHED CONTENT AND CONTRIBUTIONS

Jia, Zhe, Zhichao Shen, Zhongwen Zhan, Chenyu Li, Zhigang Peng, and Michael Gurnis. "The 2018 Fiji Mw 8.2 and 7.9 deep earthquakes: One doublet in two slabs." *Earth and Planetary Science Letters* 531 (2020): 115997. Doi: 10.1016/j.epsl.2019.115997

Z.J. participated in the conception of the project, developed the methodology, executed the analysis, and wrote most of the manuscript.

Ross, Zachary E., Benjamín Idini, **Zhe Jia**, Oliver L. Stephenson, Minyan Zhong, Xin Wang, Zhongwen Zhan et al. "Hierarchical interlocked orthogonal faulting in the 2019 Ridgecrest earthquake sequence." *Science* 366, no. 6463 (2019): 346-351. Doi: 10.1126/science.aaz0109

Z.J. participated the method development, data analysis, and the writing of the manuscript.

Jia, Zhe, Xin Wang, and Zhongwen Zhan. "Multifault models of the 2019 Ridgecrest sequence highlight complementary slip and fault junction instability." *Geophysical Research Letters* 47, no. 17 (2020): e2020GL089802. Doi: 10.1029/2020GL089802

Z.J. participated in the conception of the project, developed the methodology, executed the analysis, and wrote the manuscript.

Jia, Zhe, Zhongwen Zhan, and Hiroo Kanamori. "The 2021 South Sandwich Island Mw 8.2 earthquake: a slow event sandwiched between regular ruptures." *Geophysical Research Letters* 49, no. 3 (2022): e2021GL097104. Doi: 10.1029/2021GL097104

Z.J. participated in the conception of the project, developed the methodology, executed the analysis, and wrote the manuscript.

Jia, Zhe, Zhongwen Zhan, and Donald Helmberger. "Bayesian differential moment tensor inversion: theory and application to the North Korea nuclear tests." *Geophysical Journal International* 229, no. 3 (2022): 2034-2046. Doi: 10.1093/gji/ggac053

Z.J. participated in the conception of the project, developed the methodology, executed the analysis, and wrote the manuscript.

Jia, Zhe, and Robert W. Clayton. "Determination of Near Surface Shear-Wave Velocities in the Central Los Angeles Basin with Dense Arrays." *Journal of Geophysical Research: Solid Earth* 126, no. 5 (2021): e2020JB021369. Doi: 10.1029/2020JB021369

Z.J. participated in the conception of the project, developed the methodology, executed the analysis, and wrote the manuscript.

Zhang, Xiaotian, **Zhe Jia**, Zachary E. Ross, and Robert W. Clayton. "Extracting dispersion curves from ambient noise correlations using deep learning." *IEEE*

Transactions on Geoscience and Remote Sensing 58, no. 12 (2020): 8932-8939. Doi: 10.1029/2020GL089802

Z.J. participated the method development, data analysis, and the writing of the manuscript.

TABLE OF CONTENTS

Chapter 1

INTRODUCTION

Rapid and accurate characterization of the earthquake sources helps to mitigate seismic hazards, such as assessing ground shaking intensities and secondary hazards. Once an earthquake was detected, multiple agencies would trigger automated algorithms for the basic source properties, e.g. its location and focal mechanism. To better characterize the large events, we need to resolve the rupture complexities, such as the fault geometry, spatiotemporal rupture evolution, and the slip distribution. In the past decades, earthquake complexities are usually modeled as shear slip on a planar fault in an elastic earth medium. This finite-fault description characterized many large earthquakes very well, and provided timely and critical assessments of ground shakings and tsunami-related hazards.

However, such descriptions are progressively insufficient in analyzing the earthquake source processes, as we have observed an increasing number of large earthquakes that have ruptured multiple faults and feature unexpected mechanisms, in recent years. A remarkable example is the 2016 Mw 7.8 Kaikoura earthquake at a transpressional plate boundary, which ruptured at least 12 major fault segments, including several which are previously unidentified. Earthquakes like this would challenge the estimation of peak slip on a single fault, as well as the modeling of spatial and temporal evolution of the rupture, thus making it difficult to estimate the detailed shakings and predict the heavily damaged regions.

To better resolve the emerging earthquake complexities, we need to break the conventional assumptions used in traditional models. This requires a different way of thinking about earthquake ruptures, along with a novel set of tools and ideas to aid in the study. One fresh idea to tackle earthquake complexity is that complex earthquakes can be decomposed into simpler subevents, with individual radiation patterns and directivity effects. This simple yet flexible subevent parameterization allows us to uncover ruptures on unknown faults at unknown times, which could represent various complexities, such as multi-fault rupture, changing rupture direction and velocity, dynamic triggering, etc. I implemented this idea and developed a flexible Bayesian subevent inversion framework, which bridges a single-source model with the sophisticated finite model and allows me to capture fascinating earthquake complexities that were not considered before. In this thesis, I show the untangling of source complexities for several recent significant earthquakes/sequences in Chapters 2-4.

But some other earthquakes could appear more complex than they actually are. This is because we could introduce error to the obtained source properties by misinterpreting unknown effects of earth structure. As our computation capabilities have been dramatically enhanced and the knowledge of 3D Earth structures is also improved at both local and global scales, we are standing at the point where accounting for 3D Earth models in the source inversions becomes possible and necessary. Therefore, in Chapter 3, I develop a subevent-guided finite fault inversion algorithm using 3D Green's functions, which aims to better constrain the rupture complexities in a heterogeneous Earth environment.

Although accurate 3D Green's functions directly avoid structural-related biases for source inversions, high-quality regional 3D velocity models can be rare, because developing them requires dense seismic monitoring. To reduce the requirement of highly accurate 3D models, I came up with another idea to filter out common structural effects by making differential measurements. Based on this idea, I developed a novel moment tensor determination algorithm in a Bayesian framework, named differential moment tensor (diffMT) inversion. In Chapter 5, I show a conceptual validation of this diffMT algorithm, which illustrates its capability to improve the resolvability of earthquake focal mechanisms, thus better describing the macroscopic mechanics of the source and how energy radiates.

Towards expanding the application scenarios of high-resolution 3D velocity models, we need more of these models with broader spatial coverage. However, given the limited number of stations in a seismic array, there is an inherent trade-off between the resolution and the coverage area. To overcome this difficulty, I developed the ambient noise tomography by combining the aperture of seismic stations and density of industrial arrays. In Chapter 6, I show how this unique combination led to a 3D velocity model that covers most of the LA basin and resolves small-scale structures with high fidelity.

Chapter 2

THE 2018 FIJI M8 DEEP EARTHQUAKE DOUBLET IN TWO SLABS

Jia, Zhe, Zhichao Shen, Zhongwen Zhan, Chenyu Li, Zhigang Peng, and Michael Gurnis. "The 2018 Fiji Mw 8.2 and 7.9 deep earthquakes: One doublet in two slabs." In: *Earth and Planetary Science Letters* 531 (2020): 115997. Doi: 10.1016/j.epsl.2019.115997.

2.1 Abstract

The cold Fiji-Tonga subduction zone accounts for >75% of cataloged deep earthquakes but none of the largest ten in the last century. On 19 August 2018 and 06 September 2018, a deep earthquake doublet with moment magnitude (M_w) 8.2 and 7.9 struck the Fiji area, providing a rare opportunity to interrogate the behaviors of great deep earthquakes in cold slabs. While the aftershock productivity of the 2018 M_w 8.2 event is similar to the 2013 Okhotsk M_w 8.3 event in a cold slab, the inferred compact rupture dimensions of both the M_w 8.2 and 7.9 events appear to be similar to the 1994 Bolivia earthquake in a warm slab. This seems to contradict the traditional view that slab temperature controls deep earthquakes. However, we find that neither event was confined within the cold Tonga slab core: the M_w 8.2 ruptured mostly in the warmer rim of the Tonga slab and the M_w 7.9 occurred in a warm relic slab leaning on top of the Tonga slab. The Fiji doublet demonstrates local slab temperature as the critical factor for deep earthquakes, and reveals complex interaction of subducted slabs in Tonga.

2.2 Introduction

Since the discovery of deep earthquakes below 300 km in the 1920s, the Fiji-Tonga subduction zone has produced more than 75% of global deep seismicity above magnitude 4, but none of the ten largest deep earthquakes (Houston, 2015). This deficit of large events is reflected in Fiji-Tonga's higher Gutenberg-Richter *b* value than in other subduction zones

(Wiens and Gilbert, 1996; Zhan, 2017), and was commonly attributed to its colder slab with older incoming plate and faster plate convergence (Wiens and Gilbert, 1996; Wiens, 2001). On August 19th, 2018, the first instrumentally recorded M>8 Fiji deep earthquake occurred (Fig. 2.1A), with a centroid depth of 556 km (Fig. S2.1) and a moment magnitude (M_w) 8.2, slightly smaller than the 1994 Bolivia M_w 8.2 earthquake, the second largest deep earthquake after the 2013 Okhotsk M_w 8.3 earthquake (Table S2.1). The M_w 8.2 Fiji event produced hundreds of aftershocks, elevating seismic activity within a few hundred kilometers. On September 6th, a M_w 7.9 earthquake occurred about 250 km to the west at 655 km depth (Fig. S2.1), being the second largest deep earthquake in the Fiji-Tonga region. Background seismicity in the M_w 7.9 source area had been minimal but increased substantially since the M_w 8.2 earthquake (Fig. 2.1B). Presumably, the M_w 8.2 event triggered the M_w 7.9, forming the first magnitude 8 (M8) deep earthquake doublet (Tibi et al., 2003b; Ye et al., 2016).

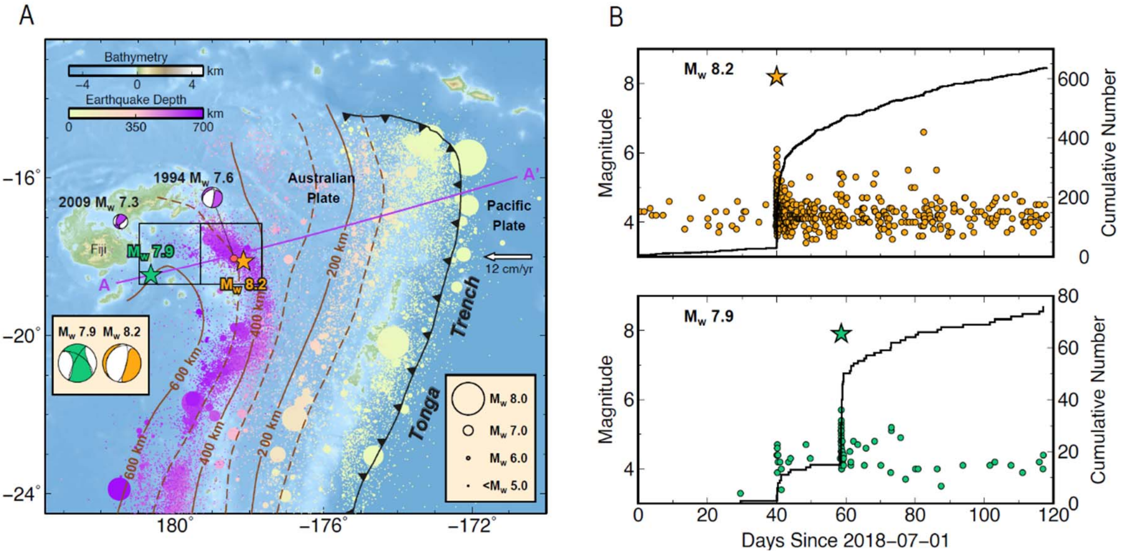

Figure 2.1. Tectonic setting and seismicity. (A) The 2018 Fiji deep earthquake doublet (M_w 8.2 and M_w 7.9) occurred in the northern end of Fiji-Tonga subduction zone where the Pacific plate subducts under the Australian plate, as illustrated by the background seismicity (dots) based on the ISC catalog and the slab depth contours from the Slab 2.0 model (Hayes et al.,

2018). The stars show the mainshock epicenter locations, and the mainshock moment tensors from Global CMT catalog are displayed in the inset. (B) Seismic activity around the M_w 8.2 and M_w 7.9 events in the black squares in (A) based on the ISC catalog. Body wave magnitudes are plotted except for the mainshocks. Solid black lines denote the cumulative number of aftershocks in the mainshock regions (boxes in A). The M_w 8.2 event triggered hundreds of aftershocks near its rupture area and also elevated activity in the source region of the later M_w 7.9 event during the three weeks in between. The M_w 7.9 event produced another tens of aftershocks around its rupture area.

The Fiji deep doublet and their aftershocks provide a unique opportunity to test our understanding of the still enigmatic deep earthquake mechanism, especially the properties of great deep earthquakes in cold slabs. The primary control on deep earthquakes appears to be slab temperature, which is often represented by the thermal parameter $\phi = a * v * \sin\theta$, where θ is slab dip, a is incoming plate age, and v is plate convergence rate (Kirby et al., 1991; Wiens and Gilbert, 1996). Deep earthquakes have only been detected in subduction zones with ϕ above 2000 km, and the maximum depths of earthquakes increase monotonically with ϕ (Gorbatov et al., 1997). In addition to the aforementioned b-value difference, deep earthquakes in cold slabs are substantially more productive in aftershocks than those in warm slabs (Wiens and Gilbert, 1996). Rupture processes of large deep earthquakes also show systematic dependence on slab temperature (Tibi et al., 2003a). For example, the 2013 Okhotsk M_w 8.3 earthquake in the cold Kuril subduction zone (ϕ~6000 km) had higher rupture speed, lower stress drop, and higher seismic radiation efficiency (i.e., lower dissipation) than the 1994 Bolivia M_w 8.2 event in the warm South America subduction zone (ϕ~2000 km) (Zhan et al., 2014). Large deep earthquakes in the cold Fiji-Tonga subduction zone (ϕ~8000 km) may then be expected to be more brittle in rupture, more efficient in seismic energy radiation, and to produce more aftershocks. To evaluate these properties, we analyze the source processes of the 2018 Fiji doublet through modeling of seismic observations, and compare their rupture properties, aftershock productivities, and thermal environments with previous large deep earthquakes.

2.3 Rupture Properties of the Fiji Doublet

In this section, we estimate the radiated seismic energy of the Fiji doublet based on body-wave magnitudes (m_B), determine focal mechanisms of their initial ruptures through P-wave first-motion polarities, and image the rupture processes through subevent inversion of globally observed seismograms.

Here we use an empirical approach that converts global estimates of body wave magnitude m_B to radiated energy E_R (Gutenberg and Richter, 1956; Kanamori and Ross, 2018). We use teleseismic (from 30° to 80°) vertical component seismograms on the Global Seismic Network (GSN) and the international Federation of Digital Seismograph Networks (FDSN) stations from IRIS DMC (Incorporated Research Institutions for Seismology Data Management Center) to estimate the body-wave magnitude m_B. After removing the instrumental responses, we convolve the displacement seismograms with the Wiechert-type instrumental response. Then, we measure the P wave peak amplitude and period (T_p) and correct for the instrument gain at the period of the peak phase to determine the ground motion amplitude (A_p). The body-wave magnitude m_B at each station is calculated by

$$m_B = log_{10}\left(\frac{A_p}{T_p}\right) + Q(\Delta, h) \tag{1}$$

where Q is an empirical function of epicentral distance Δ and earthquake depth h (Kanamori and Ross, 2018). The final body-wave magnitude is the median value of m_B from all stations. We related the body-wave magnitude m_B to radiated seismic energy E_R using an empirical equation (Gutenberg and Richter, 1956; Kanamori and Ross, 2018):

$$log_{10}E_R = 5.8 + 2.4\ m_B \tag{2}$$

where E_R is in ergs. Kanamori and Ross (2018) verified the accuracy of the above equation by comparing with previous radiated energy estimates and found differences within a factor of two for deep earthquakes. Once the radiated seismic energy is obtained, the scaled energy can be computed with E_R/M_0, where M_0 is the seismic moment from the Global CMT catalog (www.globalcmt.org).

	Body-wave magnitude (m_B)	**Radiated energy (Erg)**	**Scaled radiated energy (10^{-5})**
1994 Fiji M_w 7.5	7.17 (7.16)	1.03×10^{23}	3.35 (3.14)
1994 Bolivia M_w 8.2	7.65 (7.65)	1.42×10^{24}	5.41 (5.53)
2013 Okhotsk M_w 8.3	7.68 (7.69)	1.72×10^{24}	4.34 (4.47)
2015 Bonin M_w 7.9	7.35 (7.37)	2.72×10^{23}	3.56 (4.09)
2018 Fiji M_w 8.2	7.63	1.29×10^{24}	4.89
2018 Fiji M_w 7.9	7.32	2.31×10^{23}	2.68

Table 2.1. Comparison of body-wave magnitude (m_B), radiated energy, and scaled energy of the six large deep earthquakes discussed in this study. Numbers in red are from Kanamori and Ross (2018) as comparisons.

We find that the radiated energy estimates for the Fiji doublet are not substantially higher than for previous M8 deep earthquakes: 1.29×10^{24} ergs and 2.31×10^{23} ergs for the M_w 8.2 and M_w 7.9 earthquakes, respectively (Table 2.1). In comparison, our estimated E_R for the 1994 Bolivia and the 2013 Okhotsk earthquakes are 1.42×10^{24} ergs and 1.72×10^{24} ergs, consistent with previous measurements (Kanamori et al., 1998; Ye et al., 2013). After normalization by their seismic moments M_0, there is no substantial difference in the scaled energy E_R/M_0 for all four events (Table 2.1), given the uncertainties of E_R. Therefore, the Fiji events, although in the world's coldest subduction zone, did not radiate more seismic energy than events in warmer subduction zones. Further comparison of radiation efficiency $\eta_R = E_R/\Delta W_0$ requires estimating the available strain energy $\Delta W_0 = M_0\Delta\sigma/2\mu$, and stress drop $\Delta\sigma \propto M_0/L^3$ is highly sensitive to the earthquake rupture dimension L. Hence, to quantify whether the Fiji doublet are more seismically efficient than previous large deep earthquakes in warmer subduction zones, we need to constrain the rupture dimensions of these earthquakes consistently.

To gain insights on possible rupture complexities, we first investigate the initiations of the Fiji doublet ruptures, by examining their first-motion focal mechanisms relative to the centroid moment tensors. We manually pick the first arrivals of broadband P waves on both regional and teleseismic stations, identify their polarities, and determine the geometries of nodal planes. Fig. 2.2 shows the observed P-wave polarities and the estimated first-motion mechanisms (solid lines and shades), with substantial differences from the best-fitting double-couple mechanisms based on the Global CMT solutions (dashed lines). For the M_w 8.2 earthquake, the difference in focal mechanism (strike/dip of 56°/80° vs. 13°/70°) is mostly due to the positive polarities observed at stations to the southwest (SW) directions (Fig. 2.2A). Polarity observations of the M_w 7.9 earthquake indicate a strike-slip mechanism, with two nodal planes of strike/dip = 38°/85° and 128°/80°, both of which deviate substantially from the double-couple component of the Global CMT solution (strike/dip=305°/57° and 207°/77°) (Fig. 2.2B). The differences between the first-motion mechanisms and the centroid mechanisms indicate substantial changes in fault geometry or rake angle during the ruptures of the Fiji doublet, which we accommodate in the subevent inversions.

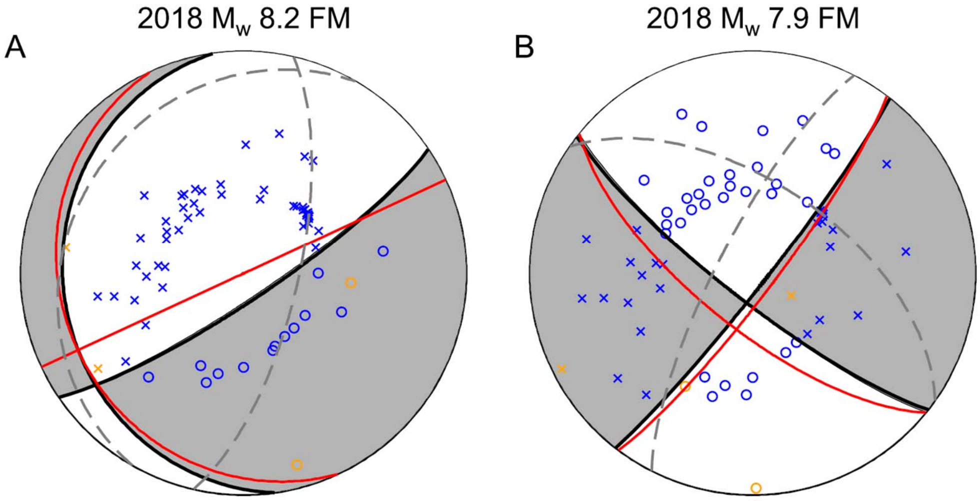

Figure 2.2. First-motion focal mechanisms for (A) the M_w 8.2 and (B) the M_w 7.9 events. Blue circles and crosses respectively indicate the positive and negative polarities from teleseismic seismograms. Orange circles and crosses respectively indicate the positive and negative polarities from regional seismograms. Dashed fault planes denote the best-fitting double-couple focal mechanisms based on the GCMT solutions. The solid fault planes are the first-motion solutions (strike, dip), (172°, 20°) and (56°, 80°) for the M_w 8.2 event, and (38°, 85°) and (128°, 80°) for the M_w 7.9 event. Red lines indicate first subevent focal mechanisms from the subevent rupture models inverted from seismic waveforms (Fig 2.3).

We image the doublet rupture processes and dimensions by subevent inversions. Our subevent inversion method parameterizes a large earthquake as a series of point sources (subevents) and uses teleseismic P, SH, and pP waveforms to constrain properties of individual subevents. It is similar to a previous method applied to the 1994 Bolivia and 2013

Okhotsk earthquakes (Zhan et al., 2014), but includes subevent focal mechanisms explicitly to quantify changes of radiation pattern along rupture. Furthermore, pP depth phases added to the inversion help resolve possible variations in subevent depths. In this method, we invert for the centroid locations, centroid times, durations, and moment tensors of all subevents. Our method combines non-linear inversion for a subset of parameters and linear inversion for the rest. We apply Markov Chain Monte Carlo (MCMC) method to sample the posterior Probability Density Functions (PDFs) of the nonlinear parameters including the timings, locations, and durations of subevents. For a given set of subevent timings, locations, and durations (i.e., one MCMC sample), we evaluate the apparent source time function for each station, and linearly invert the seismic data for the subevent moment tensors. The data misfit from the set of nonlinear parameters and the corresponding moment tensor solutions is then used to estimate the probability in the MCMC inversion. Compared with a fully non-linear inversion scheme, this hybrid approach requires much less computation to search the parameter space, and thus provides more robust solutions. The number of subevents increases iteratively until the waveforms are fit well. More details of our subevent method can be found in the supplementary material.

The subevent model for the M_w 8.2 earthquake (Fig. 2.3A, Fig. S2.2, Table S2.2) shows two stages of rupture. The first stage includes subevent E1 (centroid time τ_C=8.15 s, M_w 7.55), E2 (τ_C=10.88 s, M_w 7.66), and E3 (τ_C=13.16 s, M_w 7.61), aligned approximately in the NE direction with similar focal mechanisms (average strike/dip/rake=43°/84°/-77°, 160°/18°/-152°). E1's focal mechanism from waveform inversion confirms the first-motion polarities of teleseismic P waves (Fig. 2.2A). Posterior Probability Density Functions (PDFs) of the subevent depths suggest that E3 is about 15 km shallower than E1 and E2 (Fig. S2.3), preferring the stage 1 rupture to be on the steep NE-strike fault plane (strike/dip=43°/84°), which is also supported by the nearly vertical band of aftershocks (Fig. 2.4A). The largest subevent of stage 1, E2, appears to have triggered large slip on multiple faults in stage 2. Subevents E4 (τ_C=14.88 s, M_w 7.81), E5 (τ_C=17.47 s, M_w 7.72), and E6 (τ_C=20.81 s, M_w 7.83) are aligned towards the northwest (NW) and they have relatively similar focal mechanisms (average strike/dip/rake=3°/71°/-100°, 213°/23°/-63°). The difference in radiation pattern between the two stages (Fig. 2.2A) is evident on the teleseismic P-wave displacement seismograms with flipping polarities (Fig. 2.3B, Fig. S2.4). Posterior PDFs suggest that E2, E4, E5, and E6 rupture sequentially towards shallower depths by about 30 km (Fig. 2.4B, Fig. S2.3), rejecting the shallow west-dipping nodal plane (strike/dip=213°/23°) as the rupture plane. Furthermore, as E2, E4, E5, and E6 centroid locations are not aligned in the north-south (N-S) direction, it is also unlikely that they occurred on the N-S striking, steep fault plane (strike/dip=3°/71°). This disagreement between the subevent strikes and the alignment of their locations is also confirmed by a simpler three-subevent model (Fig. 2.5), in which the two main subevents E2 and E3 are aligned from SE to NW, being located shallower, while their strikes are north. Therefore, we conclude that the stage 2 rupture must involve multiple faults, although the exact geometry is uncertain (e.g., en echelon vs. perpendicular faults). Previous magnitude 7 deep earthquakes in Fiji-Tonga show a diversity of fault geometries (Warren et al., 2007). The sum of the subevent moment tensors explains the long period moment tensor solution of the M_w 8.2 earthquake well, including the ~10% non-double-couple (non-DC) component (Fig. S2.2). The overall subevent dimension of stage 2 is ~30 km, about the same as stage 1 but with a much larger total moment. The two stages altogether contribute to a total rupture dimension of ~50 km, consistent with the three-subevent model (Fig. 2.5). To further confirm whether the estimation of rupture dimension is insensitive to our specific subevent parameterization and choice of number of subevents, we conduct another inversion approximating the earthquake as a single Haskell source. The result is a unilateral rupture towards the NW with a length close to 60 km, roughly consistent with the values from subevent inversions. However, the Haskell source model cannot capture the distribution of moment along rupture, or the changes in depth and moment tensor.

The M_w 8.2 earthquake produced over 400 M>4 aftershocks during the following 80 days, more than any previous deep earthquake. In comparison, the 2013 Okhotsk and 1994 Bolivia earthquakes produced 71 and 4 M>4 aftershocks in the same duration, respectively. After correcting for differences in catalog completeness and mainshock magnitudes (Utsu and Ogata, 1995; Peng et al., 2007), the aftershock productivity of the 2018 Fiji M_w 8.2 is similar to the 1994 Fiji M_w 7.6 earthquake, and significantly higher than other large deep earthquakes (Fig. 2.6). However, the distribution of the Fiji M_w 8.2 aftershocks is non-uniform and does not follow the mainshock slip distribution. Here we relocate the M_w 8.2 main shock and its aftershock using a teleseismic double difference algorithm (Pesicek et al., 2010). More details can be found in the supplementary materials. The aftershocks concentrated in a NE-strike band, and are aligned with the inferred fault plane for the stage 1 rupture but are sparser around the stage 2 rupture (Fig. 2.3A, 2.4A; Fig. S2.8-S2.9), which accounts for most of the total moment. This suggests that the aftershock productivities of the two stages of the M_w 8.2 are substantially different.

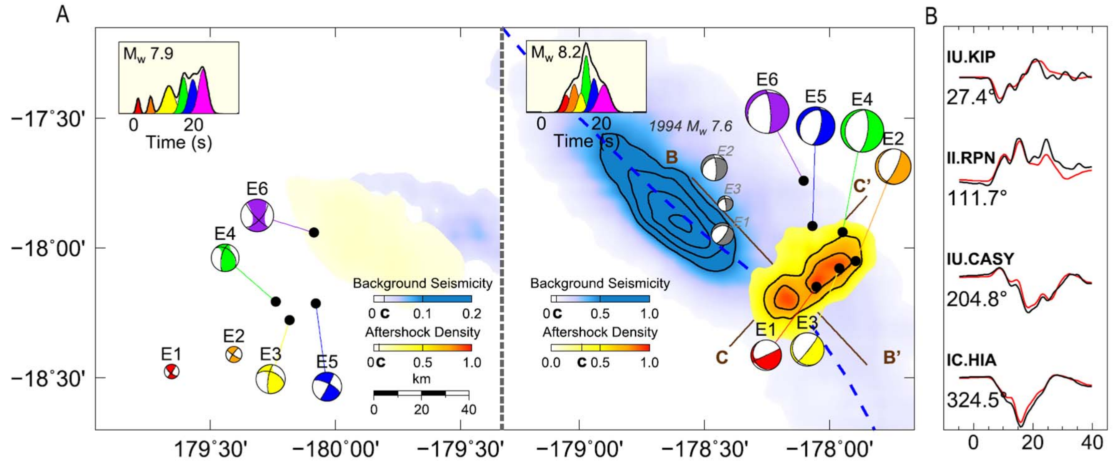

Figure 2.3. Rupture processes of the 2018 Fiji doublet. (A) Subevent models for the M_w 7.9 (left half) and the M_w 8.2 events (right half). The black dots are centroid locations of the subevents, whose moment rate functions (MRFs) are shown in the inset with the same colors as their moment tensor beach balls. Density contours of relocated aftershocks are plotted over the contours of background seismicity based on the USGS NEIC catalog. They are displayed with different color scales and truncations ("C" on the colorbars if not 0). The M_w 8.2 event initiated near the slab center (blue dashed curve as inferred from the maximum background seismicity), but ruptured mostly 30 km to the NE by subevent E2, and E4-E6. Grey beachballs are subevent model of the 1994 Fiji M_w 7.6 earthquake. (B) Representative

displacement waveform fits for the subevent model of the M_w 8.2 event at different azimuths, with data in black and synthetics in red. Early and late parts of the waveforms have opposite polarities at KIP and CASY, suggesting different focal mechanisms along the rupture.

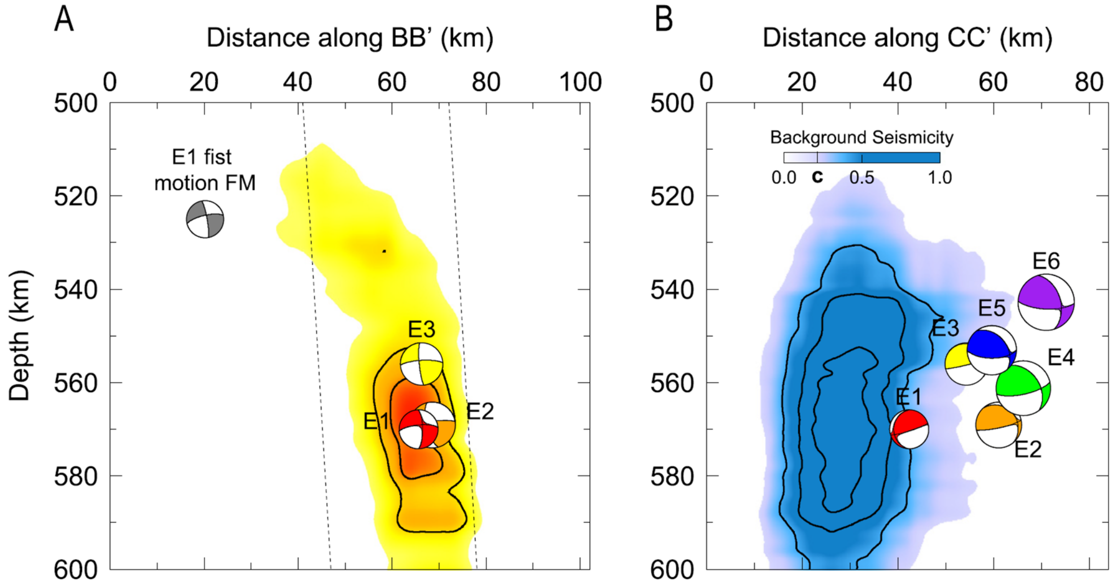

Figure 2.4. Relation of the M_w 8.2 subevents with aftershocks and background seismicity. (A) Cross section along BB' in Fig. 2.3A showing the aftershocks of M_w 8.2 event extend nearly vertically, favoring the NE-strike fault plane for stage 1. Density contours of aftershocks are displayed with same color scale as in Fig. 2.3A. (B) Cross section along CC' in Fig. 2.3A showing the M_w 8.2 subevents spread by 30 km vertically and mostly away from the cold core as inferred from the background seismicity density.

The M_w 7.9 event of the Fiji doublet has ~30% non-double-couple (non-DC) component in the USGS WPhase and the Global CMT solutions, compared with ~10% for the M_w 8.2

event. This large non-DC is reflected by the diverse subevent focal mechanisms we derived from waveforms (Fig. 2.3A, Fig. S2.10-S2.13, Table S2.3), and supported by the deviation of polarity-based focal mechanism from the best-fitting double-couple of the Global CMT solution (Fig. 2.2). The earthquake first ruptured to the east (E1-E2), then the major subevents (E3 to E6) occurred in a cluster from SW to NE direction (Fig. 2.3A). Given the uncertainty of subevent locations and focal mechanisms, it is unclear whether they ruptured on a single NE-strike fault plane or as a cascade of ruptures on multiple faults (Fig. S2.10). By including both teleseismic depth phases (*pP*) and the up-going direct P and SH waveforms recorded by a local station MSVF in our inversion, we find that the M_w 7.9 event ruptured a 20 km depth range (Fig. S2.11-S2.14). The largest four subevents from E3 to E6 account for ~90% of the total moment and are concentrated within 40 km from each other laterally (Fig. 2.3A), comparable to the subevent dimension of the M_w 8.2 event's stage 2 rupture.

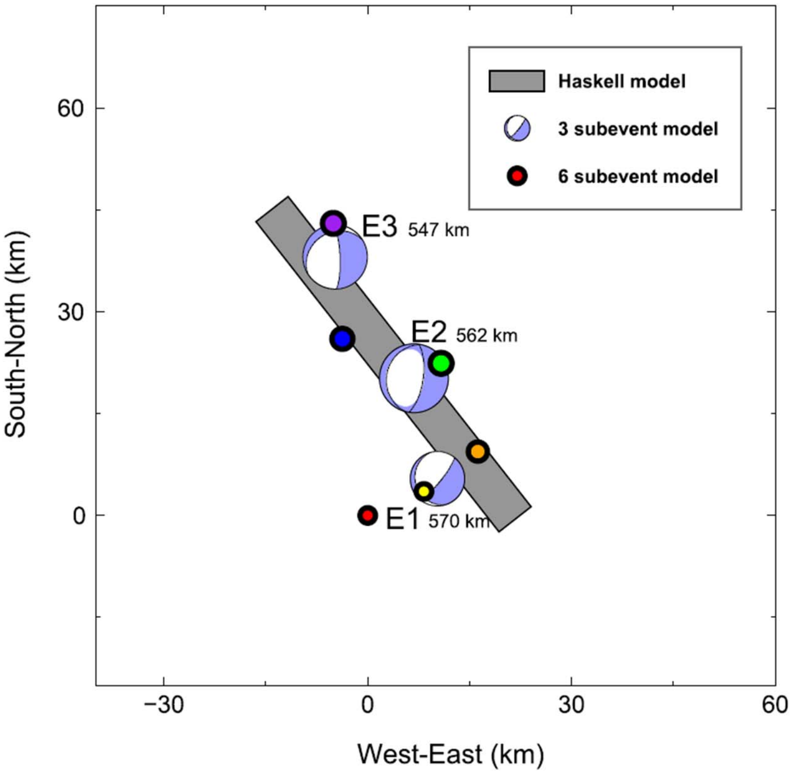

Figure 2.5. Subevent models of different complexity for the M_w 8.2 event. The Haskell model, three-subevent model, and six-subevent model are indicated by the rectangle, beachballs and circles, respectively. Centroid depths of subevents for the three-subevent model are displayed. These models of different levels of complexity reveal consistent overall dimension and directivity of the earthquake. The three-subevent model captures the changes in focal mechanisms along rupture, but not the NE strike within the first stage. Therefore, we conclude that our preferred six-subevent model does not cause artifacts due to over parameterization but still capture important features of the earthquake rupture processes. Details of the Haskell model and the 3-subevent model can be found in Fig. S2.6-S2.7.

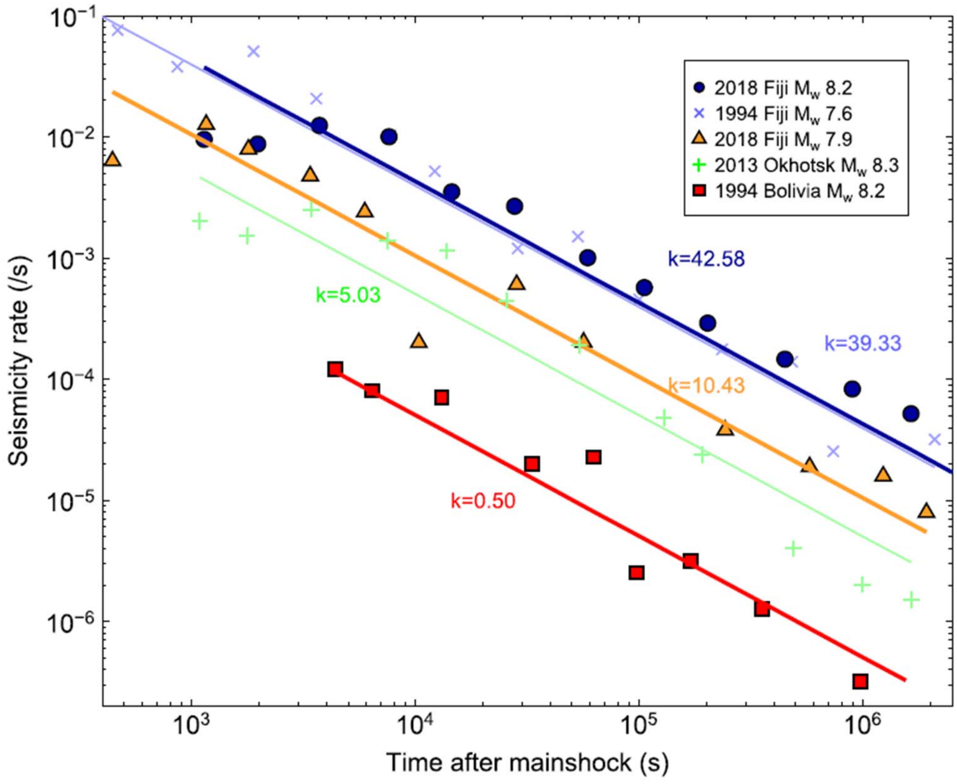

Figure 2.6. Comparison of aftershock productivities of five large deep earthquakes. Aftershock seismicity rates as function of time for the 2018 Fiji doublet, the 1994 Bolivia

and Fiji events, and the 2013 Okhotsk event based on the ISC and refined regional catalogs. The differences due to mainshock magnitude and catalog completeness have been corrected (see supplementary material for details). The aftershock catalog for the 1994 M_w 7.6 Fiji earthquake is from Wiens and McGuire (2000), and the 1994 M_w 8.2 Bolivian aftershocks are from Myers et al. (1995). The parameter k represents the aftershock productivity in the Omori law $n(t) = k/t^p$.

2.4 Implications for Temperature Dependence of Deep Earthquakes

The rupture dimensions of the Fiji doublet from our subevent models seem to contradict the expectation of higher radiation efficiency for large deep earthquakes in a cold subduction zone. Fig. 2.7 displays five large deep earthquakes' subevent models at the same scale, all derived from consistent methodology for comparison. The Fiji doublet's rupture dimensions are similar to that of the 1994 Bolivia earthquake in the warm South American subduction zone and substantially smaller than the 2013 Okhotsk earthquake in the cold Kuril subduction zone. With E_R/M_0 for all these large deep earthquakes being similar to each other (Table 2.1), the radiation efficiency (η_R) estimates depend strongly on the rupture dimensions (L), $\eta_R \propto \Delta\sigma^{-1} \propto L^3/M_0$. However, both the M_w 8.2 and the M_w 7.9 Fiji events may have ruptured more than one fault, which makes the definition of rupture dimension or even the applicability of the stress drop scaling $\Delta\sigma \propto M_0/L^3$ questionable. Furthermore, the rupture dimensions on individual faults are poorly constrained without clear subevent directivity. This is a fundamental limitation of observing the sources from far field. Nevertheless, if we take the overall area in which subevents, especially the ones with the largest moments, are located as a proxy of the rupture dimension, the relatively compact rupture dimensions of the Fiji doublet suggest inefficient ruptures in terms of seismic radiation, despite being in the world's coldest subduction zone. This seems to contradict the view that slab temperature is the primary control on the rupture behaviors of deep earthquakes.

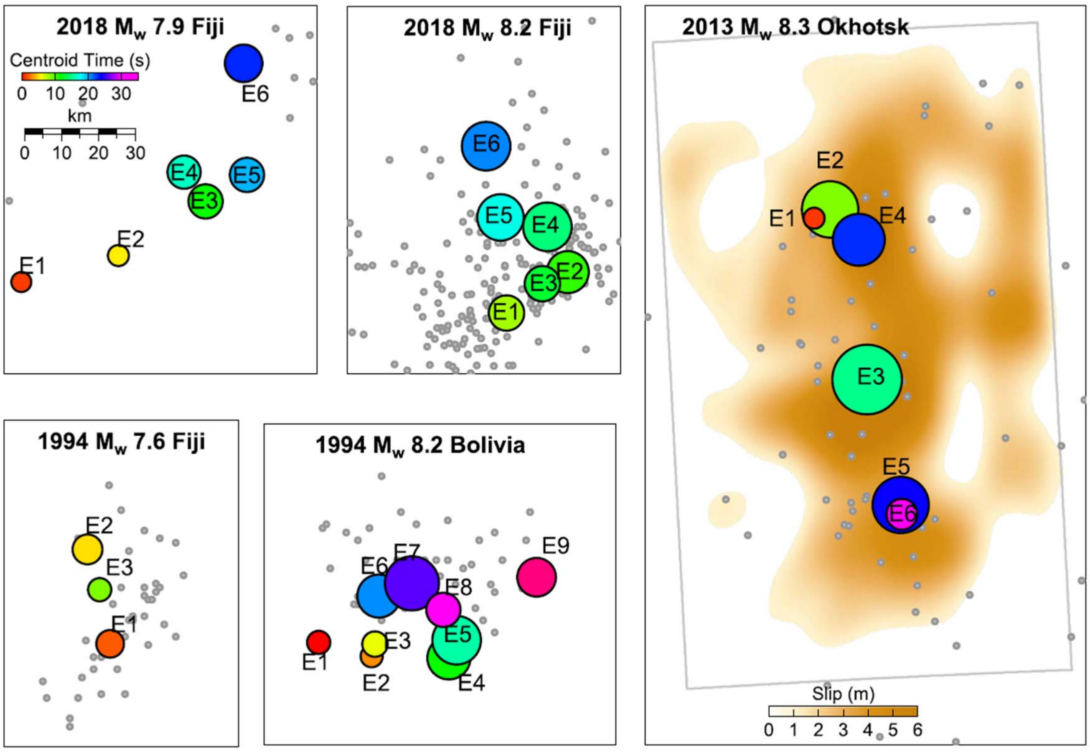

Figure 2.7. Comparison of rupture dimensions of five large deep earthquakes. Subevent models of the five deep events in Fig. 2.5 plotted at the same length scale. Color of the circles indicates subevent centroid time and size represents subevent moment. Gray dots are the aftershocks in one month following the mainshocks. Subevents of the Okhotsk earthquake are plotted on top of a finite fault slip model (Wei et al., 2013).

However, a more detailed comparison of the Fiji M_w 8.2 subevent model and the distribution of background seismicity suggest that the main rupture was not confined to the cold core of the Tonga slab, but occurred mostly in the warmer portion of the slab. Background deep seismicity is generally assumed to represent the cold brittle core of slabs (Antolik et al., 1999; Wiens, 2001). This assumption is supported by observations in areas with high-resolution tomography models and earthquake locations, such as the Japan subduction zone (Tao et al., 2018). In northern Fiji-Tonga, background seismicity forms a southeast (SE)-strike, steeply dipping band (Fig. 2.3A, 2.4B). Wiens et al. (1993) reported a deep double seismic zone with a refined regional catalog and further interpreted as top and bottom edges of a metastable olivine wedge in the cold slab core. They also noticed that the 1994 M_w 7.6 Fiji deep earthquake (Fig. 2.1A), ~40 km NW of the 2018 M_w 8.2 event, started within the background seismic band but ruptured outside the band to the north and northeast. We confirm this observation with our subevent model for the 1994 Fiji event, with a M_w 7.3 subevent E1 in the center of the seismic band and a M_w 7.4 subevent E2 towards northern edge of the band (Fig. 2.3A, Fig. 2.7, Table S2.4). The 2018 M_w 8.2 earthquake had a similar rupture process but was more complicated. It initiated near the center of the background seismicity band and ruptured on a nearly vertical fault perpendicular to the slab strike toward the northeast (NE), away from the slab core. The second stage of rupture (E2, E4~6), which accounts for most of the moment, all ruptured near the edge of the background seismic band, about 30 km away from the center line (Fig. 2.3). Thermal modeling of the subducted Tonga slab suggests that the temperature around the stage 2 rupture would be ~900 °C, 200 °C warmer than the center (Fig. 2.8B). This inferred temperature difference for the two rupture stages is also supported by the distribution of aftershocks, with most aftershocks around the lower-moment stage 1 near slab center (Fig. 2.3A). The temperature dependence of deep aftershock productivity has been observed in many subduction zones (Wiens and Gilbert, 1996), but is happening within the Fiji M_w 8.2 between the cold core and warm slab rim.

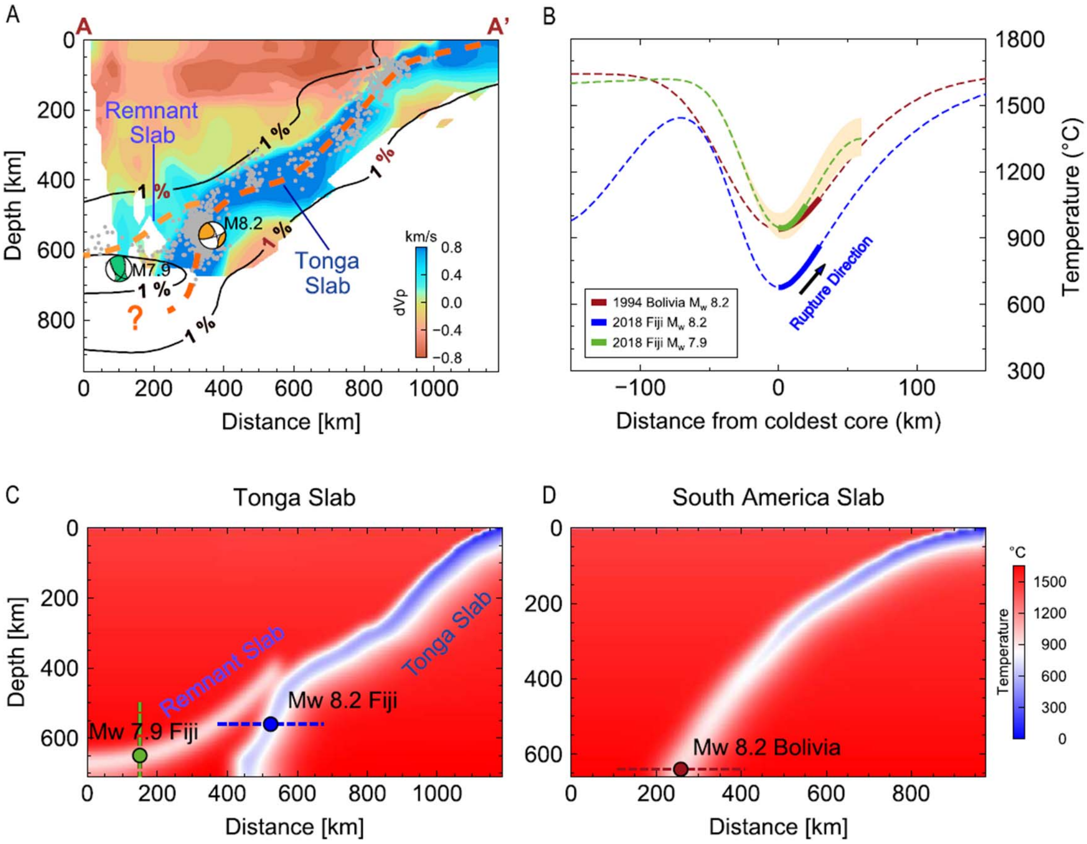

Figure 2.8. Thermal modeling of the Fiji doublet. (A) Tomographic models along cross section AA’ in Fig. 2.1A, showing the Fiji doublet with respect to the Tonga slab and the inferred remnant slab. The solid black lines are the 1% P wave velocity anomaly contours from the GAP model (Fukao and Obayashi, 2013). The background colors show the regional tomography model by Conder and Wiens (2006). The gray dots are the background seismicity. (B) Slab temperature profiles through three large deep earthquakes, whose approximate rupture extents are marked by thick line segments. Temperature uncertainty of the remnant slab is indicated by the shadow in light yellow. (C) Simulated thermal structure for the Tonga slab and the remnant slab. The dashed lines show the profiles in (B). (D) Same as (C) but for the South America slab.

The M_w 7.9 earthquake, on the other hand, appears to occur within the relic Fiji slab, which is overall warmer than the adjacent Tonga slab. This event is a good example of so-called “isolated large deep earthquakes” that occur in region with little background seismicity and produce very few aftershocks (Lundgren and Giardini, 1994). The M_w 7.9 event produced much fewer aftershocks than the M_w 8.2 earthquake (Fig. 2.6), especially if we only consider those within the mainshock rupture area (Fig. 2.7). Other examples of isolated events include the 1954 M_w 7.9 Spain, the 1970 M_w 8.0 Colombia, and the 2015 M_w 7.9 Bonin Islands earthquakes. It is proposed that isolated deep earthquakes occur in warm or remnant slabs that have difficulty nucleating spontaneously. But once started or triggered, isolated deep earthquakes can rupture and completely release the high stress accumulated over time, therefore leaving little residual stress for aftershocks (Kirby et al., 1996; Frohlich, 2006; Cai and Wiens, 2016). The 2018 M_w 7.9 Fiji earthquake occurred where the relic Fiji slab has been long inferred, based on seismicity/focal mechanisms, tomographic models, and geodynamic investigation of the tectonic history (Chen and Brudzinski, 2001; Brudzinski and Chen, 2003; Richards et al., 2011). In particular, both regional (Conder and Wiens, 2006) and global (Fukao and Obayashi, 2013) models show a high velocity zone above the Tonga slab (Fig. 2.8A). The 2009 M_w 7.3 Fiji deep earthquake (Fig. 2.1A) also triggered aftershocks that illuminated the normally aseismic relic slab (Cai and Wiens, 2016). The remnant slab presumably subducted from the initiation of the Vanuatu trench approximately 15 million years (Ma) ago (Seton et al., 2012). The consumed Australian plate would have been formed earlier by the rapid eastward migration of the Tonga subduction zone that initiated at ~50 Ma. Consequently, the lithosphere of the remnant slab would have been about ~35 Ma old (see supplementary material for details). Thermal modeling shows that the coldest core of such remnant slab would be ~1000 °C, similar to the warm South America slab and the warmer rim of the Tonga slab where the Fiji M_w 8.2 stage 2 rupture occurred (Fig. 2.8B-2.8D, Fig. S2.15). Therefore, we propose that the M_w 7.9 earthquake occurred in the relic Fiji slab. The agreements in temperature consistently explain the low background seismicity, compact subevent locations, and low aftershock productivity of the 1994 Bolivia M_w 8.2, 2018 Fiji M_w 7.9, and the stage 2 rupture of the 2018 Fiji M_w 8.2 events.

2.5 Discussion

Recently Fan et al. (2019) applied teleseismic back projection to the Fiji M_w 8.2 event and estimated that the rupture extended ~100 km to the north from the hypocenter, accompanied with changing focal mechanisms and rupture directions. Our source models of the M_w 8.2 event (Fig. 2.5) confirm the two-stage rupture with different directivity and the first stage on a vertical fault plane producing most of the aftershocks, consistent with Fan et al. (2019) 's result. However, the last subevent in our model is located ~50 km to the north of the hypocenter, indicating substantially more compact rupture dimension (50-60 km; Fig. 2.5) than the estimate of 110-150 km in Fan et al. (2019). This difference results in non-trivial difference in average stress drop and the temperature range of slab over which the M_w 8.2 event ruptured (Fig. S2.16). The sum of the six subevent moment tensors has a moment of $2.57 \times 10^{28}\ dyne - cm$, close to the Global CMT moment ($2.52 \times 10^{28}\ dyne - cm$), suggesting that we are not missing any major subevent in our model. The difference in rupture dimension between our study and Fan et al. (2019) may be due to frequency dependent seismic radiation, as commonly observed for shallow megathrust earthquakes (Koper et al., 2011; Yao et al., 2013). Back projection method tracks the radiators of high-frequency energy, while the subevent inversion images the spatial distribution of seismic moment or slip. Therefore, a subevent with strong high-frequency radiation but low moment may be missed in our models.

Earthquakes are often assumed to rupture on a single fault, although in recent years more near field data and high-resolution aftershock patterns have revealed complicated faulting geometry for several large shallow earthquakes (e.g., 2012 Sumatra, 2016 Kaikoura) (Yue et al., 2012; Hamling et al., 2017). Resolving fault plane(s) for deep earthquakes with only far-field seismic data is challenging. In this paper, we take the discrepancy between subevent focal mechanisms and locations (Fig. 2.3, Fig. 2.5) in our subevent models of the Fiji M_w 8.2 earthquake as evidences for rupture over multiple faults during stage 2, though it is unclear how the rupture propagates/jumps though these faults. Another example of multiple-fault rupture of deep earthquakes was suggested by Chen et al. (2014), where they found the subevents of the 2013 Okhotsk M_w 8.3 earthquake cannot fit onto a planar fault. This kind of rupture complexity challenges the conventional interpretation of deep earthquake properties. For example, an average rupture velocity estimated from either subevent modeling, teleseismic back-projection, or finite-fault inversion assuming a simplified fault geometry may not reflect the true source dynamics. The rupture velocity is defined by propagation of the rupture front, but one might approximate it by the subevent centroid migration speed instead. The centroidal rupture speeds V_{cr} of the M_w 8.2 event, considering the subevent depth variations, are about 4.5 km/s (Fig. S2.17) for both stages. However, we believe only the stage 1 V_{cr} is related to a continuous rupture on a vertical fault plane, and the relatively high speed is consistent with the interpretation that the M_w 8.2 event initiated in the cold slab core. On the other hand, because our far-field seismic data cannot resolve the rupture speeds of individual subevents, the stage 2 V_{cr} may represent static/dynamic triggering among subevents on different faults (Tibi et al., 2003b; Wei et al., 2013; Chen et al., 2014; Zhan and Shearer, 2014; Cai and Wiens, 2016). This dilemma also applies to the M_w 7.9 event, for which V_{cr} is ~3.1 km/s for the major subevents (Fig. S2.18) but we cannot define a clear fault plane. Therefore, the subevent rupture speeds of the doublet, which are more important than V_{cr} for the estimation of stress drops and radiation efficiency, are not well constrained and need further investigations.

2.6 Conclusion

In summary, the 2018 Fiji doublet reflects the complex interaction of slabs near the bottom of the mantle transition zone. The relic Fiji slab sank through the mantle wedge, with one end leaning onto the underlying Tonga slab and deforming the cold/brittle Tonga slab core, producing excessive amount of deep seismicity and a local rotation of stress. Meanwhile, the warm relic Fiji slab is under sub-horizontal compression, but has difficulty nucleating and releasing the stress seismically due to the lack of a brittle cold core. Most previous deep earthquakes in the Tonga slab are confined to the brittle core, or only rupture partially outside in some of the larger events (e.g., 1994 Fiji M_w 7.6). The 2018 M_w 8.2 event triggered large and complex ruptures in the warmer portion of slab and generated strong static/dynamic stress perturbations in the surrounding area, including the relic Fiji slab. Three weeks later, one of the triggered events in the relic slab succeeded in cascading into a M_w 7.9 event and released the high stress accumulated over time. Although the Fiji doublet occurred in the world's coldest subduction zone, neither was confined to the cold core of the Tonga slab. Therefore, their unexpected behaviors in terms of rupture dimension, radiation efficiency, and aftershocks support, not contradict, the traditional view that temperature is the main control on deep earthquakes. This emphasizes the importance of detailed mapping of deep earthquake ruptures along with the thermal structure implied by the tectonic evolution of the margin.

2.7 Supplementary Materials

Because ScS and sScS phases propagate vertically through the earth interior at short distances, time differences between ScS and sScS are sensitive to earthquake depth. We download three component seismograms of regional stations (0-30 degrees) from the IRIS DMC, remove the instrumental response, rotate into radial and tangential components, and filter with a two-pole Butterworth band-pass filter of 0.01-0.03 Hz. We use a frequency-wavenumber method to synthesize ScS and sScS waveforms. In the calculation, the velocity model is constructed to represent the local velocity profile by combining the Crust1.0 (Laske et al., 2013), IASP91 (Kennet, 1991) and regional tomography (Conder and Wiens, 2006), mostly to account for the slow mantle wedge. We cross-correlate the observed tangential component seismograms with synthetic waveforms for different focal depths in a time window from 50 s before to 400 s after predicted ScS arrival times. The highest correlation coefficient case corresponds to the optimal focal depth at each station. We then average values from all the stations to estimate the centroid depths of M_w 8.2 and M_w 7.9 earthquakes at 556 km and 655 km, respectively.

Our subevent method combines non-linear inversion for subevent timings, locations and durations, and linear inversion for subevent moment tensors. In the nonlinear part of the inversions, we generate 72 Markov Chains with random first samples, and finally keep 24 chains of best fit, to eliminate the dependency of the inversion on the initial values. We generate Markov chains with a Metropolis-Hasting algorithm, in which the proposal models are generated by sampling through one of the nonlinear parameters while keeping the other nonlinear parameters at their current values (Bodin et al., 2012). This approach provides higher acceptance rate than perturbing all parameters simultaneously, hence it makes our inversion more efficient. We apply a bounded uniform prior probability density function for all non-linear parameters in the inversion. We start with three subevents and increase iteratively to six subevents when main features of the waveforms are fit well. More subevents can lead to better waveform fits but do not change our conclusions significantly.

For the linear subevent moment tensor inversions, we extend the approach used by Minson and Dreger (2008) from single point source to multiple subevents. Subevent moment tensors are constrained to be deviatoric, with no isotropic components. A Tikhonov regularization is applied to minimize the total moment of all subevents. We also regularize the inversions towards double-couple focal mechanisms by penalizing the objective function using non-double-couple component fractions. Another penalty term is adopted to accommodate the moment-duration scaling relationship observed for large earthquakes (Meier et al., 2017) by rejecting models of extremely sharp or flat source time functions. To illustrate how this penalty term works, we define an aspect ratio term for i^{th} subevent

$$p_i = \frac{\sqrt{M_i}}{T_i}, \tag{1}$$

where M_i and T_i are the moment and duration of the subevent, respectively. The average aspect ratio is defined by

$$\bar{p} = \frac{1}{n}\sum_{i=1}^{n} p_i \, . \tag{2}$$

We then define a term characterizing the aspect ratio differences

$$\tilde{p} = \frac{1}{n}\sum_{i=1}^{n}\left[\max\left(\frac{p_i}{\bar{p}}, \frac{\bar{p}}{p_i}\right) - 1\right], \tag{3}$$

and define the penalty term ε=exp($\tilde{p}$/2), which is multiplied to the data misfit.

In the calculation of synthetic waveforms, we use Gaussian-shaped source time functions that accommodate predicted arrival times and durations for all subevents at all stations, and convolve them with Green's functions. The calculation of Green's functions is based on the propagator matrix method with plane wave approximation (Kikuchi and Kanamori, 1991; Qian et al., 2017). The source side velocity model is based on a combination of the Crust1.0 and iasp91 models (Kennet, 1991; Laske et al., 2013).

For the inversion of the Fiji M_w 8.2 earthquake, we use teleseismic P wave records in both displacement and velocity of 61 stations and teleseismic SH wave records in displacement of 59 stations (Fig. S2.4). We also add depth phase pP waves from 19 teleseismic stations to resolve the relative depth differences among subevents (Fig. S2.5), while the absolute centroid depth of the mainshock is constrained by ScS and sScS waves (Fig. S2.1). The data are selected from all available GSN and FDSN stations for good quality and azimuthal coverage. We remove the instrument response and linear trends of the waveforms, and rotate the two horizontal components to the radial and transverse components. We filter the waveforms at 0.005-0.3 Hz and allow time shifts up to 1.0 s for P waves and 3.0 s for SH waves to account for path complexities and picking errors. Location of the first subevent is fixed to the hypocenter location of the mainshock.

For the Fiji M_w 7.9 event, we download and process data of 62 stations for P waves, 60 stations for SH waves and 10 teleseismic stations for pP waves in the same way as that for the M_w 8.2 earthquake (Fig. S2.12-S2.13). We also include P and SH waves recorded by a local station MSVF as another source of constraints on the subevent depths (Fig. S2.14). The waveforms of MSVF are calibrated using a local earthquake of M_w 5.9 on Sept 21, 2018 through a station-specific "amplitude amplification factor" method (Chu et al., 2014). With all the data, we adopt the same subevent inversion procedures.

We use a teleseismic double-difference (tele-DD) algorithm (Pesicek et al., 2010) to relocate earthquakes deeper than 350 km during 2017-2018 around the Fiji region. The tele-DD method is modified from the double difference tomography algorithm (tomoDD) by adding ray tracer from a spherical 3-D Earth model (Zhang and Thurber, 2003). This method applies a 3-D nested regional-global velocity model for ray tracing and calculation of theoretical travel times. Here we use the MITP08 global P wave perturbation model (Li et al., 2008). We select earthquakes within 30 degrees from the epicenter of 2018 M_w 8.2 earthquake and stations within 50 degrees on the ISC catalog. The body wave phase times are downloaded from NEIC (National Earthquake Information Center) catalog to ensure the consistency of the arrival time picking. In the end, we obtain 1841 relocated deep earthquakes, including 495 aftershocks of the M_w 8.2 Fiji earthquakes in 2 months (Fig. S2.8). We use bootstrapping method to estimate relative uncertainties, and randomly select 90% of the differential times to run the algorithm for 10 times. The median relative uncertainties of all three dimensions are less than 1 km.

The aftershock catalog for the 1994 M_w 7.6 Fiji earthquake is from Wiens and McGuire (2000), and the 1994 M_w 8.2 Bolivian aftershocks are from Myers et al. (1995). Both sequences are recorded by regional seismic arrays. For the 2013 Okhotsk M_w 8.3 earthquake and the two 2018 Fiji earthquakes, we use the aftershocks listed on the ISC catalog (53)[53]("International Seismological Centre, On-line Bulletin, http://www.isc.ac.uk, Internatl. Seis. Cent., Thatcham, United Kingdom, 2011

"). We select a time window of 35 days after the mainshocks and the regions in Fig. 2.3A to define the aftershock zones for the 2018 Fiji doublet and 1994 Fiji M_w 7.6 earthquakes. For the 1994 Bolivia and 2013 Okhotsk earthquakes, we use the boxes in Fig. 2.7 to define their aftershock zones. The aftershock productivity is represented by the parameter k in Omori's law $n = k/t^p$, where n is the aftershock rate, and p is the decay rate of the aftershock rate. The seismicity rate is calculated with a moving logarithmic time window for events above the magnitude of completeness (Mc) for each sequence, following Kagan et al. (2004). We use the ZMAP software (Wiemer, 2001) to compute Mc for each sequence. For robustness and simplicity, we assume $p = 1$ for all the sequences. We then correct the aftershock productivity following the aftershock productivity law (Michael and Jones, 1998; Felzer et al., 2004; Helmstetter et al., 2005), $k \sim 10^{b(M_w - M_c)}$, where Mw and Mc are the mainshock moment magnitude and magnitude of completeness, respectively. We assume the

Gutenberg-Richter parameter $b = 1.0$ for all the sequences. The final k values correspond to $M_c = 4.0$ and $M_w = 8.2$ as for the 2018 Fiji M_w 8.2 earthquake.

The two-dimensional thermal models are generated in the following way. At the surface, the temperature of subducting lithosphere follows a half-space cooling model using updates to the digital grid of the age of oceanic plates (Müller et al., 1997). Initially the top surface of the slabs was derived from the Slabs 2.0 surface, based on detailed seismic constraints, including seismicity and seismic reflection profiles (Hayes et al., 2012), except for Tonga where the deeper structure is better represented by the RUM model (Gudmundsson and Sambridge, 1998). With the normal pointing downward from this surface, we generate an initial thermal structure of slabs based on the half space model using the age of the plate at the position of the trench. Conduction was solved for at each depth over a duration equal to the travel time to reach the depth with the local convergence velocity (using the relative velocity vector) using the model from Seton et al. (Seton et al., 2012). This is equivalent to entrainment of surrounding mantle as the slab descends, as found in corner flow models with Stokes flow (Batchelor 1967). However, within the Tonga slab there is substantial deformation within the transition zone with a strain rate up to 5×10^{-16} s^{-1} (Billen et al., 2003) and we incorporated advective thickening by pure shear for strain rates between 10^{-18} s^{-1} to 10^{-14} s^{-1} and for the range of convergence rates (since convergence rates varied during the period required to reach 660 km). This procedure results in thermal structures close to those obtained in fully dynamic models (Billen and Hirth, 2007). The tops of thermal slabs were sharp in the corner of the mantle wedge and then progressively became more diffusive with depth. The procedure allowed the generation of a range of thermal models consistent with the seismic structure. To these thermal fields, we then added an adiabatic temperature increase to derive the temperatures used in the final estimation for the thermal structure around the deep focus earthquakes, assuming a mantle temperature of 1450 °C and an adiabatic gradient of 0.3 °C/km.

The thermal structure of the relic Fiji slab was based on an initial thermal structure with a single initial age based on plate tectonic reconstruction arguments (see below). Based on the structural interpretation (Chen and Brudzinski, 2001), the Fiji relic slab lies flat in the region below central part of the North Fiji Basin, but then tilts upward as it drapes over the Tonga slab. We use the same procedure for computing the subsequent thermal structure as for the Tonga slab. The full dynamic interaction between the relic slab and the Tonga slab is beyond the scope of these exploratory temperature estimates but is likely to have some effect, especially in compressing the isothermals around both the relic slab and the top of the Tonga slab where the two slabs interact with one another.

The isolated seismicity below the North Fiji Basin has been interpreted as arising from the subduction of the Vanuatu slab as the Vanuatu trench rapidly migrated southwestward over the Miocene. The Vanuatu subduction zone is thought to have initiated at the Vitiaz trench and dates to about 12~10 Million years (Ma) following a reversal of subduction of the Pacific beneath the Australian plate (Auzende et al., 1988; Macfarlane et al., 1988). Some reconstructions have the age to be slightly older, around 15 Ma. After the initiation of subduction, the North Fiji Basin formed by rapid rollback of the New Hebrides Trench (Auzende et al., 1988). Using the plate reconstruction from Seton et al. (2012), convergence velocity varied between about 6 and 14 cm/yr since initiation of subduction.

Key to our arguments is that the plate subducting at the Vanuatu trench would have been relatively young as it would have formed by back-arc spreading generated earlier by eastward motion (roll-back) of the Tonga trench. The Tonga-Kermadec trench initiated in the vicinity of the Norfolk Ridge and New Caledonia which is to the west and south west of the present Vanuatu arc. In the Tonga forearc, the oldest rocks associated with subduction initiation have ages 51-50 Ma (Meffre et al., 2012). Hence the eastward migration of the Tonga subduction zone initiated as early as ~50 Ma. The Tasman region underwent a large-scale compressional event associated with subduction initiation (Sutherland et al., 2016), and then a large back arc region would have formed, much of which currently exists in the Oligocene to Miocene-aged South Fiji Basin (Seton et al., 2012). But the northern extension of this basin has now been lost through consumption at the Vanuatu Trench and it is this consumption which is thought to have formed the relic slab. The oldest possible age of the plate that subducted at the Vanuatu arc would have been ~50 Ma (earliest age of Tonga eastward migration) minus ~15 Ma (oldest age for Vanuatu initiation) or 35 Ma. However, it is likely that the plate subducting in the eastern end of the new Vanuatu trench would have been younger. We have computed thermal models with 25, 35, and 45 Ma old slabs, and the cold core temperature differs from -46 °C to +63°C. The uncertainty associated with the age of the subducting plate at Vanuatu is the primary source of error on thermal model for the relic slab. For the Tonga slab, the Kuril slab and the South America slab, the temperature uncertainties are assessed through simulations with varying slab descending velocities and strain rates (Table S2.6). The uncertainties of minimum temperature in these slabs are approximately ± 80 °C. Because we take plate convergence rates beyond the possible range of velocities according to the plate reconstruction from Seton et al. (2012) (Table S2.6), the temperature errors could have been overestimated.

	GCMT moment magnitude (Mw)	**GCMT moment (dyne-cm)**	**W-Phase moment magnitude (Mw)**	**W-Phase moment (dyne-cm)**
2013 Okhotsk M_w 8.3	8.33	3.95×10^{28}	8.32	3.84×10^{28}
1994 Bolivia M_w 8.2	8.21	2.63×10^{28}	8.22	2.74×10^{28}
2018 Fiji M_w 8.2	8.21	2.63×10^{28}	8.20	2.55×10^{28}
2018 Fiji M_w 7.9	7.89	8.61×10^{27}	7.90	8.90×10^{28}
2015 Bonin M_w 7.9	7.85	7.65×10^{27}	7.83	7.04×10^{28}

Table S2.1. Moments and moment magnitudes based on Global CMT and W-Phase CMT catalogs of the five large deep earthquakes discussed in this study.

	Centroid time (s)	**Duration (s)**	**Longitude (°)**	**Latitude (°)**	**Depth (km)**	**Mrr (10^{27} dyne-cm)**	**Mtt (10^{27} dyne-cm)**	**Mpp (10^{27} dyne-cm)**	**Mrt (10^{27} dyne-cm)**	**Mrp (10^{27} dyne-cm)**	**Mtp (10^{27} dyne-cm)**
E1	8.15	5.63	-178.052	-18.150	570.0	-0.0738	-0.6824	0.7561	-2.2880	-0.9928	0.4612
E2	10.88	5.65	-177.895	-18.051	569.1	-1.8049	-0.0322	1.8370	-1.6401	-3.0850	0.2761
E3	13.16	4.99	-177.961	-18.078	556.0	-0.6101	-0.4932	1.1034	-2.0180	-2.4435	0.1253

E4	14.88	5.19	-177.948	-17.940	561.2	-4.4922	0.0919	4.4003	-0.5429	-4.6718	0.6092
E5	17.47	5.80	-178.068	-17.917	553.1	-3.3914	0.5442	2.8472	-0.1296	-3.3733	1.5024
E6	20.81	8.48	-178.104	-17.742	542.8	-2.7986	-0.1346	2.9331	0.8721	-6.0541	1.6149

Table S2.2. Subevent model parameters for the 2018 M_w 8.2 Fiji earthquake. E1 is fixed at the relocated hypocenter location. Absolute depths of subevents are constrained with the centroid depth determined using ScS and sScS waves (Fig. S2.1).

	Centroid time (s)	**Duration (s)**	**Longitude (°)**	**Latitude (°)**	**Depth (km)**	**Mrr (10^{27} dyne-cm)**	**Mtt (10^{27} dyne-cm)**	**Mpp (10^{27} dyne-cm)**	**Mrt (10^{27} dyne-cm)**	**Mrp (10^{27} dyne-cm)**	**Mtp (10^{27} dyne-cm)**
E1	1.44	2.62	179.345	-18.475	645.0	0.0876	0.3615	-0.4491	0.1028	0.0929	0.0964
E2	5.61	3.10	179.594	-18.410	654.8	-0.0265	0.5367	-0.5102	-0.0316	0.1150	0.1964
E3	11.74	7.84	179.817	-18.278	658.4	0.8755	0.5239	-1.3994	-0.4602	-1.2567	1.5151
E4	16.61	5.20	179.762	-18.208	659.1	1.1716	0.6780	-1.8496	-0.3123	-1.0284	0.6051
E5	19.69	6.10	179.922	-18.214	662.2	-0.0835	1.7646	-1.6810	-0.1923	-0.7357	1.2556
E6	23.09	6.54	179.914	-17.941	648.1	1.3025	2.1382	-3.4407	0.4787	-0.7220	0.1900

Table S2.3. Same as Table S2.2 but for the M_w 7.9 Fiji earthquake. E1 is fixed at the NEIC horizontal location. Absolute depths of subevents are constrained with the centroid depth determined using ScS and sScS waves (Fig. S2.1).

	Centroid time (s)	**Duration (s)**	**Longitude (°)**	**Latitude (°)**	**Depth (km)**	**Mrr (10^{27} dyne-cm)**	**Mtt (10^{27} dyne-cm)**	**Mpp (10^{27} dyne-cm)**	**Mrt (10^{27} dyne-cm)**	**Mrp (10^{27} dyne-cm)**	**Mtp (10^{27} dyne-cm)**
E1	1.74	2.84	-178.428	-17.947	572.0	-0.7020	0.5660	0.1360	-0.3572	-0.8333	0.4044
E2	5.58	6.32	-178.462	-17.691	568.2	-0.7118	-0.1288	0.8406	0.2549	-1.3357	0.7210
E3	8.63	3.79	-178.417	-17.829	556.1	-0.0712	-0.0739	0.1452	0.0937	-0.4263	0.3215

Table S2.4. Same as Table S2.2 but for the 1994 M_w 7.6 Fiji earthquake. E1 is fixed at the ISC horizontal location. Depth of E1 is constrained using GCMT centroid depth.

	Convergence velocity (cm/yr)	**Age of subducting plate (Ma)**	**Average slab dip (°)**	**Thermal parameter (km)**
Japan-Kuril slab (2013 Okhotsk M_w 8.3)	8	105	47	6130
South America slab (1994 Bolivia M_w 8.2)	6	50	41	1950
Tonga slab (2018 Fiji M_w 8.2)	12	104	40	7990
Relic Fiji slab (2018 Fiji M_w 7.9)	9	25-35	70 (assumed)	2090-2930

Table S2.5. Calculation and comparison of thermal parameters for four subduction zones that host large deep earthquakes.

(A) **Minimum temperature for the Tonga slab (°C)**

		Strain Rate			
		1×10^{-18}	1×10^{-17}	1×10^{-16}	1×10^{-15}
Descent Velocity (cm/yr)	8.0	760.12	760.15	760.45	763.75
	12.0	687.25	687.27	687.45	689.35
	16.0	638.94	638.95	639.07	640.37
	20.0	603.05	603.06	603.15	604.14

(B) **Minimum temperature for the Japan-Kuril slab (°C)**

		Strain Rate			
		1×10^{-18}	1×10^{-17}	1×10^{-16}	1×10^{-15}
Descent Velocity (cm/yr)	4.0	876.57	876.64	877.30	885.50
	6.0	800.04	800.09	800.51	805.41
	8.0	747.95	747.98	748.29	751.62
	10.0	709.26	709.28	709.51	712.01

(C) **Minimum temperature for the South America slab (°C)**

		Strain Rate			
		1×10^{-18}	1×10^{-17}	1×10^{-16}	1×10^{-15}
Descent Velocity (cm/yr)	4.0	1021.84	1022.07	1022.69	1030.37
	5.0	978.33	978.38	978.89	984.89
	6.0	942.57	942.61	943.04	947.84
	7.0	911.99	912.03	912.39	916.47
	8.0	885.84	885.87	886.19	889.63

Table S2.6. Variations of minimum slab temperatures for the slabs discussed in this study. Different strain rates and descent velocities are considered. (A) Minimum temperature for Tonga slab at the source depth of the 2018 M_w 8.2 Fiji earthquake. The plate convergence rate varies from 8.29 to 19.45 cm/yr since 15 Ma according to the plate reconstruction from Seton et al. (2012). (B) Minimum temperature for Kuril slab at the source depth of the 2013 M_w 8.3 Okhotsk earthquake. The plate convergence rate varies from 7.77 to 9.42 cm/yr since 25 Ma according to the plate reconstructions from Seton et al. (2012). (C) Minimum temperature for South America slab at the source depth of the 1994 M_w 8.2 Bolivia earthquake. The plate convergence rate varies from 5.22 to 7.51 cm/yr since 25 Ma according to the plate reconstructions from Seton et al. (2012).

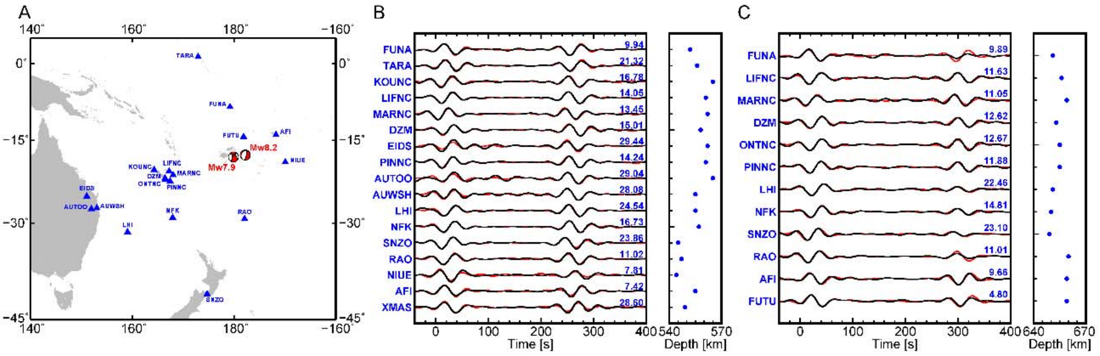

Fig. S2.1. Centroid depth determined with ScS and sScS waves for the Fiji doublet. (A) Map view of the Mw 8.2 and Mw 7.9 events and stations used for depth determination. (B) Observed (black) and synthetic (red) ScS and sScS waveforms of the Mw 8.2 event. Epicentral distances in degrees are indicated by the numbers. The optimal centroid depths of individual stations are retrieved by searching for the highest cross-correlation coefficient between data and synthetics, and are shown in the right panel. The averaged centroid depth is 556 km. (C) Similar to (B) but for the Mw 7.9 event. The averaged centroid depth is 655 km.

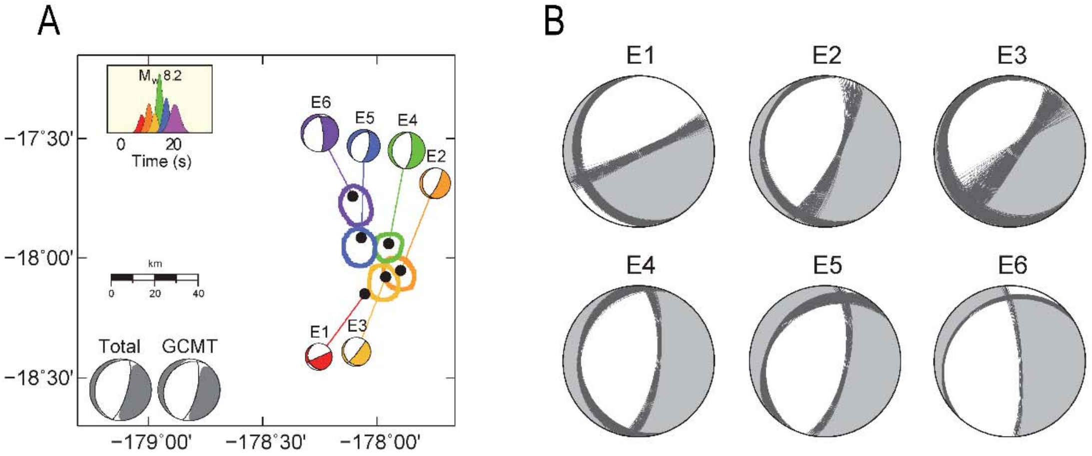

Fig. S2.2. Uncertainties of subevent locations and focal mechanisms for the M_w 8.2 Fiji event. (A) Similar to Fig. 2.3A but with location contours. The contours indicate 95% confidential limits of the horizontal locations for all subevents, derived from Markov Chain samples. E1 is fixed at the USGS NEIC epicenter location. Gray beachballs show comparison between the total moment tensor and the GCMT moment tensor. (B) Scatter of double couple focal mechanisms derived from Markov Chain samples.

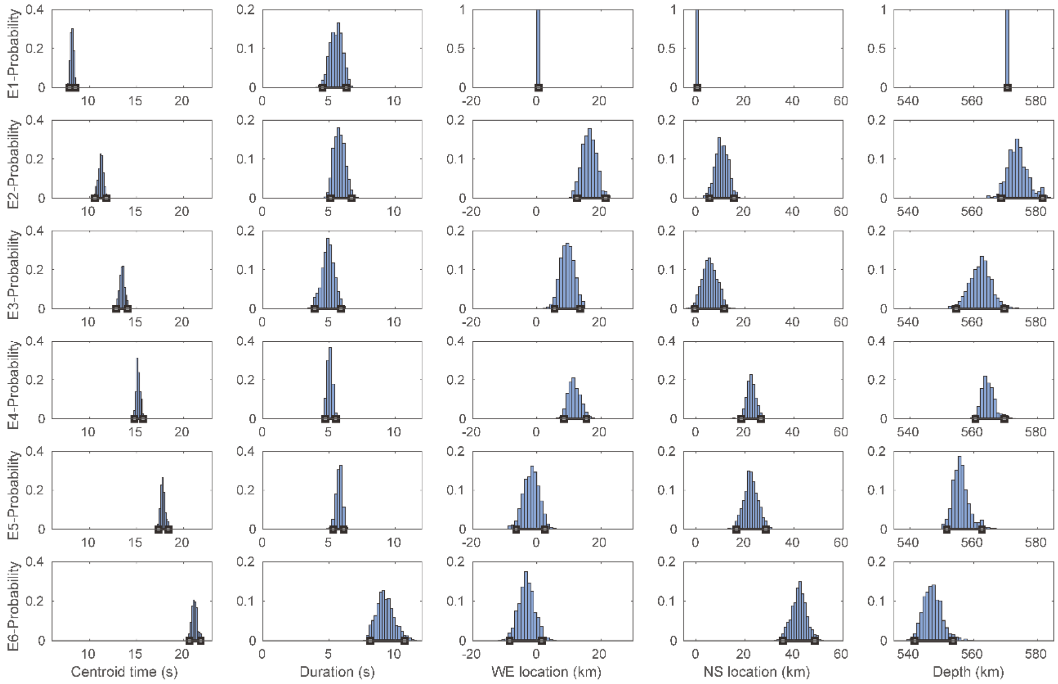

Fig. S2.3. Posterior probability density distributions for the M$_w$ 8.2 Fiji event. Columns from left to right indicates the density distribution of subevent centroid times, durations, east-trending locations, north-trending locations and centroid depths. Rows show the distributions of subevent E1 to E6. Black squares and lines indicate the error bars corresponding to the 95% confidential interval.

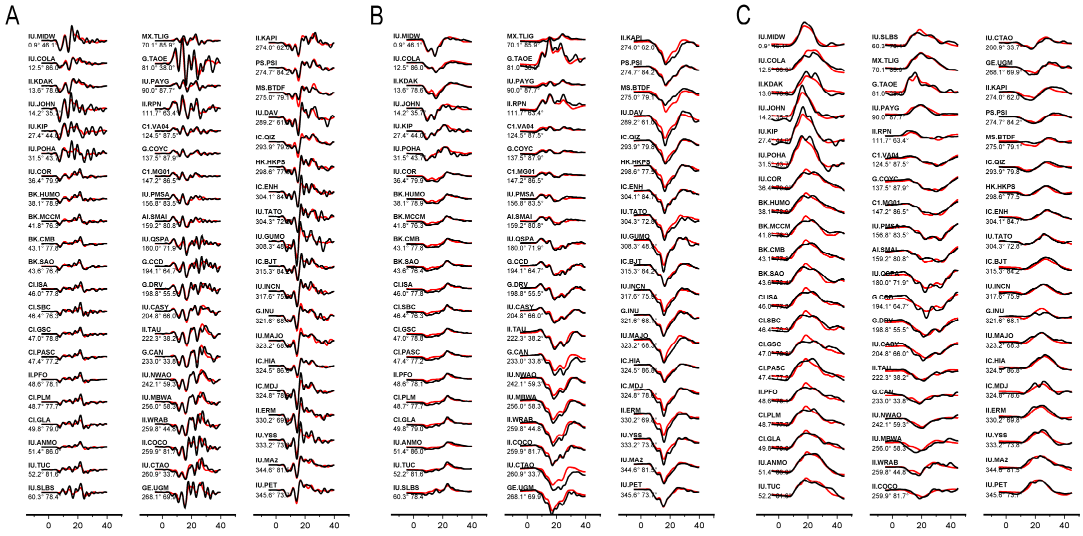

Fig. S2.4. Waveform fits for the preferred subevent model of the M$_w$ 8.2 Fiji earthquake. The waveform records (black) and synthetics (red) are filtered between 0.005-0.33 Hz. The numbers below each trace are the azimuth and distance in degrees. (A) P waves in velocity. (B) P waves in displacement. (C) SH waves in displacement.

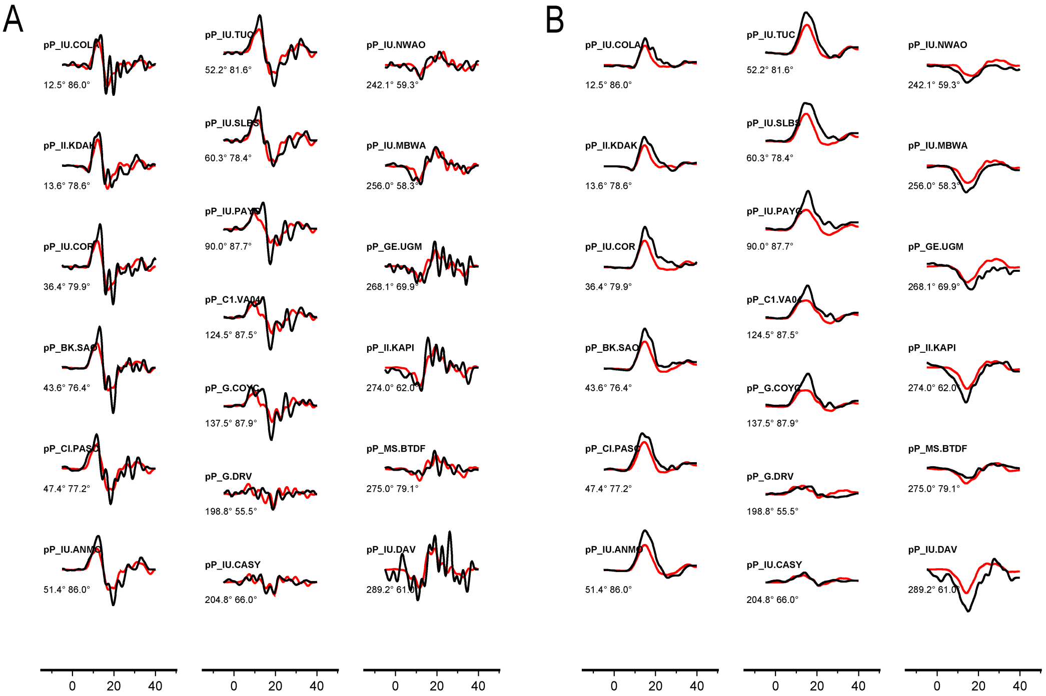

Fig. S2.5. Depth phase pP waveform fits for the preferred subevent model of the M_w 8.2 Fiji event. The waveform records (black) and synthetics (red) are filtered between 0.005-0.33 Hz. The numbers below each trace are the azimuth and distance in degrees. (A) pP waves in velocity. (B) pP waves in displacement.

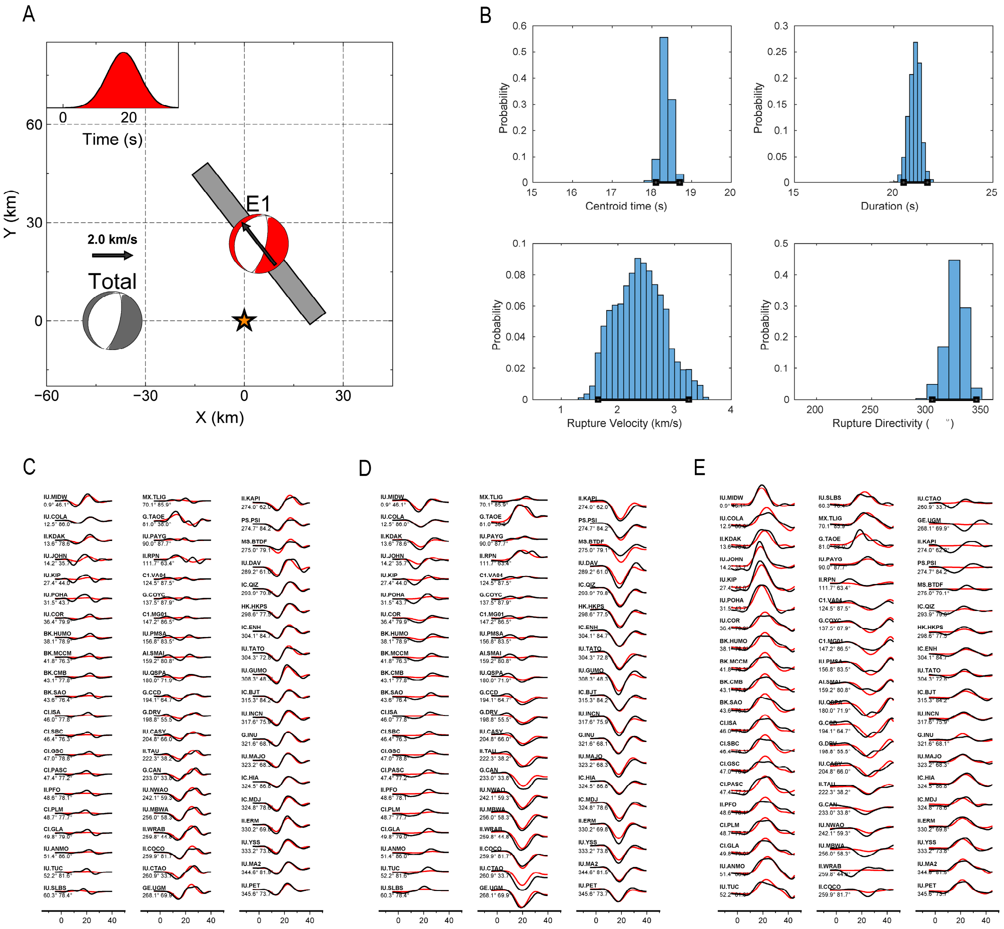

Fig. S2.6. 1-subevent (Haskell source) inversion for the M_W 8.2 Fiji event. The mainshock is characterized by a Haskell rupture model as a planar fault of finite length, with uniform dislocation and constant unilateral rupture velocity (Haskell, 1964; Heaton, 1990), thereby providing constraints on subevent's rupture directivities. (A) Similar to Fig. 2.3A but for the Haskell model with fault dimension and directivity. The long edge of the gray rectangle shows length of the Haskell source. Rupture directivity is indicated by the black arrow which length is proportional to the rupture velocity. (B) Posterior probability density distributions for the 1-subevent source parameters. (C-E) Waveform fits for the 1-subevent model. The waveform records (black) and synthetics (red) are filtered between 0.005-0.1 Hz. (C) P waves in velocity. (D) P waves in displacement. (E) SH waves in displacement.

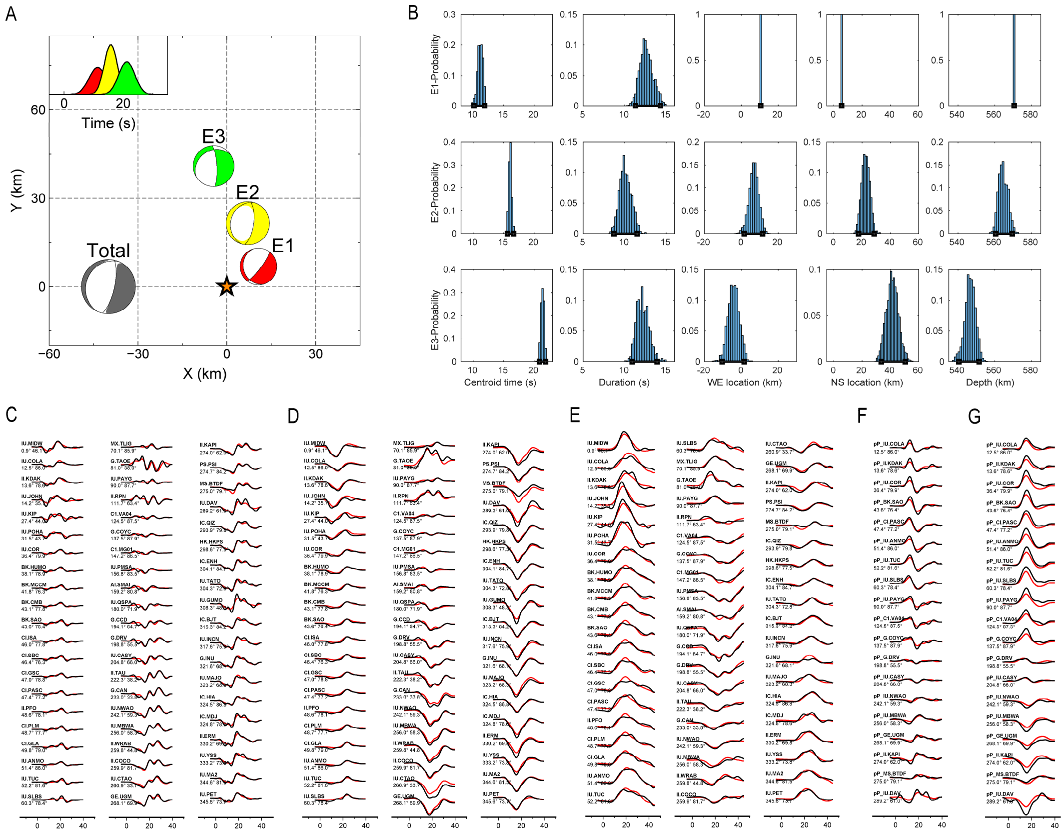

Fig. S2.7. 3-subevent inversion for the M_w 8.2 Fiji event. (A) Similar to Fig. 2.6A but for the 3-subevent model. (B) Posterior probability density distributions for the 3-subevent source parameters. (C-G) Waveform fits for the 3-subevent model. The waveform records (black) and synthetics (red) are filtered between 0.005-0.15 Hz. (C) P waves in velocity. (D) P waves in displacement. (E) SH waves in displacement. (F) pP waves in velocity. (G) pP waves in displacement.

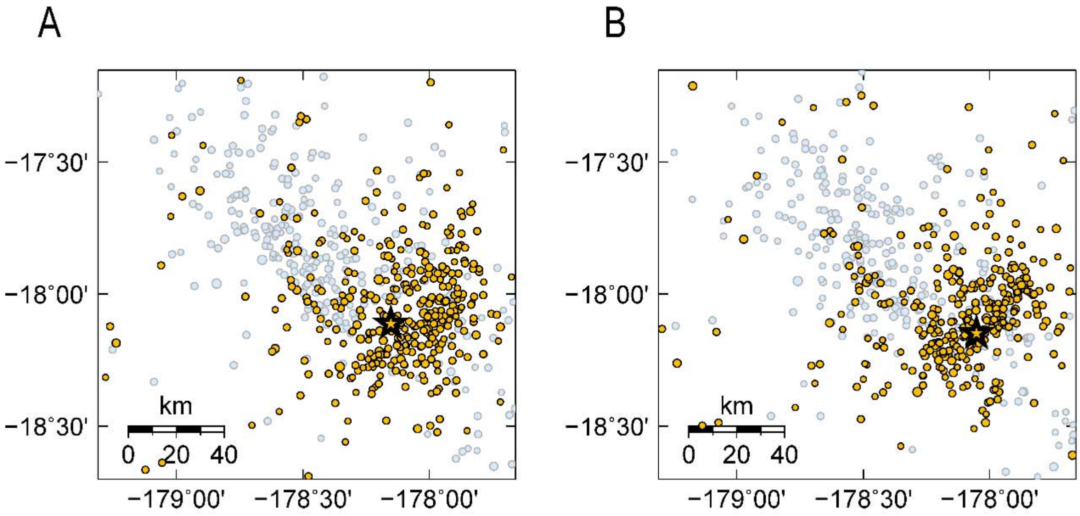

Fig. S2.8. The M_w 8.2 Fiji main shock and its aftershocks in two months before (A) and after relocation (B). The mainshock is indicated by the star. Aftershocks and historical seismicity since 2017 are represented by orange and light blue circles, respectively.

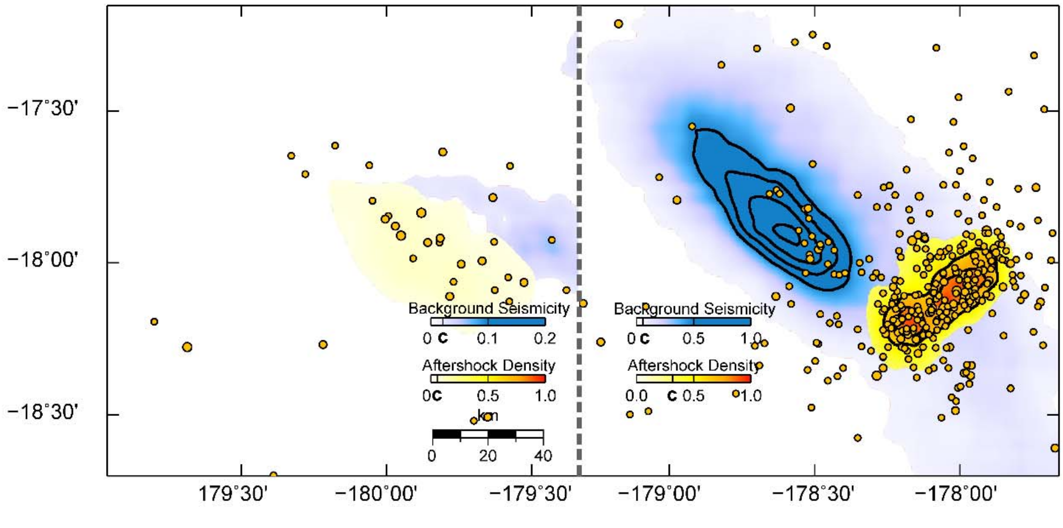

Fig. S2.9. Distribution of aftershocks of the two Fiji events overlaying on the aftershock density and background seismicity density. The M_w 8.2 Fiji main shock and its aftershocks are relocated (Fig. S2.8). Orange dots are the aftershocks in two month following the mainshocks. The densities are calculated using a kernel method to smooth the location. Black solid lines are the density contours. The colors and contours are the same as that in Fig. 2.3A, with the truncations marked on the color bar as “C”.

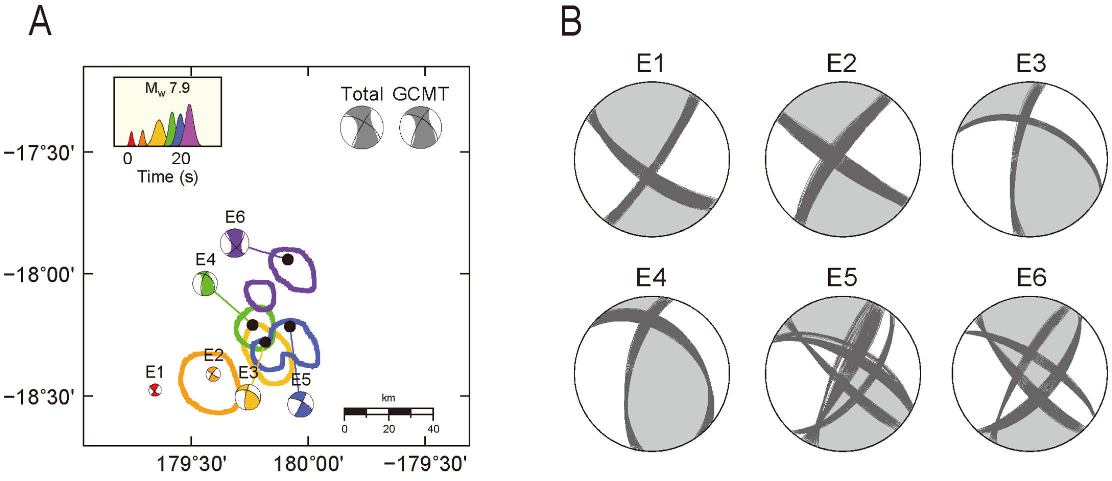

Fig. S2.10. Same as Fig. S2.2 but for the M_w 7.9 Fiji event.

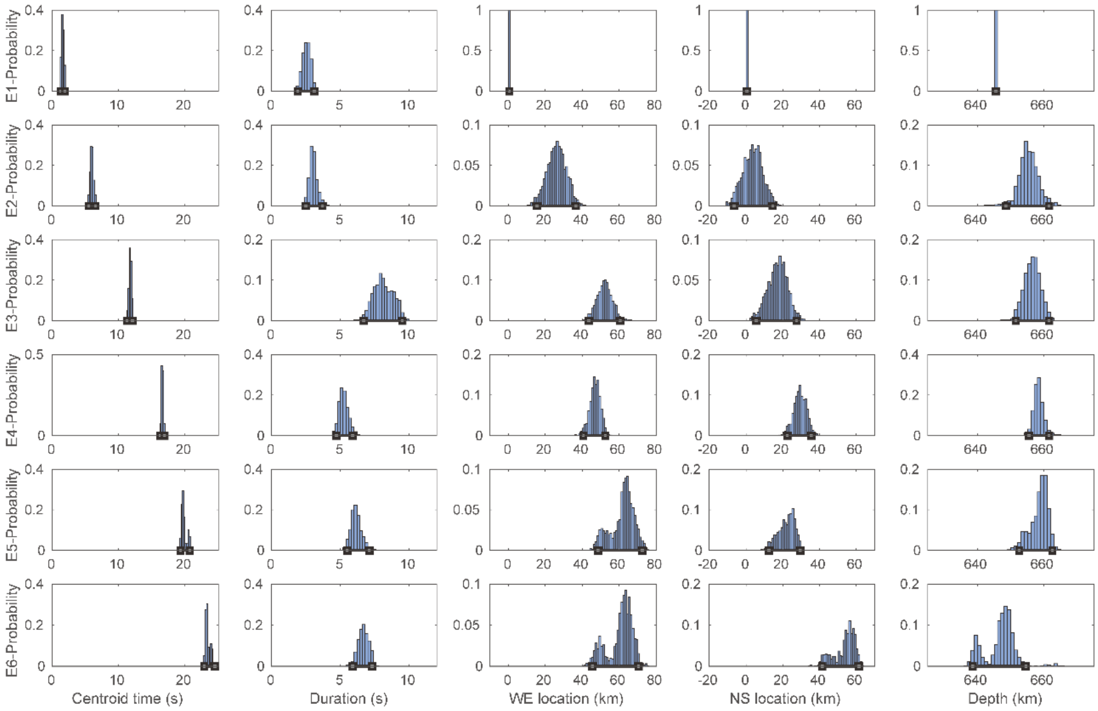

Fig. S2.11. Same as Fig. S2.3 but for the M_w 7.9 Fiji event.

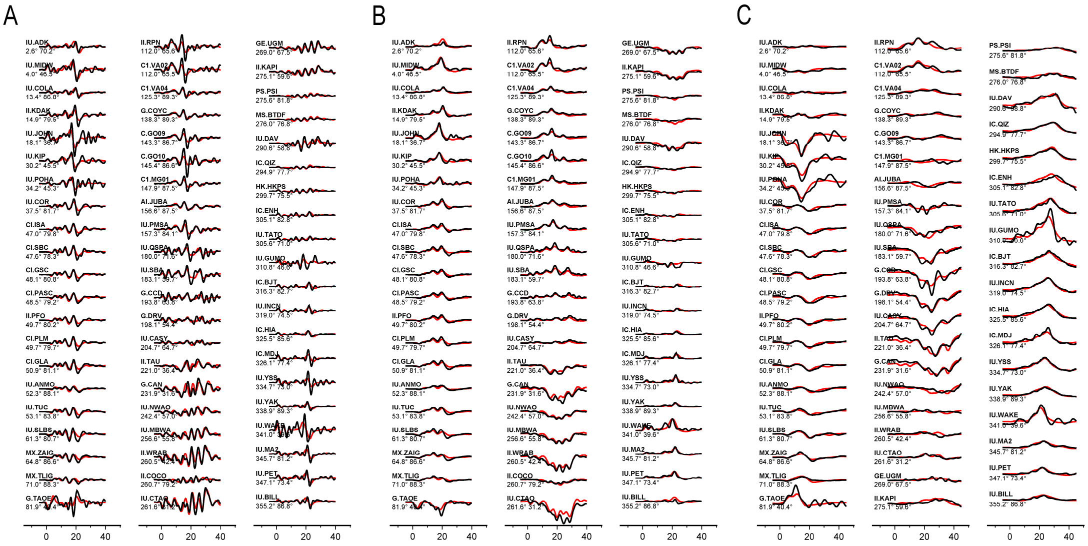

Fig. S2.12. Same as Fig. S2.4 but for the M_w 7.9 Fiji earthquake.

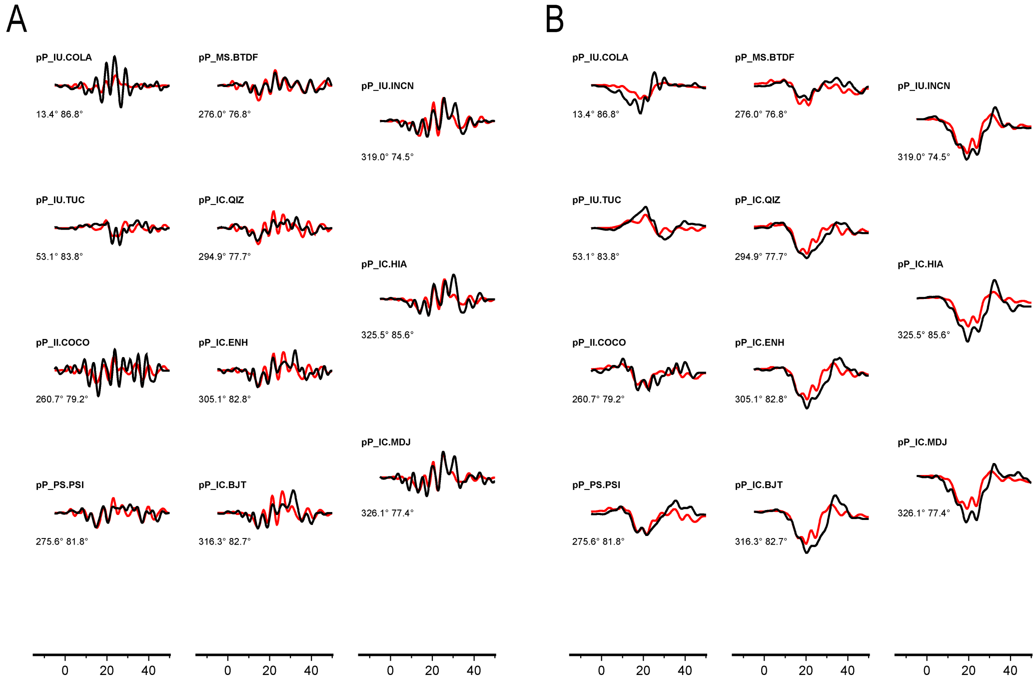

Fig. S2.13. Same as Fig. S2.5 but for the M_w 7.9 Fiji earthquake.

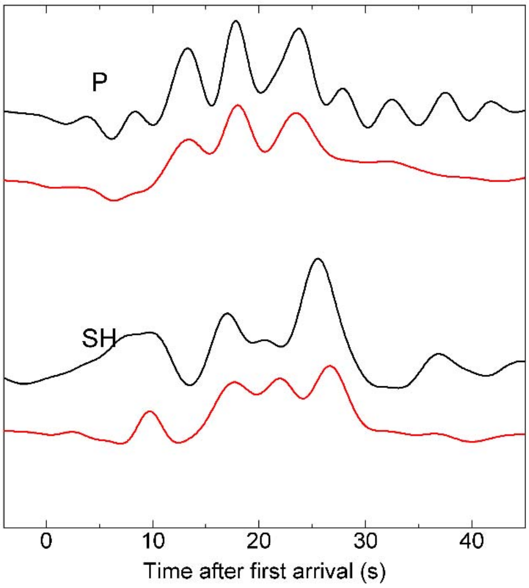

Fig. S2.14. Fittings of up-going P and SH waveforms at station MSVF for the M_w 7.9 event. The waveforms are in displacement, and filtered between 0.005-0.33 Hz. Data and synthetics are plotted in black and red, respectively. Note that the P and SH waves are not plotted in the same amplitude scale.

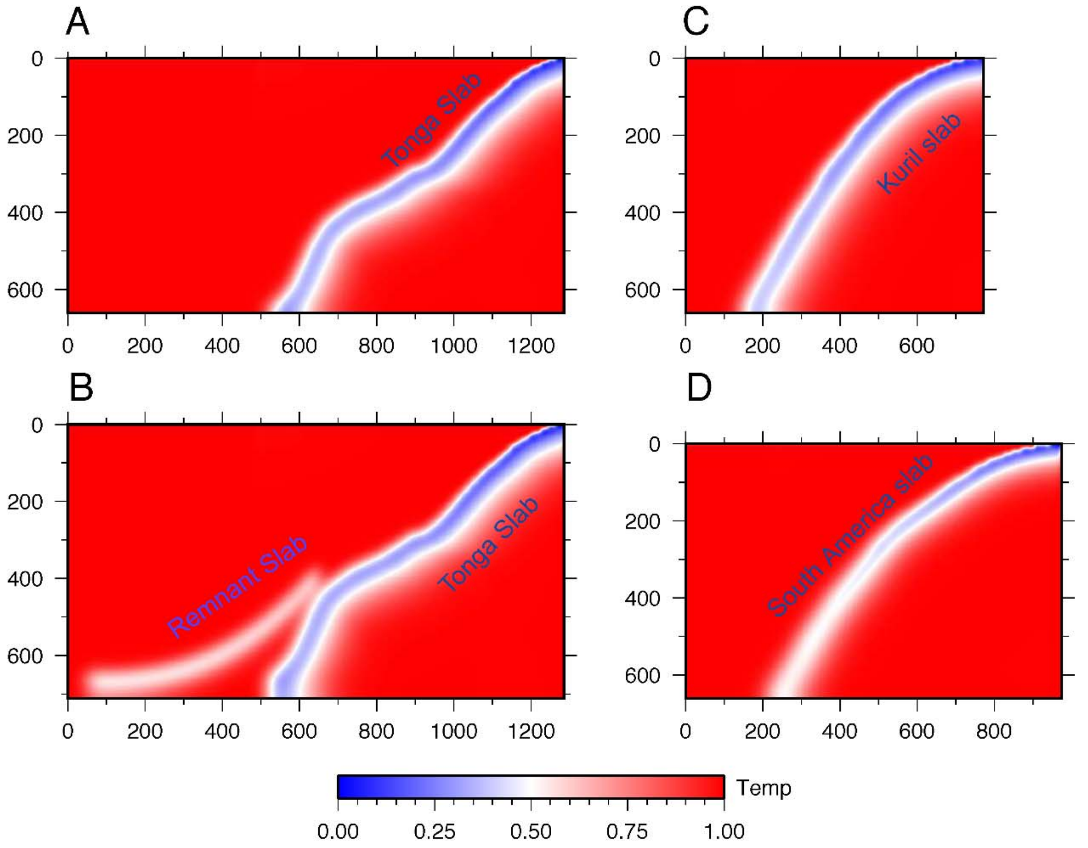

Fig. S2.15. Thermal structure of representative models without adiabatic component of the temperature. The non-dimensional temperature is normalized by 1450 °C. (A) Tonga slab with a convergence velocity of 12 cm/yr and a strain rate of 10^{-15} s^{-1} below 410 km. (B) Tonga slab with relic slab added as described in the supplementary text. (C) Okhotsk slab with a convergence velocity of 8 cm/yr and a strain rate of 10^{-18} s^{-1}. (D) Bolivia slab with a convergence velocity of 6 cm/yr and strain rate of 10^{-18} s^{-1}.

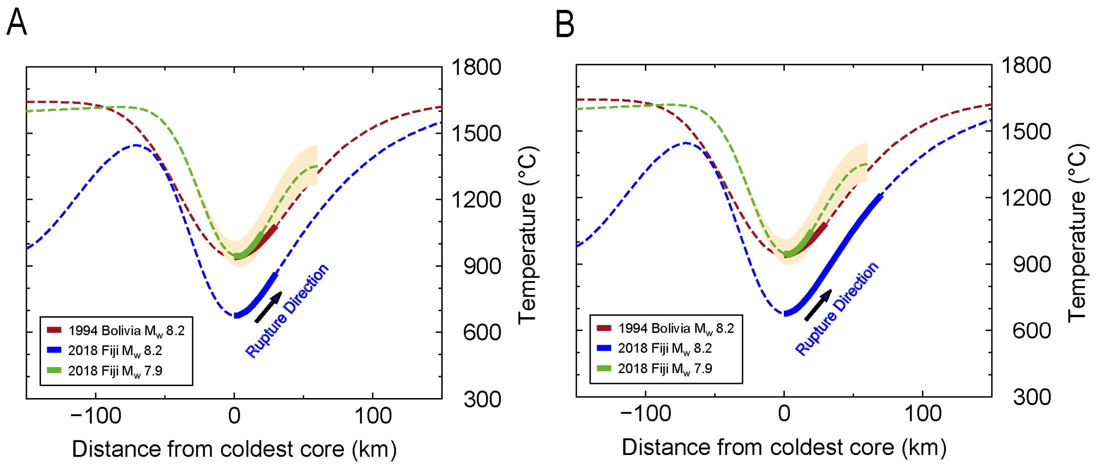

Fig. S2.16. Comparison of the thermal structure across the Mw 8.2 event using the furthest distance of the rupture from the slab cold core based on (A) our model and (B) Fan et al. (2019). The ranges for the 1994 Bolivia Mw 8.2 and 2018 Fiji Mw 7.9 are the same as in Figure 2.8B.

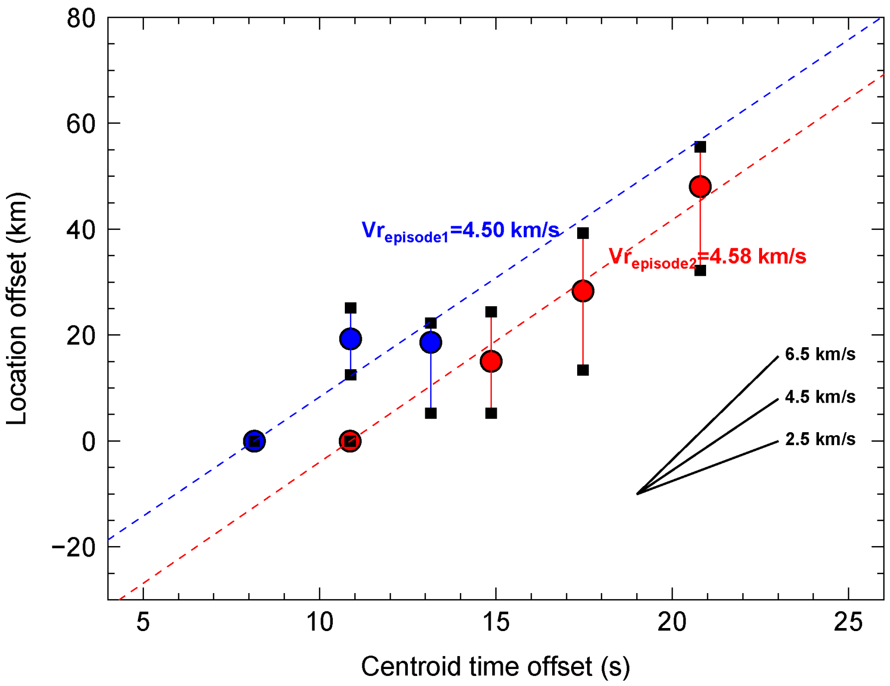

Fig. S2.17. Centroidal rupture velocities in the two episodes of the M_w 8.2 event. Blue dots are the location offset of subevent E1 to E3 projected on the profile CC' (Fig. 2.3). Red dots are the location offset of subevent E2, E4, E5, E6 projected on the profile BB' (Fig. 2.3). Depth changes are also considered in the calculation of these offset distances. The dashed lines show the best fitting rupture velocities. The black squares denote the uncertainties of the subevent locations based on MCMC samples.

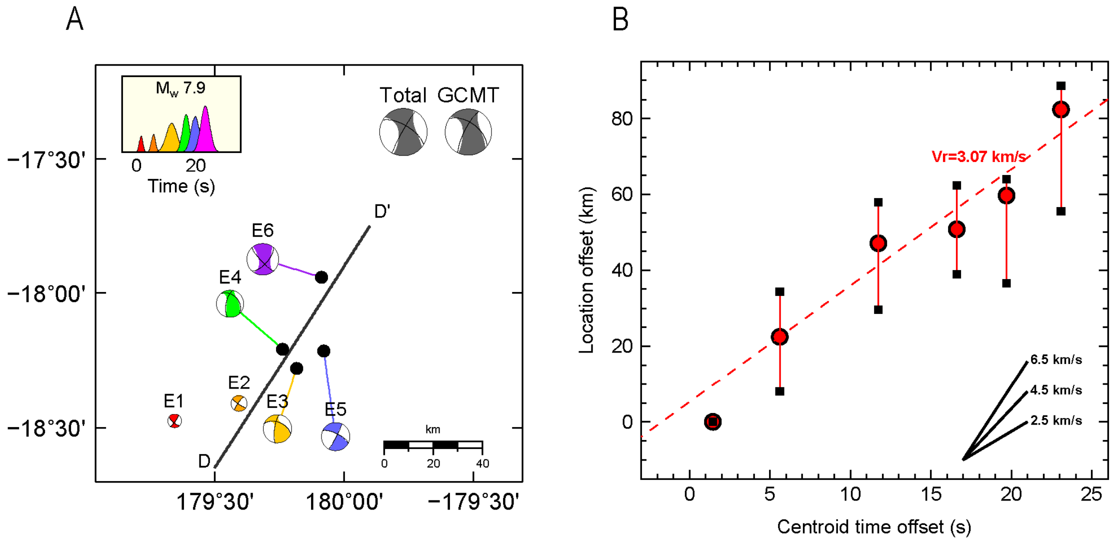

Fig. S2.18. Same as Fig. S2.17 but for the major subevents of the M_w 7.9 earthquake. The subevents are projected on the profile DD' in (A) for calculating the location offsets, with depth differences considered too.

2.8 References

International Seismological Centre, On-line Bulletin, http://www.isc.ac.uk, Internatl. Seis. Cent., Thatcham, United Kingdom, 2011

Antolik, M., Dreger, D., Romanowicz, B., 1999. Rupture processes of large deep-focus earthquakes from inversion of moment rate functions. J. Geophys. Res. 104, 863-894.

Auzende, J.-M., Lafoy, Y., Marsset, B., 1988. Recent geodynamic evolution of the north Fiji basin (southwest Pacific). Geology 16, 925-929.

Batchelor , G.K., 1967. An Introduction to Fluid Dynamics Cambridge University Press, Cambridge, UK.

Billen, M., Hirth, G., 2007. Rheologic controls on slab dynamics. Geochem. Geophys. Geosyst. 8.

Billen, M.I., Gurnis, M., Simons, M., 2003. Multiscale dynamics of the Tonga-Kermadec subduction zone. Geophys. J. Int. 153, 359-388.

Bodin, T., Sambridge, M., Tkalčić, H., Arroucau, P., Gallagher, K., Rawlinson, N., 2012. Transdimensional inversion of receiver functions and surface wave dispersion. Journal of Geophysical Research: Solid Earth 117.

Brudzinski, M.R., Chen, W.P., 2003. A petrologic anomaly accompanying outboard earthquakes beneath Fiji-Tonga: Corresponding evidence from broadband P and S waveforms. Journal of Geophysical Research: Solid Earth 108.

Cai, C., Wiens, D.A., 2016. Dynamic triggering of deep earthquakes within a fossil slab. Geophys. Res. Lett. 43, 9492-9499.

Chen, W.P., Brudzinski, M.R., 2001. Evidence for a large-scale remnant of subducted lithosphere beneath Fiji. Science 292, 2475-2479.

Chen, Y., Wen, L., Ji, C., 2014. A cascading failure during the 24 May 2013 great Okhotsk deep earthquake. J. Geophys. Res. 119, 3035-3049.

Chu, R., Ni, S., Pitarka, A., Helmberger, D.V., 2014. Inversion of source parameters for moderate earthquakes using short-period teleseismic P waves. Pure Appl. Geophys. 171, 1329-1341.

Conder, J.A., Wiens, D.A., 2006. Seismic structure beneath the Tonga arc and Lau back-arc basin determined from joint Vp, Vp/Vs tomography. Geochem. Geophys. Geosyst. 7.

Fan, W., Wei, S.S., Tian, D., McGuire, J.J., Wiens, D.A., 2019. Complex and Diverse Rupture Processes of the 2018 M w 8.2 and M w 7.9 Tonga-Fiji Deep Earthquakes. Geophys. Res. Lett. 46, 2434-2448.

Felzer, K.R., Abercrombie, R.E., Ekström, G.r., 2004. A common origin for aftershocks, foreshocks, and multiplets. Bull. Seismol. Soc. Am. 94, 88-98.

Frohlich, C., 2006. Deep earthquakes. Cambridge University Press, Cambridge, UK.

Fukao, Y., Obayashi, M., 2013. Subducted slabs stagnant above, penetrating through, and trapped below the 660 km discontinuity. J. Geophys. Res. 118, 5920-5938.

Gorbatov, A., Kostoglodov, V., Suárez, G., Gordeev, E., 1997. Seismicity and structure of the Kamchatka subduction zone. Journal of Geophysical Research: Solid Earth 102, 17883-17898.

Gudmundsson, O., Sambridge, M., 1998. A regionalized upper mantle (RUM) seismic model. J. Geophys. Res. 103, 7121-7136.

Gutenberg, B., Richter, C.F., 1956. Earthquake magnitude, intensity, energy, and acceleration: (Second paper). Bull. Seismol. Soc. Am. 46, 105-145.

Hamling, I.J., Hreinsdóttir, S., Clark, K., Elliott, J., Liang, C., Fielding, E., Litchfield, N., Villamor, P., Wallace, L., Wright, T.J., 2017. Complex multifault rupture during the 2016 Mw 7.8 Kaikōura earthquake, New Zealand. Science 356, eaam7194.

Haskell, N., 1964. Total energy and energy spectral density of elastic wave radiation from propagating faults. Bull. Seismol. Soc. Am. 54, 1811-1841.

Hayes, G.P., Moore, G.L., Portner, D.E., Hearne, M., Flamme, H., Furtney, M., Smoczyk, G.M., 2018. Slab2, a comprehensive subduction zone geometry model. Science 362, 58-61.

Hayes, G.P., Wald, D.J., Johnson, R.L., 2012. Slab 1.0: a three-dimensional model of global subduction zone geometries. J. geophys. Res.: Solid Earth 117.

Heaton, T.H., 1990. Evidence for and implications of self-healing pulses of slip in earthquake rupture. Phys. Earth Planet. Inter. 64, 1-20.

Helmstetter, A., Kagan, Y.Y., Jackson, D.D., 2005. Importance of small earthquakes for stress transfers and earthquake triggering. Journal of Geophysical Research: Solid Earth 110.

Houston, H., 2015. Deep Earthquakes. 329-354.

Kagan, Y.Y., 2004. Short-term properties of earthquake catalogs and models of earthquake source. Bull. Seismol. Soc. Am. 94, 1207-1228.

Kanamori, H., Anderson, D.L., Heaton, T.H., 1998. Frictional melting during the rupture of the 1994 Bolivian earthquake. Science 279, 839-842.

Kanamori, H., Ross, Z.E., 2018. Reviving mB. Geophys. J. Int.

Kennet, B., 1991. IASPEI 1991 seismological tables. Terra Nova 3, 122-122.

Kikuchi, M., Kanamori, H., 1991. Inversion of complex body waves—III. Bull. Seismol. Soc. Am. 81, 2335-2350.

Kirby, S.H., Durham, W.B., Stern, L.A., 1991. Mantle phase changes and deep-earthquake faulting in subducting lithosphere. Science 252, 216-225.

Kirby, S.H., Stein, S., Okal, E.A., Rubie, D.C., 1996. Metastable mantle phase transformations and deep earthquakes in subducting oceanic lithosphere. Rev. Geophys. 34, 261-306.

Koper, K.D., Hutko, A.R., Lay, T., Ammon, C.J., Kanamori, H., 2011. Frequency-dependent rupture process of the 2011 M w 9.0 Tohoku Earthquake: Comparison of short-period P wave backprojection images and broadband seismic rupture models. Earth, planets and space 63, 16.

Laske, G., Masters, G., Ma, Z., Pasyanos, M., 2013. Update on CRUST1.0 - A 1-degree global model of Earth’s crust. Geophys. Res. Abstracts 15, Abstract EGU2013-2658.

Li, C., van der Hilst, R.D., Engdahl, E.R., Burdick, S., 2008. A new global model for P wave speed variations in Earth's mantle. Geochem. Geophys. Geosyst. 9.

Lundgren, P., Giardini, D., 1994. Isolated deep earthquakes and the fate of subduction in the mantle. J. Geophys. Res. 99, 15833.

Macfarlane, A., Carney, J.N., Crawford, A.J., Greene, H.G., 1988. Vanuatu - A review of the onshore geology, in: Greene, H.G., Wong, F.L. (Eds.), Geology and offshore resources of Pacific island arcs - Vanuatu region, Circum-Pacific Council for Energy and Mineral Resources Earth Science Series. Circum-Pacific Council for Energy and Mineral Resources, Houston, TX, pp. 45-91.

Meffre, S., Falloon, T.J., Crawford, T.J., Hoernle, K., Hauff, F., Duncan, R.A., Bloomer, S.H., Wright, D.J., 2012. Basalts erupted along the Tongan fore arc during subduction initiation: Evidence from geochronology of dredged rocks from the Tonga fore arc and trench. Geochem. Geophys. Geosyst. 13.

Meier, M.-A., Ampuero, J., Heaton, T.H., 2017. The hidden simplicity of subduction megathrust earthquakes. Science 357, 1277-1281.

Michael, A.J., Jones, L.M., 1998. Seismicity alert probabilities at Parkfield, California, revisited. Bull. Seismol. Soc. Am. 88, 117-130.

Minson, S.E., Dreger, D.S., 2008. Stable inversions for complete moment tensors. Geophys. J. Int. 174, 585-592.

Müller, R.D., Roest, U.R., Royer, J.-Y., Gahagan, L.M., Sclater, J.G., 1997. Digital isochrons of the world's ocean floor. J. Geophys. Res. 102, 3211-3214.

Myers, S.C., Wallace, T.C., Beck, S.L., Silver, P.G., Zandt, G., Vandecar, J., Minaya, E., 1995. Implications of spatial and temporal development of the aftershock sequence for the Mw 8.3 June 9, 1994 deep Bolivian earthquake. Geophys. Res. Lett. 22, 2269-2272.

Peng, Z., Vidale, J.E., Ishii, M., Helmstetter, A., 2007. Seismicity rate immediately before and after main shock rupture from high-frequency waveforms in Japan. Journal of Geophysical Research: Solid Earth 112.

Pesicek, J., Thurber, C., Zhang, H., DeShon, H., Engdahl, E., Widiyantoro, S., 2010. Teleseismic double-difference relocation of earthquakes along the Sumatra-Andaman subduction zone using a 3-D model. Journal of Geophysical Research: Solid Earth 115.

Qian, Y., Ni, S., Wei, S., Almeida, R., Zhang, H., 2017. The effects of core-reflected waves on finite fault inversions with teleseismic body wave data. Geophys. J. Int. 211, 958-973.

Richards, S., Holm, R., Barber, G., 2011. When slabs collide: A tectonic assessment of deep earthquakes in the Tonga-Vanuatu region. Geology 39, 787-790.

Seton, M., Müller, R., Zahirovic, S., Gaina, C., Torsvik, T., Shephard, G., Talsma, A., Gurnis, M., Turner, M., Maus, S., 2012. Global continental and ocean basin reconstructions since 200 Ma. Earth-Science Reviews 113, 212-270.

Sutherland, R., Collot, J., Bache, F., Henrys, S., D., B., Browne, G.H., F., L.M.J., Morgans , H.E.G., Hollis, C.J., Clowes, C., Mortimer, N., Rouillard, P., Gurnis, M., Etienne, S., Stratford, W., 2016. Widespread compression associated with forced Tonga-Kermadec subduction initiation. Nature Geoscience.

Tao, K., Grand, S.P., Niu, F., 2018. Seismic structure of the upper mantle beneath Eastern Asia from full waveform seismic tomography. Geochem. Geophys. Geosyst. 19, 2732-2763.

Tibi, R., Bock, G., Wiens, D.A., 2003a. Source characteristics of large deep earthquakes: Constraint on the faulting mechanism at great depths. J. Geophys. Res. 108, 2091.

Tibi, R., Wiens, D.A., Inoue, H., 2003b. Remote triggering of deep earthquakes in the 2002 Tonga sequences. Nature 424, 921-925.

Utsu, T., Ogata, Y., 1995. The centenary of the Omori formula for a decay law of aftershock activity. JPE 43, 1-33.

Warren, L.M., Hughes, A.N., Silver, P.G., 2007. Earthquake mechanics and deformation in the Tonga-Kermadec subduction zone from fault plane orientations of intermediate-and deep-focus earthquakes. Journal of Geophysical Research: Solid Earth 112.

Wei, S., Helmberger, D., Zhan, Z., Graves, R., 2013. Rupture complexity of theMw8.3 sea of okhotsk earthquake: Rapid triggering of complementary earthquakes? Geophys. Res. Lett. 40, 5034-5039.

Wiemer, S., 2001. A software package to analyze seismicity: ZMAP. Seismol. Res. Lett. 72, 373-382.

Wiens, D.A., 2001. Seismological constraints on the mechanism of deep earthquakes: temperature dependence of deep earthquake source properties. Phys. Earth Planet. Inter. 127, 145-163.

Wiens, D.A., Gilbert, H.J., 1996. Effect of slab temperature on deep-earthquake aftershock productivity and magnitude-frequency relations. Nature 384, 153-156.

Wiens, D.A., McGuire, J.J., 2000. Aftershocks of the March 9, 1994, Tonga earthquake: The strongest known deep aftershock sequence. Journal of Geophysical Research: Solid Earth 105, 19067-19083.

Wiens, D.A., McGuire, J.J., Shore, P.J., 1993. Evidence for transformational faulting from a deep double seismic zone in Tonga. Nature 364, 790-793.

Yao, H., Shearer, P.M., Gerstoft, P., 2013. Compressive sensing of frequency-dependent seismic radiation from subduction zone megathrust ruptures. Proc. Natl. Acad. Sci. 110, 4512-4517.

Ye, L., Lay, T., Kanamori, H., Koper, K.D., 2013. Energy release of the 2013 Mw 8.3 Sea of Okhotsk earthquake and deep slab stress heterogeneity. Science 341, 1380-1384.

Ye, L., Lay, T., Kanamori, H., Zhan, Z., Duputel, Z., 2016. Diverse rupture processes in the 2015 Peru deep earthquake doublet. Science advances 2, e1600581.

Yue, H., Lay, T., Koper, K.D., 2012. En échelon and orthogonal fault ruptures of the 11 April 2012 great intraplate earthquakes. Nature 490, 245.

Zhan, Z., 2017. Gutenberg–Richter law for deep earthquakes revisited: a dual-mechanism hypothesis. Earth Planet. Sci. Lett. 461, 1-7.

Zhan, Z., Kanamori, H., Tsai, V.C., Helmberger, D.V., Wei, S., 2014. Rupture complexity of the 1994 Bolivia and 2013 Sea of Okhotsk deep earthquakes. Earth Planet. Sci. Lett. 385, 89-96.

Zhan, Z., Shearer, P.M., 2014. Dynamic Triggering of Deep Earthquakes—a Global Perspective, AGU Fall Meeting, San Francisco, Calif.

Zhang, H., Thurber, C.H., 2003. Double-difference tomography: The method and its application to the Hayward fault, California. Bull. Seismol. Soc. Am. 93, 1875-1889.

Chapter 3

MULTI-FAULT STRUCTURE OF THE 2019 RIDGECREST SEQUENCE

Ross, Zachary E., Benjamín Idini, Zhe Jia, Oliver L. Stephenson, Minyan Zhong, Xin Wang, Zhongwen Zhan et al. "Hierarchical interlocked orthogonal faulting in the 2019 Ridgecrest earthquake sequence." In: *Science* 366, no. 6463 (2019): 346-351. Doi: 10.1126/science.aaz0109

Jia, Zhe, Xin Wang, and Zhongwen Zhan. "Multifault models of the 2019 Ridgecrest sequence highlight complementary slip and fault junction instability." In: *Geophysical Research Letters* 47, no. 17 (2020): e2020GL089802. Doi: 10.1029/2020GL089802.

3.1 Abstract

A nearly 20-year hiatus in major seismic activity in southern California ended on 4 July 2019 with a sequence of intersecting earthquakes near the city of Ridgecrest, California. This sequence included a foreshock with a moment magnitude (Mw) of 6.4 followed by a Mw 7.1 mainshock nearly 34 hours later. Integrative view of this sequence shows it ruptured an unmapped network of interlocking orthogonal faults, which poses challenges in understanding the physical processes. Modeling of the ruptures relies on fault geometries at depth, which are usually assumed based on surface traces and aftershocks. Here we use seismic and geodetic data to jointly constrain the fault geometries and slip distributions. We first represent the first-order rupture processes with a series of subevents, then conduct slip inversions with subevent-guided fault geometries. We find that the foreshock sequentially ruptured the NW- and SW-striking faults starting from their junction. The mainshock initiated at a complex three-fault junction along the extension of the foreshock NW rupture, with major slip first occurring bilaterally near the hypocenter and then minor unilateral slip later to the southeast end. The slip distributions of the foreshock and mainshock are complementary to each other on the overlapping fault section.

3.2 Introduction

In July 2019, a sequence of earthquakes including a Mw 6.4 foreshock and a Mw 7.1 mainshock struck the Ridgecrest region in the Eastern California Shear Zone in United States. This sequence, together with the 1992 Mw 7.3 Landers earthquake and 1999 Mw 7.1 Hector Mine earthquake, account for part of the slip budget between Pacific plate and North America plate (Hauksson et al., 1993; Hauksson et al., 2002). Field measurements, geodetic observations, and aftershock relocations indicate that the Ridgecrest sequence ruptured the surface along several interlocking and orthogonal faults surrounding the main rupture zone (Ross et al., 2019; Xu et al., 2020). These complexities pose challenges in understanding the rupture physics and regional hazard assessments. Using fault geometry assumptions based on surface traces and aftershock patterns, investigations of the Ridgecrest rupture processes and slip distributions have formed a consensus that the Mw 6.4 foreshock ruptured a NE-SW fault segment, followed by the Mw 7.1 mainshock occurring on the ~40 km NW-SE striking fault (Barnhart et al., 2019; Liu et al., 2019; Ross et al., 2019; Chen et al., 2020; Goldberg et al., 2020; Ramos et al., 2020; Wang et al., 2020). However, the kinematic details of the foreshock rupture remain controversial, as some studies suggest the foreshock involved two orthogonal segments (Liu et al., 2019; Ross et al., 2019; Yang et al., 2020), while others prefer that the foreshock only ruptured the NE-SW fault branch(s) (Barnhart et al., 2019; Goldberg et al., 2020). Furthermore, the M7.1 rupture process at depth and its relation with the surface traces are still unclear.

Although surface rupture traces and aftershock distributions are closely related to the fault geometries, faults with major slips at depth may not be directly manifested by these observations. For the Ridgecrest sequence, the surface trace observations show the multi-scale complexity of the fault system (DuRoss et al., 2020; Ponti et al., 2020), which appears inconsistent with the deeper aftershock seismicity (Wang and Zhan, 2020b). Specifically, the foreshock surface rupture traces do not verify its NW striking aftershock band, and the mainshock surface ruptures are offset by ~2 km from its aftershock zone at most (Fig. 3.1A). This discrepancy could cause ambiguity in fault geometry choices, thus potentially biasing the slip distribution in finite-fault inversions (Ragon et al., 2019). To characterize the first order spatiotemporal rupture complexity while avoiding this ambiguity, subevent methods have been developed and successfully applied to complex large earthquakes (Zhan et al., 2014; Shi et al., 2018; Jia et al., 2020). Subevent inversions parameterize earthquakes into multiple point source subevents of varying focal mechanisms, timings, and locations. This parameterization allows simple yet flexible accommodation of multiple fault segments, and often captures the first-order rupture complexities.

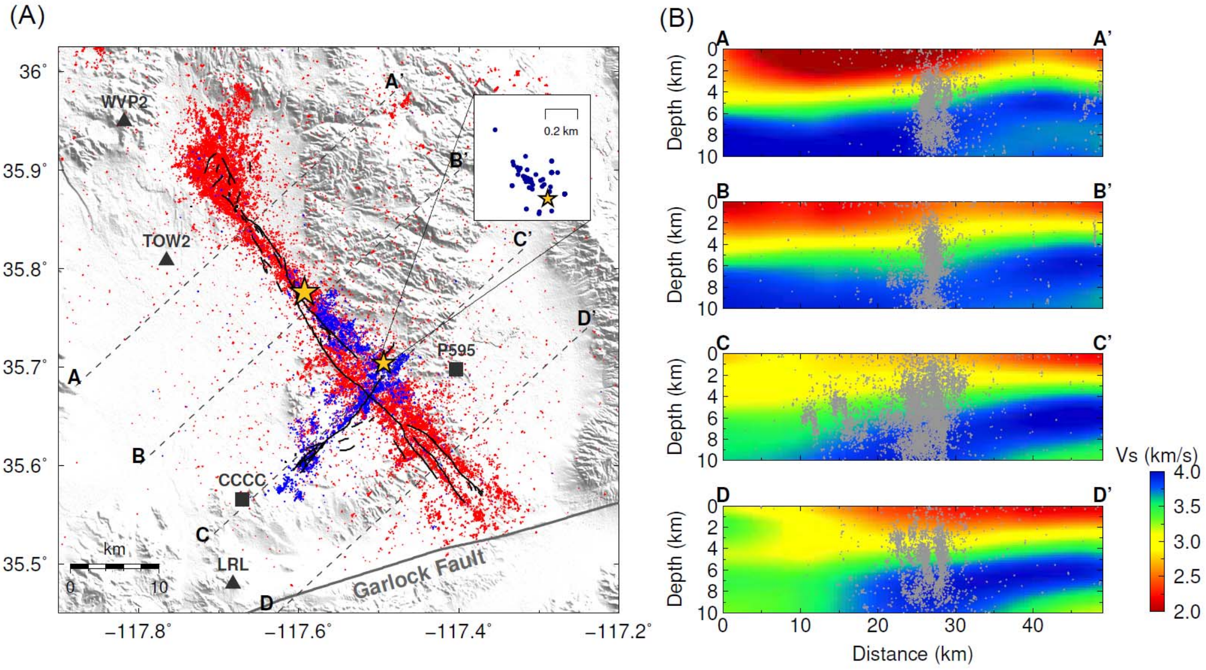

Figure 3.1. Overview of the seismicity and structure of the Ridgecrest region. (A) Aftershocks and surface ruptures of the Ridgecrest sequence. Events preceding and after the Mw 7.1 mainshock are indicated by blue and red dots, respectively. The inset box shows the foreshocks of the Mw 6.4 event. Black lines delineate mapped surface ruptures (Brandenberg et al., 2019). The black triangles and squares are the seismic and HRGPS stations, respectively. (B) Four cross sections in (A) showing the seismic structure. The

background color represents the shear wave velocities from the CVM-S4.26 velocity model (Lee et al., 2014b). The gray dots are the Ridgecrest seismicity projected on these planes.

For example, our previous subevent model of the Mw 6.4 Ridgecrest foreshock shows that it ruptured two conjugate faults (Ross et al., 2019). On the basis of kinematic subevent inversion of seismograms from the dense regional seismic network and global seismic stations, we found the Mw 6.4 earthquake had a duration of about 12 s, with three subevents best explaining the data (Fig. 3.2). These three subevents coincide with at least three faults. The 6-km-long northwest trending fault slipped first, with an equivalent Mw 6.1 (subevent E1). This is consistent with the hypocenter of this event, which is located about 2 km northwest of the long southwest trending fault. Thus, a rupture propagated over a short southwest-trending fault with only about 5 km of surface break, yet the equivalent magnitude for this segment, was the Mw 6.2 subevent (E2). Our analysis of this subevent indicates that it is required by the data and that the magnitude is well resolved. However, this subevent may also include slip on an adjacent northwest-trending orthogonal fault. Because the seismicity on the E2 segment extends across the main fault of the mainshock, part of the slip probably occurred on the other side, but only at depth. The rupture then jumped to a larger southwest-trending fault that is about 15 km long, producing again an equivalent seismic moment to an Mw 6.2 earthquake (E3) and a large surface rupture. Our kinematic subevent model of the Mw 7.1 mainshock shows that the rupture lasted for about 22 s and can be explained by four subevents (Fig. 3.2). The initial 5 s of the rupture had little moment, whereas the subevent with the largest moment (subevent E1, Mw 6.9) occurred close to the hypocenter between 5 and 10 s. This subevent appears to have ruptured bilaterally, given its large seismic moment. Centroid locations of the later subevents propagated very slowly to the southeast, suggesting a unilateral rupture. The final subevent, E4 (at 20 s), occurred ~25 km southeast of the first subevent E1 (at 7 s), indicating a slow average rupture velocity of roughly 2 km/s.

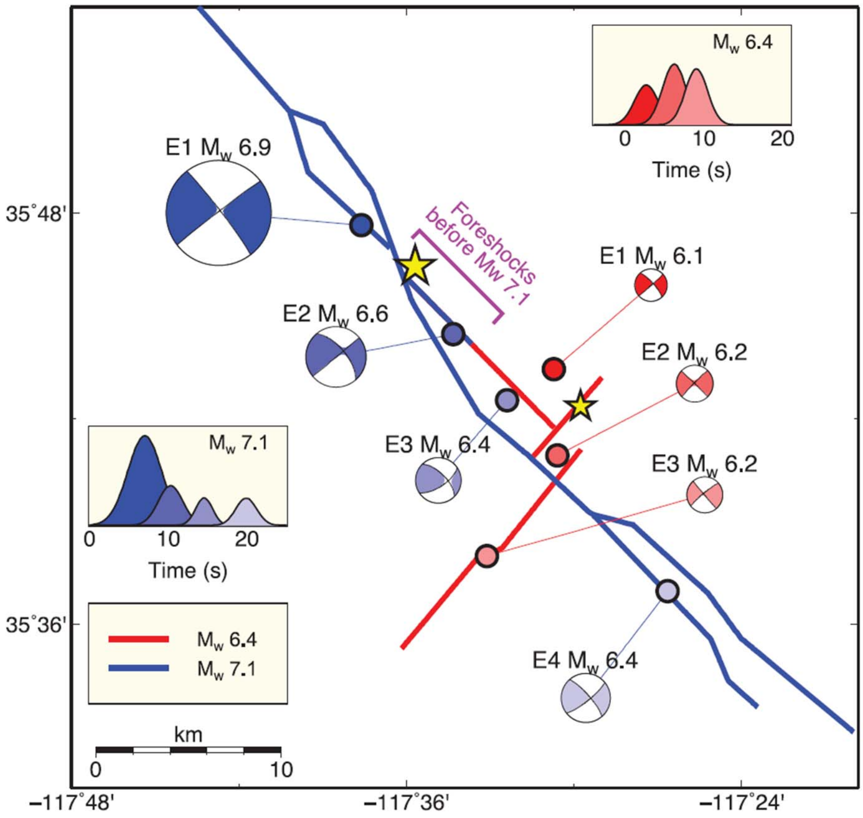

Figure 3.2. Kinematic summary of the Ridgecrest sequence rupture processes. The Mw 6.4 foreshock ruptured three main faults. This event was followed by foreshock activity along a northwest-trending fault and eventually triggered the Mw 7.1 event. The mainshock had four main subevents and ruptured bilaterally. Both events have very slow rupture velocities of ~2 km/s.

However, subevent models usually assume point sources and 1D Green's functions, thus are limited in understanding the relationship between the foreshock and mainshock slip patterns. 3D seismic structural effects may bias rupture models if not accounted for appropriately (Graves and Wald, 2001). As a good approximation in many cases, 1D Earth models are broadly used in slip inversions, including most of the studies so far on the Ridgecrest sequence (Liu et al., 2019; Ross et al., 2019; Chen et al., 2020; Goldberg et al., 2020). However, the complex tectonic setting around the Ridgecrest sequence, which sits next to a deep sedimentary basin between the Sierra Nevada and Argus Range, makes it necessary to incorporate a realistic 3D structural model in the source inversions (Wang and Zhan, 2020b). A series of 3D community velocity models (CVM) for Southern California has been proposed through integrating seismic tomography, reflection/refraction surveys, well logs, and geologic studies (Lee et al., 2014b; Small et al., 2017). Examinations of different CVM models suggest that the CVM-S4.26 model well predicts seismograms up to 0.2 Hz (Lee et al., 2014a). Application of CVM-S4.26 on automated moment tensor inversion in the Los Angeles and Ridgecrest regions also demonstrated the model's effectiveness (Wang and Zhan, 2020a, b).

In this paper, we will further improve the subevent inversion with 3D Green's functions to investigate the rupture processes and fault geometries of the Ridgecrest sequence. We will then use the subevent models to guide multiple-fault slip inversions to reveal details of the rupture processes. While the subevent inversions still use only seismic data, we add geodetic observations to the multi-fault inversions to provide tighter constraints on the detailed slip patterns. Finally, we will discuss the complexity of the fault system, the relationship between the foreshock and mainshock slips, and the importance of fault junctions in the sequence.

3.3 Data and Method

We use a variety of data including near-field (within 100 km) strong-motion (0.02-0.2Hz) and teleseismic (between 30° and 90°) waveforms (0.01-0.2Hz) (Fig. S3.1) in subevent inversions, and add near-field high-rate GPS (HRGPS) time series (<0.2Hz) and Interferometric Synthetic Aperture Radar (InSAR) data in our finite-fault analysis. In particular, the dense strong motion data help resolve the rupture episodes, while the teleseismic body waves provide tight constraints on the subevent depths and strike/dip angles, both critical to the accurate determination of fault geometries. For the multi-fault inversions, we further incorporated the geodetic data including 20 HRGPS stations and InSAR line-of-sight (LOS) measurements from the ALOS-2 and Sentinel-1 satellites. For the HRGPS data used in slip inversions, we excluded the vertical components due to the low signal-to-noise ratio. The InSAR data spans both the Mw 6.4 foreshock and the Mw 7.1 mainshock, providing constraints only on the summation of slip distributions from these two events. Therefore, we forward calculated the LOS displacement of the foreshock slip model derived by other data, subtracted it from the InSAR data, and incorporated the residual displacement field in the mainshock slip inversion together with the other datasets.

For the inversions of the near field strong-motion and HRGPS data, we used a strain-Green's-tensor based 3D finite difference (FD) method (Graves, 1996) to compute the 3D Green's functions (see Text S1 for details). Ray paths for the teleseismic stations are nearly vertical at the source side and therefore less sensitive to lateral structural variations. We applied a propagator matrix method with plane wave approximation (Qian et al., 2017) for generating the teleseismic Green's functions, using a 4-layer 1D model at the source side (Ross et al., 2019). For the InSAR data, we calculated synthetic LOS displacement assuming rectangular subfaults in an elastic half-space (Okada, 1985).

We adopt both subevent and finite-fault inversions to estimate the fault geometries and rupture process. Our subevent method is based on a multiple point source method that was initially performed on deep earthquakes (Zhan et al., 2014; Zhan and Kanamori, 2016), and further developed to accommodate multiple fault ruptures (Ross et al., 2019; Jia et al., 2020). In the subevent inversion, a large earthquake is parameterized by several point source subevents of varying centroid times, durations, locations, and focal mechanisms (Text S2). After we retrieved the subevent model, we determined the number of fault segments and their geometries based on the subevent temporal evolutions, locations, and strike/dip angles. Constraints from subevent centroidal rupture directivity help resolve the nodal plane ambiguities, but choice of the number of faults is still subjective. The subevent models only identify substantially distinct fault geometries while ignoring kinematically insignificant complexities. We grid each fault segment into 2km*2km subfault patches, on each of which the rake angle, rupture time, and rupture speed are determined/guided with the corresponding subevent mechanism, centroid times, and centroidal rupture speed, respectively. We assume the subfault source time function (STF) is a triangle with 2-s duration. With the fault geometry, rake angles, rupture fronts, and shape of STF fixed, the multiple finite-fault problem now reduces to a linearized inversion with slip amplitudes as the only unknown parameters (Hartzell and Heaton, 1983) (Text S3).

3.4 Results

Fig. 3.3A presents the subevent model and slip distribution of the Mw 6.4 foreshock. With a source duration of ~10s, the subevent model suggests the foreshock ruptured at least two orthogonal faults. Subevent E1 (Mw 6.1) is located about 3 km northwest of the hypocenter, with a location error of 95% confidence less than 2 km (Fig. 3.3A), suggesting rupture on the northwest striking fault in the first episode. Subevent E2 (Mw 6.1) occurs at the cross of the conjugate faults, followed by subevent E3 (Mw 6.2) located ~10km southwest, indicating the rupture changes its direction towards the southwest in the second episode. This two-fault rupture process agrees with our previous subevent model using 1D Green’s functions (Ross et al., 2019) but has lower uncertainty (Fig. S3.2-S3.4).

Based on the locations and strike/dip angles of subevents E1 and E3, we constructed two finite-fault planes for slip inversion: NW-striking F1 (strike/dip = 320°/80°) and SW-striking F2 (strike/dip = 228°/90°). The centroid times of subevents E1 (2.5 s) and E3 (8.5 s) guided the rupture fronts at the corresponding faults, and the rupture velocity of 2.0 km/s was chosen through a grid search (Fig. S3.5). The depths of rupture onsets on F1 and F2 are 9 km and 5 km, the same as the centroid depths of E1 and E3. The slip distribution shows moderate slip (peak slip of 0.7 m) on F1, and major slip (peak slip of 1.2 m) on F2. The F2 slip broke to the surface while the F1 slip did not, consistent with field geology observations (Milliner and Donnellan, 2020). The predicted strong motion, HRGPS, and teleseismic waveforms fit data well (examples in Fig. 3.3B, full dataset in Fig. S3.6). We further estimated the uncertainty of our slip model with a cut-half Jackknifing approach, and found that the slip error is generally less than 10% of the slip values (Fig. S3.7). Due to the limited data resolvability, how the rupture propagated from F1 to F2 through the fault junction remains unclear.

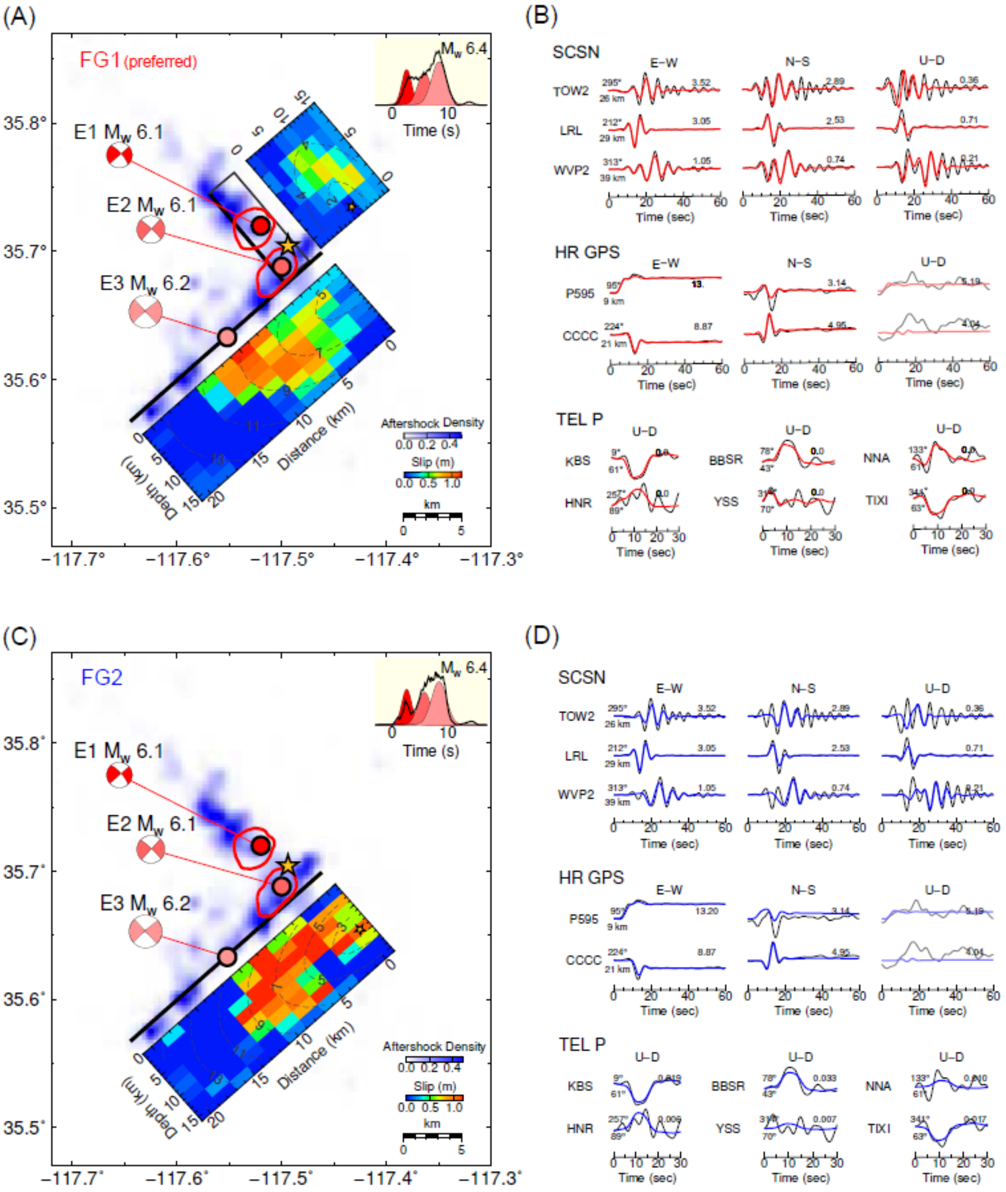

Figure 3.3. Rupture models of the Mw 6.4 event. (A) Subevent model (red dots and beachballs) and two-fault slip distribution (colored grids). The density of seismicity

between the Mw 6.4 and the Mw 7.1 events is displayed by the blue background color. The solid red contours indicate 95% confidential limits of the subevent locations. Subevent E3 is fixed at a location of the maximum surface offset point. The black lines show geometries of the two fault segments: the vertical NE-SW segment is denoted by its surface trace as a thick black line, while the 80° dipping NW-SE branch is projected into a rectangle. The inset box shows moment rate functions of individual subevents (red waveforms), and from the slip model (black line). (B) Representative fits of strong ground motion (SCSN), HRGPS and teleseismic P (TEL P) waves for the two-fault slip model, with data in black and synthetics in red, respectively. The U-D component of HRGPS data, as shown in lighter colors, are not used in the inversion. The numbers leading and tailing the waveforms are the azimuths/distances, and maximum absolute data amplitudes in cm/s (SCSN) or cm (HRGPS and TEL P), respectively. Complete data fittings are shown in Fig. S3.2. (C) Same as A, but for the one-fault slip model that only preserves the NE-SW striking segment. (D) Same as B, but for the one-fault slip mode. The synthetic waveforms are colored in blue.

We conducted a test to evaluate the importance of F1, the NW branch of the orthogonal faults, to the Mw 6.4 foreshock data fitting. In addition to our preferred two-fault geometric setting (FG1), we consider an alternative fault geometry (FG2) in which we allow the rupture on the SW-striking F2 only (Fig. 3.3C). The rupture velocity of FG2 is set to be 1.5 km/s to accommodate the rupture beginning on F2. We found that the two-fault model fits the strong motion, HRGPS, and teleseismic waveforms systematically better than the single fault model (Fig. 3.3D). We attribute the improved data fittings, especially for the early wiggles of strong motion waveforms, to the requirement of an initial northwestward rupture directivity. We also tested a third scenario, FG3 (Fig. S3.8) to accommodate a secondary SW-striking surface rupture found in DuRoss et al. (2020). The synthetics for FG3 do not match data as well as the conjugate fault model FG1 (Fig. S3.8), indicating that the first fault ruptured is NW-SE striking.

Our subevent model of the Mw 7.1 mainshock (Fig. 3.4A) shows an initiation with a small subevent E1 (Mw 6.1) close to the hypocenter. As the first episode, the rupture propagated to the northwest indicated by E2 (Mw 6.7) located ~6 km from the hypocenter, then towards the southeast as shown by the largest subevent E3 (Mw 6.8), accounting for over 70% of the total moment. The second episode features a unilateral rupture towards the southwest (subevents E4-E5). The waveform fittings and uncertainty analysis of the subevent model are shown in Fig. S3.9-S3.11. Strike angles of all major subevents (E2-E5) are well constrained (Fig. S3.11) to be ~320° , consistent with the throughgoing aftershock band at depth (Wang and Zhan, 2020b), but contradicting the curved surface rupture traces (Fig. 3.1A). To reconcile these observations, we set three fault segments for slip inversion, including two major fault segments F1-F2 and a shallower subparallel fault branch F3 (Fig. 3.4). F1 and F2 have the same strike angle of 320°, and F1 is vertically dipping while F2 has a dip of 80° based on average dip angle of subevents E3-E5. F3 has a strike of 329° following the surface traces, and a dip angle of 70° as guided by the subevent E3's focal mechanism, therefore connects the curved surface traces and the steeper through-going faults F1-F2. Similar to the foreshock inversion, we generated the rupture fronts based on the subevent timings, and attributed an overall rupture velocity of 1.7 km/s based on the timings and locations of subevents E3 and E5. We obtained the best fitting slip model (Fig. 3.4, Fig. S3.12) with the Jackknifing error less than 20% in general (Fig. S3.13). The largest slip asperity occupies the two sides of the hypocenter, corresponding to the subevents E1, E2, and part of E3. Although the throughgoing faults have a maximum slip of ~6m, the major surface rupture (~4m) is contributed by the subparallel branch F3, which corresponds to the remainder of E3. The third slip asperity is located at the junction with the orthogonal fault involved in the foreshock, and the fourth further to the southeast, accommodating the subevents E4-E5. The overall slip distribution along the NW-SE fault agrees with other slip inversions results (Barnhart et al., 2019; Chen et al., 2020; Goldberg et al., 2020).

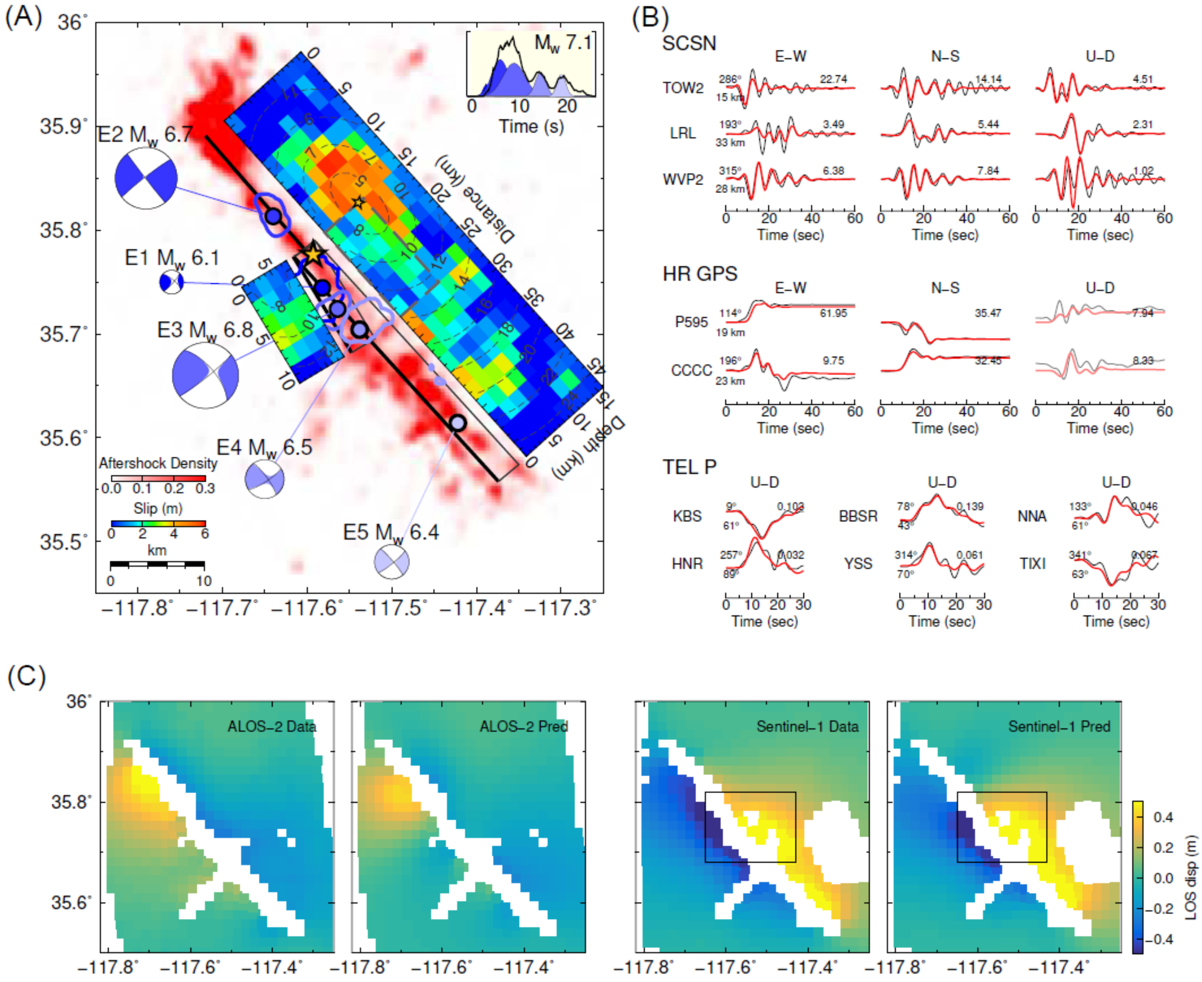

Figure 3.4. Subevent model and slip distribution of the Mw 7.1 event. (A) Same configuration as Fig. 3.3A, but for the Mw 7.1 mainshock. Aftershocks of the Mw 7.1 event are displayed by red in the background. The blue dots, beachballs, and source time functions indicate the corresponding mainshock subevents. E5 is fixed according to the southeastward slip patch in a static slip model. (B) Same as Fig. 3.3B, but for the mainshock. (C) Decimated data and model predictions for the unwrapped ALOS-2 and Sentinel-1 InSAR line-of-sight displacements. The black box corresponds to the region for model comparison in Fig. S3.14.

Though guided by subevent locations and focal mechanisms in our slip inversion, fault geometries are more commonly assumed based on surface traces, centroid moment tensors, or aftershock patterns. To evaluate the different assumptions and their impacts on the models, we generated three alternative fault geometries and compared their slip models with our preferred one (Fig. S3.14). The first fault model FG1, constructed with vertical faults following the surface rupture segments (Goldberg et al., 2020; Pollitz et al., 2020), fails to predict the large teleseismic P wave amplitudes from certain azimuths. FG2 is assumed to have a single vertical fault plane (e.g. Zhang et al., 2020), which is commonly applied when only the centroid moment tensor and/or aftershock distribution is available. This model predicts teleseismic P waves slightly better, but is unable to fit the Sentinel-1 InSAR data. Compared with FG2, the southern fault strand of FG3 dips slightly (80°) towards the northeast, and this change produces substantial improvements on the fittings of teleseismic waveforms, yet large misfit for the InSAR data is still observed. FG4, the preferred model in this study as discussed above, improves the fitting of Sentinel-1 InSAR data significantly.

3.5 Discussion

A remarkable feature of the Ridgecrest sequence is the overall lambda-shaped fault configuration with orthogonal segments (Hudnut et al., 2020). Through unconfined subevent inversions and finite-fault modeling with varying fault geometries, we found that the foreshock ruptured two perpendicular fault segments. The rupture on the NW-SE segment is not only supported by the aftershock distributions (Fig. 3.1), but also delineated by a bunch of small earthquakes preceding it (inset box in Fig. 3.1A; Shelly (2020)). The discrepancy between the conjugate aftershocks patterns and the SW-striking surface traces can thus be reconciled by the deep slip on the NW-striking plane which did not break to the surface (Fig. 3.3A). Coseismic rupture of orthogonal faults has been considered rare, because sharp bends can act as geometrical barriers to earthquakes (Aki, 1979; Nielsen and Knopoff, 1998). But in recent years, orthogonal fault ruptures have been observed for multiple events, including the 2012 Sumatra earthquake (Meng et al., 2012) and the 2018

Alaska earthquake (Lay et al., 2018). This suggests that ruptures can be controlled by the interaction between differently oriented faults, such as weak spots at fault intersections (Talwani, 1999) and transient stress triggering (King et al., 1994). On the other hand, orthogonal fault ruptures could repeatedly occur according to the reported abundance of orthogonal structures in Southern California (Ross et al., 2017), which challenges traditional wisdom of regional hazard assessments.

The Mw 6.4 foreshock and the Mw 7.1 mainshock occurred sequentially within 34 hours in the same fault system, raising the question how these two events associate with each other. Our slip models indicate that the NW-SE striking segment of the foreshock has the same geometric properties as the southern fault segment of the mainshock. Therefore, we suggest it is the same fault ruptured by both events (Fig. 3.5). More specifically, the mainshock ruptured around the high coseismic slip zone of the foreshock at about 10-km depth. The foreshock initiated near the junction of two orthogonal NW- and SW-striking fault segments, and then ruptured the two sequentially. Although the foreshock northwestward rupture was terminated possibly due to a barrier or the geological complications, it increased the shear stress in the extension of fault. The slip on the orthogonal NE-SW segment can generate positive Coulomb stress change at the mainshock hypocenter as well (Barnhart et al., 2019; Goldberg et al., 2020). These stress perturbations caused the emergence of a number of small events between the foreshock and mainshock in space and time, including a Mw 5.4 earthquake on July 5th. The seismicity slowly migrated towards the northwest (Fig. 3.5) and eventually triggered the nucleation of the Mw 7.1 mainshock at another fault junction. This junction connects a twisted through-going NW-SE striking fault and a subparallel fault segment at shallow depth (Fig. 3.5). Note that the twisting is consistent with the strike variation of surface ruptures (Fig. 3.5), but the deeper aftershocks form a narrow straight band, and the dipping subparallel fault in our model reconciles them, consistent with a systematic study on the source parameters of Ridgecrest aftershocks (Wang and Zhan, 2020b). Besides the Ridgecrest foreshock and mainshock, initiation of a multi-fault earthquake at fault junction has also been observed for the 1999 Hector Mine earthquake (Oglesby et al., 2003), and has been attributed to be potential weak zones due to their geometric incompatibilities (Andrews, 1989; Gabrielov et al., 1996) . The instability of fault junctions has also been associated with enhanced permeability and higher fluid pressure (Sibson, 1996). The mainshock slip distribution complements the foreshock slip on the through-going northwest striking fault, suggesting that the mainshock extended the failure and completed the stress release after the foreshock.

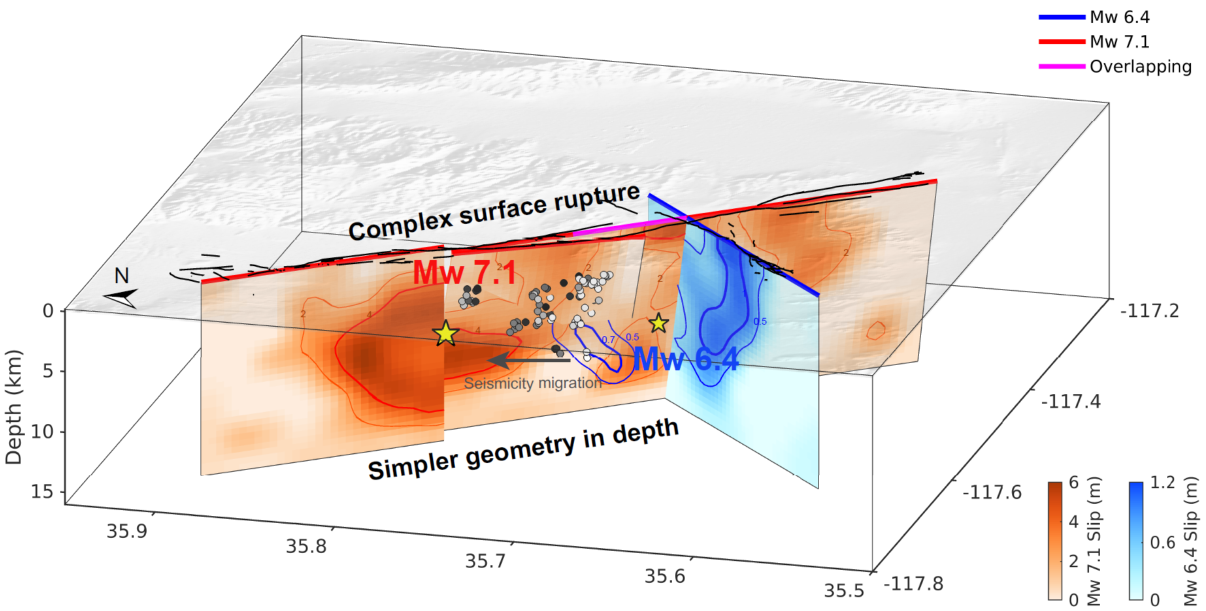

Figure 3.5. 3D configuration of the fault system ruptured by the Ridgecrest sequence. Displayed in different color scales, slip contours of the Mw 6.4 foreshock and the Mw 7.1 mainshock are shown in blue and red. Circles of white to black colors indicate the temporal evolution of aftershocks (magnitude>2.5) between the Mw 6.4 and Mw 7.1 events. Black lines delineate observed surface ruptures. The foreshock ruptures orthogonal fault segments, followed by aftershocks migrating towards the hypocenter of the Mw 7.1 mainshock. The mainshock ruptures subparallel surface traces, but these segments merge to a throughgoing fault in deeper depths.

3.6 Conclusion

We developed a novel subevent to multi-fault approach to estimate the rupture processes and the fault geometries of the Ridgecrest sequence. On July 4th, the Mw 6.4 foreshock initiated near the cross of two orthogonal faults, and ruptured towards NW first and then SW. Although the NW rupture did not extend long, it likely caused dynamic/static stress accumulation at the Mw 7.1 mainshock hypocenter, as manifested by the migration of seismicity. Two days later, the mainshock nucleated at a complex three-fault junction along the extension of the foreshock NW segment. It ruptured first bilaterally, then unilaterally on faults that broke multiple surface traces though merged into a twisted but through-going fault at depth. Its slip distribution complemented the area ruptured by the foreshock. In summary, the Ridgecrest sequence demonstrated remarkable interactions of two multi-fault ruptures, both started at fault junctions. These observations, which are uncovered by an assembly of seismological, geodetic, and remote sensing datasets, attest to the linkage between multi-fault ruptures of the foreshock and the mainshock, as well as the importance of fault junction instabilities.

3.7 Supplementary Materials

For the inversions of the near-field (epicentral distance within 100 km) observations, including 27 strong ground motion time series and 20 high-rate GPS traces, we adopt a 3D finite difference algorithm (Graves, 1996) to calculate 3D Green's functions, using SCEC CVM-4.26 velocity model (Small et al., 2017) as input. However, unlike 1D Green's functions that only depend on source-receiver distances and azimuths, the 3D Green's functions have a nonlinear relationship with the source locations. Therefore, we need to retrieve 3D Green's functions from all virtual source locations for rupture inversions, and this can be highly computational consuming. To reduce the computational cost, we employed the strain Green's tensor and source-receiver reciprocity approach following Wang and Zhan (2020a), in which we swap the locations of virtue sources and receivers for the same elastic response (Eisner and Clayton, 2001; Zhao et al., 2006). In this way, each station is treated as a seismic source. Thus the number of FD wavefield simulations is reduced to 47 (number of stations), which is much less than the number of virtue sources (thousands of grids in the source region). We calculated 3D Green's functions with a grid spacing of 100 m, leading to the numerical accuracy of up to 0.5 Hz (Wang and Zhan, 2020a). We saved our Green's function database on a mesh of 2km*2km*1km for all 47 near-field stations. To reach source location resolution beyond the mesh precision, we interpolated the 3D Green's functions to all possible locations through a trilinear interpolation.

We adopt subevent inversion for the rupture processes of the foreshock and mainshock. In this method, we decompose large earthquake as a series of point source subevents, and simultaneously resolve their source parameters. Each subevent has 10 unknown parameters, including subevent locations (3), centroid times (1), source time durations (1) and deviatoric moment tensors (5). When the number of subevents n is large, resolving all $10*n$ unknown parameters through a purely nonlinear framework is inefficient. Therefore, we divide our inversion procedure into two stages, in which we optimize part of source parameters nonlinearly, while invert for other parameters in a linear way.

In the outer stage, we search nonlinear parameters (subevent locations, centroid times and source durations) through Monte Carlo Markov chains (MCMC) with a Metropolis-Hasting algorithm. In each Markov Chain step, we propose new models through sampling one of the nonlinear parameters while keeping the other nonlinear parameter at their current values (Bodin et al., 2012). This approach ensures an overall high acceptance rate, and therefore improves the convergence efficiency of the MCMC inversion. Given the proposed nonlinear parameters in each MCMC step, we still need a set of subevent deviatoric moment tensors to forward calculate synthetic waveforms. These moment tensor components are linearly related to the observed time series and Green's functions (Jost and Herrmann, 1989), which allows an individual linear inversion of moment tensors when subevent locations and timing are available. Therefore, we determine moment tensor components in the inner stage of each MCMC step. We first predict apparent source time functions (ASTFs) at all stations with corresponding nonlinear parameters, and then convolve these ASTFs with Green's functions. We further invert for deviatoric subevent moment tensors through extending the algorithm by Minson and Dreger (2008) to multiple point sources.

We generate 72 Markov Chains from random initial samples, and eventually keep 24 best fitting chains to avoid being trapped in local minima. The MCMC sampling follows a Bayesian framework, in which the prior probability density function for all nonlinear parameters are bounded uniform distributions. We also introduce a penalty term to address the moment-duration scaling relationship of large earthquakes (Meier et al., 2017; Minson et al., 2018), to reject subevent source time functions of unrealistic aspect ratios. Although the instrumental/noise error of the seismic recordings are typically very small, additional error can be caused by inaccurate assumptions of the wave propagation processes (e.g. inaccurate velocity model, finite source effect, etc.). Therefore, we introduce data errors which are empirically set to be 10% of the final misfits between data and synthetics. These errors eventually propagate to subevent model errors. For both the foreshock and mainshock, we start with one subevent and iteratively increase the number of subevents, until the waveforms are well fitted and no significant subevent is missing for agreement with the long period moment.

We use an assembly of near field strong ground motion traces (27 stations), teleseismic P waves (33 stations) and teleseismic SH waves (39 stations) in our subevent inversions. The weighting of these three datasets is set to 1:6000:800. This weighting scheme is consistent with the finite fault inversions in this study (supplementary text) which leads to similar misfit contributions from different data types (Table. S3.3). Because it's usually difficult to precisely pick the first arrival times, we allow maximum time shifts of 3s, 2s, and 5s for the strong motion, P and SH waves in our inversions, respectively. Since all traces can shift simultaneously, the absolute locations of all subevents can move together. To reduce this systematic error, we need to fix the location of one subevent while allowing other subevents to move freely in the whole space. Similar to Ross et al. (2019), we anchored the location of the third subevent for the Mw 6.4 foreshock at an arbitrarily selected maximum surface offset point on the southwest striking fault plane. For the Mw 7.1 mainshock, we fixed the last subevent at the location near the southeastern end of the major fault, where a slip patch is observed from various slip inversions (Barnhart et al., 2019; Liu et al., 2019; Ross et al., 2019). The subevent location reliability is assessed by the Markov Chain ensemble distributions in Fig. S3.3 and Fig. S3.10.

In our finite fault inversion, we estimated the minimum number of necessary fault segments for both the foreshock and mainshock using their subevent models. This is performed by analyzing whether each subevent pair can be put on same fault plane, given their locations and strike/dip angles. The nodal plane ambiguities are largely avoided from the spatial temporal evolution of subevents. Each fault segments goes through the location of these subevents, and their strike, dip, and rake angles are consistent with the corresponding subevent focal mechanisms. We discretized each fault segment into subfault grids which horizontal and depth intervals are both 2 km. The maximum fault depth is 16 km. All subfault grids have triangle moment rate functions with a duration of 2s. Given the rupture directivity and times estimated from the subevent model, we assume that the rupture starts from a subfault grid of the same depth as the corresponding subevent, but the starting point locates at one edge of the whole fault segment. We further tracked the rupture initiation time back from the subevent centroid time using subevent centroidal velocity as a proxy of rupture velocity. We further generated rupture contours and calculate the rupture time for each subfault grid.

For the Mw 6.4 foreshock, we constructed two orthogonal fault segments. The NW trending segment has a strike of 320° and dip of 80°. The SW striking segment has a strike of 228° and is vertically dipping. The rupture initiation depths of the NW- and SW-trending faults are 9 km and 5 km, respectively. The subevent E2 of the foreshock may reflect slip on both NW- and SW- trending fault segments. Thus the calculation of subevent centroidal rupture velocity based on E2-E3 can be biased. Instead, we find an optimal rupture velocity of 2.0 km/s through a grid search (Fig. S3.5). For the Mw 7.1 mainshock, we constructed two major fault segments F1 (strike/dip: 320°/90°) and F2 (strike/dip: 320°/80°), and a shallower subparallel fault branch F3 (strike/dip: 329°/70°), to reconcile the steep (68°) dip angle of subevent E3 and the curved surface rupture traces (Fig. 3.1A). We use a rupture velocity of 1.7 km/s approximated from centroidal velocity from subevent E3 and E5.

Once we set up the fault geometries, focal mechanisms, and rupture times, we only have slip amplitudes as unresolved parameters. Here we use a linearized finite fault inversion method of Hartzell and Heaton (1983) to determine the slip distributions. In this framework, the observed data and the subfault patch synthetics form a linear system,

$$\begin{bmatrix} G_{SM}^{1} & G_{SM}^{2} & \cdots & G_{SM}^{n} \\ G_{TelPdisp}^{1} & G_{TelPdisp}^{2} & \cdots & G_{TelPdisp}^{n} \\ G_{TelPvel}^{1} & G_{TelPvel}^{2} & \cdots & G_{TelPvel}^{n} \\ G_{TelSHdisp}^{1} & G_{TelSHdisp}^{2} & \cdots & G_{TelSHdisp}^{n} \\ G_{HRGPS}^{1} & G_{HRGPS}^{2} & \cdots & G_{HRGPS}^{n} \\ G_{InSAR}^{1} & G_{InSAR}^{2} & \cdots & G_{InSAR}^{n} \end{bmatrix} * \begin{bmatrix} m^{1} \\ m^{2} \\ \vdots \\ m^{n} \end{bmatrix} = \begin{bmatrix} d_{SM} \\ d_{TelPdisp} \\ d_{TelPvel} \\ d_{TelSHdisp} \\ d_{HRGPS} \\ d_{InSAR} \end{bmatrix}$$

in which $m^{1\cdots n}$ is the slip vector of all subfault grids, $d_{[data\ type]}$ is the data vector including a variety of data types (Strong motion, teleseismic P waves in displacement, teleseismic P waves in velocity, teleseismic SH waves in displacement, high-rate GPS, and InSAR). $G_{[data\ type]}^{1\cdots n}$ is the synthetics of different data types for unit slip on subfault grids from 1 to *n*. For the seismic and HRGPS data, both $G_{[data\ type]}^{1\cdots n}$ and $d_{[data\ type]}$ are stringing time series of all stations from end to end. For the InSAR data, data and Green's functions are gridded surface line-of-sight displacements. Therefore, all time points of seismic and HRGPS records, and all displacements of the InSAR data are included in the inversion. This linear relationship can be directly solved through a least square solution, but the result is unstable because this inverse problem is usually ill-posed. To stabilize the inversion, we introduce four types of constraints, including 1) non-negative constraints on the slip, 2) minimization of the slip difference between adjacent subfault grids, 3) minimizing slip at the non-surface boundaries of the faults, and 4) minimizing the L2 norm of the slip distribution (Hartzell and Heaton, 1986; Ji et al., 2002). These constraints allow us to reject unphysical solutions (negative slip, enormously large strain) and avoid overfitting. To flexibly incorporate these constraints, we solve the inverse problem through the CVX optimization algorithm (Grant and Boyd, 2014). The slip uncertainties are estimated using a cut-half Jackknifing approach in which we randomly remove half of all data points and run the slip inversion. We repeated this process 100 times, and then calculated the standard deviation of the obtained slip models for an approximation of the model error (Fig. S3.7, S3.13).

Compared with the subevent inversions, we added high-rate GPS and InSAR in the finite fault inversions. The weighting of regional strong ground motion, teleseismic P waves, teleseismic SH waves, high-rate GPS time series and InSAR interferograms in our slip inversions is 1:6000:800:0.25:10. This weighting scheme results in comparable misfit contributions of the different datasets (Table S3.3), and insignificant changes of the weightings don't substantially alter the inversion results. For the high-rate GPS data, we didn't use the vertical component time series in our inversions due to their low signal-to-noise ratio. Instead, we simply forward predicted the synthetics of vertical component HRGPS and compared them with the data (Fig. 3.2, 3.3; Fig. S3.6, S3.12). The InSAR data spans over both the Mw 6.4 foreshock and the Mw 7.1 mainshock, forming a trade-off of their individual contributions. Considering the foreshock causes much less surface deformation than the mainshock, we excluded the InSAR data from the foreshock slip inversion. Using the foreshock slip model derived from other datasets, we forward calculated its line-of-sight displacements, and assume this as foreshock contribution. We then subtracted the InSAR data by the foreshock LOS displacements, and attributed the residual as InSAR data for being incorporated in the mainshock slip inversion.

	Centroid time (s)	**Duration (s)**	**Longitude (°)**	**Latitude (°)**	**Depth (km)**	**Mrr (10^{26} dyne-cm)**	**Mtt (10^{26} dyne-cm)**	**Mpp (10^{26} dyne-cm)**	**Mrt (10^{26} dyne-cm)**	**Mrp (10^{26} dyne-cm)**	**Mtp (10^{26} dyne-cm)**
E1	2.64	3.61	-117.520	35.720	8.90	0.000	-0.143	0.142	0.027	0.025	0.018
E2	5.79	4.81	-117.500	35.688	5.81	0.000	-0.179	0.180	0.012	0.014	-0.014
E3	8.43	5.57	-117.552	35.633	4.42	0.006	-0.279	0.272	0.011	-0.014	0.024

Table S3.1. Subevent model parameters for the M 6.4 foreshock.

	Centroid time (s)	**Duration (s)**	**Longitude (°)**	**Latitude (°)**	**Depth (km)**	**Mrr (10^{26} dyne-cm)**	**Mtt (10^{26} dyne-cm)**	**Mpp (10^{26} dyne-cm)**	**Mrt (10^{26} dyne-cm)**	**Mrp (10^{26} dyne-cm)**	**Mtp (10^{26} dyne-cm)**
E1	3.78	2.26	-117.582	35.745	6.49	-0.007	-0.163	0.169	0.009	0.080	-0.021
E2	6.68	7.08	-117.640	35.813	7.30	0.001	-1.534	1.533	0.035	-0.144	0.391
E3	9.58	9.52	-117.564	35.724	5.03	0.067	-1.762	1.696	0.423	0.594	0.332
E4	15.15	4.34	-117.538	35.704	5.89	0.109	-0.638	0.529	0.023	0.145	0.222
E5	19.51	5.83	-117.422	35.614	5.83	0.004	-0.465	0.461	-0.001	0.085	0.083

Table S3.2. Subevent model parameters for the M 7.1 mainshock.

	Total misfit	**Strong motion**	**Tel P**	**Tel SH**	**HR GPS**	**InSAR**
Mw 6.4	33.5	19.4	18.8	11.7	16.1	NaN
Mw 7.1	141.1	80.1	56.4	42.8	30.6	27.1

Table S3.3. Contributions to misfit from different data types in the finite fault inversions.

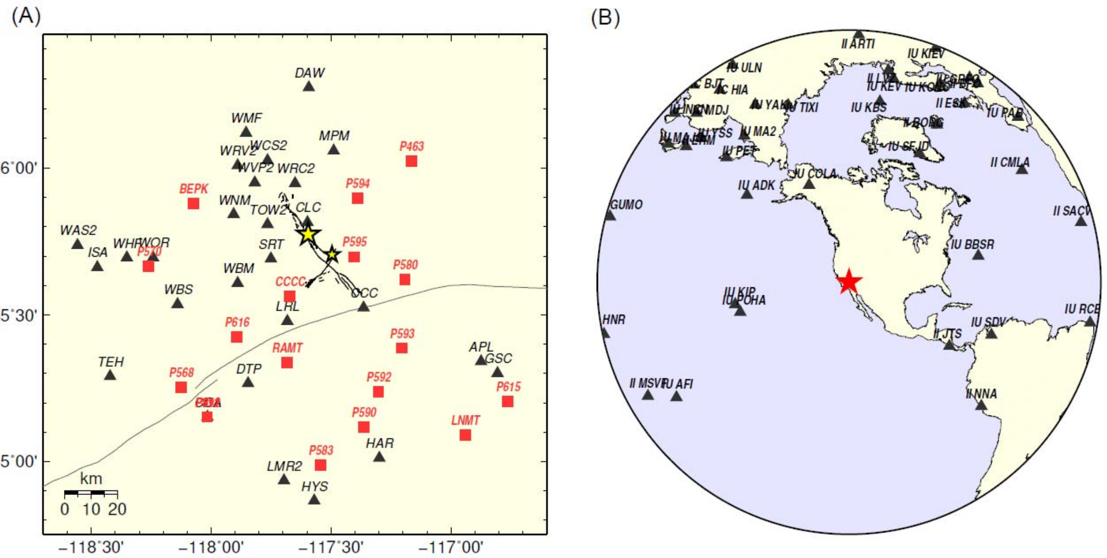

Figure S3.1. Seismic and GPS stations used in this study. (A) Distribution of the 27 near field strong motion stations (black triangles) and 19 high-rate GPS stations (red squares). The yellow stars indicate the hypocenter of the Mw 6.4 foreshock and Mw 7.1 mainshock. The black and gray lines delineate the Ridgecrest and Garlock faults in Fig. 3.1. (B) Distribution of 39 teleseismic stations (black triangles) used in this study. The red star shows the hypocenter of the Mw 7.1 mainshock.

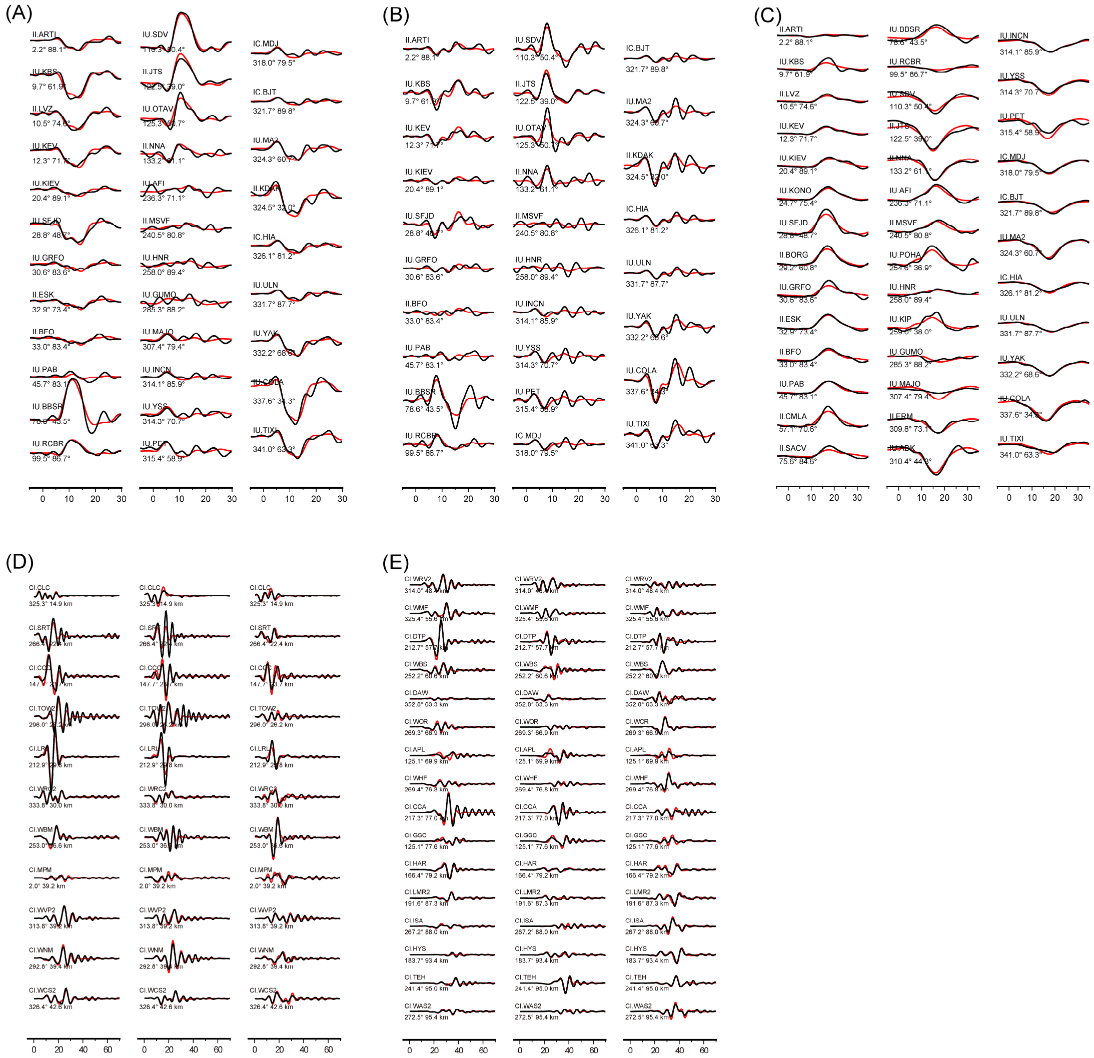

Figure S3.2. Waveform fits for the preferred subevent model of the Mw 6.4 foreshock. Black and red lines indicate data and synthetic waveforms, respectively. The numbers below each trace show the station azimuth and distance, respectively. (A) P waves in displacement. (B) P waves in velocity. (C) SH waves in displacement. (D-E) Near field strong ground motion waveforms.

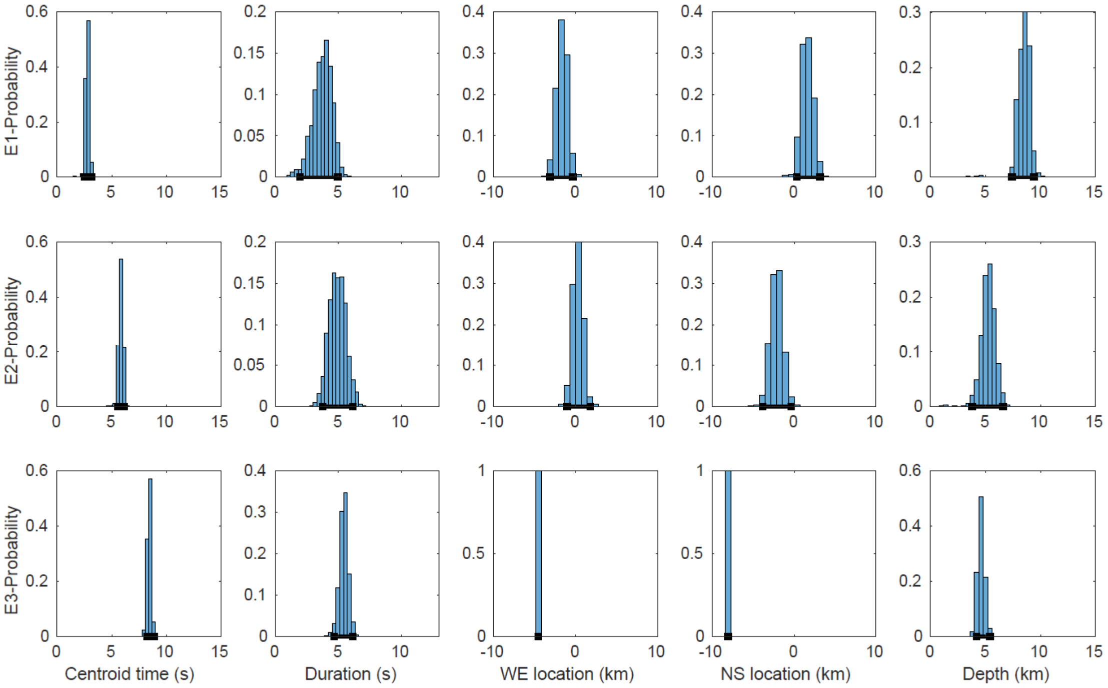

Figure S3.3. Distributions of Markov Chain samples in the subevent inversion of the Mw 6.4 foreshock. Columns from left to right show the density distribution of subevent centroid times, durations, west-east locations, north-south locations and centroid depths. Rows indicate subevent E1-E3. Black squares and lines denote error bars corresponding to 95 % confidential interval.

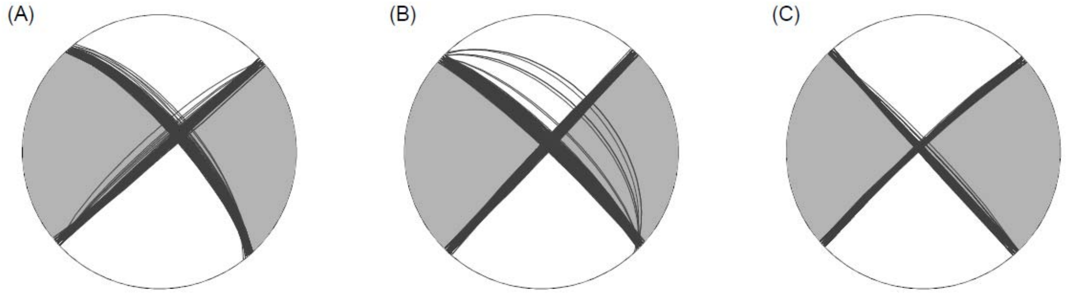

Figure S3.4. Scatters of double couple focal mechanisms for subevent E1 (A), E2 (B) and E3 (C) of the Mw 6.4 foreshock.

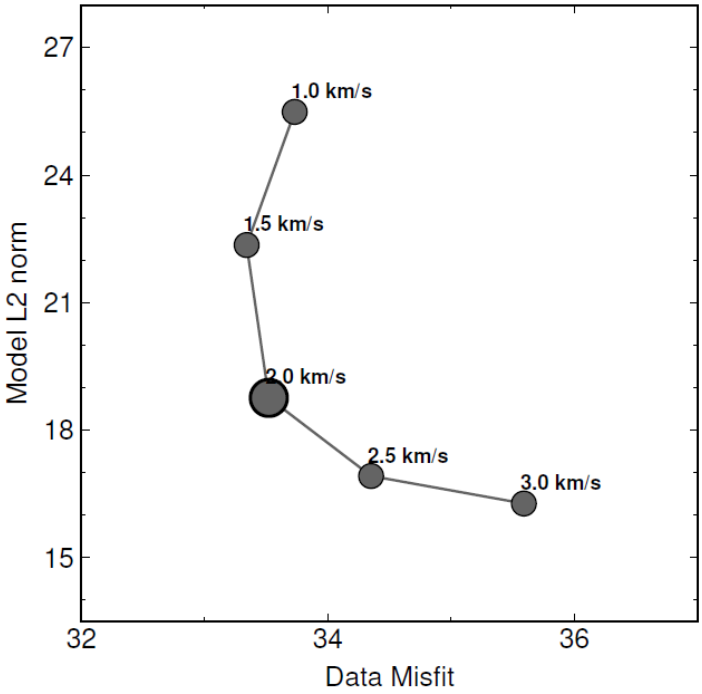

Figure S3.5. Grid-search of the rupture velocity for the Mw 6.4 foreshock slip inversions. When the rupture velocity is 2.0 km/s, both the data misfit and L2 norm of the slip model are low.

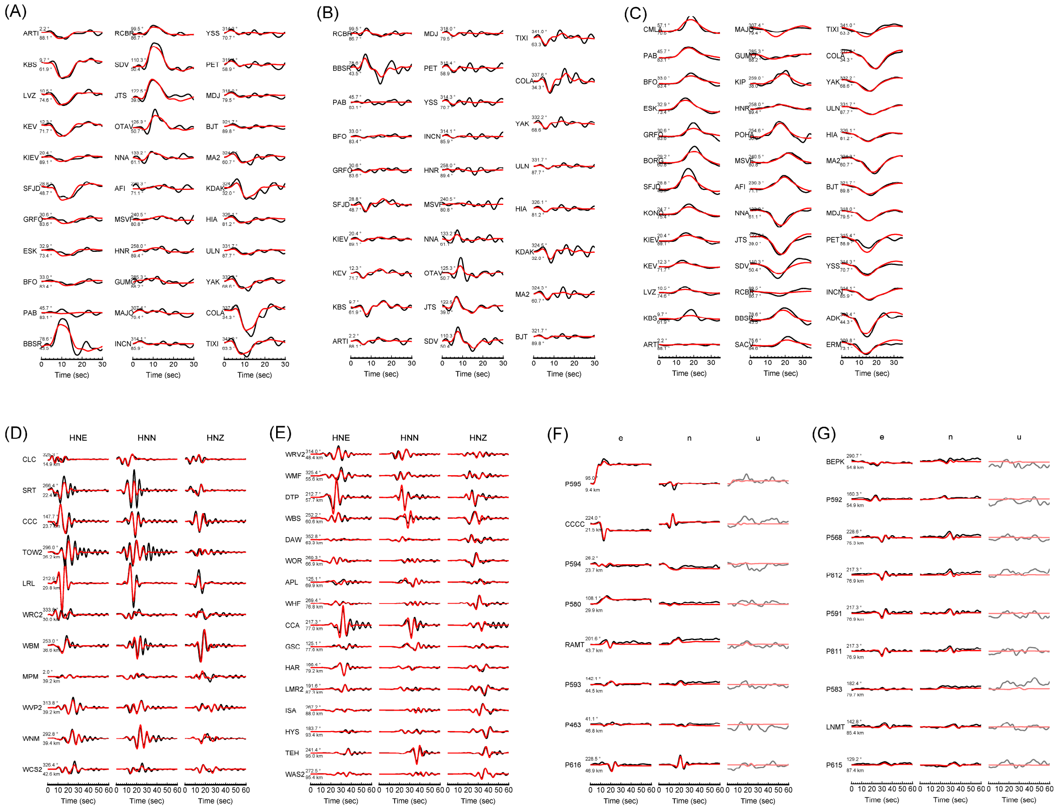

Figure S3.6. Waveform fits for the preferred 2-fault slip model of the Mw 6.4 foreshock. Black and red lines indicate data and synthetic waveforms, respectively. The numbers leading the waveforms are the azimuths and epicentral distances. (A) P waves in displacement. (B) P waves in velocity. (C) SH waves in displacement. (D-E) Near field strong ground motion waveforms. (F-G) Near-field HRGPS time series. The U-D component of the HRGPS data, as shown in lighter colors, are not used in the inversion.

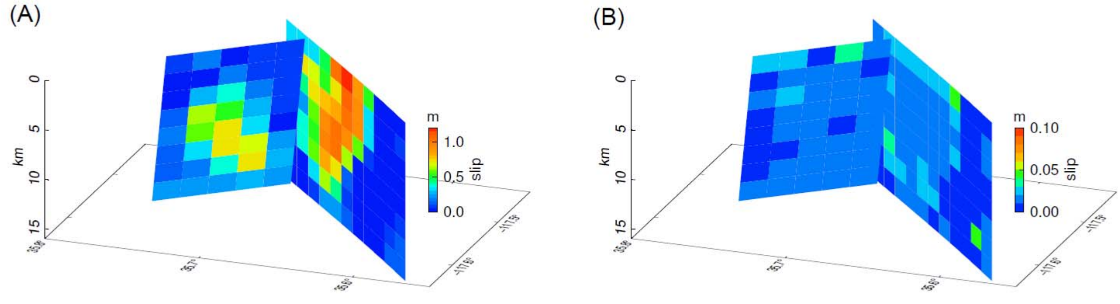

Figure S3.7. Assessment of model error with the Jackknifing test for the Mw 6.4 foreshock. (A) Slip distribution. (B) Standard deviation.

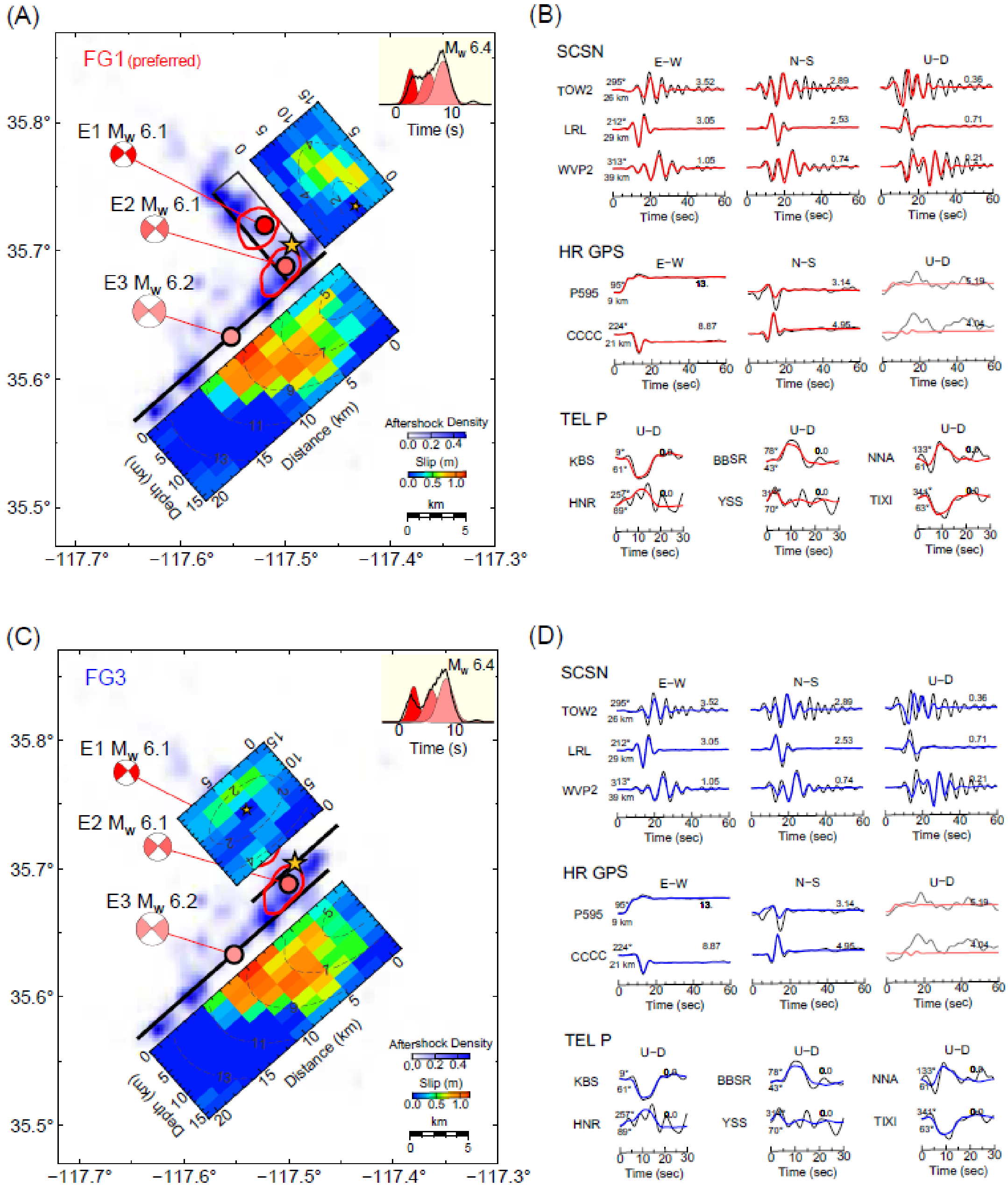

Figure S3.8. Same as Fig. 3.3 but for the comparison between conjugate fault model FG1 (A-B) and parallel fault model FG3 (C-D). The synthetics from FG1 fits the N-S and U-D components of stations TOW2 and WVP2 better than FG3.

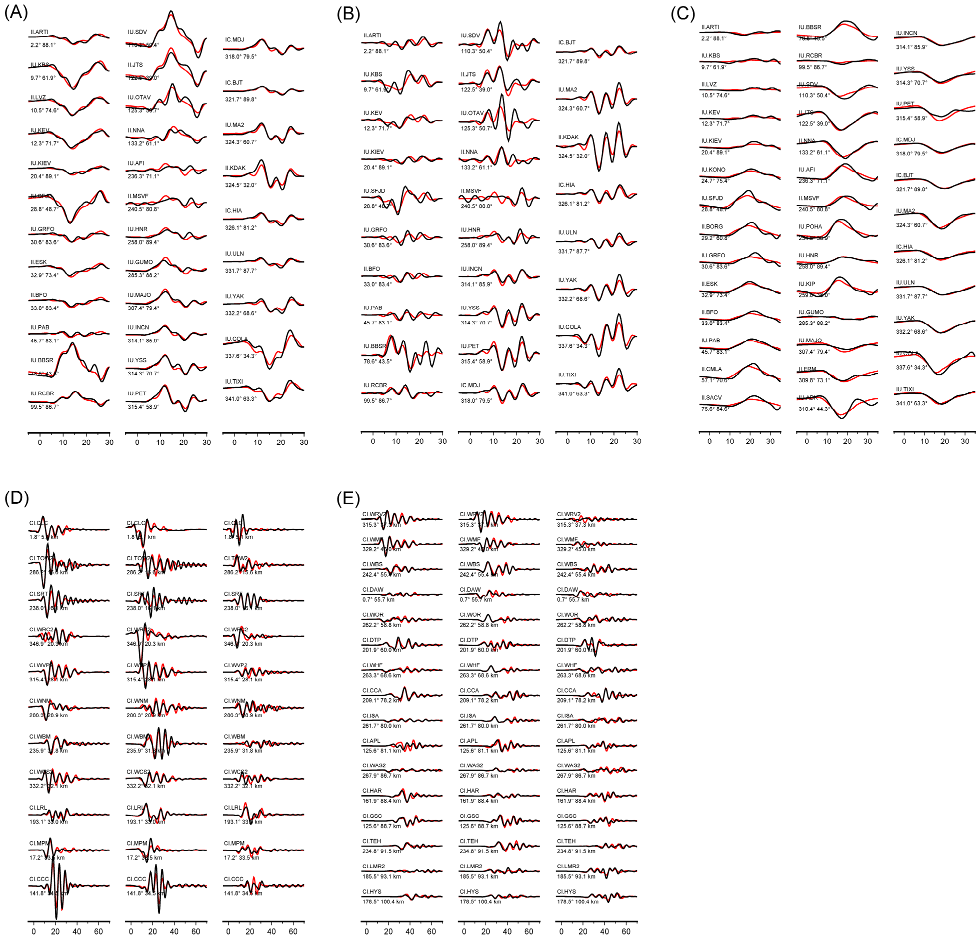

Figure S3.9. Same as Fig. S3.2 but for the Mw 7.1 mainshock.

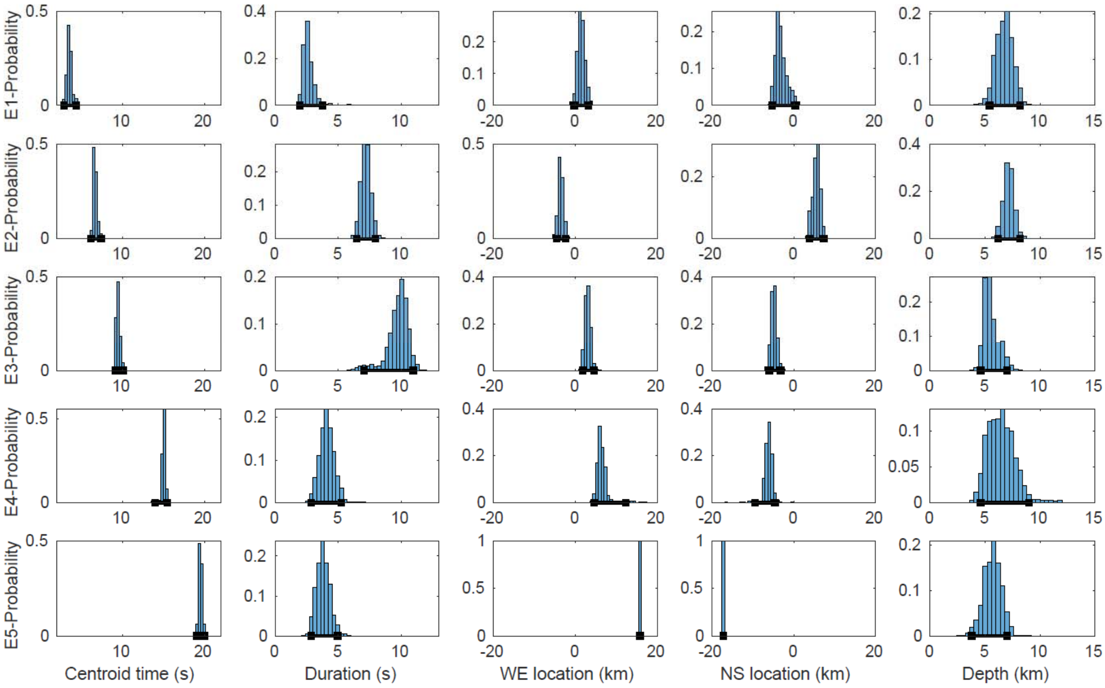

Figure S3.10. Same as Fig. S3.3 but for the Mw 7.1 mainshock.

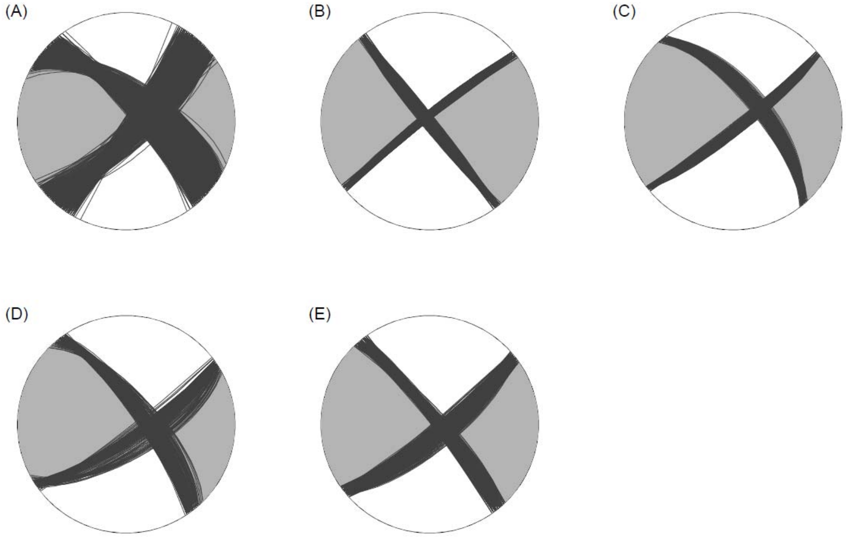

Figure S3.11. Same as Fig. S3.4 but for the Mw 7.1 mainshock.

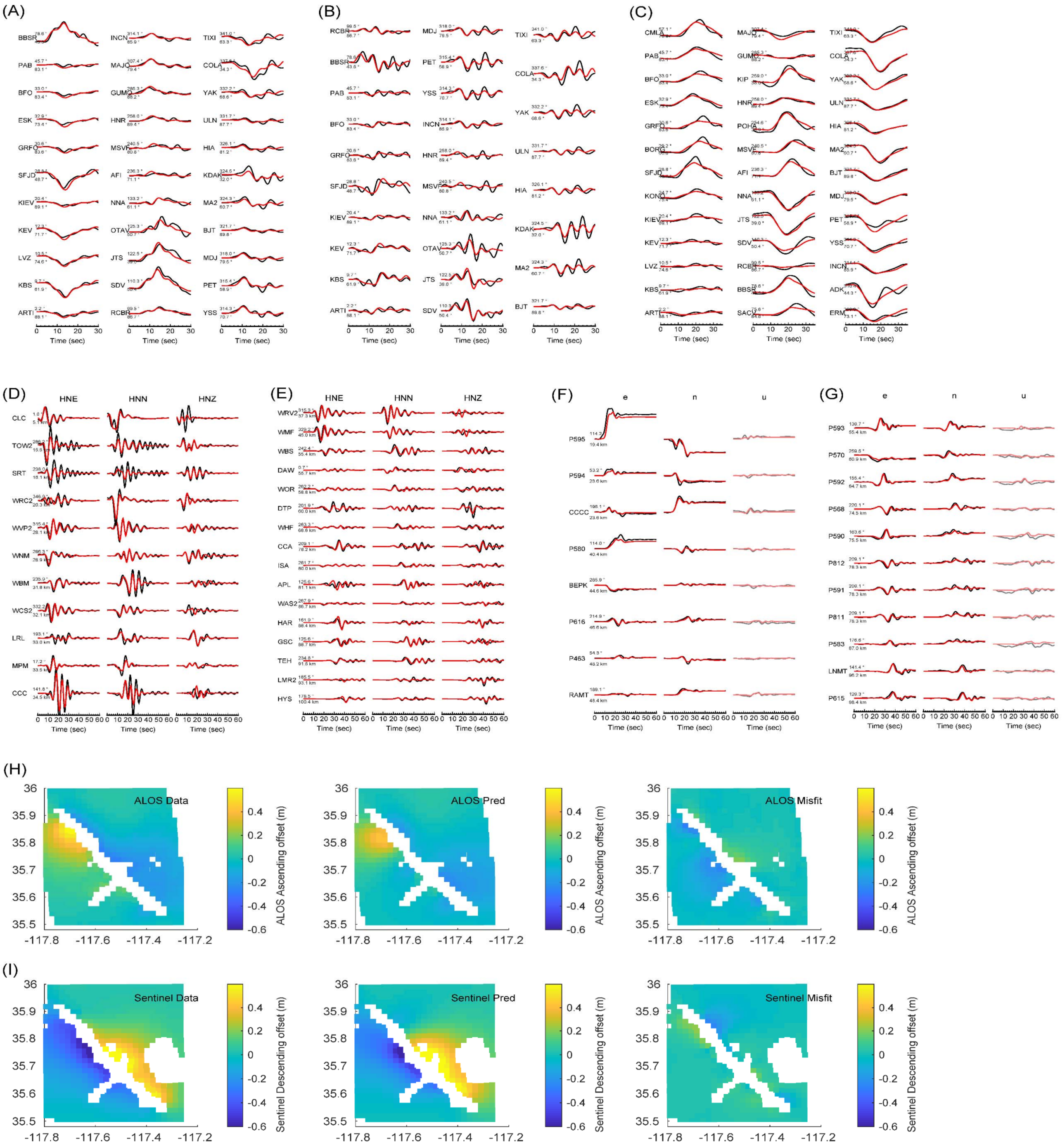

Figure S3.12. Data fittings for the preferred slip model of the Mw 7.1 mainshock. (A-G) Same as Fig. S3.6 but for the Mw 7.1 mainshock. (H-I) Fittings of InSAR LOS displacements for the ALOS-1 ascending and Sentinel-2 descending tracks, respectively.

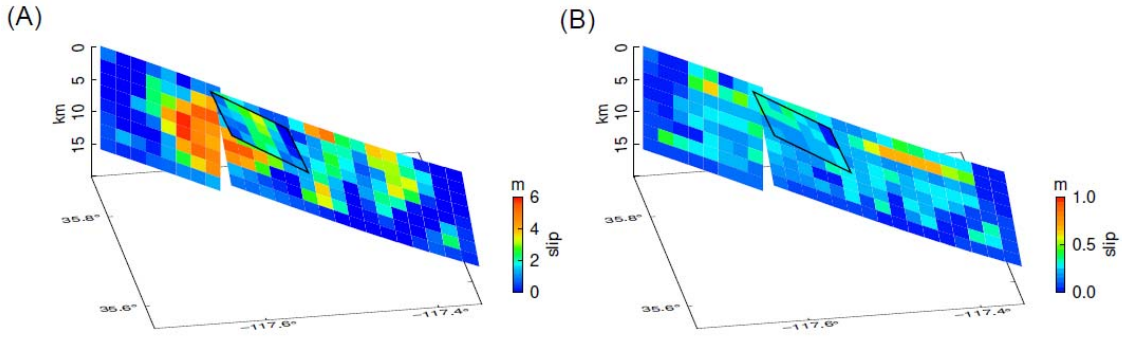

Figure S3.13. Same as Fig. S3.7 but for the Mw 7.1 mainshock.

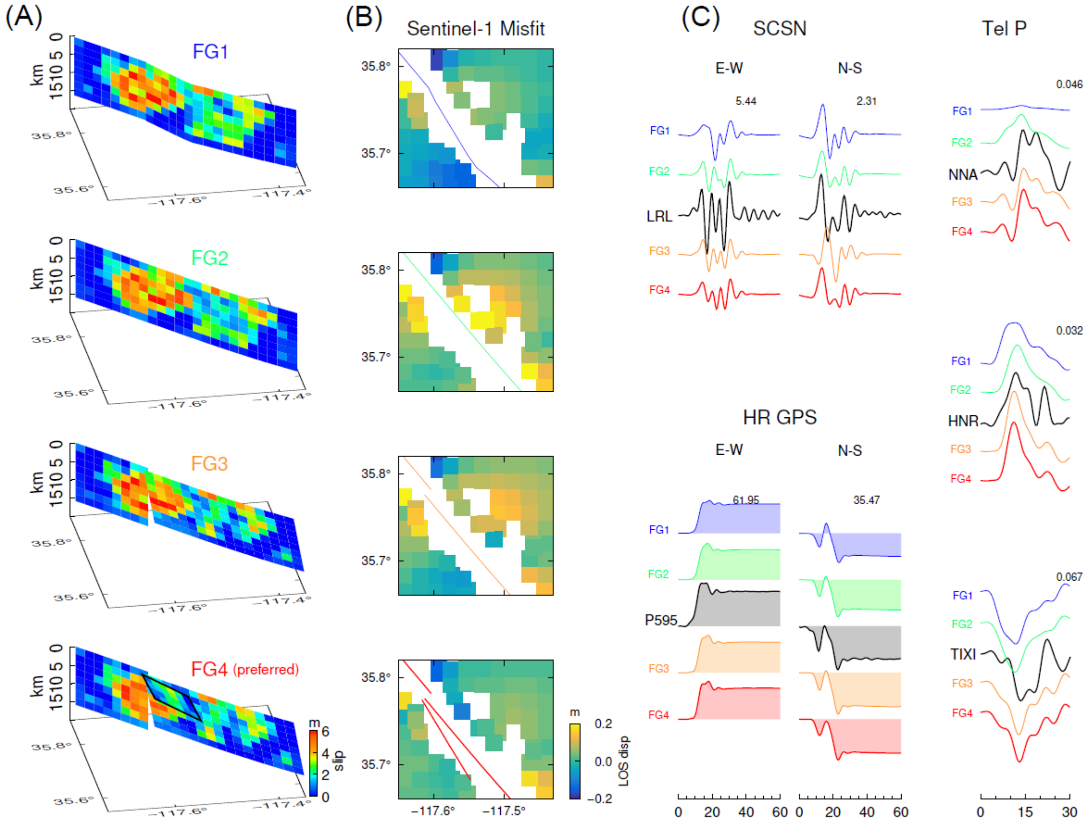

Figure S3.14. Comparison of 4 finite fault slip models for the Mw 7.1 mainshock assuming different fault geometries. (A) Slip distributions inferred from four fault geometries FG1-

FG4, in which FG4 is preferred in this study (same as Fig. 3.4A). (B) Sentinel-1 InSAR displacement misfits for four geometrical settings. Solid lines in blue, green, orange, and red show the fault surfaces for the corresponding models FG1-4, respectively. (C) Comparison of strong ground motion (SCSN), HRGPS, and Telseismic P waveforms. Data is shown in black, and synthetics for models FG1-FG4 are indicated by blue, green, orange, and red traces, respectively.

3.8 References

Aki, K., 1979. Characterization of barriers on an earthquake fault. Journal of Geophysical Research: Solid Earth 84, 6140-6148.

Andrews, D., 1989. Mechanics of fault junctions. Journal of Geophysical Research: Solid Earth 94, 9389-9397.

Barnhart, W.D., Hayes, G.P., Gold, R.D., 2019. The July 2019 Ridgecrest, California, Earthquake Sequence: Kinematics of Slip and Stressing in Cross-Fault Ruptures. Geophysical Research Letters 46, 11859-11867.

Bodin, T., Sambridge, M., Tkalčić, H., Arroucau, P., Gallagher, K., Rawlinson, N., 2012. Transdimensional inversion of receiver functions and surface wave dispersion. Journal of Geophysical Research: Solid Earth 117.

Brandenberg, S.J., Wang, P., Nweke, C.C., Hudson, K., Mazzoni, S., Bozorgnia, Y., Hudnut, K.W., Davis, C.A., Ahdi, S.K., Zareian, F., 2019. Preliminary report on engineering and geological effects of the July 2019 Ridgecrest earthquake sequence. Geotechnical Extreme Event Reconnaissance Association.

Chen, K., Avouac, J.-P., Aati, S., Milliner, C., Zheng, F., Shi, C., 2020. Cascading and pulse-like ruptures during the 2019 Ridgecrest earthquakes in the Eastern California Shear Zone. Nature Communications 11, 1-8.

DuRoss, C.B., Gold, R.D., Dawson, T.E., Scharer, K.M., Kendrick, K.J., Akciz, S.O., Angster, S.J., Bachhuber, J., Bacon, S., Bennett, S.E., 2020. Surface displacement distributions for the July 2019 Ridgecrest, California, earthquake ruptures. Bulletin of the Seismological Society of America 110, 1400-1418.

Eisner, L., Clayton, R.W., 2001. A reciprocity method for multiple-source simulations. Bulletin of the Seismological Society of America 91, 553-560.

Gabrielov, A., Keilis-Borok, V., Jackson, D.D., 1996. Geometric incompatibility in a fault system. Proceedings of the National Academy of Sciences 93, 3838-3842.

Goldberg, D.E., Melgar, D., Sahakian, V., Thomas, A., Xu, X., Crowell, B., Geng, J., 2020. Complex rupture of an immature fault zone: A simultaneous kinematic model of the 2019 Ridgecrest, CA earthquakes. Geophysical Research Letters 47, e2019GL086382.

Grant, M., Boyd, S., 2014. CVX: Matlab software for disciplined convex programming, version 2.1.

Graves, R.W., 1996. Simulating seismic wave propagation in 3D elastic media using staggered-grid finite differences. Bulletin of the Seismological Society of America 86, 1091-1106.

Graves, R.W., Wald, D.J., 2001. Resolution analysis of finite fault source inversion using one-and three-dimensional Green's functions: 1. Strong motions. Journal of Geophysical Research: Solid Earth 106, 8745-8766.

Hartzell, S.H., Heaton, T.H., 1983. Inversion of strong ground motion and teleseismic waveform data for the fault rupture history of the 1979 Imperial Valley, California, earthquake. Bulletin of the Seismological Society of America 73, 1553-1583.

Hartzell, S.H., Heaton, T.H., 1986. Rupture history of the 1984 Morgan Hill, California, earthquake from the inversion of strong motion records. Bulletin of the Seismological Society of America 76, 649-674.

Hauksson, E., Jones, L.M., Hutton, K., 2002. The 1999 M w 7.1 Hector Mine, California, earthquake sequence: complex conjugate strike-slip faulting. Bulletin of the Seismological Society of America 92, 1154-1170.

Hauksson, E., Jones, L.M., Hutton, K., Eberhart-Phillips, D., 1993. The 1992 Landers earthquake sequence: Seismological observations. Journal of Geophysical Research: Solid Earth 98, 19835-19858.

Hudnut, K.W., Brooks, B.A., Scharer, K., Hernandez, J.L., Dawson, T.E., Oskin, M.E., Ramon Arrowsmith, J., Goulet, C.A., Blake, K., Boggs, M.L., 2020. Airborne lidar and electro-optical imagery along surface ruptures of the 2019 Ridgecrest earthquake sequence, southern California. Seismological Research Letters.

Ji, C., Wald, D.J., Helmberger, D.V., 2002. Source description of the 1999 Hector Mine, California, earthquake, part I: Wavelet domain inversion theory and resolution analysis. Bulletin of the Seismological Society of America 92, 1192-1207.

Jia, Z., Shen, Z., Zhan, Z., Li, C., Peng, Z., Gurnis, M., 2020. The 2018 Fiji Mw 8.2 and 7.9 deep earthquakes: One doublet in two slabs. Earth Planet. Sci. Lett. 531, 115997.

Jost, M.u., Herrmann, R., 1989. A student's guide to and review of moment tensors. Seismological Research Letters 60, 37-57.

King, G.C., Stein, R.S., Lin, J., 1994. Static stress changes and the triggering of earthquakes. Bulletin of the Seismological Society of America 84, 935-953.

Lay, T., Ye, L., Bai, Y., Cheung, K.F., Kanamori, H., 2018. The 2018 MW 7.9 Gulf of Alaska earthquake: Multiple fault rupture in the Pacific plate. Geophysical Research Letters 45, 9542-9551.

Lee, E.J., Chen, P., Jordan, T.H., 2014a. Testing waveform predictions of 3D velocity models against two recent Los Angeles earthquakes. Seismological Research Letters 85, 1275-1284.

Lee, E.J., Chen, P., Jordan, T.H., Maechling, P.B., Denolle, M.A., Beroza, G.C., 2014b. Full-3-D tomography for crustal structure in southern California based on the scattering-integral and the adjoint-wavefield methods. Journal of Geophysical Research: Solid Earth 119, 6421-6451.

Liu, C., Lay, T., Brodsky, E.E., Dascher-Cousineau, K., Xiong, X., 2019. Coseismic Rupture Process of the Large 2019 Ridgecrest Earthquakes From Joint Inversion of Geodetic and Seismological Observations. Geophysical Research Letters 46, 11820-11829.

Meier, M.-A., Ampuero, J., Heaton, T.H., 2017. The hidden simplicity of subduction megathrust earthquakes. Science 357, 1277-1281.

Meng, L., Ampuero, J.-P., Stock, J., Duputel, Z., Luo, Y., Tsai, V., 2012. Earthquake in a maze: Compressional rupture branching during the 2012 Mw 8.6 Sumatra earthquake. Science 337, 724-726.

Milliner, C., Donnellan, A., 2020. Using Daily Observations from Planet Labs Satellite Imagery to Separate the Surface Deformation between the 4 July M w 6.4 Foreshock and 5 July M w 7.1 Mainshock during the 2019 Ridgecrest Earthquake Sequence. Seismological Research Letters.

Minson, S.E., Dreger, D.S., 2008. Stable inversions for complete moment tensors. Geophys. J. Int. 174, 585-592.

Minson, S.E., Meier, M.-A., Baltay, A.S., Hanks, T.C., Cochran, E.S., 2018. The limits of earthquake early warning: Timeliness of ground motion estimates. Science advances 4, eaaq0504.

Nielsen, S.B., Knopoff, L., 1998. The equivalent strength of geometrical barriers to earthquakes. Journal of Geophysical Research: Solid Earth 103, 9953-9965.

Oglesby, D.D., Day, S.M., Li, Y.-G., Vidale, J.E., 2003. The 1999 Hector Mine earthquake: The dynamics of a branched fault system. Bulletin of the Seismological Society of America 93, 2459-2476.

Okada, Y., 1985. Surface deformation due to shear and tensile faults in a half-space. Bulletin of the seismological society of America 75, 1135-1154.

Pollitz, F.F., Murray, J.R., Svarc, J.L., Wicks, C., Roeloffs, E., Minson, S.E., Scharer, K., Kendrick, K., Hudnut, K.W., Nevitt, J., 2020. Kinematics of Fault Slip Associated with the 4–6 July 2019 Ridgecrest, California, Earthquake Sequence. Bulletin of the Seismological Society of America.

Ponti, D.J., Blair, J.L., Rosa, C.M., Thomas, K., Pickering, A.J., Akciz, S., Angster, S., Avouac, J.P., Bachhuber, J., Bacon, S., 2020. Documentation of Surface Fault Rupture and Ground-Deformation Features Produced by the 4 and 5 July 2019 Mw 6.4 and Mw 7.1 Ridgecrest Earthquake Sequence. Seismological Research Letters.

Qian, Y., Ni, S., Wei, S., Almeida, R., Zhang, H., 2017. The effects of core-reflected waves on finite fault inversions with teleseismic body wave data. Geophysical Journal International 211, 936-951.

Ragon, T., Sladen, A., Simons, M., 2019. Accounting for uncertain fault geometry in earthquake source inversions–II: application to the M w 6.2 Amatrice earthquake, central Italy. Geophysical Journal International 218, 689-707.

Ramos, M.D., Neo, J.C., Thakur, P., Huang, Y., Wei, S., 2020. Stress Changes on the Garlock fault during and after the 2019 Ridgecrest Earthquake Sequence. Bulletin of the Seismological Society of America.

Ross, Z.E., Hauksson, E., Ben-Zion, Y., 2017. Abundant off-fault seismicity and orthogonal structures in the San Jacinto fault zone. Science Advances 3, e1601946.

Ross, Z.E., Idini, B., Jia, Z., Stephenson, O.L., Zhong, M., Wang, X., Zhan, Z., Simons, M., Fielding, E.J., Yun, S.-H., 2019. Hierarchical interlocked orthogonal faulting in the 2019 Ridgecrest earthquake sequence. Science 366, 346-351.

Shelly, D.R., 2020. A high-resolution seismic catalog for the initial 2019 Ridgecrest earthquake sequence: Foreshocks, aftershocks, and faulting complexity. Seismological Research Letters.

Shi, Q., Wei, S., Chen, M., 2018. An MCMC multiple point sources inversion scheme and its application to the 2016 Kumamoto M w 6.2 earthquake. Geophys. J. Int. 215, 737-752.

Sibson, R.H., 1996. Structural permeability of fluid-driven fault-fracture meshes. Journal of Structural Geology 18, 1031-1042.

Small, P., Gill, D., Maechling, P.J., Taborda, R., Callaghan, S., Jordan, T.H., Olsen, K.B., Ely, G.P., Goulet, C., 2017. The SCEC unified community velocity model software framework. Seismological Research Letters 88, 1539-1552.

Talwani, P., 1999. Fault geometry and earthquakes in continental interiors. Tectonophysics 305, 371-379.

Wang, K., Dreger, D.S., Tinti, E., Bürgmann, R., Taira, T.a., 2020. Rupture Process of the 2019 Ridgecrest, California M w 6.4 Foreshock and M w 7.1 Earthquake Constrained by Seismic and Geodetic Data. Bulletin of the Seismological Society of America 110, 1603-1626.

Wang, X., Zhan, Z., 2020a. Moving from 1-D to 3-D velocity model: automated waveform-based earthquake moment tensor inversion in the Los Angeles region. Geophysical Journal International 220, 218-234.

Wang, X., Zhan, Z., 2020b. Seismotectonics and fault geometries of the 2019 Ridgecrest sequence: insight from aftershock moment tensor catalog using 3D Green's functions. Journal of Geophysical Research: Solid Earth, e2020JB019577.

Xu, X., Sandwell, D.T., Smith-Konter, B., 2020. Coseismic Displacements and Surface Fractures from Sentinel-1 InSAR: 2019 Ridgecrest Earthquakes. Seismological Research Letters.

Yang, J., Zhu, H., Lumley, D., 2020. Time-lapse imaging of coseismic ruptures for the 2019 Ridgecrest earthquakes using multi-azimuth back-projection with regional seismic data and a 3D crustal velocity model. Geophysical Research Letters, e2020GL087181.

Zhan, Z., Kanamori, H., 2016. Recurring large deep earthquakes in Hindu Kush driven by a sinking slab. Geophys. Res. Lett. 43, 7433-7441.

Zhan, Z., Kanamori, H., Tsai, V.C., Helmberger, D.V., Wei, S., 2014. Rupture complexity of the 1994 Bolivia and 2013 Sea of Okhotsk deep earthquakes. Earth and Planetary Science Letters 385, 89-96.

Zhang, Y., Zheng, X., Chen, Q., Liu, X., Huang, X., Yang, Y., Xu, Q., Zhao, J., 2020. Automatic inversion of rupture processes of the foreshock and mainshock and correlation of the seismicity during the 2019 Ridgecrest earthquake sequence. Seismological Research Letters 91, 1556-1566.

Zhao, L., Chen, P., Jordan, T.H., 2006. Strain Green's tensors, reciprocity, and their applications to seismic source and structure studies. Bulletin of the Seismological Society of America 96, 1753-1763.

Chapter 4

A SLOW M8 EVENT SANDWICHED BETWEEN REGULAR RUPTURES

Jia, Zhe, Zhongwen Zhan, and Hiroo Kanamori. "The 2021 South Sandwich Island Mw 8.2 earthquake: a slow event sandwiched between regular ruptures." In: *Geophysical Research Letters* 49, no. 3 (2022): e2021GL097104. Doi: 10.1029/2021GL097104.

4.1 Abstract

We determined the rupture sequence of the Aug 12, 2021 M_W 8.2 South Sandwich Island earthquake which appears to be a complex sequence in both time and space. Notable tsunamis were recorded by tide gauges at global distances. Given the complexity of this event, we conducted a multiple subevent inversion on broadband seismograms, to resolve its complex variations of fault geometry, location, depth, and temporal characteristics. We found that the rupture initiated as a regular deep thrust earthquake; it then ruptured shallower and triggered a silent and dominantly slow subevent extending ~200 km to the south, and ended with 2 other regular subevents. The total duration is ~260s, unusually long for an M_W 8.2 event. Our result is qualitatively consistent with other moment tensor solutions and the deviant m_B-M_W and M_S-M_W relations, and provides a more quantitative space-temporal pattern of this unusual sequence.

4.2 Introduction

Large megathrust earthquakes on the subduction interface extend from near-trench to depths and display very different depth-varying slip behaviors (Lay et al., 2012). Large earthquakes that rupture the shallowest portion of the subduction interface (<15km) can generate devastating tsunamis, but they appear to rupture slowly with inefficient excitation of short-period seismic waves disproportionately to their seismic moment and tsunami. These earthquakes are “tsunami earthquakes” (Kanamori, 1972). At deeper depths

(15~50km), large thrust earthquakes have faster rupture velocities and stronger radiation of short-period seismic energy with inefficient tsunami generation. Their contrasting rupture characteristics are well interpreted by two distinct types of fault properties; the slow slip of shallow tsunami earthquakes is commonly attributed to weak sediments and low rigidity of the upper plate (Bilek and Lay, 1999; Sallarès and Ranero, 2019; Sallarès et al., 2021), while the brittle failures of unstable fault patches explain the fast deeper earthquakes.

On August 12, 2021, a great earthquake (M_w >8) struck the South Sandwich Island region of the south Atlantic Ocean (Fig. 4.1a). This event occurred close to the South Sandwich trench, where the South American plate subducts beneath the South Sandwich plate at a velocity of 7 cm/year (Pelayo and Wiens, 1989). A remarkable observation of this earthquake is its far reaching-tsunamis. The tsunamis spread to the north Atlantic, Pacific, and Indian Oceans, where tide gauges measured peak amplitudes of ~20 cm at over 10,000 km distance from the source (Fig. S4.1). Although modeling these tide gauge observations is challenging because of the lack of detailed bathymetry data between the source and gauges, the observed tsunamis at global distances appear to suggest that the South Sandwich Island earthquake could be categorized as a regular shallow tsunamigenic earthquake.

However, the South Sandwich Island earthquake seems to have extended to large depths with a complex temporal history. The early report (PDE) from the National Earthquake Information Center (NEIC) of the US Geological Survey listed 2 events within 3 minutes: 1. NEIC1, At 18:32:52 (UTC) (25.03° W, 57.68° S, Depth=47.2 km, M_w=7.5) and 2. NEIC2, At 18:35:17 (25.26° W, 58.38° S, Depth=22.8 km, M_w=8.1). In this paper, we call collectively the earthquake sequence which started at 18:32:52 (UTC) and lasted for about 300s, the 2021 South Sandwich Island earthquake, and we refer the 1st (NEIC1) and 2nd (NEIC2) events as the foreshock and the mainshock, respectively. The Global Centroid Moment Tensor Project (GCMT) (Ekström et al., 2012) reported 2 events: 1. GCMT1 (202108121832A, centroid time: 18:35:25, M_w=8.3, 24.34° W, 59.48° S, Depth=20.0 km) and 2. GCMT2 (202108121835A, centroid time: 18:36:13, M_w=7.9, 25.15° W, 60.47° S, 15.1 km). USGS NEIC also reported a moment tensor solution at the centroid time around 18:36 with M_{wc}=7.98 and depth=10 km with an alternative solution with M_{ww}=8.13 and depth=35.5 km (more details in supporting table S4.1). Given the variability of these solutions, we attempted W-phase inversion. Because of the complex interference of the waveforms of several events, only with a very narrow long-period pass band (0.00125 to 0.002 Hz, i.e., 500 to 800 s), we could obtain a solution that can fit long-period waveforms satisfactorily for 40 stations (more details in supporting text, Fig. S4.2-4.3).

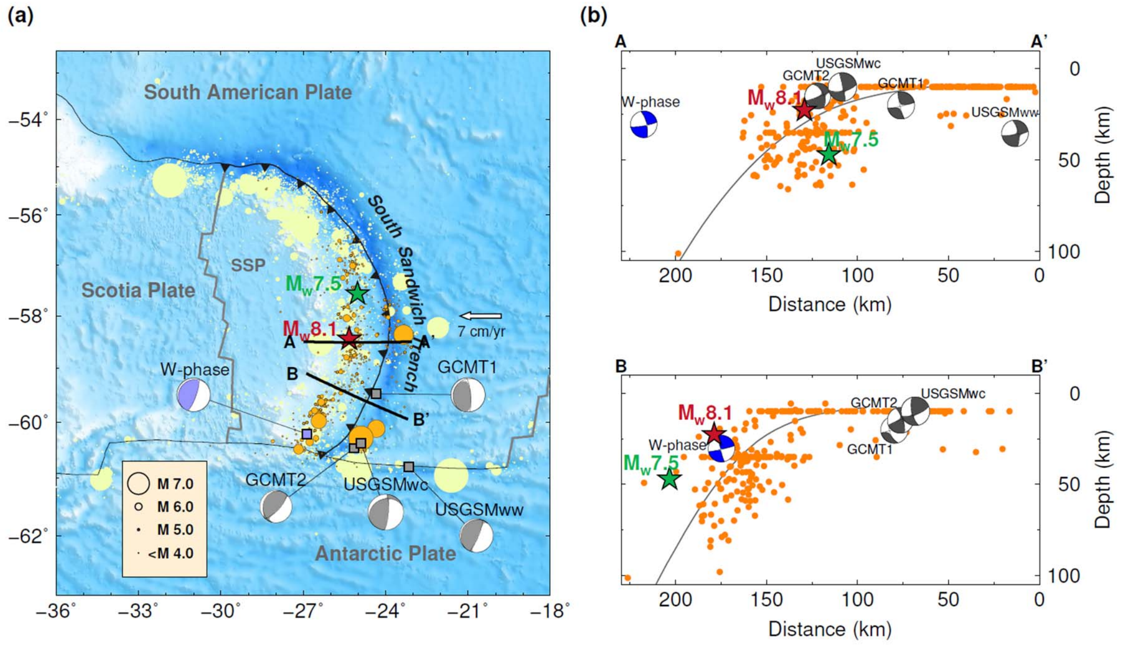

Figure 4.1. Overview of the tectonic setting and seismicity. (a) Tectonics of the South Sandwich region. The M_w 7.5 foreshock (green star) and the M_w 8.1 mainshock (red star) occurred close to the South Sandwich Trench, where the South America Plate subducts under the South Sandwich Plate (SSP). Yellow circles show the background seismicity according to the ISC catalog. Orange circles indicate the aftershocks within two weeks of the South Sandwich event. The beachballs display our W-phase moment tensor (in blue),

USGS NEIC M_{wc}, M_{ww}, and two Global CMT solutions (in gray). (b) Cross-sections along the black line segments in (a). The orange dots indicate the aftershocks within 100 km of the profiles. The black line represents the Slab 2.0 interface. Beachballs and stars are the same as (a), but for side view.

The depths reported by different catalogs range from 10 to 50 km, and the hypocenters scatter around the Slab 2.0 (Hayes et al., 2018) interface (Fig. 4.1b). This is probably caused by difficulty in locating the events accurately, due to the complex interference of seismic waves from the foreshock and mainshock. Nevertheless, the deeper depths of the South Sandwich Island earthquake appear to contradict the shallow slip inferred from the global-spreading tsunami. While detailed rupture analyses would be needed to understand this disparity, it is difficult to define a physical fault plane for slip inversions due to the diverse locations and focal mechanisms from different sources (Fig. 4.1). In addition, the aftershocks extend ~400km along the curved subduction zone, making a planar fault unphysical. Thus, we need to analyze the rupture properties of this earthquake with flexibility in fault geometries, while maintaining the depth-dependent complexities.

In this study, we first investigate the overall spectral characteristics of the event. Then, we determine the kinematic rupture process with a multiple subevent inversion of broad-band seismic waveforms, and evaluate the contributions of subevents and discuss their relationships.

4.3 General Spectral Characteristics

Given the complex rupture characteristics of the 2021 South Sandwich Island earthquake, we first investigate this event using 3 magnitude scales, m_B, M_S, and M_W. Although m_B and M_S are old somewhat qualitative parameters, they are available for global earthquakes and useful for understanding the spectral characteristics of the South Sandwich Island sequence in global context. To the first order, m_B, M_S, and M_w represent the spectral amplitudes of the sequence at about 4s, 20s, and 200s or even longer period.

For the measurement of m_B, we used the method described in Kanamori and Ross (2019) which follows the method developed by Gutenberg and Richter (1956). We used the vertical component P-waves recorded at 54 global network stations (epicentral distance of 30°-80°, Fig. S4.4), which include peak amplitudes for the mainshock. The medians of station m_B are 6.87 and 7.10 for the foreshock and the mainshock, respectively. Fig. 4.2a compares the m_B-M_w relationship for these events with the m_B values of about 3,000 events with $M_w \geq 6$ for a period from 1988 to 2018 taken from Kanamori and Ross (2019). The m_B data for the global events shown by small dots represent the range for ensemble of global events. The m_B for the mainshock is probably the upper bound because the time window for the m_B measurements contains some energy from the foreshock, only 145s earlier. The m_B values for the foreshock and the mainshock are 0.4 and 0.6 m_B unit, respectively, smaller than the average global m_B-M_w trend; this indicates that these events, especially the mainshock, are deficient in short-period energy.

We made a similar comparison of M_S vs. M_w relationship. We computed M_S using 20 s surface waves from 483 global seismic stations (distance range of 30°-120°), and measured the peak ground motion amplitudes. Since the surface waves of the foreshock and mainshock overlap, we could not measure M_S for each event separately, and obtained just one M_S=7.68 (Fig. S4.5). Compared with the empirical global M_S-M_w relationship (Di Giacomo et al., 2015) from the ISC M_S dataset, the observed M_S is 0.5 smaller than the average trend (Fig. 4.2b).

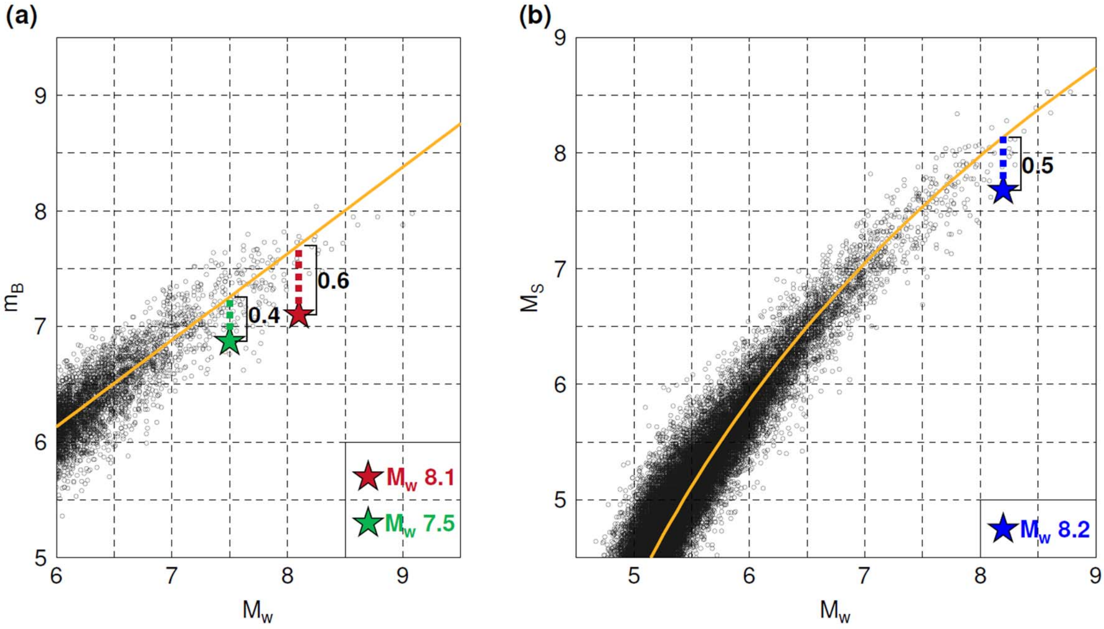

Figure 4.2. m_B and M_S measurements for the South Sandwich Island sequence. (a) Body wave magnitude m_B for the M_w 7.5 foreshock (green star) and the M_w 8.1 mainshock (red star). The solid yellow line indicates the general trend, m_B=0.75 M_w+1.63 (Kanamori and Ross, 2019), which is regressed from the database of global earthquakes for the period 1988-2018 (black circles). (b) Surface wave magnitude M_S for the sequence. The solid yellow line shows the empirical relation, M_w = exp(-0.222+0.233M_S)+2.863, regressed from the historical earthquakes (black circles) in the GCMT catalog (Di Giacomo et al., 2015).

The smaller m_B and M_S than the global average trends indicate depleted seismic energy release at short periods and slow rupturing characteristics (Kanamori, 1972; Kanamori and Ross, 2019). As shown in Fig. 4.2a-b, the South Sandwich Island earthquake is among the biggest outliers from the general trend. Other anomalous events similar to the South Sandwich Island earthquake includes the 1992 Nicaragua M_w 7.6, the 1994 Java M_w 7.8, the1996 Peru M_w 7.5, the 2006 M_w 7.7 Java, and the 2010 M_w 7.8 Mentawai Island earthquakes, all of which are well-known shallow slow tsunami earthquakes. This similarity suggests that the South Sandwich Island earthquake probably involved a substantial slow rupture component at the shallow subduction interface.

4.4 Multiple Subevent Inversion

To image the detailed rupture process of the earthquake, we applied the multiple subevent inversion method. Our subevent inversion algorithm represents a complex rupture with multiple simpler sources, each of which can have different timings, locations, source durations and focal mechanisms (Zhan et al., 2014; Ross et al., 2019; Jia et al., 2020a; Jia et al., 2020b). This simple parameterization allows flexible representation of time history and fault geometries, thereby capturing the first-order spatiotemporal rupture complexities. Our subevent method is particularly suitable for describing the South Sandwich Island earthquake which contains at least two major events in 3 minutes and involves potential fault geometry variations along the curved South Sandwich trench. As the possible slow rupture may propagate long distance with strong directivity effects, we introduce a finite subevent with a unilateral Haskell rupture model with a constant rupture velocity (Haskell, 1964). In this study, we use the Haskell model only for the long duration (>100s) subevent with potentially significant rupture directivity. We applied a Markov Chain Monte Carlo inversion in a Bayesian framework, and increased the number of subevents iteratively until the waveforms fit well (supporting text S2 for more details).

We collected 58 teleseismic (distance of 30°-90°) P velocity and displacement records, 43 teleseismic SH displacement records, and 12 three-component regional (distance within 40°) full waveforms in displacement (Fig. S4.6) for the subevent inversion. We removed their instrumental responses, and filtered the P and SH waves between 0.005-0.05 Hz for modeling short period features. For the regional full waves, we used them in two datasets with different filter bands. One of them with a 0.002-0.02 Hz passband represents intermediate period waves, and the other with 0.002-0.0033 Hz, long period motions. This combination of short, intermediate, and long period bands allows mapping the ruptures of different length scales simultaneously. The teleseismic Green's functions are calculated combining the propagator matrix method and plane wave approximation (Kikuchi and Kanamori, 1991; Qian et al., 2017), using the CRUST 2.0 (Laske et al., 2001) model at the source region and the IASPEI91 model (Kennet, 1991) at other places. The regional full-wave synthetics are computed with a frequency-wavenumber integration algorithm (Zhu and Rivera, 2002), using the PREM model (Dziewonski and Anderson, 1981).

Our subevent model consists of 5 subevents that span ~300 km along the trench (Fig. 4.3, supporting table S4.2). We fixed the first subevent at the NEIC M_w 7.5 event hypocenter. Data fittings (Fig. 4.3c, Fig. S4.7) and model uncertainties (Fig. 4.3b, Fig. S4.8) suggest that the source parameters are well constrained. The rupture begins with two short-duration subevents E1 (centroid time τ_C=13s after the origin time, duration d_C=23s, M_w 7.2) and E2 (τ_C=36s, d_C=19s, M_w 7.2), which in total (M_w 7.4) generally represents the NEIC M_w 7.5 foreshock. They have close locations and similar shallow dipping thrust focal mechanisms (average strike/dip/rake=157°/18°/82°), but the centroid depth of E1 is deep (39 km) while E2 is shallow (7 km), suggesting an up-dip rupture propagation along the plate interface. They are located near a patch of dense aftershock seismicity (Fig. 4.3a).

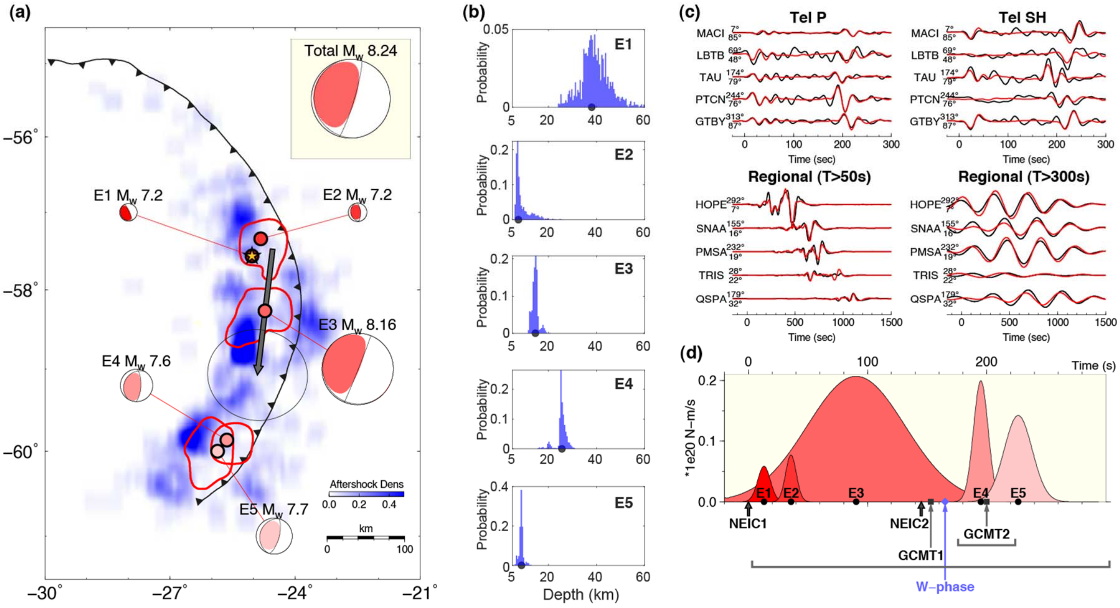

Figure 4.3. Rupture process of the South Sandwich Island sequence. (a) Subevent locations (red dots) and focal mechanisms (red beachballs). Yellow star indicates the hypocenter, collocated with the first subevent E1. The red contours show 95% confidence limits of the subevent locations. The gray arrow at E3 indicates its rupture directivity, and its length reflects rupture length. The black contour at the arrow end shows the 95% confidence limit of the rupture length and direction of E3, assuming the back end as the starting point. The aftershock density is displayed by the blue background color. The inset box shows the summation of subevent moment tensors. (b) Marginal probability distributions of subevent centroid depths. Gray circles show the final depths. (c) Representative data (black) and synthetic (red) waveform fits for teleseismic P and SH waves (0.005-0.05 Hz), vertical component intermediate period (0.002-0.02 Hz), and long period regional (0.002-0.0033 Hz) full waves. The numbers leading the traces are azimuths and distances. (d) Moment rate functions for all subevents. The black circles indicate subevent centroid times. The dark arrows point to two NEIC event origin times. Gray squares and blue diamond indicate centroid times of the GCMT and W-phase solutions, and the underneath solid lines denote the corresponding source durations.

Concurrent with the rupture initiation represented by E1-E2 in the first 50 s, the subevent E3 (τ_C=90s, M_w 8.16) emerged and continued for ~180 s. E3 contributes the most seismic moment of the South Sandwich Island earthquake, and its moment rate function (Fig. 4.3d) has a remarkably smaller aspect ratio (peak moment rate over duration, $1.2*10^{17}$ N-m/s^2) than regular subevents E1-E2 (average of $3.3*10^{17}$ N-m/s^2). As a Haskell source, E3 initiates close to the locations of E1-E2, and unilaterally propagates towards the south with a slow velocity (~1 km/s) and a long fault length (~180 km). E3 is located at 14 km depth with an uncertainty of ±5 km (Fig. 4.3b), and it has a very shallow-dipping thrust mechanism (strike/dip/rake=134°/4°/22°), although the strike and rake angles are not well constrained due to the shallow dip angle (Fig. S4.9). The shallow slow slip of E3 presumably transfers the stress along the slab, which explains the downdip dense aftershock seismicity as well as the triggered outer-rise earthquakes (Fig. 4.3).

The rupture terminated with the final two subevents E4 (τ_C=195s, d_C=26s, M_w 7.6) and E5 (τ_C=226s, d_C=50s, M_w 7.7) at 250-300 km south of the epicenter. They occurred about 3 minutes after the rupture initiation. E4 and E5 are also shallow dipping thrust subevents (average strike/dip/rake=206°/23°/106°), but their strike angles are ~50 degrees rotated clockwise from E1-E2. This rotation is consistent with the geometry of the curved South Sandwich Island trench. Their locations are close to the downdip high-density aftershock patch (Fig. 4.3). This spatial pattern is similar to that for the other two major slip asperities (E1-E2 and E3). The depth of E4 (25 km) is significantly deeper than E5 (9 km), indicating coexisting megathrust slip at different depth domains. Moment rate functions of E4-E5 display similar aspect ratios (average of 5.3*10^{17} N-m/s^2) to E1-E2, indicating that E4 and E5 are, unlike E3, more like regular ruptures.

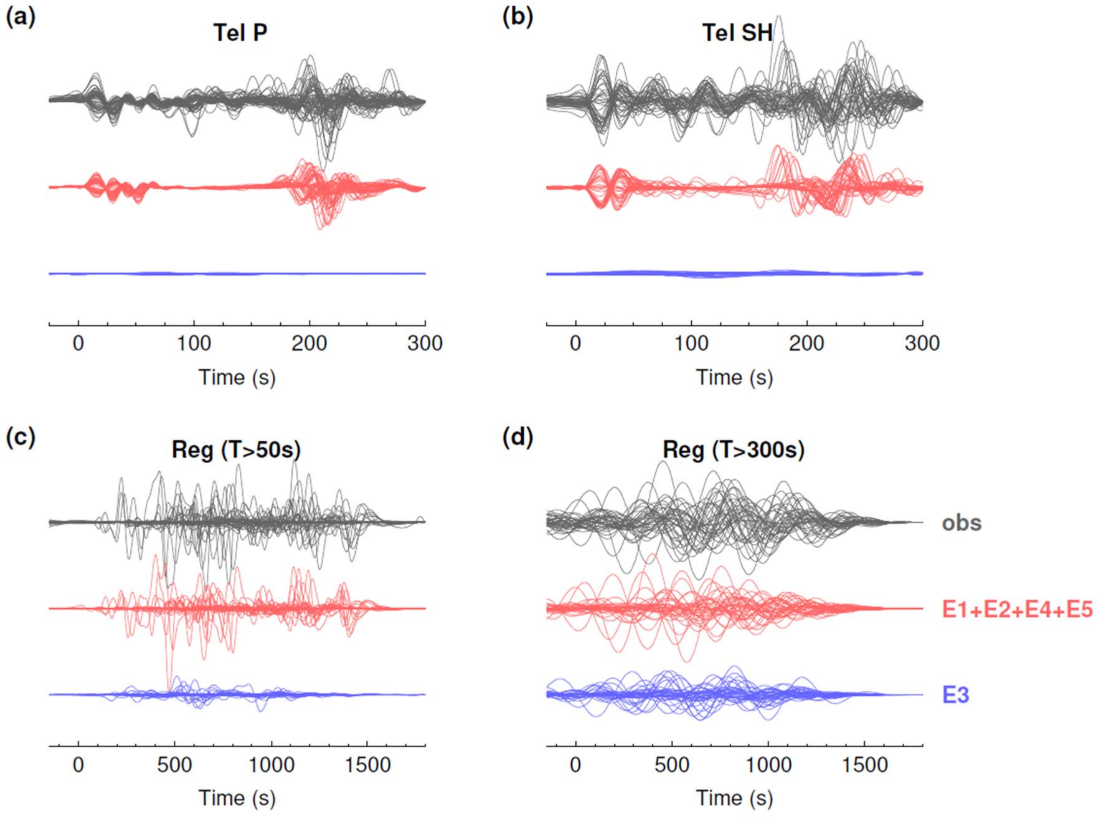

Figure 4.4. Waveform contributions from two groups of subevents. The observed data for all stations are plotted together in black lines. The total contribution from regular subevents E1, E2, E4, and E5 are in red lines. The synthetics of the slow subevent E3 are indicated by blue lines. (a) P waves, (b) SH waves, (c) Intermediate period (0.002-0.02 Hz), and (d) long period (0.002-0.0033 Hz) regional full waveforms.

The low aspect ratio, slow rupture velocity, overall shallow depth, and shallow-dipping mechanism of E3 suggest that it is a “slow earthquake” at the shallow subduction interface. This feature can be most prominently demonstrated in Fig. 4.4. The regular subevents E1, E2, E4, and E5 contribute almost all of the short and intermediate period waveforms, while E3 barely excited short and intermediate period signals (Fig. 4.4a-4.4c, Fig. S4.10). In contrast, E3 generated large long-period waves, comparable to the sum of all other subevents (Fig. 4.4d, Fig. S4.10). The diminished short period excitation explains the smaller-than-average m_B and M_S of E3 (Fig. 4.2).

Fig. 4.3d compares the overall rupture sequence determined by our multiple subevent inversion with the events determined by other methods. The sequence starts with E1 which is the foreshock (NEIC1). The long duration subevent E3 connects the short duration subevents E1-E2 at the beginning and E4-E5 at the end, forming a continuous megathrust rupture process. This approximately corresponds to the unusually long-duration GCMT1 (M_W 8.3) in the middle of the rupture extent (Fig. 4.1). The GCMT2 (M_W 7.9, half duration=24 s), with the centroid time 48 s later than GCMT1 probably overlaps with GCMT1 in time, and roughly corresponds to E4-E5 at the southern tip with rotated strike angles (Fig. 4.1). The W-phase solution, which is similar to the NEIC M_{WW}, probably represents a very long-period component of the latter half of the sequence (Fig. 4.1, Fig. S4.2).

4.5 Discussion and Conclusions

The 2021 South Sandwich Island (M_W 8.2) earthquake is a complex multiple event, including a slow subevent E3 connecting other regular thrust subevents at the beginning and the end. The slow subevent E3 contributes 70% of the total seismic moment of the sequence. The large moment and the relatively shallow depth of E3, with weak short-period seismic radiation, make this sequence as a whole look like a tsunami earthquake. The total duration of the whole sequence (E1 to E5) is about 260s; thus, the centroid time shift, 130s, estimated from the half duration is anomalously long on the centroid time delay vs. M_W scaling relation obtained by (Duputel et al., 2013), as shown by Fig. 4.5. The 2002 Guerrero earthquake (Kostoglodov et al., 2003) and the 2006 Java earthquake (Ammon et al., 2006), both of which are slow tsunami earthquakes, share a similar trend on Fig. 4.5. Thus, the South Sandwich Island earthquake appears to be a hybrid of deep rupture and slow tsunamigenic slip; this explains the somewhat unusual combination of the relatively large depth and the globally-observed tsunami.

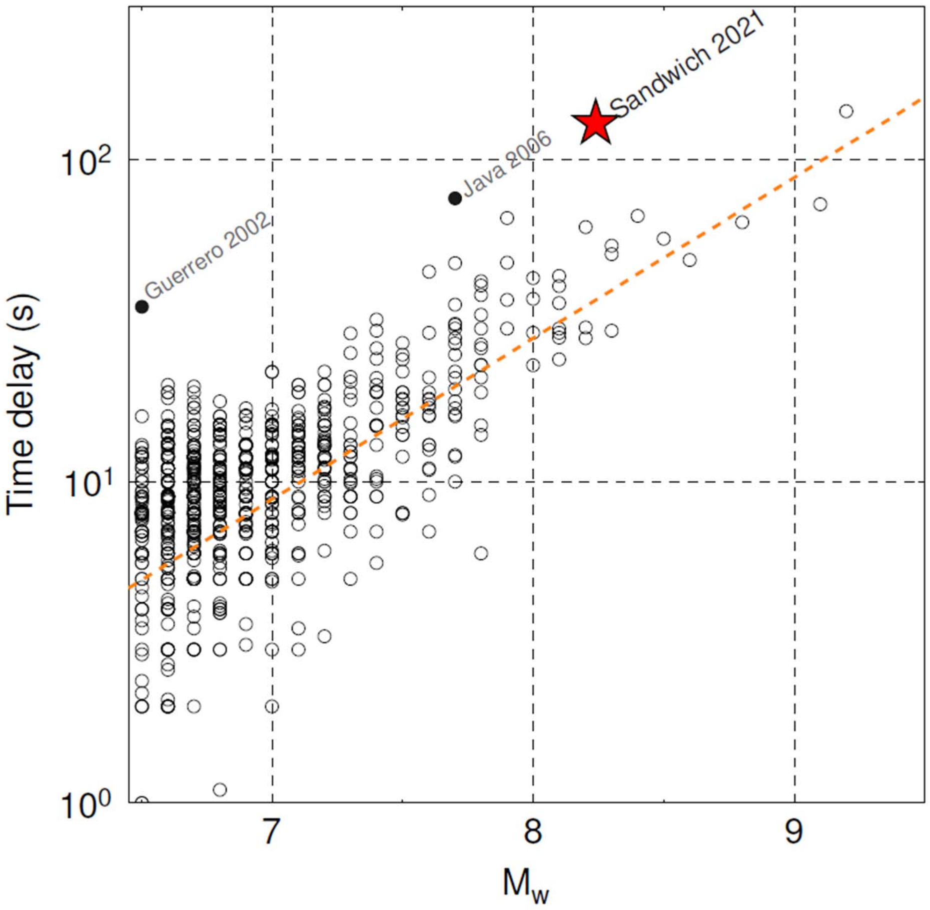

Figure 4.5. Relation between time delay (half duration) and M_w for the South Sandwich Island event (red star). Black circles represent the time delays of historical events from the W-phase measurements, the orange dashed line indicates an exponential relationship using the stress parameter of 0.37 MPa (Duputel et al., 2013).

Although the shallowest subduction interface is often considered seismically inactive due to the velocity-strengthening frictional properties (Scholz, 1998), some large tsunami earthquakes were found to host major slip at near-trench depths (Kanamori and Kikuchi, 1993; Lay et al., 2011). Lower upper plate rock rigidity at shallow depths has been illustrated to produce tsunami earthquake-like properties, including depleted short period seismic energy and slow rupture, (Bilek and Lay, 1999; Sallarès and Ranero, 2019; Sallarès et al., 2021), which well explains our observations for E3, suggesting the subduction zone geologic conditions could largely impact the tsunami potential. However, the slow component of the South Sandwich Island earthquake may have a broader depth extent than the traditional tsunami earthquakes. The slow subevent E3 has an overall shallow centroid depth of 14 km, which explains its global-spreading tsunamis and the two large (~M_w 7) outer-rise aftershocks (Fig. 4.1) due to the possible stress transfer at shallow subduction interface (Simons et al., 2011; Sladen and Trevisan, 2018) . However, it is probably not confined in the near-trench depths like other tsunami earthquakes, but could have extended to deeper domains, which is consistent with absence of observation of devastating tsunami. The deeper slip could trigger slow rupture by dynamic weakening (Ma, 2012; Noda and Lapusta, 2013), making the slip span over a broad depth range. However, the detailed depth-dependent slip distribution of the slow subevent remains unclear and difficult to resolve, because of the tradeoff between seismic moment, dip angle, and depth (Tsai et al., 2011). This requires further investigations.

In summary, the 2021 South Sandwich Island M_w 8.2 earthquake involves a complex depth-varying rupture process. The complex interaction of deep regular slip and shallow slow subevent explains the somewhat contradicting combination of the deep subevents, the tsunami earthquake-like features with diminished short-period seismic radiation, and the global-spreading tsunamis. This highlights the importance of accurately mapping the slow components of megathrust earthquakes over a broad frequency band for reliable tsunami warning.

4.6 Supplementary Materials

NEIC PDE listed 2 events:

8/12/2021 18:32:52 (UTC), depth=47.2 km, M_w=7.5

8/12/2021 18:35:17 (UTC), depth=22.8 km, M_w=8.1

These 2 events are only 145 s apart, and the standard W phase inversion for the 1st event could not converge at any reasonable solution because the W phases from the 2 events interfered. The standard inversion for the 2nd event did not work either for the same reason. For the 2nd event, only after several trials using different frequency bands, we could achieve a reasonable waveform fit with a relatively narrow low-frequency band 0.00125 to 0.002 Hz (*i.e.*, 500 to 800 s). This solution (Fig. S4.2) can fit the W phase waveforms reasonably well for 45 phases at 40 stations (Fig. S4.2). However, because of the very narrow band and the complex interference of phases, the centroid location, especially the depth, is poorly constrained (Fig. S4.3). The overall mechanism and size of the event seem to be reasonably well constrained. The centroid time shift, t_c, is 20 s from 18:35:17(UTC) which means that the centroid time of this event is 18:35:37(UTC) which is 165 s after the origin time of the 1st event. Thus we consider that this event approximately corresponds to the GCMT event 202108121832A (referred to as GCMT1, centroid time 18:35:25 UTC, M_w=8.3). However, the quality of the solution is not up to the standard W phase solution because of the complex waveform interferences of the multiple events of the sequence.

We applied our subevent inversion method to simultaneously estimate the source parameters of 5 subevents. Each subevent has 10 point-source parameters, including 3 parameters for the subevent horizontal location and depth, a centroid time, a source time duration, and 5 deviatoric moment tensor elements. For the long-period subevent E3, we added two finiteness parameters, rupture velocity and rupture direction, to accommodate a Haskell unilateral rupture source with a constant rupture velocity. In this Haskell model, the dependence of the apparent source duration on rupture direction can be given by the following equation (local rise time is ignored),

$$D = D_0 \cdot \left(1 - \frac{V_r}{c} \cdot \cos(\theta - \varphi)\right),$$

where D is the apparent source duration for a station of azimuth φ, D_0 is the rupture duration, V_r is the rupture velocity, c is the phase velocity, and θ is the rupture direction. In this study, we calculate phase velocities for teleseismic P and SH waves with ray tracing, using the IASPEI91 model. Because the regional full waveforms are dominated by surface waves, we assume c to be 4 km/s as approximate Rayleigh and Love phase velocities at a dominant period of 50s and 300s. Overall, this hybrid parameterization of point source and Haskell subevents has 52 unknown parameters.

To improve the searching efficiency, we divide our inversion procedure into two stages, where we search a part of these parameters nonlinearly and invert the data for other parameters in a linear way. The outer stage has a Markov Chain Monte Carlo (MCMC) inversion sampler that searches nonlinear parameters (subevent locations, centroid times, source durations, rupture velocity and rupture direction). Its random walk process to propose new models is driven by a Metropolis-Hasting algorithm. In each step, the model is proposed by perturbing one of the nonlinear parameters while keeping the other nonlinear parameter at their current values. Selection of the parameter being perturbed is random. This approach ensures a high acceptance rate and improves the efficiency of converging to an optimum, which, if given broad model space being searched and high quality data fitting, should be close to the global optima. For each set of nonlinear parameters, we can linearly invert the data for the moment tensors of subevents as the inner stage, because the observed time series can be linearly related by subevent moment tensors and their Green's functions when subevent locations and timing are available. In practice, we predict apparent source time functions at all stations using the subevent locations and timings, then convolve them with the corresponding Green's functions, and eventually invert for deviatoric subevent moment tensors by extending the linear framework to multiple sources. In this way, only 27 nonlinear parameters are searched through the MCMC inversion, and it's much easier to extensively explore the model space.

We generated 72 Markov Chains and eventually kept 24 of them to avoid being trapped in local minima. The initial sample for each chain is randomly generated from bounded uniform distributions. Our MCMC inversion incorporates a Bayesian framework that propagates the data error and prior knowledge to the model error. We set the prior of all unknown parameters to be uniform distributions. We also empirically set the data error to be 10% to accommodate the inaccurate assumptions of the wave propagation processes, even though the true data error (noise and instrumental error) of the seismic waves are very small. This data error eventually turns to the width of the Markov Chain sample distributions, which reflects the marginal posterior probability density functions.

We used 58 vertical component teleseismic (epicentral distance of 30°-90°) P waves in both displacement and velocity, 43 transverse component teleseismic SH waves in displacement, 12 three-component regional (epicentral distance within 40°) full waveforms in displacement in our subevent inversion from the Global Seismic Network and the International Federation of Digital Seismograph Networks. The weighting of these three datasets is set to be 20:10:1 to scale the teleseismic waves up for similar final misfit contributions. For the inversion of teleseismic waves, we calculate the Green's functions with a hybrid method that combines propagator matrix and ray theory, and use a combination of the CRUST2.0 velocity model at the source location with an IASPEI91 model in the deeper earth. A limitation of this forward simulation method is that it does not consider PP or SS phases, but since the M_w 7.5 foreshock is much smaller than the M_w 8.1 mainshock, the PP and SS amplitudes of the foreshock do not overwhelm the P and S of the mainshock, the waveform interferences are limited. We also compute the regional full waveform synthetics with a frequency-wavenumber integration algorithm using the PREM model as an average structure from sea to land. We used the P and S arrival times predicted from ray tracing with the IASPEI91 model, and allowed maximum time shifts of 4s, 6s, and 10s for the P, SH, and regional full waves. Because all subevents could move their horizontal locations together with the seismograms shifting simultaneously, we need to fix the horizontal location of one subevent. Therefore, we anchored the location of the first subevent E1 at the hypocenter of the M_w 7.5 foreshock, assuming the rupture dimension between the initiation and centroid of E1 is small compared with the full sequence.

	Initiation time (UTC)	Centroid time (UTC)	Longitude (°)	Latitude (°)	Depth (km)	Magnitude	Strike (°)	Dip (°)	Rake (°)
NEIC1	18:32:52	NaN	-25.03	-57.68	47.2	7.5	NaN	NaN	NaN
NEIC2	18:35:17	NaN	-25.26	-58.38	22.8	8.1	NaN	NaN	NaN
GCMT1	NaN	18:35:25	-24.34	-59.48	20.0	8.3	204	14	118
GCMT2	NaN	18:36:13	-25.15	-60.47	15.1	7.9	195	22	64
USGSMwc	NaN	18:35:58	-24.90	-60.38	10.0	7.98	248	27	151
USGSMww	NaN	18:36:56	-23.16	-60.80	35.5	8.13	223	11	110
W-phase	NaN	18:35:33	-26.88	-60.22	30.5	8.12	222	14	112

Table S4.1. Source parameters for the South Sandwich Island earthquake from different catalogs.

	Centroid time (s)	Duration (s)	Longitude (°)	Latitude (°)	Depth (km)	Mrr (10^{20} N-m)	Mtt (10^{20} N-m)	Mpp (10^{20} N-m)	Mrt (10^{20} N-m)	Mrp (10^{20} N-m)	Mtp (10^{20} N-m)
E1	13.08	22.74	-25.03	-57.57	39.38	0.314	-0.104	-0.211	-0.301	0.669	0.083
E2	35.72	19.37	-24.82	-57.34	7.09	0.747	-0.151	-0.595	0.018	0.551	0.095
E3	90.38	176.12	-24.72	-58.28	14.26	2.469	-1.547	-0.922	8.191	19.743	2.049
E4	195.01	26.33	-25.64	-59.86	25.28	2.153	-0.304	-1.849	-0.236	2.268	-0.622
E5	226.37	50.40	-25.86	-60.00	8.94	3.315	-0.940	-2.375	0.704	2.917	-0.512

	M0 (10^{20} N-m)	M_w	Strike (°)	Dip (°)	Rake (°)	Rupture Velocity (km/s)	Rupture direction (°)
E1	0.79	7.20	150	11	84	NaN	NaN
E2	0.88	7.23	164	26	79	NaN	NaN
E3	21.58	8.16	134	4	22	1.01	187.06
E4	3.11	7.59	213	24	118	NaN	NaN
E5	4.25	7.69	199	22	94	NaN	NaN

Table S4.2. Subevent model parameters for the South Sandwich Island earthquake.

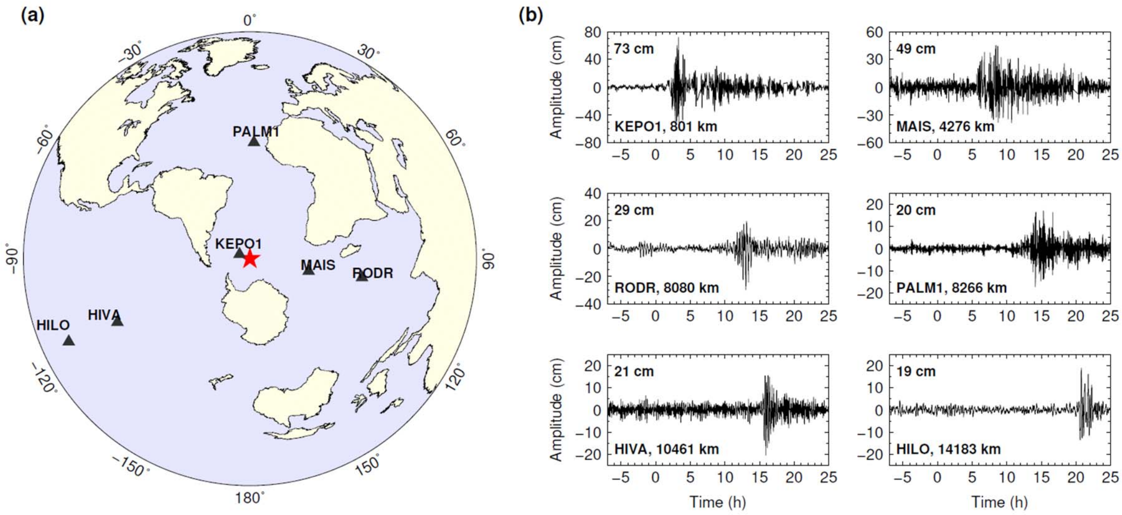

Figure S4.1. Tsunami of the South Sandwich Island sequence observed by tide gauges. (a) Distributions of the tide gauge stations (black triangles). The red star indicates the hypocenter of the South Sandwich Island sequence. (b) Waveforms recorded at the tide gauges in (a). The waveforms are high-pass filtered to periods shorter than 5 hours. The number above each trace shows the peak absolute amplitude of the tsunami. Below each trace the tide gauge station name and the distance from the South Sandwich Island earthquake source are shown.

(a)

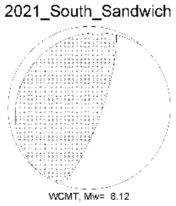

Moment Tensor [dyn-cm x 1e28]: 0.8130 -0.2078 -0.6052 0.5270 1.6134 -0.3721
Scalar moment [dyn-cm]: 1.89e+28
Best Nodal planes (strike/dip/rake): NP1: 221.8/ 13.7/ 111.8 NP2: 19.4/ 77.3/ 84.8
Eigenvalues [dyn-cm x 1e28]: 1.8945 -0.0185 -1.8760 (Mw = 8.12)
Fit Quality: RMS: 0.00343 mm (0.417) GAP: 93.9°, C# 724
Filter parameters: filt_order 4 filt_cf1 : 0.00125 filt_cf2 : 0.00200 filt_pass : 1

(b)

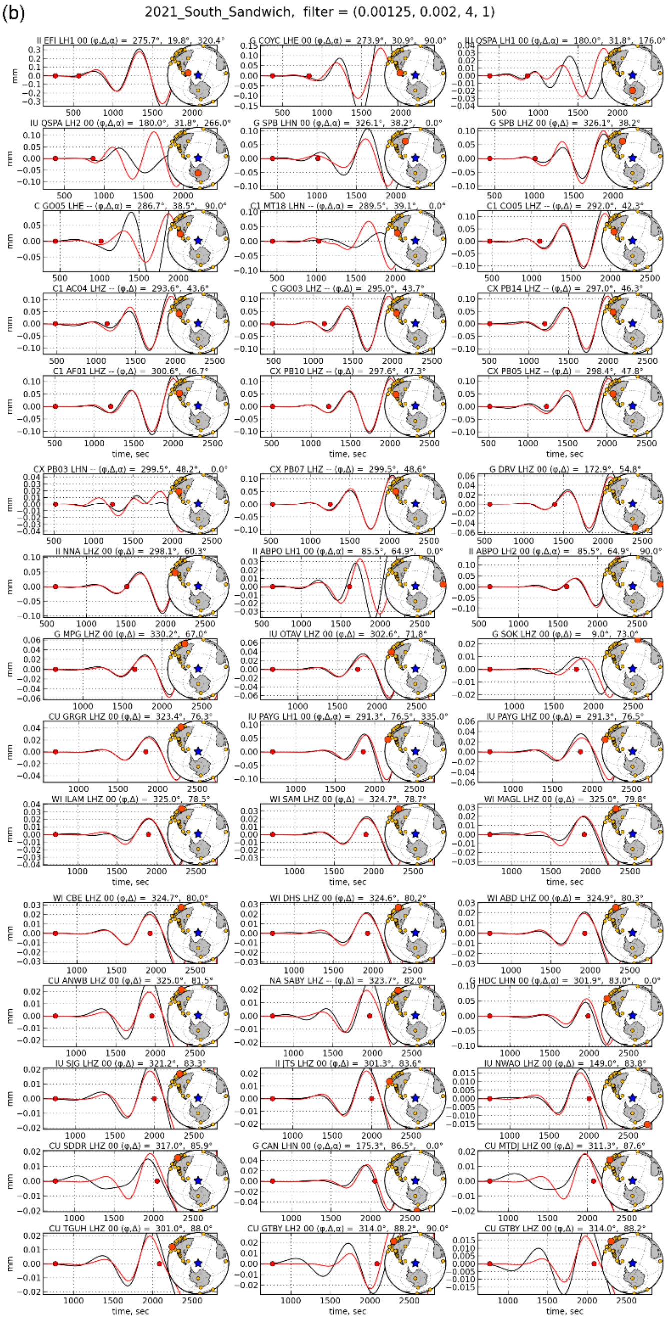

Figure S4.2. Long period W-phase point source solution for the 2021 South Sandwich Island sequence. (a) W-phase moment tensor and source parameters. The beachball shows the deviatoric moment tensor. The following lines display the moment tensor elements, scalar moment, and eigenvalues. The centroid depth is 30.5 km. (b) W-phase waveforms (between the red dots) for observation (black) and synthetics (red). Location of each station is indicated by the big red dot among the total set of stations used.

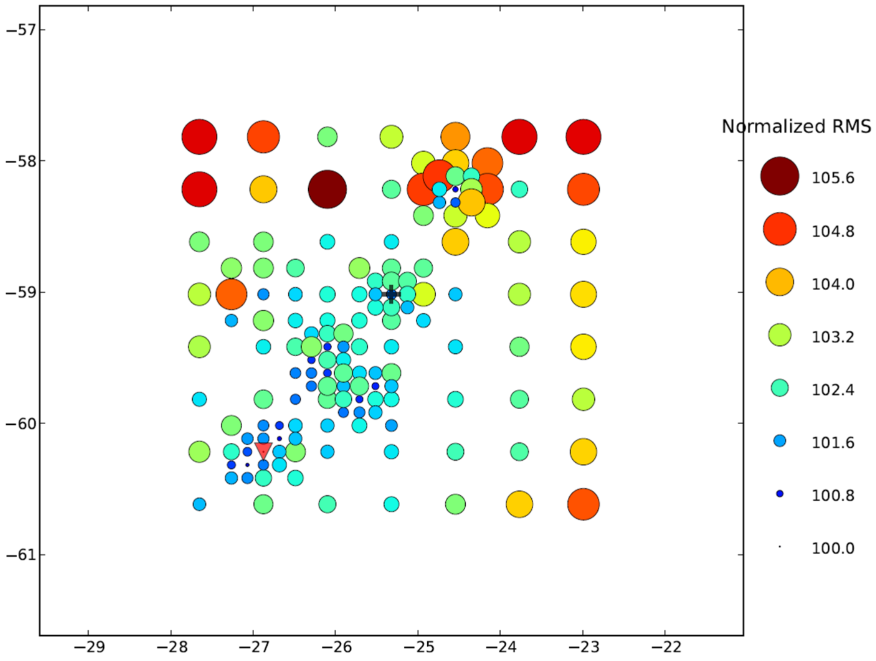

Figure S4.3. Resolution of location for the W-phase inversion. Circles indicate the searched locations. Their sizes and colors show the normalized root mean square misfit.

(a) m_B for the M_w 7.5

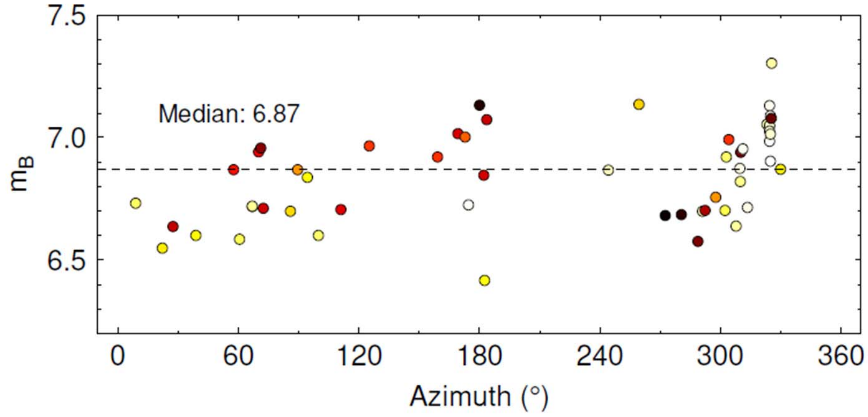

(b) m_B for the M_w 8.1

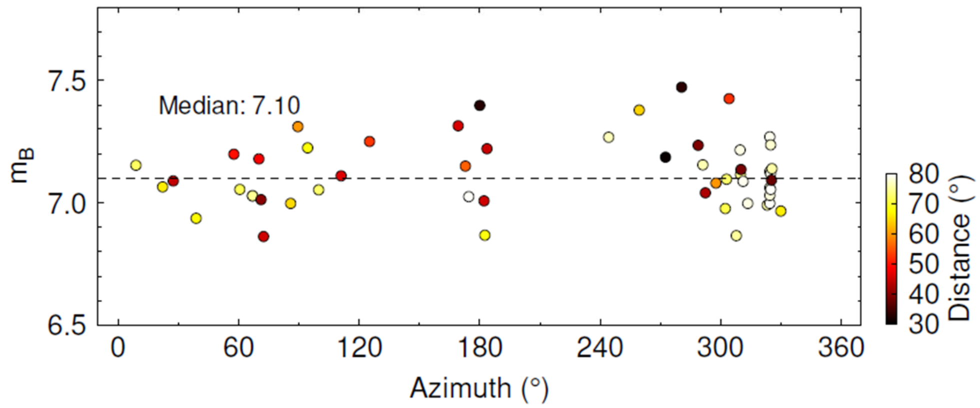

Figure S4.4. Body wave magnitudes of the South Sandwich Island sequence. (a) Individual body wave magnitudes m_B using stations at different azimuths (colored circles) for the M_w 7.5 foreshock. Colors show the epicentral distances. The black dashed line shows the median m_B of 6.87. (b) Same as (a), but for the M_w 8.1 mainshock. The median m_B is 7.10.

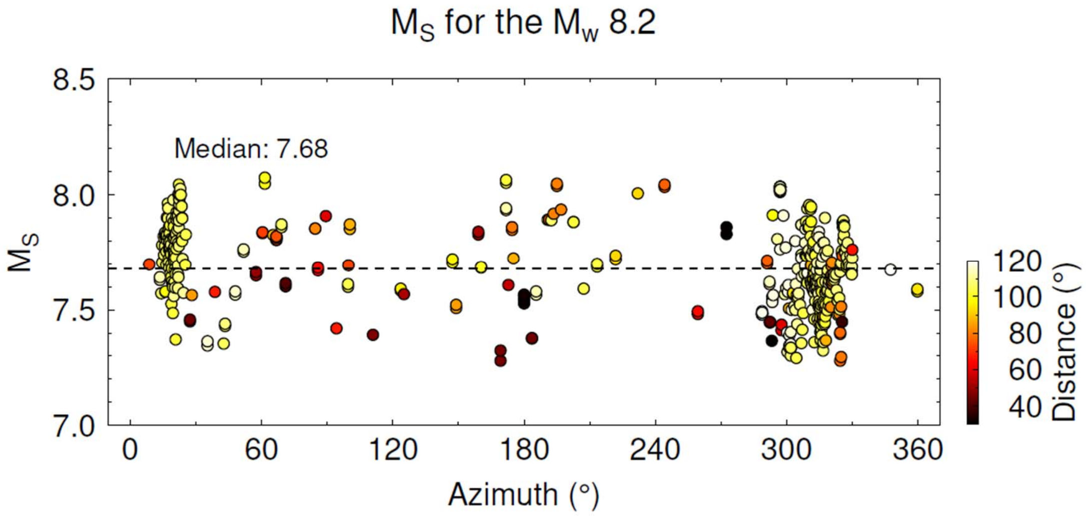

Figure S4.5. Surface wave magnitudes of the South Sandwich Island sequence. (a) Individual surface wave magnitudes M_S using stations at different azimuths (colored circles) for the overall M_w 8.2 South Sandwich Island sequence. Colors show the epicentral distances. The black dashed line shows the median m_S of 7.68.

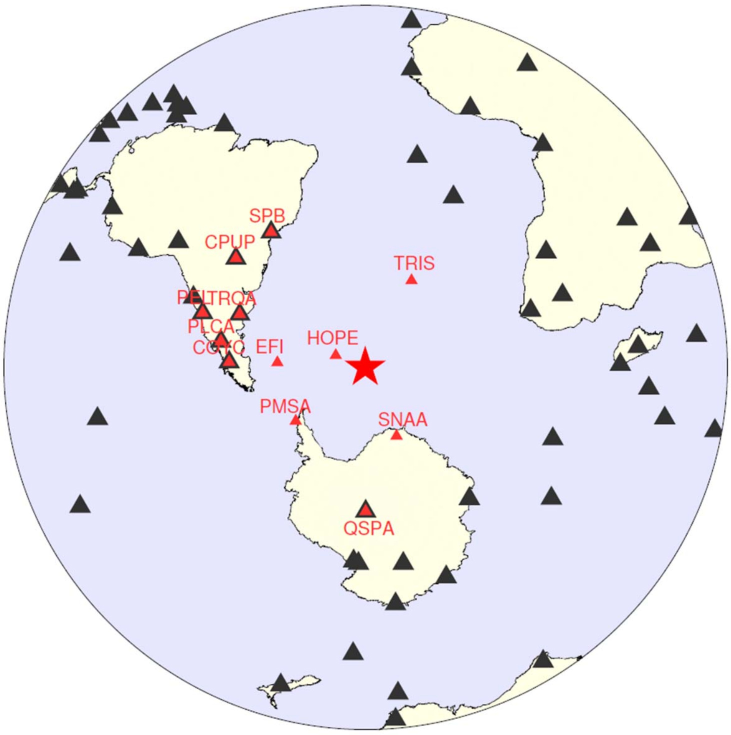

Figure S4.6. Seismic stations used in the subevent inversion. The red star shows the hypocenter of the South Sandwich Island sequence. Black and red triangles indicate the teleseismic (epicentral distance between 30° and 90°) and regional (epicentral distance within 40°) stations. Note that 7 of them are used for both teleseismic and regional inversions.

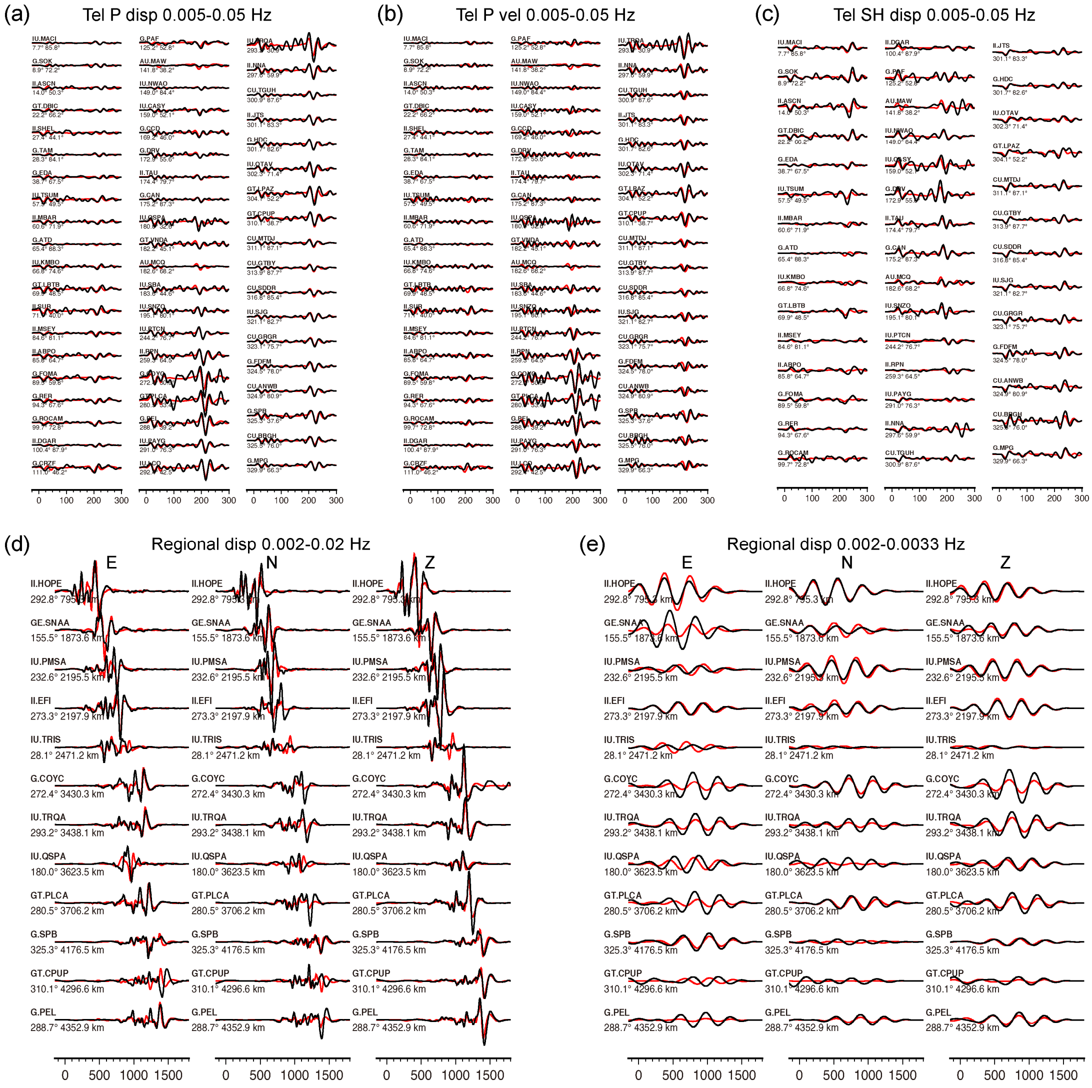

Figure S4.7. Waveform fits of the preferred subevent model for the South Sandwich Island sequence. Observed data and synthetics are indicated by black and red lines, respectively. The numbers leading each trace are the station azimuth and distance. (a) P waves in displacement. (b) P waves in velocity. (c) SH waves in displacement. (d) Intermediate period (0.002-0.02 Hz) regional full waveforms in displacement. (e) Long period (0.002-0.0033 Hz) regional full waveforms in displacement.

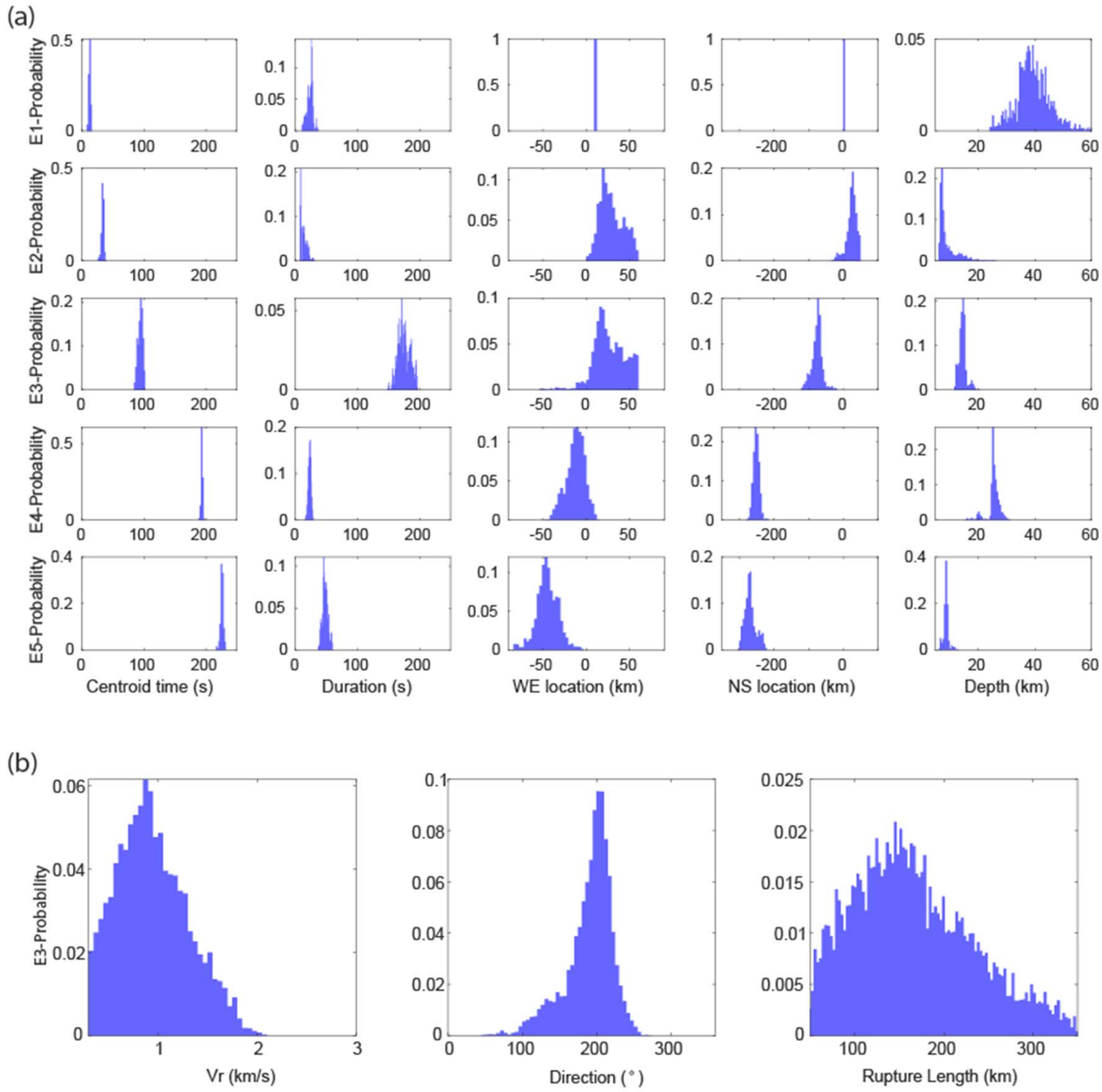

Figure S4.8. Assessment of subevent model uncertainties with the Markov Chain sample distributions. (a) Markov Chain sample distributions of the point source parameters. Columns from left to right indicate the marginal probability density distribution of subevent centroid times, durations, west-east locations, north-south locations and centroid depths. Rows represent subevents E1-E5. (b) Markov Chain sample distributions of finiteness parameters for the subevent E3. Columns are the rupture velocity, rupture direction (in degrees clockwise from the north), and rupture length.

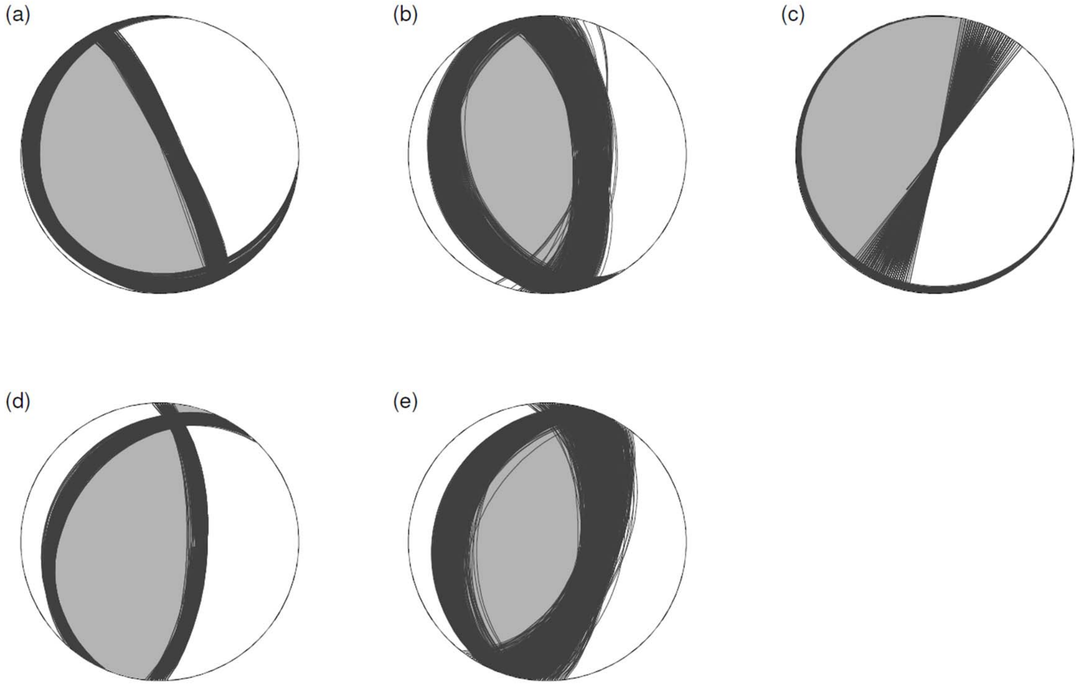

Figure S4.9. Ranges of double couple focal mechanisms for subevent E1 (a), E2 (b), E3 (c), E4 (d), and E5 (e) of the South Sandwich Island sequence.

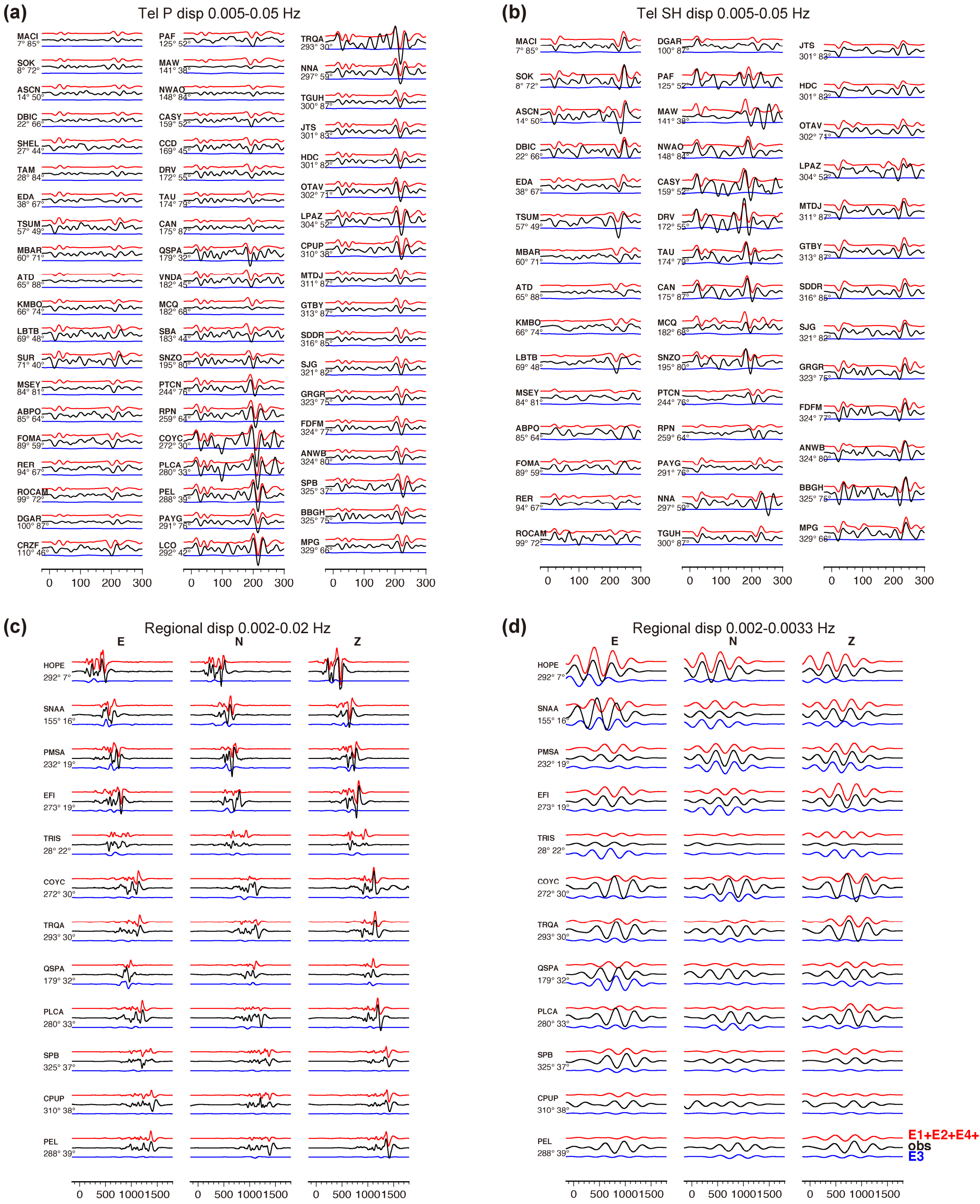

Figure S4.10. Contributions to waveforms from different groups of subevents. Black lines show the observed seismograms. Red lines represent the total contributions from regular subevents E1, E2, E4, and E5. Blue lines indicate the contribution from the slow subevent E3. Numbers leading traces are the station azimuths and distances. (a) P waves in displacement. (b) SH waves in displacement. (c) Intermediate period (0.002-0.02 Hz) regional full waveforms in displacement. (d) Long period (0.002-0.0033 Hz) regional full waveforms in displacement.

4.7 References

Ammon, C.J., Kanamori, H., Lay, T., Velasco, A.A., 2006. The 17 July 2006 Java tsunami earthquake. Geophys. Res. Lett. 33.

Bilek, S.L., Lay, T., 1999. Rigidity variations with depth along interplate megathrust faults in subduction zones. Nature 400, 443-446.

Di Giacomo, D., Bondár, I., Storchak, D.A., Engdahl, E.R., Bormann, P., Harris, J., 2015. ISC-GEM: Global Instrumental Earthquake Catalogue (1900–2009), III. Re-computed MS and mb, proxy MW, final magnitude composition and completeness assessment. Phys. Earth Planet. Inter. 239, 33-47.

Duputel, Z., Tsai, V.C., Rivera, L., Kanamori, H., 2013. Using centroid time-delays to characterize source durations and identify earthquakes with unique characteristics. Earth Planet. Sci. Lett. 374, 92-100.

Dziewonski, A.M., Anderson, D.L., 1981. Preliminary reference Earth model. Phys. Earth Planet. Inter. 25, 297-356.

Ekström, G., Nettles, M., Dziewoński, A., 2012. The global CMT project 2004–2010: Centroid-moment tensors for 13,017 earthquakes. Phys. Earth Planet. Inter. 200, 1-9.

Gutenberg, B., Richter, C.F., 1956. Earthquake magnitude, intensity, energy, and acceleration: (Second paper). Bull. Seismol. Soc. Am. 46, 105-145.

Haskell, N., 1964. Total energy and energy spectral density of elastic wave radiation from propagating faults. Bull. Seismol. Soc. Am. 54, 1811-1841.

Hayes, G.P., Moore, G.L., Portner, D.E., Hearne, M., Flamme, H., Furtney, M., Smoczyk, G.M., 2018. Slab2, a comprehensive subduction zone geometry model. Science 362, 58-61.

Jia, Z., Shen, Z., Zhan, Z., Li, C., Peng, Z., Gurnis, M., 2020a. The 2018 Fiji Mw 8.2 and 7.9 deep earthquakes: One doublet in two slabs. Earth Planet. Sci. Lett. 531, 115997.

Jia, Z., Wang, X., Zhan, Z., 2020b. Multifault Models of the 2019 Ridgecrest Sequence Highlight Complementary Slip and Fault Junction Instability. Geophys. Res. Lett. 47, e2020GL089802.

Kanamori, H., 1972. Mechanism of tsunami earthquakes. Phys. Earth Planet. Inter. 6, 346-359.

Kanamori, H., Kikuchi, M., 1993. The 1992 Nicaragua earthquake: a slow tsunami earthquake associated with subducted sediments. Nature 361, 714-716.

Kanamori, H., Ross, Z.E., 2019. Reviving m B. Geophys. J. Int. 216, 1798-1816.

Kennet, B., 1991. IASPEI 1991 seismological tables. Terra Nova 3, 122-122.

Kikuchi, M., Kanamori, H., 1991. Inversion of complex body waves—III. Bull. Seismol. Soc. Am. 81, 2335-2350.

Kostoglodov, V., Singh, S.K., Santiago, J.A., Franco, S.I., Larson, K.M., Lowry, A.R., Bilham, R., 2003. A large silent earthquake in the Guerrero seismic gap, Mexico. Geophys. Res. Lett. 30.

Laske, G., Masters, G., Reif, C., 2001. CRUST 2.0: A new global crustal model at 2× 2 degrees. Institute of Geophysics and Planetary Physics, The University of California, San Diego, website http://mahi. ucsd. edu/Gabi/rem. dir/crust/crust2. html.

Lay, T., Ammon, C.J., Kanamori, H., Yamazaki, Y., Cheung, K.F., Hutko, A.R., 2011. The 25 October 2010 Mentawai tsunami earthquake (Mw 7.8) and the tsunami hazard presented by shallow megathrust ruptures. Geophys. Res. Lett. 38.

Lay, T., Kanamori, H., Ammon, C.J., Koper, K.D., Hutko, A.R., Ye, L., Yue, H., Rushing, T.M., 2012. Depth-varying rupture properties of subduction zone megathrust faults. J. Geophys. Res. 117.

Ma, S., 2012. A self-consistent mechanism for slow dynamic deformation and tsunami generation for earthquakes in the shallow subduction zone. Geophys. Res. Lett. 39.

Noda, H., Lapusta, N., 2013. Stable creeping fault segments can become destructive as a result of dynamic weakening. Nature 493, 518-521.

Pelayo, A.M., Wiens, D.A., 1989. Seismotectonics and relative plate motions in the Scotia Sea region. Journal of Geophysical Research: Solid Earth 94, 7293-7320.

Qian, Y., Ni, S., Wei, S., Almeida, R., Zhang, H., 2017. The effects of core-reflected waves on finite fault inversions with teleseismic body wave data. Geophys. J. Int. 211, 958-973.

Ross, Z.E., Idini, B., Jia, Z., Stephenson, O.L., Zhong, M., Wang, X., Zhan, Z., Simons, M., Fielding, E.J., Yun, S.-H., 2019. Hierarchical interlocked orthogonal faulting in the 2019 Ridgecrest earthquake sequence. Science 366, 346-351.

Sallarès, V., Prada, M., Riquelme, S., Meléndez, A., Calahorrano, A., Grevemeyer, I., Ranero, C.R., 2021. Large slip, long duration, and moderate shaking of the Nicaragua 1992 tsunami earthquake caused by low near-trench rock rigidity. Science Advances 7, eabg8659.

Sallarès, V., Ranero, C.R., 2019. Upper-plate rigidity determines depth-varying rupture behaviour of megathrust earthquakes. Nature 576, 96-101.

Scholz, C.H., 1998. Earthquakes and friction laws. Nature 391, 37-42.

Simons, M., Minson, S.E., Sladen, A., Ortega, F., Jiang, J., Owen, S.E., Meng, L., Ampuero, J.P., Wei, S., Chu, R., Helmberger, D.V., Kanamori, H., Hetland, E., Moore, A.W., Webb, F.H., 2011. The 2011 magnitude 9.0 Tohoku-Oki earthquake: mosaicking the megathrust from seconds to centuries. Science 332, 1421-1425.

Sladen, A., Trevisan, J., 2018. Shallow megathrust earthquake ruptures betrayed by their outer-trench aftershocks signature. Earth Planet. Sci. Lett. 483, 105-113.

Tsai, V.C., Hayes, G.P., Duputel, Z., 2011. Constraints on the long-period moment-dip tradeoff for the Tohoku earthquake. Geophys. Res. Lett. 38.

Zhan, Z., Kanamori, H., Tsai, V.C., Helmberger, D.V., Wei, S., 2014. Rupture complexity of the 1994 Bolivia and 2013 Sea of Okhotsk deep earthquakes. Earth Planet. Sci. Lett. 385, 89-96.

Zhu, L., Rivera, L.A., 2002. A note on the dynamic and static displacements from a point source in multilayered media. Geophys. J. Int. 148, 619-627.

Chapter 5

A BAYESIAN DIFFERENTIAL MOMENT TENSOR INVERSION METHOD

Jia, Zhe, Zhongwen Zhan, and Donald Helmberger. "Bayesian differential moment tensor inversion: theory and application to the North Korea nuclear tests." In: *Geophysical Journal International* 229, no. 3 (2022): 2034-2046. Doi: 10.1093/gji/ggac053.

5.1 Abstract

Moment tensors are key to seismic discrimination but often require accurate Green's functions for estimation. This limits the regions, frequency bands, and wave types in moment tensor inversions. In this study, we propose a differential moment tensor inversion (diffMT) method that uses relative measurements to remove the path effects shared by clustered events, thereby improving the accuracy of source parameters. Using results from regular inversions as a priori distribution, we apply Bayesian Markov Chain Monte Carlo to invert the body- and surface-wave amplitude ratios of an event pair for refined moment tensors of both events. Applications to three North Korea nuclear tests from 2013 to 2016 demonstrate that diffMT reduces the uncertainties substantially compared with the traditional waveform-based moment tensor inversion. Our results suggest high percentages of explosive components with similar double-couple components for the North Korea nuclear tests.

5.2 Introduction

Seismic moment tensor provides a point-source approximation of the radiation pattern and a measure of the event size. Different combinations of isotropic (ISO), double couple (DC), and compensated linear vector dipole (CLVD) components can manifest the first-order physics of different event types, such as natural earthquakes, collapses, landslides, and nuclear explosions, thus being used for their discrimination (Ford et al., 2009; Cesca et al., 2017; Alvizuri and Tape, 2018). Furthermore, double-couple focal mechanisms provide important insights on regional stress state (Hauksson, 1994; Hardebeck and Hauksson, 2001; Wang and Zhan, 2020b), plate interface morphology (Hayes et al., 2009; Zhan et al., 2012; Bazargani et al., 2013), and slab dynamics (Yang et al., 2017; Liu et al., 2021). In the past few decades, moment tensor inversion has gradually progressed from polarity-based to waveform-based inversion (Zhu and Helmberger, 1996; Kanamori and Rivera, 2008; Ekström et al., 2012). At the theoretical level, Tape and Tape (2012, 2013, 2015) proposed a mathematically intuitive way to view the moment tensors and examine the explosive and tensile mechanisms. Zhu and Ben-Zion (2013) developed a parameterization of full moment tensors with well-defined parameters for source inversion. These progresses in theory and inversion, together with the improving Earth structural modeling, reduce the focal mechanism errors to about 20 degrees for most moderate to large events in the centroid moment tensor catalogs (Duputel et al., 2012).

However, accurate full moment tensor inversions for shallow sources are still challenging. Robust moment tensor solutions are usually only retrievable at long periods (e.g. T>20s, (Minson and Dreger, 2008)) that are insensitive to small-scale structural heterogeneities. However, earthquakes and explosions of small to moderate size usually have limited near-field coverage and weak signals at long periods. For the short-period waves, modeling them is difficult because existing 3D crustal velocity models are often inadequate in capturing small scale heterogeneities at regional distances. Using inaccurate earth structural models could introduce errors in focal mechanisms and non-DC proportions (Frohlich and Davis, 1999). Taking the North Korea nuclear explosions as an example, different studies show nontrivial differences of moment tensor solutions (Cesca et al., 2017; Alvizuri and Tape, 2018; Chiang et al., 2018). For better azimuthal and take-off angle coverage, approaches that jointly invert regional and teleseismic waves have been proposed (Ni et al., 2010; Ford et al., 2012), but they still encounter difficulties from inaccurate Green's functions.

To accurately determine the moment tensors when the path structure is complex, approaches using 3D Green's functions have been introduced (Covellone and Savage, 2012; Wang and Zhan, 2020a). Most models used to calculate the 3D Green's function are travel-time- and waveform- based tomographic models. Travel time tomographic models, such as the LLNL model by Simmons et al. (2012) and the SALSA3D model by Ballard et al. (2016), can predict body waves arrivals with significantly reduced errors than 1D models, thereby being used to precisely detect and locate small seismic events. However, they are usually restricted by the smoothing in the inversions, and may not accurately fit the seismic waveforms. On the other hand, waveform-based tomographic models are more promising in explaining wiggles on seismograms (Fichtner et al., 2009; Tape et al., 2009; Bozdağ et al., 2016). But most global and continental scale models use long-period waveforms (e.g. T>17s globally) for inversion, due to the high computational cost. Only for specific areas of dense seismic monitoring, adjoint tomographic inversions based on higher frequency seismic waveforms have been developed and implemented in source inversions (Lee et al., 2014; Savage et al., 2014; Jia et al., 2020b).

To reduce the requirement of highly accurate velocity models, the empirical Green's function (EGF) methods are developed to study clustered explosions and earthquakes. Sites of artificial explosions are often clustered and share similar path and site effects. For example, all the North Korea nuclear tests were in the Punggye-ri site, within a few km from each other (Zhang and Wen, 2013, 2015; Wang and Hutko, 2018; Xu et al., 2020). As shown in Fig. 5.1, the regional waveforms from the Feb 2013 and Jan 2016 North Korea tests are highly similar at both broadband and long periods (T>5s), suggesting overlapping paths and common station terms. This similarity makes nuclear tests ideal for EGF methods, which removes the structural terms using relative measurements. Ni et al. (2010) used tectonic earthquakes to calibrate the path and site effects, thereby improving the moment tensor inversions of nuclear tests. Lay et al. (1984) inter-correlated source time functions and waveforms of two nuclear events to remove path influences and determine their yield and depths, and the method has also been applied on the North Korean nuclear explosions (Voytan et al., 2019). For tectonic earthquakes, smaller EGF events can help investigate the mechanisms and ruptures of mainshocks, including the 1994 Northridge earthquake (Dreger, 1994) and the 2004 Sumatra earthquake (Vallée, 2007).

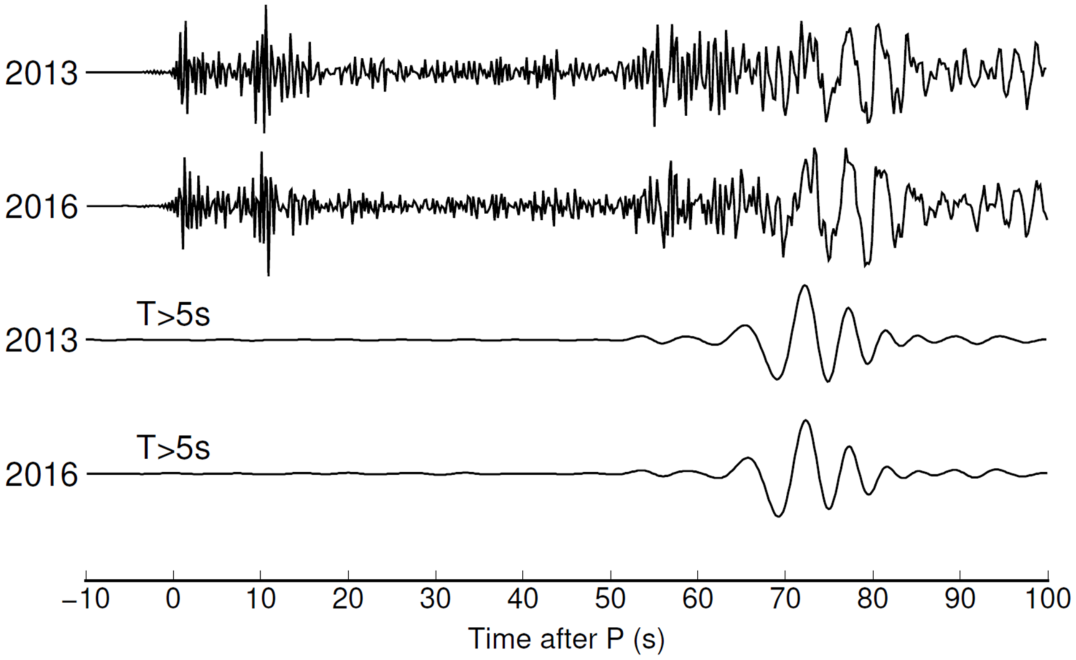

Figure 5.1. Waveform similarity of the Feb 2013 and Jan 2016 nuclear tests. The similarities in both broadband (top two) and low-passed filtered (bottom two) waveforms recorded at station MDJ suggest shared path/site effects. Note that P waves are only visible at short periods. The epicentral distance is about 400km.

Among the EGF approaches, relative moment tensor inversion methods stand out as a particular category. Similar to the double-difference relocation algorithm which removes common travel time anomalies for more precise locations (Waldhauser and Ellsworth, 2000), relative moment tensor inversions eliminate the path and site amplifications to reduce moment tensor errors. Plourde and Bostock (2019) used relative amplitudes of body waves among a cluster of seismic events to improve focal mechanisms. EGF methods greatly reduce moment tensor errors, but they can also introduce bias by assuming the reference event is well resolved. Dahm (1996) avoided the assumption on a single reference event by using arbitrary a priori constraint, but facing the issues of interference bias and lack of uncertainty assessments. To better assess errors and to avoid arbitrary selection of reference events, we need to incorporate Bayesian statistics to the relative moment tensor inversion methods with appropriate a priori information.

In this study, we develop a differential moment tensor inversion (diffMT) algorithm to study paired seismic events in a Bayesian framework. We take amplitude ratios of various seismic phases to cancel out path and site effects, and expect reduced moment tensor errors. For nuclear tests, these should translate to better explosion discriminations and yield estimations. We verify the diffMT algorithm using synthetic data, and apply it to three North Korea nuclear tests between 2013 and 2016. We compare our results with traditional waveform inversion solutions, and analyze the explosion and tectonic release components of these tests.

5.3 Methods

Our diffMT method refines the waveform-based moment tensor prior distribution with additional differential measurements for an event pair. There are two steps. First, we apply the generalized Cut-and-Paste (gCAP) inversion for moment tensor solutions and their uncertainties as the prior information. We then measure the amplitude ratios for regional and teleseismic P waves, regional Rayleigh and Love waves, and conduct Markov Chain Monte Carlo (MCMC) inversion on these differential measurements for the posterior distributions of moment tensor components.

Our first step is equivalent to most traditional moment tensor inversions. In this study, we use gCAP (Zhu and Ben-Zion, 2013) as our main driver for the waveform inversion, as improved by Bai et al. (2020) to combine near-field and teleseismic data. The CAP methodology (Zhao and Helmberger, 1994; Zhu and Helmberger, 1996) breaks seismograms into Pnl and S/Surface waves, and models them simultaneously but allows different time shifts between observations and synthetics to accommodate inaccurate velocity models and earthquake locations. The generalized CAP (gCAP) method relieves the double couple restriction for full moment tensor inversions. Here, we search for six independent parameters, including moment magnitude (M_w), isotropic (ISO), and compensated linear vector dipole factor (CLVD) components (ζ and χ), strike, dip, and rake (Zhu and Ben-Zion, 2013). The proportion of isotropic (Λ^{ISO}), double couple (Λ^{DC}), and compensated linear vector dipole (Λ^{CLVD}) components are represented by

$$\Lambda^{ISO} = \zeta^2 \tag{1}$$

$$\Lambda^{DC} = (1 - \zeta^2) * (1 - \chi^2) \tag{2}$$

$$\Lambda^{CLVD} = (1 - \zeta^2) * \chi^2. \tag{3}$$

We use the bootstrapping resampling approach (Zhan et al., 2012; Jia et al., 2017) to estimate the source parameter uncertainties, which is used as a priori constraint for the following Bayesian MCMC inversions. Calculations of Green's functions are based on the propagator matrix method with plane wave approximation (Kikuchi and Kanamori, 1991) for the teleseismic body waves, and the frequency-wavenumber integration method (Zhu and Rivera, 2002) for regional surface waves.

We calculate amplitude ratios of regional Pn/P, teleseismic P, regional Rayleigh and Love waves from two events to cancel out the path and site effects. The far-field seismic waves of an event pair can be represented by

$$u_1(\boldsymbol{x}, t) = M_{ij}^1 * G_{ij}(\boldsymbol{x}, t) * S_1(t) * r(\boldsymbol{x}), \tag{4}$$

$$u_2(\boldsymbol{x}, t) = M_{ij}^2 * G_{ij}(\boldsymbol{x}, t) * S_2(t) * r(\boldsymbol{x}), \tag{5}$$

where M_{ij} is the full moment tensor, G_{ij} is the Green's function, S is the source time function, and r is the station amplification term. If we use body waves at periods longer than the source durations, we can reasonably approximate the studied events as point sources, and remove common path/site effects by taking amplitude ratios. For regional and teleseismic P waves recorded at the same station, the amplitude ratios of point sources are equivalent to their radiation pattern ratios, which is a function of take-off angle and azimuth, based on ray theory being implemented in a layered elastic media (Dahm, 1996).

On the other hand, the surface wave amplitude ratios are complex functions of the moment tensors and depths. When the source depth h is much less than the wavelength as in the case of nuclear tests, certain surface wave eigenfunction terms are reduced to 0,

$$l_2(h) = \mu \frac{dl_1}{dz}\bigg|_h = 0, \tag{6}$$

$$r_3(h) = \mu \left(\frac{dl_1}{dz} - kr_2\right)\bigg|_h = 0, \tag{7}$$

$$r_4(h) = 0, \tag{8}$$

where *r* and *l* are components of the Rayleigh and Love wave motion-stress vectors, and the excitation of Rayleigh and Love waves is given by

$$\boldsymbol{u}^{Rayl}(\boldsymbol{x}, \omega) = \boldsymbol{G^R}[U_1 + U_2 cos2\phi + U_3 sin2\phi], \tag{9}$$

$$\boldsymbol{u}^{Love}(\boldsymbol{x}, \omega) = \boldsymbol{G^L}[U_2 sin2\phi - U_3 cos2\phi], \tag{10}$$

where $\boldsymbol{G^R}$ and $\boldsymbol{G^L}$ are given by

$$\boldsymbol{G^R}(\boldsymbol{x}; h, \omega) = \sum_n \frac{k_n r_1(h)}{8cUI_1} \sqrt{\frac{2}{\pi k_n r}} \exp\left[i\left(k_n r + \frac{\pi}{4}\right)\right][r_1(z)\hat{\boldsymbol{r}} + ir_2(z)\hat{\boldsymbol{z}}], \tag{11}$$

$$\boldsymbol{G^L}(\boldsymbol{x}; h, \omega) = \sum_n \frac{ik_n l_1(h)}{8cUI_1} \sqrt{\frac{2}{\pi k_n r}} \exp\left[i\left(k_n r + \frac{\pi}{4}\right)\right] l_1(z)\hat{\boldsymbol{\phi}}, \tag{12}$$

in which μ is the shear modulus, *r* is the distance, *z* is the depth, $\hat{\boldsymbol{r}}, \hat{\boldsymbol{z}}, \boldsymbol{\phi}$ are the unit vectors for 3 cylindrical coordinates, and k_n is the nth root of the wave number (Aki and Richards, 2002). The radiation pattern coefficients U_1, U_2, U_3 are given by

$$U_1 = \frac{1}{2}\left(\boldsymbol{M}_{xx} + \boldsymbol{M}_{yy}\right) - \left(1 - \frac{2\beta^2}{\alpha^2}\right)\boldsymbol{M}_{zz}, \tag{13}$$

$$U_2 = \frac{1}{2}\left(\boldsymbol{M}_{xx} - \boldsymbol{M}_{yy}\right), \tag{14}$$

$$U_3 = \boldsymbol{M}_{xy}. \tag{15}$$

When two events E1 and E2 are both shallow and closely located, they share similar $\boldsymbol{G^R}$ and $\boldsymbol{G^L}$. Hence these terms can be canceled out by calculating the amplitude ratios. The analytical form of Rayleigh and Love wave amplitude ratios would be functions of moment tensors $\boldsymbol{M}_{E1}, \boldsymbol{M}_{E2}$, Vp/Vs ratios β/α, and station azimuth ϕ,

$$\boldsymbol{A^R}|_{\frac{E1}{E2}} = \frac{(U_1 + U_2 cos2\phi + U_3 sin2\phi)|_{E1}}{(U_1 + U_2 cos2\phi + U_3 sin2\phi)|_{E2}}, \tag{16}$$

$$\boldsymbol{A^L}|_{\frac{E1}{E2}} = \frac{(U_2 sin2\phi - U_3 cos2\phi)|_{E1}}{(U_2 sin2\phi - U_3 cos2\phi)|_{E2}}. \tag{17}$$

This means we can also take the path effects away by calculating amplitude ratios of surface waves.

For vertical component P waves, we cut 3-second time windows right after the hand-picked P arrivals, and cross-correlate to measure the amplitude ratios. We calculate two different terms,

$$A^1 = \frac{\int \boldsymbol{u}(\tau - t)\boldsymbol{v}(\tau)d\tau}{\int \boldsymbol{v}^2(\tau)d\tau} \tag{18}$$

$$A^2 = \frac{\int \boldsymbol{u}^2(\tau)d\tau}{\int \boldsymbol{u}(\tau - t)\boldsymbol{v}(\tau)d\tau} \tag{19}$$

where ***u(t)*** and ***v(t)*** are the wave segments of two events after cross-correlation. The terms A^1 and A^2 are similar to the waveform-coherency-based amplitude ratio defined in an adjoint tomographic inversion (Tao et al., 2017) and reflect the waveform similarity of the cross correlations. The term A^1 generally represents $\boldsymbol{u}/\boldsymbol{v}$, while A^2 represents $1/(\boldsymbol{v}/\boldsymbol{u})$ after an appropriate time shift. If $\boldsymbol{u}$ and $\boldsymbol{v}$ have the same waveform shape (correlation coefficient =1), A^1 and A^2 would be identical and equal to the amplitude amplification factor (AAF) (Tan and Helmberger, 2007). Otherwise, A^1 will be smaller and A^2 will be larger than the AAF. Therefore, it's logical to take A^1 and A^2 as lower and upper bound to assess the waveform-coherency-dependent amplitude ratio variations. We take the natural logarithm of the absolute values of A^1 and A^2, and choose their mean as data and the half deviation as data uncertainty. Besides, we extract the polarity difference from cross correlations as part of the differential data. We use 1 and -1 to represent the same and opposite polarities of the event pair at each station, and use their difference (2) as 3 times standard deviation error (99% confidentce limit).

Measurement of the Rayleigh and Love wave amplitude ratios and errors is similar to that of body waves. We choose the time window to be 60s centered at the peak envelope amplitudes for cross correlations. Specifically for Rayleigh waves, we take the largest deviation between $ln(|A^1|)$ and $ln(|A^2|)$ for both radial and vertical components for the amplitude ratio errors.

We use the Metropolis-Hasting Markov Chain Monte-Carlo (MCMC) method to estimate the posterior probability density functions (PDFs) by fitting the differential measurements (i.e., amplitude ratios and polarity differences) of body and surface waves. The MCMC inversion follows a Bayesian framework, which produces model distribution from data fittings and the a priori information (Tarantola, 2005),

$$p(\boldsymbol{m}|\boldsymbol{d}) \propto p(\boldsymbol{m}) * l(\boldsymbol{d}|\boldsymbol{m}), \tag{18}$$

where the $p(\boldsymbol{m})$ and $p(\boldsymbol{m}|\boldsymbol{d})$ are prior and posterior PDFs, respectively. d indicates the amplitude ratio data, including logarithmic amplitude ratios and polarity differences. m represents the 6 independent source parameters (M_W, ζ, χ, strike, dip, and rake) for each event, in total 12 parameters for an event pair. Conversion from the data to model is performed through the likelihood function, which describes how the predictions from a model fit the data within data error. Our likelihood function is defined as the following equation,

$$l(\boldsymbol{d}|\boldsymbol{m}) = \frac{1}{\sqrt{(2\pi)^N|\boldsymbol{C_d}|}} exp\left(-\frac{1}{2}(G(\boldsymbol{m}) - \boldsymbol{d})^T \boldsymbol{C_d^{-1}}(G(\boldsymbol{m}) - \boldsymbol{d})\right), \tag{19}$$

where G is the forward simulation operator, and $\boldsymbol{C_d}$ is the data covariance matrix. We assume that $\boldsymbol{C_d}$ is diagonal:

$$\boldsymbol{C_d}_{ii} = \sigma_i^2, \qquad i \in [1, N] \tag{20}$$

$$\boldsymbol{C_d}_{(i+N)(i+N)} = \varepsilon_i^2, \qquad i \in [1, N] \tag{21}$$

where σ_i and ε_i are the standard deviation errors of logarithmic amplitude ratio and polarity difference at the i^{th} station, respectively. To avoid the inversion being dominated by data points of minimal errors, we set σ_i to be no less than 0.05, corresponding to ~5% amplitude ratio difference. Here we assumed no correlation between data errors for different stations, different phases, and various measurement types (amplitude ratios vs. polarities), which may not best reflect the true covariance. But because the P and surface waves are well separated, and Rayleigh and Love waves have orthogonal direction of vibration, their interferences are unlikely substantial. It's also reasonable to ignore the covariance between amplitude ratios and polarities, as they would be correlated only when the observation is close to the nodal, which is the minority of all stations.

We use Markov Chain Monte Carlo (MCMC) method to sample the posterior PDF $p(m|d)$. For low-dimension problems, brutal force algorithms are sufficient to sample the posterior PDF. When the dimensionality increases (e.g. >10), the volume of the model space increases exponentially, and the available trials become too sparse to grid-search the models. Instead, MCMC allows us to sample higher dimension distributions of known form but difficult to grid-search. Guided by the form of the posterior PDF, a Markov Chain randomly walks through the model space and results in an ensemble of models which density follows the target distribution. The models move to higher posterior probabilities with Gaussian random perturbations, and can still accept less likely models and thus jump out of the local minimums (Hastings, 1970).

We generate 200 Markov Chains, and eventually keep 1/4 chains with highest posterior probability to avoid being trapped in low posterior minima. For each chain, we randomly generate 200 samples, and select the one of highest posterior probability as the initial draw. We apply the Gaussian proposal distributions to perturb the model at each step towards a new model. The Gaussian proposal distribution of each parameter has a standard deviation of 1/10 standard deviation of its prior distribution. We follow the Metropolis Hasting algorithm (Hastings, 1970) to drive the random walk, but different from conventional Metropolis-Hasting algorithm which perturb all parameters simultaneously, we propose new models by sampling one parameter while keeping the other parameters at their current values (Jia et al., 2020a). The parameter being perturbed is randomly selected. This approach ensures a high acceptance rate and improves the efficiency of convergence. Our Markov Chains usually converge in hundreds to thousands of iterations, but we choose a conservative number of burn-in samples to be 20000. After the burn-in stage, we keep the next 20000 samples in each chain, and combine 50 chains to form the final ensemble for the posterior PDFs.

5.4 Synthetic Test

We first benchmarked diffMT with synthetics, using the configuration of two collocated nuclear tests at the North Korea test site. Nuclear events have shallow burial depths and short duration, thus fitting our assumptions well. We put the pair at a depth of 0.6 km, and with the E1 moment tensor as (M_w 4.53, $\boldsymbol{\Lambda}^{\boldsymbol{ISO}}$=86%, strike/dip/rake=70°/40°/70°) and the E2 moment tensor as (M_w 4.44, $\boldsymbol{\Lambda}^{\boldsymbol{ISO}}$=73%, strike/dip/rake=160°/30°/90°). Using these source parameters, we calculated synthetic seismograms for 8 regional (within epicentral distance of 15°) and 33 teleseismic (epicentral distance between 30° and 90°) stations (Fig. 5.2a). The velocity model used is based on a combination of a 3-layer 1D elastic model (Ford et al., 2009) and the iasp91 model (Kennett et al., 1995). We collected real seismic noise for the used stations, and added them to the synthetic waveforms (Fig. 5.2b) for a similar level of signal-to-noise ratio (SNR) as natural nuclear test events. After adding the noise, the synthetic surface waves still have high SNRs, while the body waves are generally hard to observe in broadband. This is similar to the real data for most North Korea nuclear tests.

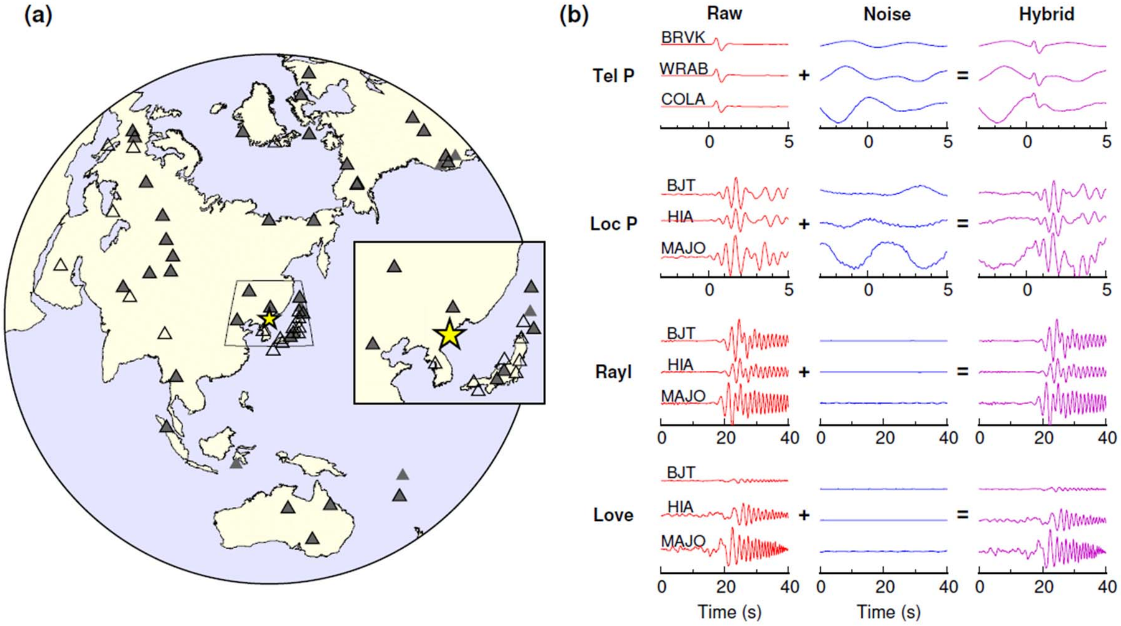

Figure 5.2. Generation of synthetic waveforms in our test. (A) Configuration of collocated sources (yellow star) and the seismic stations (gray triangles). Black-outlined triangles are the stations used in the following real-data inversions. The inset box shows the regional stations. (B) Adding real noise (blue lines) to the raw seismograms (red lines) for the hybrid synthetic data (purple lines).

We first applied the gCAP inversion on the two events. We filtered the data and synthetics between 0.03-0.1 Hz for regional surface waves and 0.5-1.0 Hz for teleseismic body waves.

Modeling the real site amplifications of high frequency P waves is difficult, so we normalized the P waves data to the synthetic wave amplitudes and only fit the waveform shapes. We also fixed the source depths to 0.6 km, approximated from Voytan et al. (2019), due to the limited data resolution. The moment tensor results have ~60% isotropic components for both E1 and E2 (Fig. 5.3), which is smaller than the input model. Moreover, the double couple focal mechanisms deviate ~30 degrees from the input values. We estimated the moment tensor standard deviation errors using 200 bootstrapping resamples, and observed substantial uncertainties for both E1 and E2 (Fig. S5.1). Given the minor data misfits (Fig. 5.3), the nontrivial moment tensor errors reflect poor data constraints due to limited frequency band and sparse network.

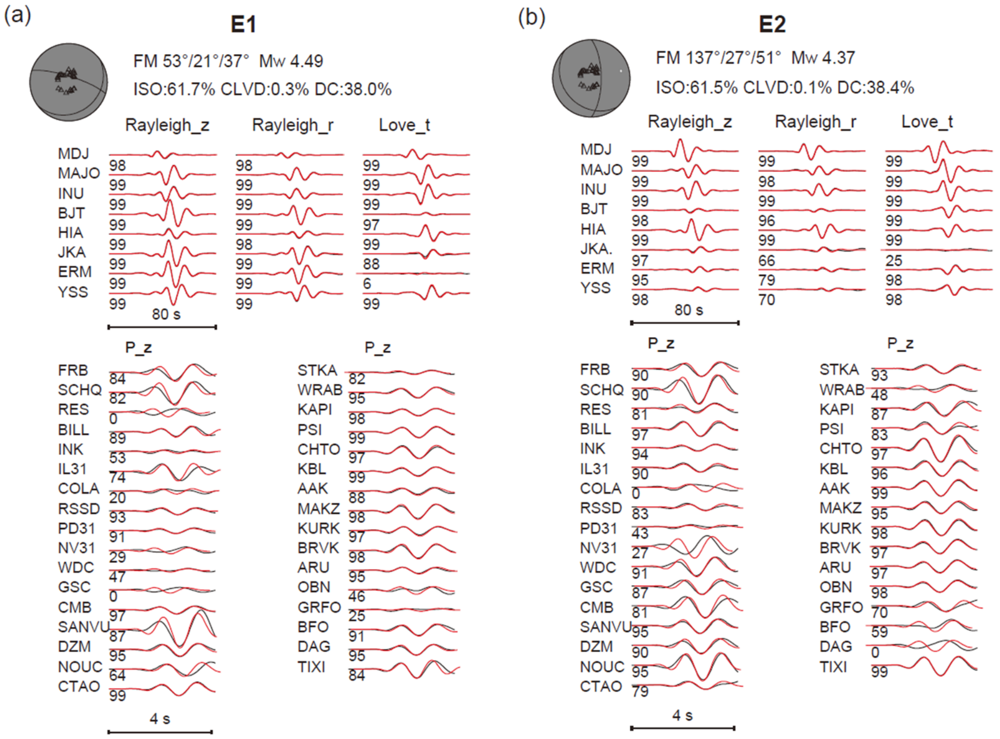

Figure 5.3. gCAP inversion results for the two synthetic events. The black and red lines indicate data and synthetic waveforms, respectively. The numbers leading the waveforms are the cross-correlation coefficients between data and synthetics.

After obtaining the gCAP solutions and uncertainties, we converted them to Gaussian a priori information for the diffMT inversion. We measured the amplitude ratios of regional and teleseismic P waves, and regional Rayleigh and Love waves. We filtered the surface waves between 0.03-0.1 Hz, consistent with the gCAP inversion. For the P waves, we applied 0.5-2.0 Hz filter band for higher signal-to-noise ratios. Most waveforms of the two events show high similarity, with polarity flips for some surface wave components (Fig. 5.4a). The amplitude ratios show clear azimuthal variations (Fig. 5.4b), which are presumably caused by the radiation pattern difference of the two events.

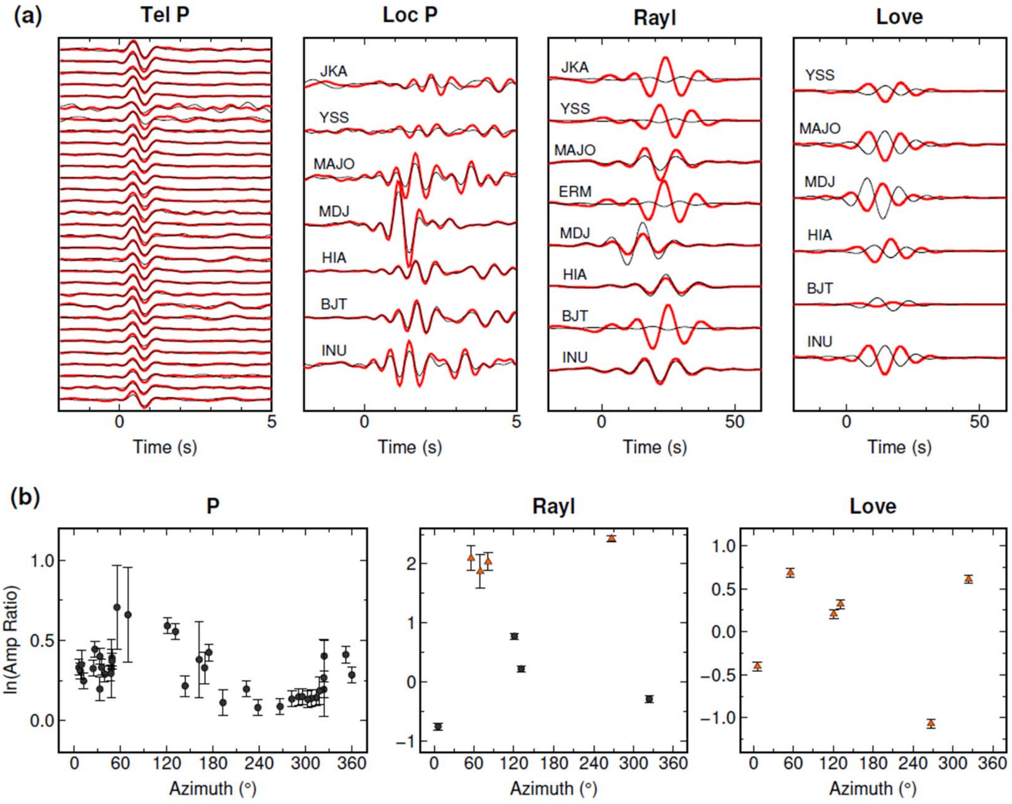

Figure 5.4. Measurement of amplitude ratios between two synthetic events. (A) Cross-correlated waveforms for teleseismic P (Tel P), regional P (Loc P), Rayleigh and Love

waves, respectively. (B) Amplitude ratios for P, Rayleigh and Love waves as a function of the station azimuth. The Tel P and Loc P observations are plotted together. Black circles and orange triangles represent consistent and flipping polarities, respectively. The standard deviation errors are shown with the error bars.

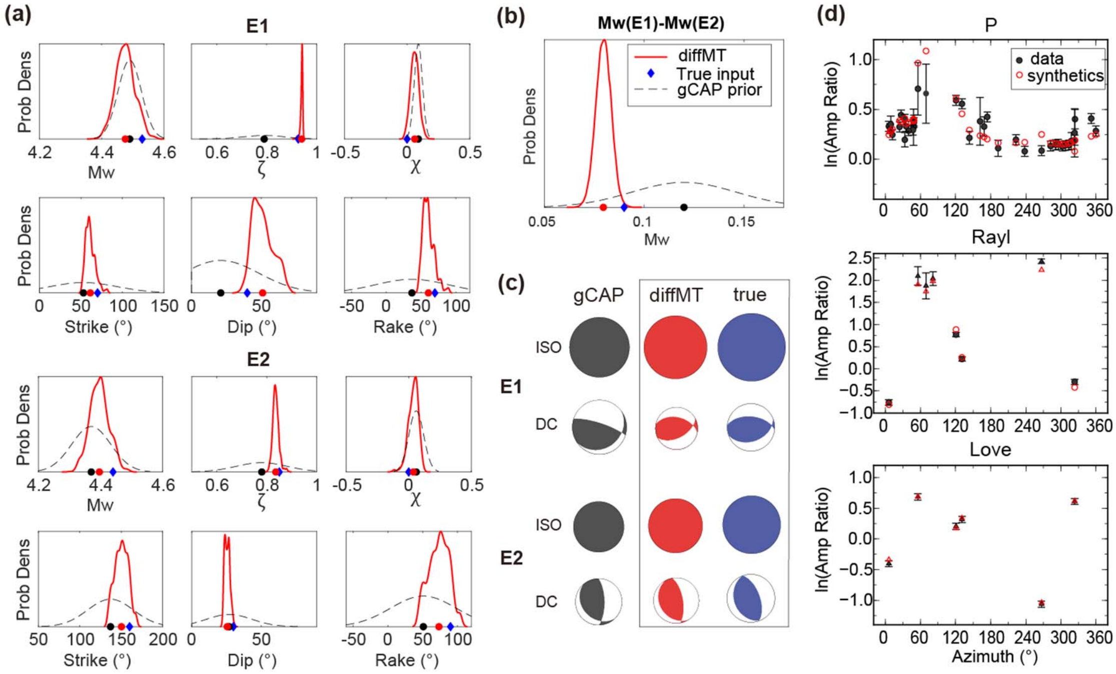

Figure 5.5. DiffMT inversion results for the two synthetic events. (a) The gCAP prior (dashed black lines) and the diffMT posterior (red lines) PDFs of the moment tensor solutions of the two events. The prior (gCAP) is from Gaussian fitting of bootstrapping uncertainties. Black and red dots indicate the gCAP optimal solution and mean of the diffMT posterior distribution, respectively. Blue diamond represents the true input value. See legend in (b). (b) The prior (dashed black lines) and posterior (red lines) PDFs of the moment magnitude difference between E1 and E2. Symbols are similar to that in (a). (c) Comparison of the isotropic (DC) and double couple (DC) focal mechanisms for the gCAP (black) and diffMT (red) solutions. Blue beachballs show the true focal mechanisms. The sizes of beachballs are proportional to the corresponding magnitudes. (d) Amplitude ratio

fittings for the diffMT solution. Black squares and red symbols show the amplitude ratio data and predictions from the moment tensor models, respectively. Circles and triangles represent consistent and flipping polarities, respectively.

With the amplitude ratio data derived from absolute amplitudes, we conducted diffMT inversion using MCMC sampling. The inversion results and data fittings are shown in Fig. 5.5. The posterior probability density functions (PDFs) are significantly narrower than the prior PDFs, showing reduced moment tensor uncertainties (Fig. 5.5a). The optimal source parameters from diffMT inversion are also closer to the true input values, and the moment magnitude difference is 0.08, closer to the true difference (0.09) than the prior difference (0.12) (Fig. 5.5b). The 3D rotation angle between diffMT (61°/51°/61°) and true solution of E1 is 13°, significantly less than the 27° rotation between the gCAP and true solution (Fig. 5.5c). Similar improvement is observed for E2, where the 3D rotation angle between diffMT (150°/26°/73°) and the true solution is 10°, less than the rotation angle between the gCAP and true solution (22°) (Fig. 5.5c). This is primarily because the azimuthal variations of the amplitude ratios, which is well fit by the diffMT synthetics (Fig. 5.5d), provide additional constraints that improve the moment tensor accuracy.

5.5 Application on North Korea Nuclear Tests

We applied our diffMT algorithm to the three North Korea nuclear tests on Feb 2013, Jan 2016 and Sep 2016, respectively, by conducting inversions on three event pairs using seismograms from regional (within epicentral distance of 15°) and teleseismic (epicentral distance between 30° and 90°) stations (Fig. 5.3). The number of observations for all 3 events are not identical due to the varying station availability across the time period, but since the overlapping stations are the majority, the azimuthal and distance coverage differences are trivial. Similar to the synthetic test, we first run gCAP inversion using the regional surface waves in velocity filtered between 0.03-0.1 Hz, and the teleseismic P waves in velocity filtered between 0.5-1.0 Hz. The narrow P wave filter band is a compromise between signal observability and modeling capability. We fixed the depths to be 0.6 km, similar to the estimations from Voytan et al. (2019), to avoid depth ambiguities. The inversion results show that both the regional and teleseismic waveforms are fit well (Fig. 5.6). We observe 50~70% isotropic component for these events, which is generally consistent with other moment tensor inversion studies (Ford et al., 2009; Cesca et al., 2017; Chiang et al., 2018). The distributions of the moment tensors estimated from the bootstrapping resampling suggest that all the source parameter components have large uncertainties (Fig. S5.2). Particularly, the isotropic component fraction and double couple orientations are not well constrained. The wide range of model uncertainties makes it difficult to discriminate the explosions or to analyze the tectonic release mechanisms.

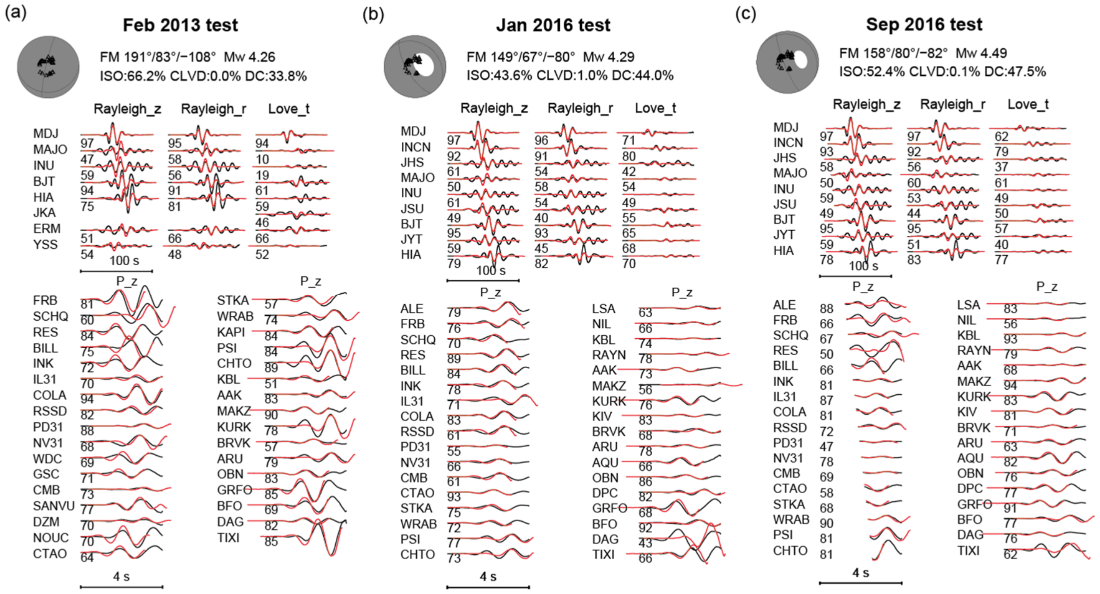

Figure 5.6. gCAP inversion results for the 3 studied North Korea nuclear explosions on (A) Feb 2013, (B) Jan 2016, and (C) Sep 2016, respectively. The symbols are similar to that in Fig. 5.3.

We measure amplitude ratios of the 3 event pairs among these three tests, using regional and teleseismic P waves between 0.5-2.0 Hz, and the Rayleigh and Love waves between 0.03-0.1 Hz. Waveforms of different events show high similarity, indicating robust measurements of the amplitude ratios (Fig. S5.3). The amplitude ratios have moderate azimuthal variation patterns (Fig. 5.7), which suggests different double-couple mechanisms under the dominant isotropic components.

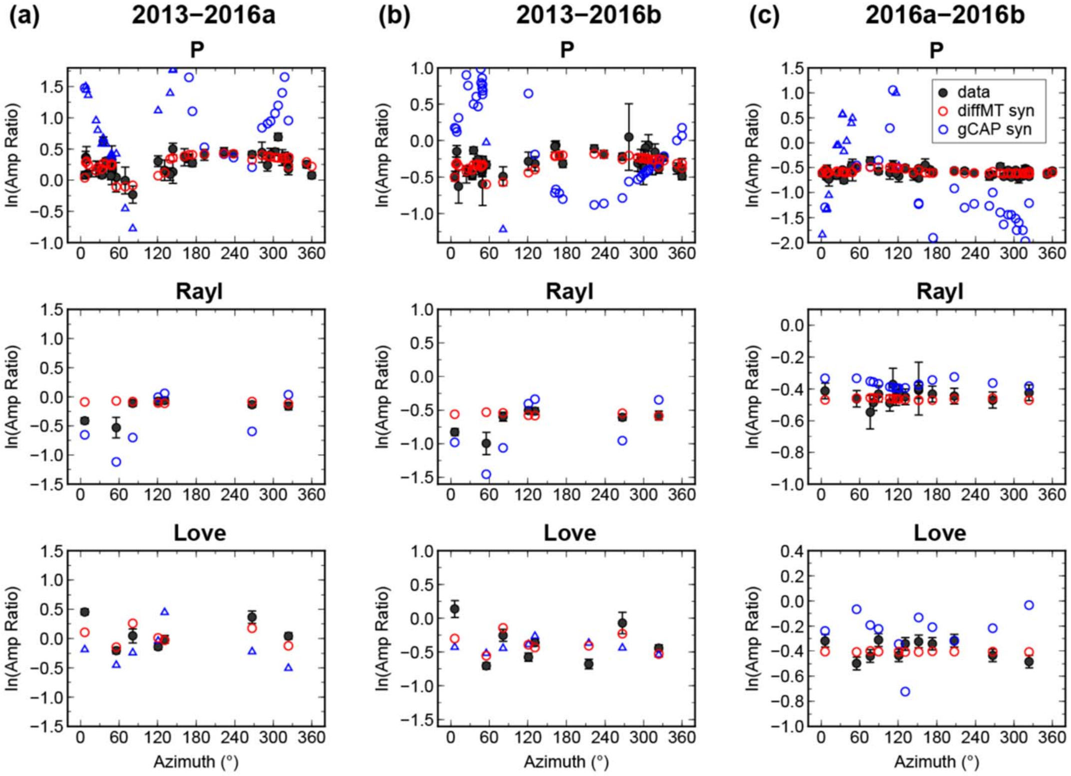

Figure 5.7. Amplitude ratios among the Feb 2013, Jan 2016 (2016a), and Sep 2016 (2016b) events. Three pairs are shown in (a)-(c), respectively. Circles and triangles represent consistent and flipping polarities, respectively. Black symbols with error bars show the amplitude ratio measurements. Blue and red symbols indicate the amplitude ratio predictions from the gCAP and diffMT solutions, respectively.

We further applied three separate diffMT inversions on these pairs. We did not choose doing one inversion for all events, due to the rapidly growing number of unknowns (N*6) for N events, which would pose a significant challenge to the nonlinear searching efficiency. Conducting multiple paired inversions would be the most applicable way of diffMT application on the real-world seismic event clusters. To avoid the inversion being trapped to pure isotropic sources ($\zeta=1$) which generates very low Love wave amplitudes and numerically unstable ratios, we tapered the prior of ζ (equation 1) from its maximum bootstrapping value (0.98/0.96/0.96 for the Feb 2013, Jan 2016, and Sep 2016 events) to 1. The existence of Love waves also does not support pure isotropic source mechanisms. The diffMT posterior probability density functions (PDFs) are shown in Fig. 5.8. The posterior PDFs for each event are generally consistent from different pairs (Fig. 5.8a). Still, we can observe mismatches for some components, such as the rake angle for the Feb 2013 event, and CLVD parameter for the two 2016 tests (Fig. 5.8a). This is because models that fit amplitude ratio data for different pairs can have different biases from varying data errors. As long as they have overlapping model space, they do not contradict each other since the overlapped models could fit the data for both pairs. On the other hand, the CLVD factor χ may not be well constrained, because the CLVD component is a minor term accompanied with the DC mechanism (Zhu and Ben Zion, 2013), while the DC part is already second order compared to the dominant isotropic mechanism.

We multiplied the diffMT posterior PDFs of each event from different pairs for the overall posterior distributions (Fig. 5.8b). The posterior PDFs are significantly narrower than the prior PDFs, suggesting tighter constraints from the amplitude ratio measurements. In particular, the proportion of the isotropic components (ζ^2) are much better resolved and significantly more dominant (~90%) than the prior distributions (Fig. 5.9), which strongly suggest explosive source mechanisms. Meanwhile, diffMT inversions reduce the uncertainties of the moment magnitude differences (average standard deviation error of 0.04 for prior and 0.01 for posterior) (Fig. 5.8c), and make it much easier to compare the size of these nuclear tests. Therefore, the diffMT results could improve explosion discrimination and size comparison for the studied North Korea nuclear tests.

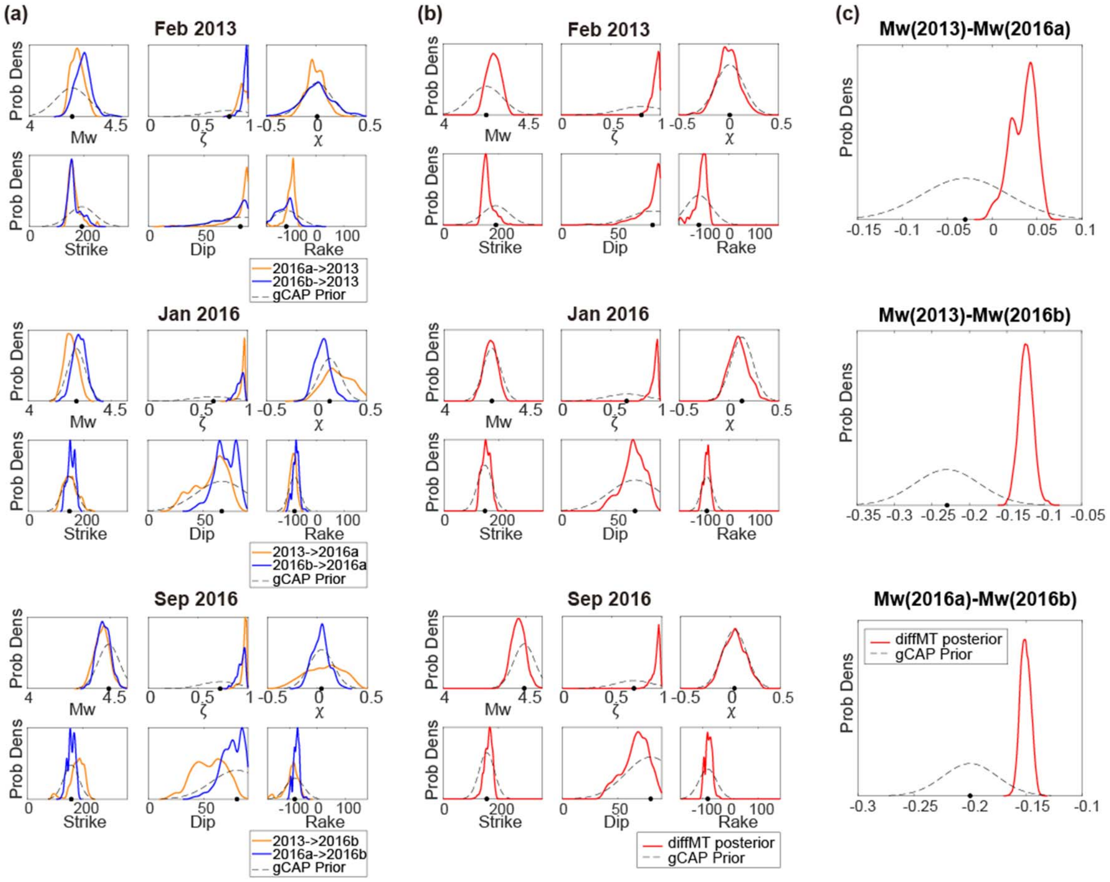

Figure 5.8. DiffMT inversion results for the event pair of the Feb 2013 and Jan 2016 tests. (a) The gCAP prior (dashed black lines) and the diffMT posterior (solid lines) PDFs of the moment tensor solutions of the two events. Solid lines in different colors indicate the posterior PDFs derived with different pairing events. Black dots show the optimal gCAP solution. (b) Combined posterior PDFs (solid red lines) plotted with the gCAP prior PDFs (dashed black lines). (c) The prior (dashed black lines) and posterior (red lines) PDFs of the moment magnitude differences.

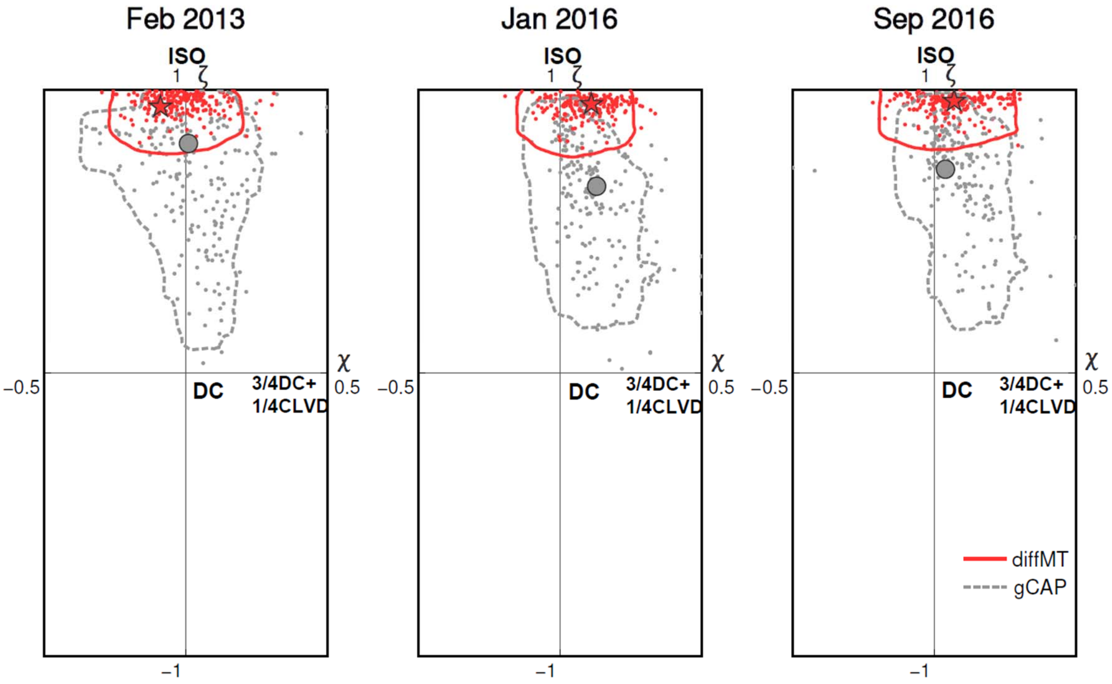

Figure 5.9. Prior (gCAP) and posterior (diffMT) distributions of ζ and χ for the three studied events. Red star and gray circle indicate diffMT and gCAP solution, respectively. The diffMT samples (red scattered dots) are contoured by the 90% confidence limit lines (red solid line), while the gray scattered dots and dashed lines are the gCAP samples and 90% confidence limits.

Moreover, diffMT inversion significantly reduces the uncertainty of the DC component (strike, dip, rake in Fig. 5.8b). To illustrate the improvement, we compared the double couple focal mechanism ensembles for the gCAP prior and diffMT posterior distributions (Fig. 5.10). The gCAP prior ensemble shows highly scattered strike and dip angles. In contrast, the diffMT focal mechanisms converge well, with strike and dip variances generally less than 40 degrees. The diffMT solutions suggest a similar high angle dip-slip as the tectonic release for the three nuclear tests.

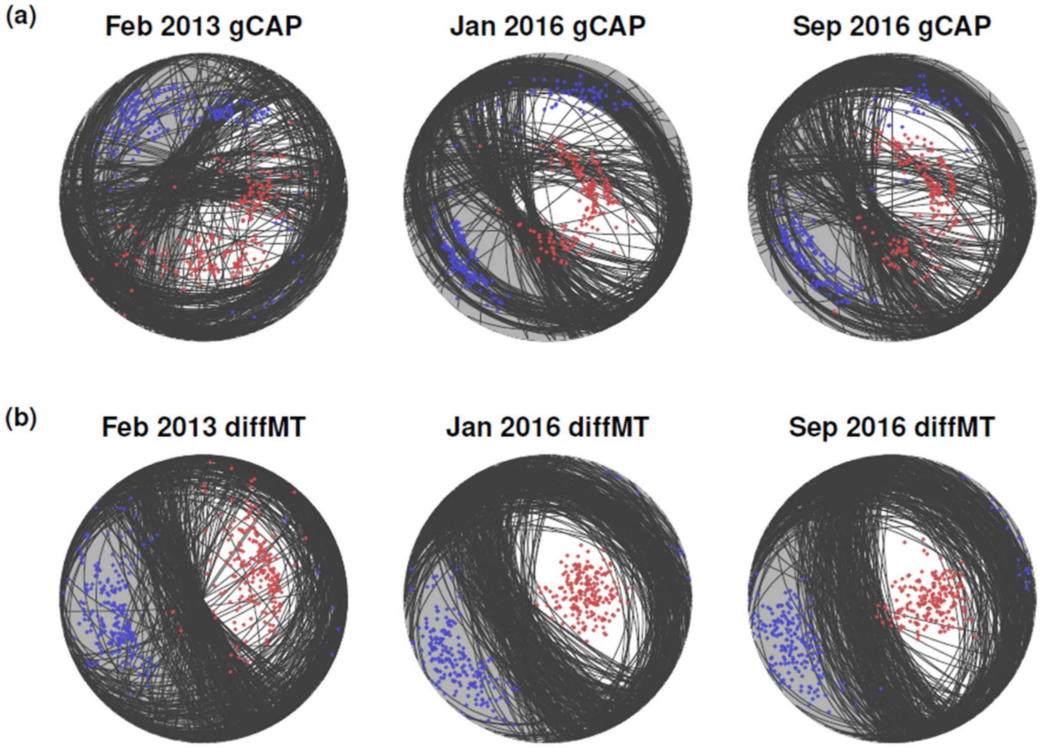

Figure 5.10. Scatter plot of the focal mechanisms from the (a) gCAP prior and (b) diffMT posterior ensembles. Red and blue dots are the P and T axes of the focal mechanisms, respectively.

5.6 Discussion

Our application of the diffMT inversion on the North Korea nuclear tests shows better-resolved moment tensors. Although the gCAP inversion uses absolute body and surface wave amplitudes, it does not capture the patterns of amplitude ratios which provide extra constraints on moment tensors. The gCAP and diffMT solutions fit the regional and teleseismic waveforms almost equally well (Fig. S5.4), suggesting that the absolute amplitude information can hardly distinguish the two moment tensor solutions. In contrast, our final diffMT solution, which is sampled near the mean of the posterior distributions, fits amplitude ratios significantly better than the gCAP solution (Fig. 5.7). This is because the absolute amplitude information contains the unknown path and site effects that cause misfits that translates to model uncertainties assuming a simple velocity model. On the other hand, diffMT does not require highly accurate velocity models, thus finding better MT solutions from the gCAP ensembles.

Relative moment tensor inversions have been developed and implemented in various studies (Dahm, 1996; Plourde and Bostock, 2019; Voytan et al., 2019; Xu et al., 2020). Compared with these methods, our diffMT inversion uses a two-step approach to combine the waveforms with the amplitude ratio information, and quantify moment tensor uncertainties in a Bayesian framework, which provides a natural uncertainty analysis. Introducing the Bayesian framework also eliminates the need of choosing reference events, and avoids the magnitude trade-offs with constraints from the priors. Moreover, diffMT includes surface waves, making it suitable for events with sparse local observations. However, our method still introduces certain assumptions which may bring additional model errors. We did not consider depth phases in the P wave amplitude ratio modeling. Although the influence of 1D depth phases appears insignificant (Fig. S5.5), the impact of depth phase variations due to the 3D surface topographic reflections are moderate and need further investigations(Rodgers et al., 2010; Avants, 2014). Besides, the calculations of body wave amplitude ratios rely on take-off angles calculated with a layered model, and the influence of the source side structural heterogeneities on the ray parameters is presumably low but not negligible. Overall, structural heterogeneities may still bias our inversion results, suggesting that full numerical wavefield simulations with more realistic earth models are needed in the future.

We summarized our final diffMT solutions in Table 5.1. The proportions of the isotropic components are all around 90% (Table 5.1), substantially more dominant than the gCAP estimates of around 50-70%, or some other solutions of 50%-60% for the North Korea nuclear tests (Ford et al., 2009; Vavryčuk and Kim, 2014; Cesca et al., 2017). Note that surface waves alone can not discriminate the isotropic and vertical-dipping CLVD sources, as their radiation patterns are similar around the edge of focal sphere. However, the P waves can cover the central portion of the beachball, and the strength of the azimuthal-varying P amplitude ratios constrains how much they deviate from uniform radiation (isotropic source). The moment magnitudes of these three events are 4.31, 4.28, and 4.43, respectively, suggesting similar sizes for the Feb 2013 and Jan 2016 tests, followed by the larger Sep 2016 test. Double couple components are mostly dip-slip normal faulting events, and the steep dip angles of tectonic release are suggested by various studies in this region (Ford et al., 2009; Barth, 2014; Cesca et al., 2017). The DC orientations are also consistent with Cesca et al. (2017). But similar to the bottlenecks of most moment tensor inversion, our diffMT algorithm only resolve point source moment tensors for events with clear body and surface waves. Therefore, we skipped the 2009 North Korea nuclear test in our study due to the low SNRs (Fig. S5.6). We also did not include the Sep 2017 test (M 6.3), because it likely involves sequential explosions, tectonic releases, and collapses (Xu et al., 2020), which introduces wave complexities (Fig. S5.6) beyond the point-source assumption. Further investigations of time-dependent source parameters are needed for large and complicated nuclear explosions.

The ISO/DC/CLVD decomposition used in this paper, while used extensively in nuclear monitoring (Ford et al., 2009; Vavryčuk and Kim, 2014; Cesca et al., 2017; Chiang et al., 2018), is not the only physical interpretation. Following Aki&Richard's classical model, full moment tensor could be viewed as oblique opening of the fault for one of the two non-perpendicular planes (Aki and Richards, 2002; Tape and Tape, 2013). Also, a moment tensor can be decomposed as a crack tensor plus a double couple (CDC), in which the tensile crack direction is perpendicular to the fault plane of shear motion (Tape and Tape, 2013; Alvizuri and Tape, 2018). These various kinematic expressions of seismic source can lead to different understandings of the physical processes of nuclear tests.

In our current parameterization of the diffMT inversion, we assume Gaussian priors for the source parameters, which may not best represent the moment tensor variety in the parameter space, and encounter wrap-around at the boundaries. In practice, we truncated the Gaussian functions at the boundaries to avoid jumps for strike/dip/rake. Although moderate changes of prior shape won't significantly influence the diffMT inversion, there are better ways to avoid the non-uniformity of the source parameter distributions. For example, Tape and Tape (2013, 2015) formulate 5 uniformed parameters that can be mapped to an eigenvalue vector and a triple, to represent unique moment tensors. This way leads to even distributions of moment tensors in the parameter space, which could benefit the prior selection for the diffMT in the future.

	M_w	**ζ**	**χ**	**Strike**	**Dip**	**Rake**	Λ^{ISO}(%)	Λ^{DC}(%)	Λ^{CLVD}(%)
Feb 2013 (prior)	$4.26^{+0.20}_{-0.20}$	$0.81^{+0.19}_{-0.44}$	$0.01^{+0.14}_{-0.14}$	191^{+96}_{-96}	83^{+7}_{-40}	-108^{+94}_{-72}	66^{+34}_{-50}	34^{+50}_{-34}	0^{+2}_{-0}
Feb 2013 (diffMT)	$\mathbf{4.31^{+0.06}_{-0.07}}$	$\mathbf{0.94^{+0.06}_{-0.07}}$	$\mathbf{-0.09^{+0.27}_{-0.1}}$	$\mathbf{154^{+51}_{-17}}$	$\mathbf{79^{+10}_{-22}}$	$\mathbf{-92^{+21}_{-58}}$	$\mathbf{88^{+12}_{-12}}$	$\mathbf{12^{+11}_{-11}}$	$\mathbf{0^{+1}_{-0}}$
Jan 2016 (prior)	$4.29^{+0.10}_{-0.10}$	$0.66^{+0.34}_{-0.40}$	$0.13^{+0.22}_{-0.22}$	149^{+53}_{-53}	67^{+23}_{-46}	-80^{+41}_{-41}	44^{+56}_{-37}	56^{+27}_{-43}	0^{+8}_{-0}
Jan 2016 (diffMT)	$\mathbf{4.28^{+0.07}_{-0.07}}$	$\mathbf{0.95^{+0.03}_{-0.09}}$	$\mathbf{0.11^{+0.15}_{-0.17}}$	$\mathbf{161^{+18}_{-33}}$	$\mathbf{61^{+20}_{-16}}$	$\mathbf{-90^{+28}_{-10}}$	$\mathbf{91^{+5}_{-17}}$	$\mathbf{9^{+17}_{-6}}$	$\mathbf{0^{+1}_{-0}}$
Sep 2016 (prior)	$4.49^{+0.13}_{-0.13}$	$0.72^{+0.28}_{-0.37}$	$0.04^{+0.24}_{-0.24}$	158^{+56}_{-56}	80^{+10}_{-46}	-82^{+64}_{-64}	52^{+48}_{-40}	48^{+40}_{-42}	0^{+6}_{-0}
Sep 2016 (diffMT)	$\mathbf{4.43^{+0.09}_{-0.05}}$	$\mathbf{0.96^{+0.03}_{-0.09}}$	$\mathbf{0.07^{+0.16}_{-0.21}}$	$\mathbf{163^{+21}_{-25}}$	$\mathbf{66^{+18}_{-23}}$	$\mathbf{-89^{+30}_{-10}}$	$\mathbf{92^{+6}_{-16}}$	$\mathbf{8^{+16}_{-6}}$	$\mathbf{0^{+1}_{-0}}$

Table 5.1. Moment tensor solutions for the 3 studied North Korea nuclear tests.

5.7 Conclusions

We developed a differential moment tensor (DiffMT) inversion algorithm that resolves moment tensors of clustered seismic event pairs using relative measurements. It starts with a conventional moment tensor inversion for the a priori solutions, followed by inversion on amplitude ratio information for the refinements. Application of diffMT on three North Korea nuclear tests between 2013 and 2016 leads to reduced errors of isotropic components and double couple focal mechanisms. Their moment tensors have ~90% explosive components, which are more dominant compared with some conventional results of 50%~60%, providing opportunity for better explosion discrimination. The associated tectonic release components are small but nontrivial high angle dip-slip mechanisms. The seismic moment differences between events are also better resolved, which could improve energy estimation of nuclear tests. With tighter constraints on the double couple focal mechanisms, we expect the diffMT method to be applied to various types of seismic events.

5.8 Supplementary Materials

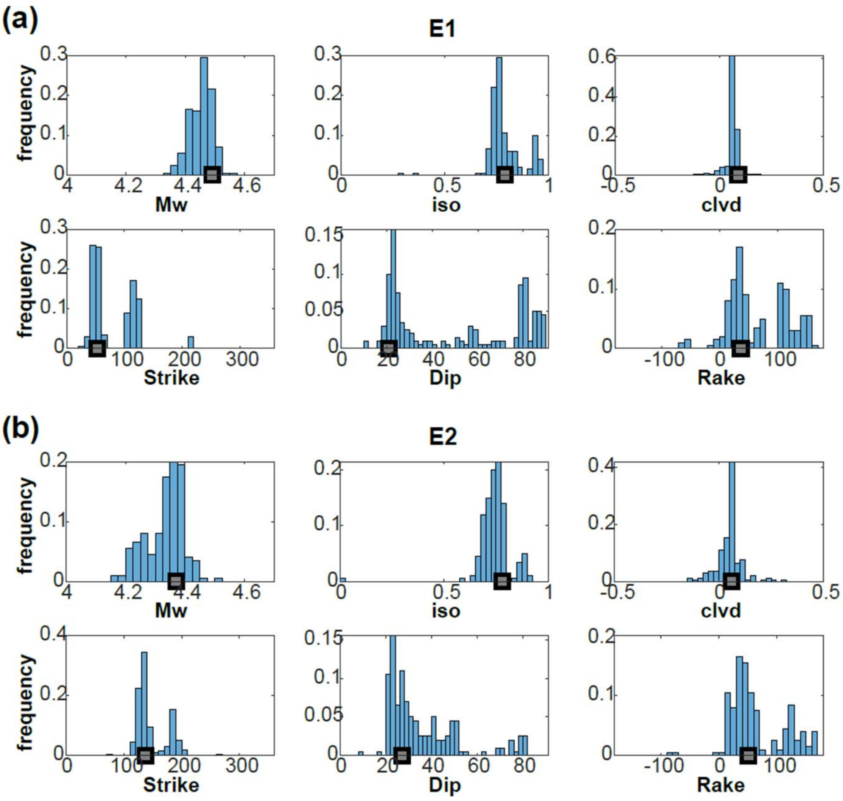

Figure S5.1. Distribution of gCAP source parameters from bootstrapping sampling in the synthetic test. Results for E1 and E2 are shown in panels (a) and (b), respectively.

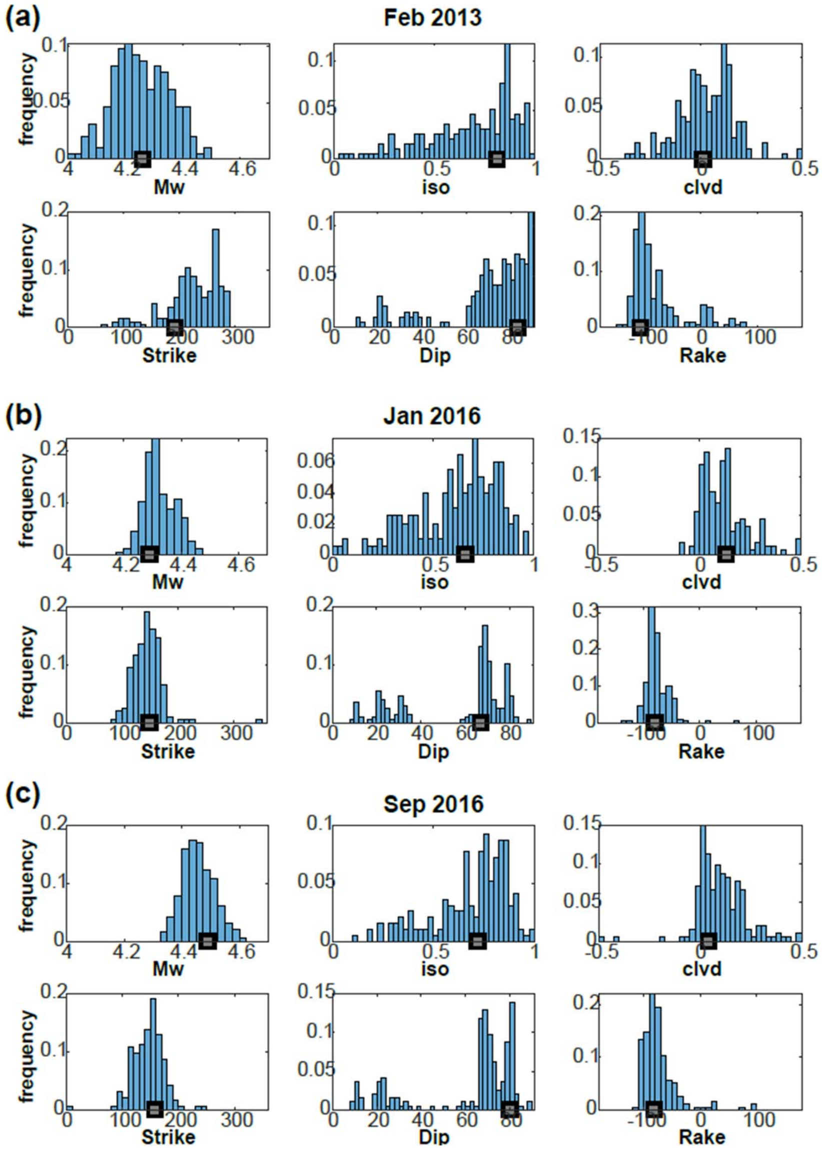

Figure S5.2. Same as Fig. S5.1, but for the 3 studied North Korea nuclear explosions.

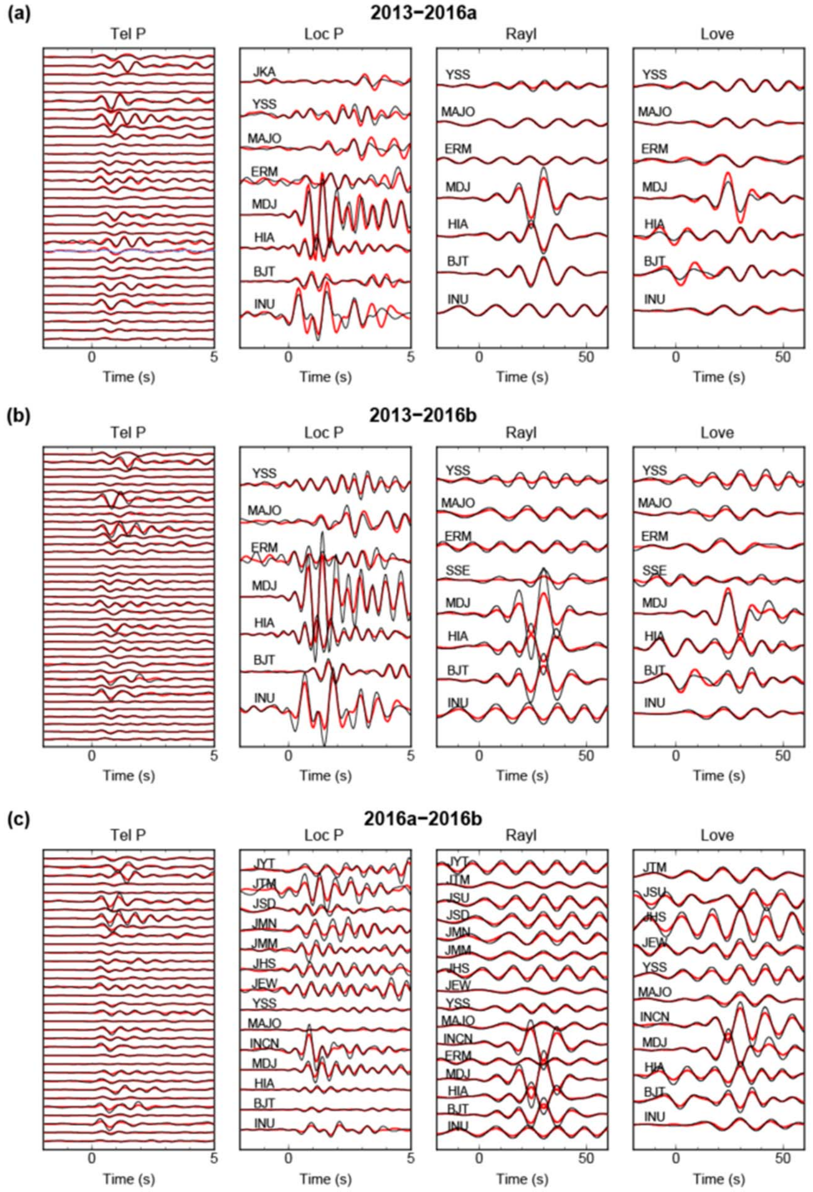

Figure S5.3. Measurement of amplitude ratios among 3 studied North Korea nuclear explosions. The symbols are similar to that in Fig. 5.5a.

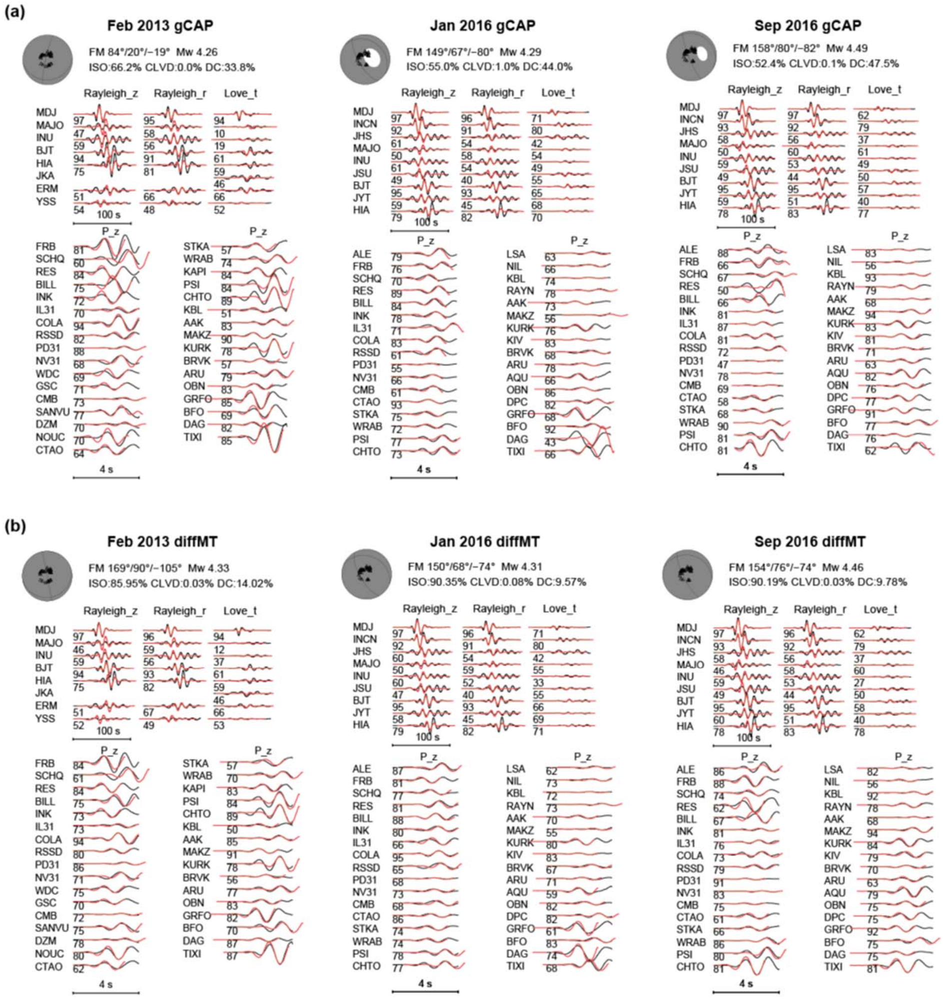

Figure S5.4. Comparison of waveform fittings for the (a) gCAP and (b) diffMT solutions. The fitting difference is hardly observable, suggesting that the moment tensor difference of these two solutions can’t be resolved by the gCAP waveform inversion.

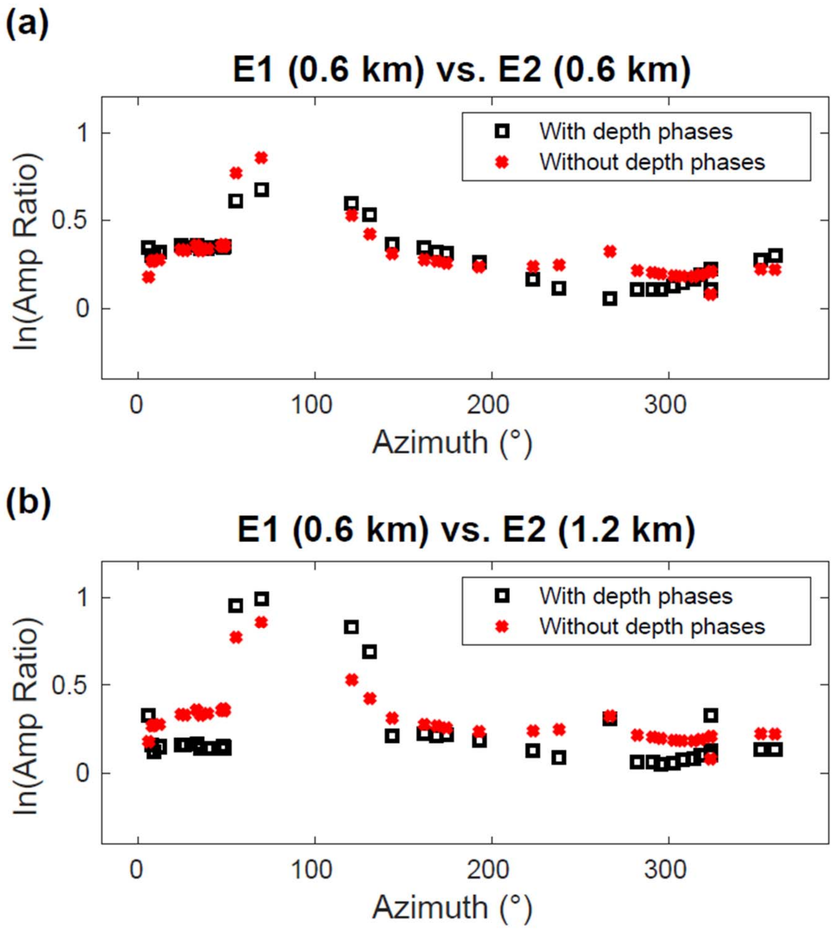

Figure S5.5. Influence of 1D depth phases (pP, sP) on the body wave amplitude ratios for the synthetic events E1 and E2. (a) Comparison of P wave amplitude ratios from waveform cross correlation (with depth phases) (black squares) and analytical calculation (without depth phases) (red crosses). The depths used to generate synthetic waveforms are both 0.6 km for E1 and E2. (b) Same as (a), but the depths used to generate synthetic waveforms are 0.6 and 1.2 km for E1 and E2, respectively.

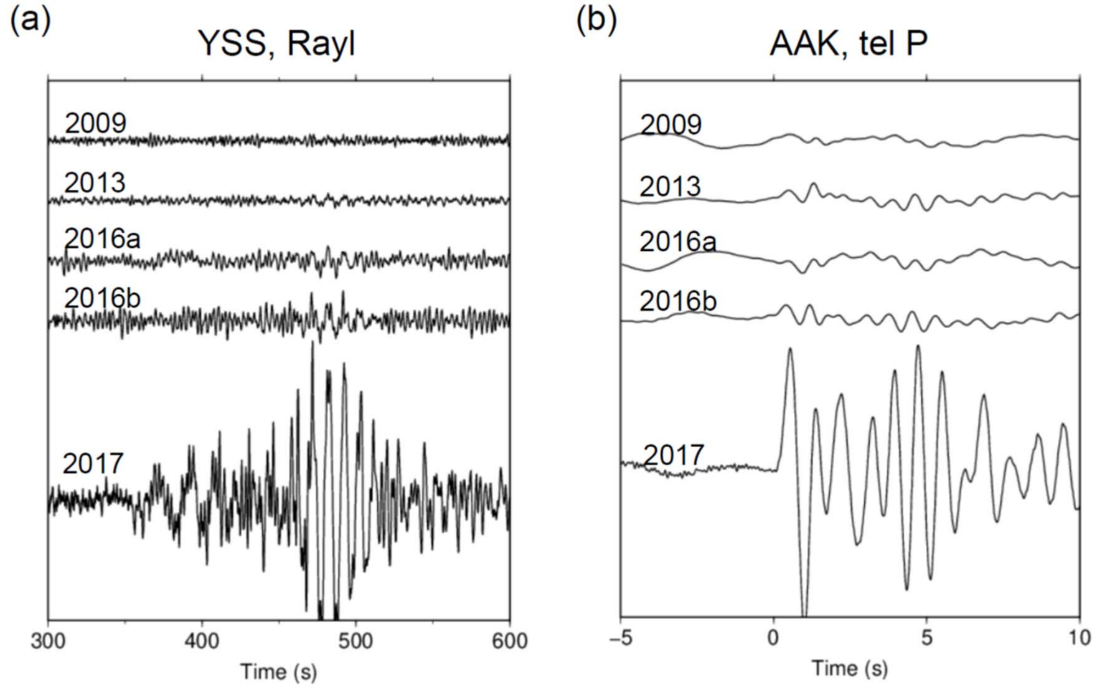

Figure S5.6. Seismograms of the North Korea nuclear explosions recorded at (a) a regional and (b) a teleseismic station. 0

5.9 References

Aki, K., Richards, P.G., 2002. Quantitative seismology.

Alvizuri, C., Tape, C., 2018. Full moment tensor analysis of nuclear explosions in North Korea. Seismol. Res. Lett. 89, 2139-2151.

Avants, M., 2014. Effects of near-source heterogeneity on wave fields emanating from crustal sources observed at regional and teleseismic distances. UC Santa Cruz.

Bai, Q., Ni, S., Chu, R., Jia, Z., 2020. gCAPjoint, A Software Package for Full Moment Tensor Inversion of Moderately Strong Earthquakes with Local and Teleseismic Waveforms. Seismological Society of America 91, 3550-3562.

Ballard, S., Hipp, J.R., Begnaud, M.L., Young, C.J., Encarnacao, A.V., Chael, E.P., Phillips, W.S., 2016. SALSA3D: A tomographic model of compressional wave slowness in the

Earth’s mantle for improved travel-time prediction and travel-time prediction uncertainty. Bull. Seismol. Soc. Am. 106, 2900-2916.

Barth, A., 2014. Significant release of shear energy of the North Korean nuclear test on February 12, 2013. JSeis 18, 605-615.

Bazargani, F., Hale, D., Hayes, G.P., 2013. Tensor-Guided Fitting of Subducting Slab Depths. Bull. Seismol. Soc. Am. 103, 2657-2669.

Bozdağ, E., Peter, D., Lefebvre, M., Komatitsch, D., Tromp, J., Hill, J., Podhorszki, N., Pugmire, D., 2016. Global adjoint tomography: first-generation model. Geophysical Journal International 207, 1739-1766.

Cesca, S., Heimann, S., Kriegerowski, M., Saul, J., Dahm, T., 2017. Moment tensor inversion for nuclear explosions: What can we learn from the 6 January and 9 September 2016 nuclear tests, North Korea? Seismol. Res. Lett. 88, 300-310.

Chiang, A., Ichinose, G.A., Dreger, D.S., Ford, S.R., Matzel, E.M., Myers, S.C., Walter, W., 2018. Moment Tensor Source-Type Analysis for the Democratic People’s Republic of Korea–Declared Nuclear Explosions (2006–2017) and 3 September 2017 Collapse Event. Seismol. Res. Lett. 89, 2152-2165.

Covellone, B.M., Savage, B., 2012. A quantitative comparison between 1D and 3D source inversion methodologies: Application to the Middle East. Bulletin of the Seismological Society of America 102, 2189-2199.

Dahm, T., 1996. Relative moment tensor inversion based on ray theory: theory and synthetic tests. Geophysical Journal International 124, 245-257.

Dreger, D., 1994. Empirical Green's function study of the January 17, 1994 Northridge, California earthquake. Geophys. Res. Lett. 21, 2633-2636.

Duputel, Z., Rivera, L., Kanamori, H., Hayes, G., 2012. W phase source inversion for moderate to large earthquakes (1990–2010). Geophys. J. Int. 189, 1125-1147.

Ekström, G., Nettles, M., Dziewoński, A., 2012. The global CMT project 2004–2010: Centroid-moment tensors for 13,017 earthquakes. Physics of the Earth and Planetary Interiors 200, 1-9.

Fichtner, A., Kennett, B.L., Igel, H., Bunge, H.-P., 2009. Full seismic waveform tomography for upper-mantle structure in the Australasian region using adjoint methods. Geophysical Journal International 179, 1703-1725.

Ford, S.R., Dreger, D.S., Walter, W.R., 2009. Source analysis of the memorial day explosion, Kimchaek, North Korea. Geophys. Res. Lett. 36.

Ford, S.R., Walter, W.R., Dreger, D.S., 2012. Event discrimination using regional moment tensors with teleseismic-P constraints. Bulletin of the Seismological Society of America 102, 867-872.

Frohlich, C., Davis, S.D., 1999. How well constrained are well-constrained T, B, and P axes in moment tensor catalogs? Journal of Geophysical Research: Solid Earth 104, 4901-4910.

Hardebeck, J.L., Hauksson, E., 2001. Crustal stress field in southern California and its implications for fault mechanics. Journal of Geophysical Research: Solid Earth 106, 21859-21882.

Hastings, W.K., 1970. Monte Carlo sampling methods using Markov chains and their applications.

Hauksson, E., 1994. State of stress from focal mechanisms before and after the 1992 Landers earthquake sequence. Bull. Seismol. Soc. Am. 84, 917-934.

Hayes, G.P., Wald, D.J., Keranen, K., 2009. Advancing techniques to constrain the geometry of the seismic rupture plane on subduction interfaces a priori: Higher-order functional fits. Geochem. Geophys. Geosyst. 10.

Jia, Z., Ni, S., Chu, R., Zhan, Z., 2017. Joint inversion for earthquake depths using local waveforms and amplitude spectra of Rayleigh waves. Pure and Applied Geophysics 174, 261-277.

Jia, Z., Shen, Z., Zhan, Z., Li, C., Peng, Z., Gurnis, M., 2020a. The 2018 Fiji Mw 8.2 and 7.9 deep earthquakes: One doublet in two slabs. Earth Planet. Sci. Lett. 531, 115997.

Jia, Z., Wang, X., Zhan, Z., 2020b. Multifault Models of the 2019 Ridgecrest Sequence Highlight Complementary Slip and Fault Junction Instability. Geophys. Res. Lett. 47, e2020GL089802.

Kanamori, H., Rivera, L., 2008. Source inversion ofWphase: speeding up seismic tsunami warning. Geophys. J. Int. 175, 222-238.

Kennett, B.L., Engdahl, E., Buland, R., 1995. Constraints on seismic velocities in the Earth from traveltimes. Geophysical Journal International 122, 108-124.

Kikuchi, M., Kanamori, H., 1991. Inversion of complex body waves—III. Bull. Seismol. Soc. Am. 81, 2335-2350.

Lay, T., Burdick, L., Helmberger, D.V., 1984. Estimating the yields of the Amchitka tests by waveform intercorrelation. Geophysical Journal International 78, 181-207.

Lee, E.J., Chen, P., Jordan, T.H., Maechling, P.B., Denolle, M.A., Beroza, G.C., 2014. Full-3-D tomography for crustal structure in southern California based on the scattering-integral and the adjoint-wavefield methods. Journal of Geophysical Research: Solid Earth 119, 6421-6451.

Liu, H., Gurnis, M., Leng, W., Jia, Z., Zhan, Z., 2021. Tonga Slab Morphology and Stress Variations Controlled by a Relic Slab: Implications for Deep Earthquakes in the Tonga-Fiji Region. Geophys. Res. Lett. 48, e2020GL091331.

Minson, S.E., Dreger, D.S., 2008. Stable inversions for complete moment tensors. Geophys. J. Int. 174, 585-592.

Ni, S., Helmberger, D., Pitarka, A., 2010. Rapid source estimation from global calibrated paths. Seismological Research Letters 81, 498-504.

Plourde, A.P., Bostock, M.G., 2019. Relative moment tensors and deep Yakutat seismicity. Geophysical Journal International 219, 1447-1462.

Rodgers, A.J., Petersson, N.A., Sjogreen, B., 2010. Simulation of topographic effects on seismic waves from shallow explosions near the North Korean nuclear test site with emphasis on shear wave generation. Journal of Geophysical Research: Solid Earth 115.

Savage, B., Morency, C., Covellone, B.M., Rodgers, A., Tromp, J., 2014. Short-period, anelastic and anisotropic, waveform-based 3D Middle East model to improve nuclear explosion monitoring. RHODE ISLAND UNIV KINGSTON KINGSTON United States.

Simmons, N.A., Myers, S.C., Johannesson, G., Matzel, E., 2012. LLNL-G3Dv3: Global P wave tomography model for improved regional and teleseismic travel time prediction. Journal of Geophysical Research: Solid Earth 117.

Tan, Y., Helmberger, D., 2007. A new method for determining small earthquake source parameters using short-period P waves. Bull. Seismol. Soc. Am. 97, 1176-1195.

Tao, K., Grand, S.P., Niu, F., 2017. Full-waveform inversion of triplicated data using a normalized-correlation-coefficient-based misfit function. Geophys. J. Int. 210, 1517-1524.

Tape, C., Liu, Q., Maggi, A., Tromp, J., 2009. Adjoint tomography of the southern California crust. Science 325, 988-992.

Tape, W., Tape, C., 2012. A geometric setting for moment tensors. Geophysical Journal International 190, 476-498.

Tape, W., Tape, C., 2013. The classical model for moment tensors. Geophys. J. Int. 195, 1701-1720.

Tape, W., Tape, C., 2015. A uniform parametrization of moment tensors. Geophys. J. Int. 202, 2074-2081.

Tarantola, A., 2005. Inverse problem theory and methods for model parameter estimation. SIAM.

Vallée, M., 2007. Rupture properties of the giant Sumatra earthquake imaged by empirical Green's function analysis. Bull. Seismol. Soc. Am. 97, S103-S114.

Vavryčuk, V., Kim, S.G., 2014. Nonisotropic radiation of the 2013 North Korean nuclear explosion. Geophys. Res. Lett. 41, 7048-7056.

Voytan, D.P., Lay, T., Chaves, E.J., Ohman, J.T., 2019. Yield estimates for the six north Korean nuclear tests from teleseismic P wave modeling and intercorrelation of P and Pn recordings. Journal of Geophysical Research: Solid Earth 124, 4916-4939.

Waldhauser, F., Ellsworth, W.L., 2000. A double-difference earthquake location algorithm: Method and application to the northern Hayward fault, California. Bull. Seismol. Soc. Am. 90, 1353-1368.

Wang, D., Hutko, A.R., 2018. Relative relocations of the North Korean nuclear tests from 2006 to 2017 using the Hi-Net array in Japan. Geophysical Research Letters 45, 7481-7487.

Wang, X., Zhan, Z., 2020a. Moving from 1-D to 3-D velocity model: automated waveform-based earthquake moment tensor inversion in the Los Angeles region. Geophysical Journal International 220, 218-234.

Wang, X., Zhan, Z., 2020b. Seismotectonics and Fault Geometries of the 2019 Ridgecrest Sequence: Insight From Aftershock Moment Tensor Catalog Using 3-D Green's Functions. Journal of Geophysical Research: Solid Earth 125, e2020JB019577.

Xu, H., Ni, S., Liu, W., Zhu, H., Wang, X., 2020. Focal mechanisms of the 2017 North Korean nuclear test and its early collapse event. Geophys. J. Int. 220, 737-752.

Yang, T., Gurnis, M., Zhan, Z., 2017. Trench motion-controlled slab morphology and stress variations: Implications for the isolated 2015 Bonin Islands deep earthquake. Geophys. Res. Lett. 44, 6641-6650.

Zhan, Z., Helmberger, D., Simons, M., Kanamori, H., Wu, W., Cubas, N., Duputel, Z., Chu, R., Tsai, V.C., Avouac, J.-P., 2012. Anomalously steep dips of earthquakes in the 2011 Tohoku-Oki source region and possible explanations. Earth Planet. Sci. Lett. 353, 121-133.

Zhang, M., Wen, L., 2013. High-precision location and yield of North Korea's 2013 nuclear test. Geophysical Research Letters 40, 2941-2946.

Zhang, M., Wen, L., 2015. Seismological evidence for a low-yield nuclear test on 12 May 2010 in North Korea. Seismological Research Letters 86, 138-145.

Zhao, L.S., Helmberger, D.V., 1994. Source estimation from broad-band regional seismograms. Bulletin of the Seismological Society of America 84, 91-104.

Zhu, L., Ben-Zion, Y., 2013. Parametrization of general seismic potency and moment tensors for source inversion of seismic waveform data. Geophysical Journal International 194, 839-843.

Zhu, L., Helmberger, D.V., 1996. Advancement in source estimation techniques using broadband regional seismograms. Bulletin of the Seismological Society of America 86, 1634-1641.

Zhu, L., Rivera, L.A., 2002. A note on the dynamic and static displacements from a point source in multilayered media. Geophys. J. Int. 148, 619-627.

Chapter 6

RESOLVING THE LOS ANGELES BASIN STRUCTURE WITH DENSE ARRAYS

Jia, Zhe, and Robert W. Clayton. "Determination of Near Surface Shear-Wave Velocities in the Central Los Angeles Basin with Dense Arrays." In: *Journal of Geophysical Research: Solid Earth* 126, no. 5 (2021): e2020JB021369. Doi: 10.1029/2020JB021369.

6.1 Abstract

In this study, we investigate the shallow shear wave velocity structure of the Los Angeles Basin in southern California, using ambient noise correlations between 5 dense arrays and 21 broadband stations from the Southern California Seismic Network (SCSN). We observe clear fundamental mode and first overtone Rayleigh waves in the frequency band 0.25-2.0 Hz, and obtain group velocity maps through tomography. We further derive a 3D shear wave velocity model, covering a large portion of the central LA Basin for the depths shallower than 3 km. We found that the small scale shallow velocity structure heterogeneities are better resolved compared with the SCEC Community velocity models. Our model captures the presence of the Newport-Inglewood fault by a NW-SE trending high velocity belt. Our model provides more accurate constraints on local ground motion predictions with detailed mapping of structural heterogeneities.

6.2 Introduction

Los Angeles (LA) Basin is a major sedimentary basin that formed as part of the extension following the rotation of the Transverse Ranges in the Miocene. It has a depth of approximately 8 km at its deepest point and has strong lateral variations in its near-surface structure [*Shaw et al.*, 2015] due to variations of the depositional environment across the basin. Both the depth extent and near surface velocities strongly affect the amplification of ground motions. The deeper structure of the basin controls the low-frequency resonance behavior of the motion, which is important for high-rise buildings, while the shallower velocities primarily affect the motions at frequencies of 1 Hz or higher. The latter is important for community infrastructure and buildings that are less than 10-stories high. Recent studies have shown that the ground motions can vary laterally by a factor of 5 over a kilometer distance (Clayton et al., 2019), which poses a significant earthquake hazard concern in the densely populated greater LA area; consequently it is important to constrain the near-surface structure and wave velocities of the LA Basin.

Studies of the detailed basin velocity structure rely on the analysis of earthquake seismic records, borehole geophysical data, geologic inference, and seismic reflection profiles. Structural models of the southern California region have also been conducted using seismic observations including receiver functions (Zhu and Kanamori, 2000; Ma and Clayton, 2016) and seismic tomography (Hauksson, 2000; Tape et al., 2009; Qiu et al., 2019). On the other hand, Suss and Shaw (2003) measured P wave velocities of the central LA Basin through a normal moveout analysis of oil-company reflection surveys and from borehole sonic logs. All of these approaches provide constraints on the structure of the LA Basin on a variety of length scales. These various approaches have resulted in a series of 3D community velocity models (CVM) for southern California (Lee et al., 2014b; Shaw et al., 2015; Small et al., 2017). The CVM models are reported to be capable of forward predicting waveforms up to 0.2 Hz (Lee et al., 2014a; Taborda et al., 2016; Jia et al., 2020). However, the LA Basin is only covered by approximately 20 Southern California Seismic Network broadband stations, which limits the spatial resolution of the tomography based approaches. Reflection surveys and borehole logs used for velocity analysis are of much higher precision, but they are generally only available in the oil producing areas which constitute only a small portion of the LA Basin. The detailed structure of the LA Basin is difficult to determine because it requires dense arrays of seismic instruments deployed in urban areas.

In recent years, the development of ambient noise tomography and the increasingly extensive usage of dense seismic arrays are two innovations that allow a more detailed and comprehensive structural analysis. Ambient noise surface wave tomography has been widely applied in imaging subsurface structure (Shapiro et al., 2005; Lin et al., 2008; Ekström, 2014). Ambient noise tomography involves noise correlations, which turns coherent seismic noise recorded by different stations into Green's functions between these stations, assuming a diffuse and isotropic noise field (Snieder, 2004). The dominant signal in the vertical-vertical correlations is the Rayleigh wave. The next steps include measuring dispersions of surface waves with a frequency-time analysis (Levshin et al., 1972; Bensen et al., 2007), standard seismic tomography (Barmin et al., 2001) and nonlinear shear wave inversions (Herrmann, 2013). Ambient noise tomography has been traditionally used to investigate regional and continental scale structure with long period (T>5s) surface waves obtained from correlations between broadband seismic stations. Recent developments in dense array deployments extend the ambient-noise based structural studies to higher frequencies, making seismic imaging of local and shallow velocity structure easily applicable (Lin et al., 2013; Roux et al., 2016; Castellanos et al., 2020).

Five temporary dense arrays of totaled more than 16000 high-frequency velocity sensors were deployed by oil companies from 2011 to 2018 in the Los Angeles region (Fig. 6.1). Most of these arrays are located above oil fields associated with the Newport-Inglewood fault. An exception is the Santa Fe Springs survey, which is closer to the northeastern edge of the basin. The stations are deployed for different time spans from 3 weeks to 5 months and recorded continuously during those times. This means they not only record the active source signals of the survey but also the passive ambient noise. Although the dense nodal arrays only cover small areas, and each of them was deployed at different times, they all overlap in time with the long-term SCSN broadband seismic stations which span over the whole LA Basin. This long span time and dense coverage of the inter-array ambient noise correlations provide a unique opportunity to investigate the detailed shallow structural heterogeneities of the central LA Basin.

In this study, we will illustrate the effectiveness of noise correlations between the broadband SCSN stations and the high-frequency dense array nodal sensors between 0.2-

2.0 Hz. We then perform frequency-time analysis on the noise correlation functions to retrieve Rayleigh-wave dispersion curves. Using a standard straight-ray tomography approach, we generate group velocity maps, which are then inverted for the shear-wave velocity structure. We then assess the model errors, and discuss the effect of our model on strong ground motion predictions.

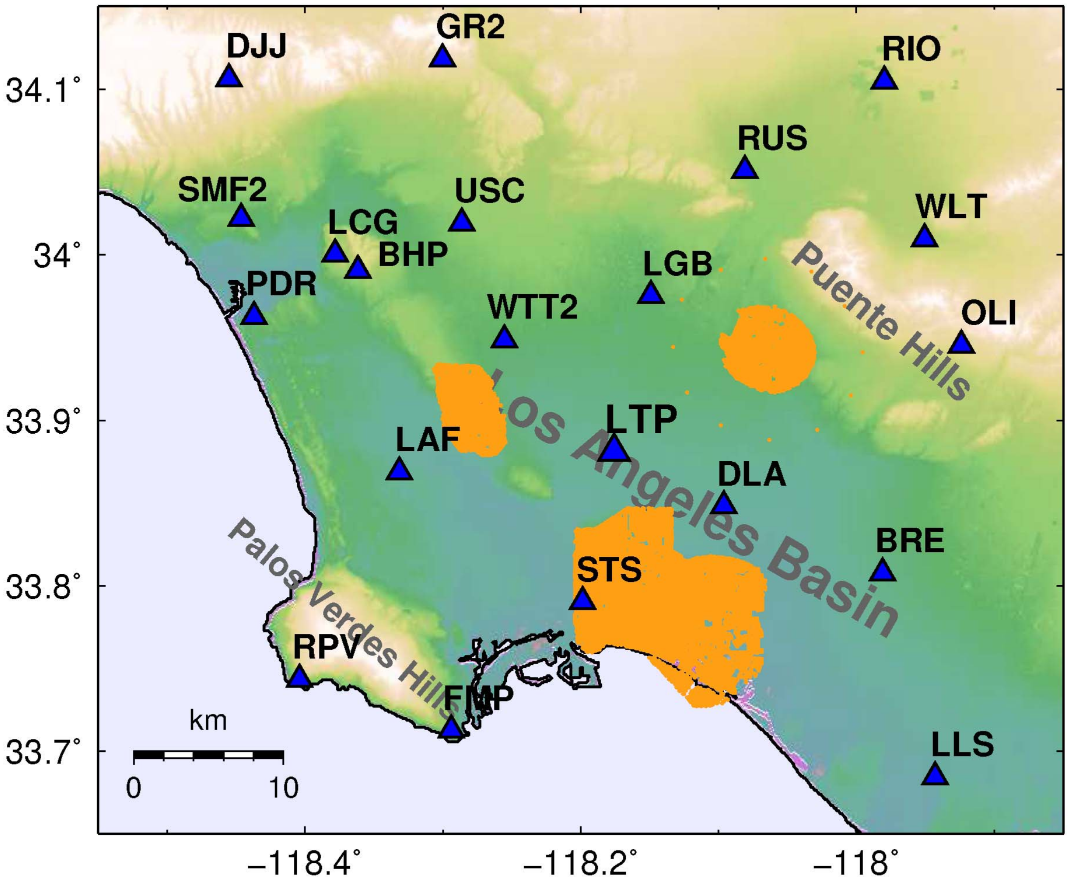

Figure 6.1. Distribution of the 21 broadband seismic stations (blue triangles) and 5 dense oil company nodal arrays (orange shaded areas) used in this study, the largest of which has 3 side-by-side surveys.

6.3 Data and Method

We collect the ambient noise data recorded by the industrial arrays (16,000 short-period vertical component nodes) and SCSN stations (21 broadband sensors) in their overlapping time periods. This results in at least 500 hours of noise data for each of the node-broadband pairs (Fig. 6.1). The industry data is recorded with dense arrays (100 stations/km^2) in which each station is a vertical-component velocity sensor with a corner frequency of 10 Hz. These geophones are deployed in a relatively noisy urban setting, and although they are most sensitive to frequencies above 10 Hz, several studies have shown that noise correlations within the dense arrays can produce Rayleigh waves in the frequency band of 0.1~10 Hz (Lin et al., 2013; Ben-Zion et al., 2015; Nakata et al., 2015).

We follow Bensen et al. (2007) to calculate the inter-array noise correlation functions (NCFs). We cut the vertical component noise data of both SCSN stations and dense arrays into one hour segments, and then perform time domain normalization and spectral whitening to suppress the influence of earthquakes and other coherent signals. Due to the reduced instrumental responses at lower frequencies for the dense array geophones, we normalize the spectrum of geophone noise data by their spectral amplitudes. That is, we force the amplitudes of all frequencies to be uniform and only keep their phase information. We then calculate the NCF of all possible inter-array station pairs, and stack these 1-hour correlations over a three-week span. We have computed 353006 noise correlations, including 106800 for array LB3D, 104811 for SB3D, 50660 for SFS, 48840 for ELB, and 41895 for ROSE. We summarize these numbers in Table S6.1. Finally, we average both sides of each NCF by flipping the virtual source and receiver, forming symmetric waves on the positive side and negative side (Lin et al., 2008). In addition to the inter-array correlations, we also calculate the intra-array correlations within the SCSN stations. An example of the distance-sorted stacked NCFs is shown in Fig. 6.2. For a relatively broad frequency band between 0.2-2.0 Hz (Fig. 6.2a), we observe a clear trend of the Rayleigh wave moveout but it is difficult to distinguish the separate modes. However, for relatively higher frequencies between 0.5-2.0 Hz (Fig. 6.2b), we observe splitting of the modes, indicating that both fundamental and first overtone Rayleigh waves exist in the NCFs. The propagations of these multi-modal Rayleigh waves are shown in Fig. 6.3, as wavefields recorded by four dense arrays using the SCSN station LTP as a virtual source. We observe both slower waves with large amplitudes and faster but weaker signals for the four different directions. These are the fundamental mode and first overtone Rayleigh waves, respectively. Note that the wave propagation within every single dense array involves nontrivial phase distortions, amplitude variations, and frequency content differences. Presumably, these different paths could have very different small scale scatter distributions. Another possible cause is the difference of intrinsic attenuation effect along these ray paths. More intensely scattered high frequency waves and less intrinsic attenuation can make the surface wavefield more complex. The observed wavefield complexities suggest significant structural heterogeneities along the ray paths.

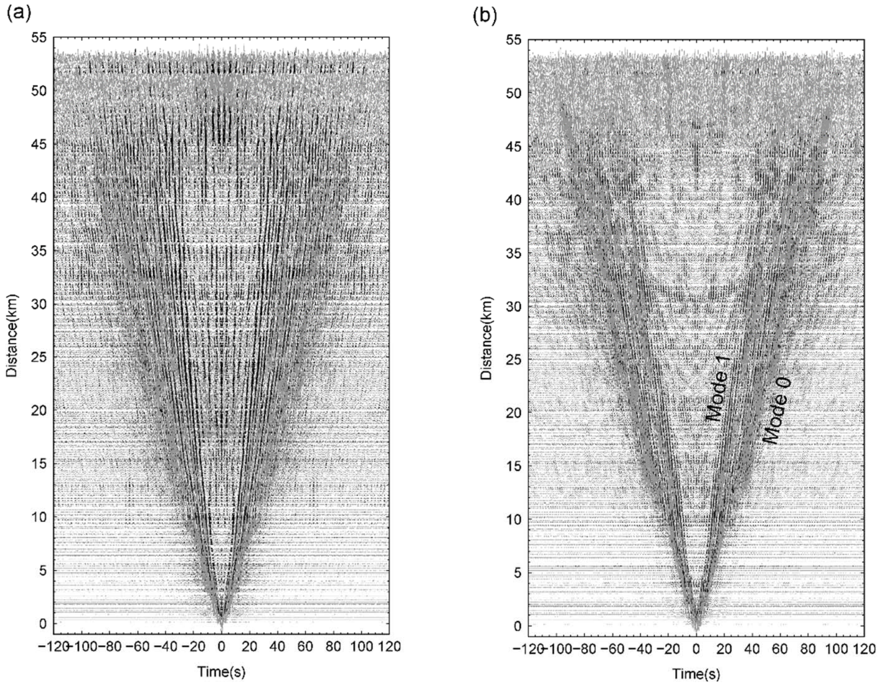

Figure 6.2. Inter-array noise correlation functions between SCSN stations and dense nodal arrays. (a) Noise correlation functions stacked in distance bins between 0.2-2.0 Hz. (b) High frequency (0.5-2.0 Hz) filtered noise correlation functions stacked in distance bins.

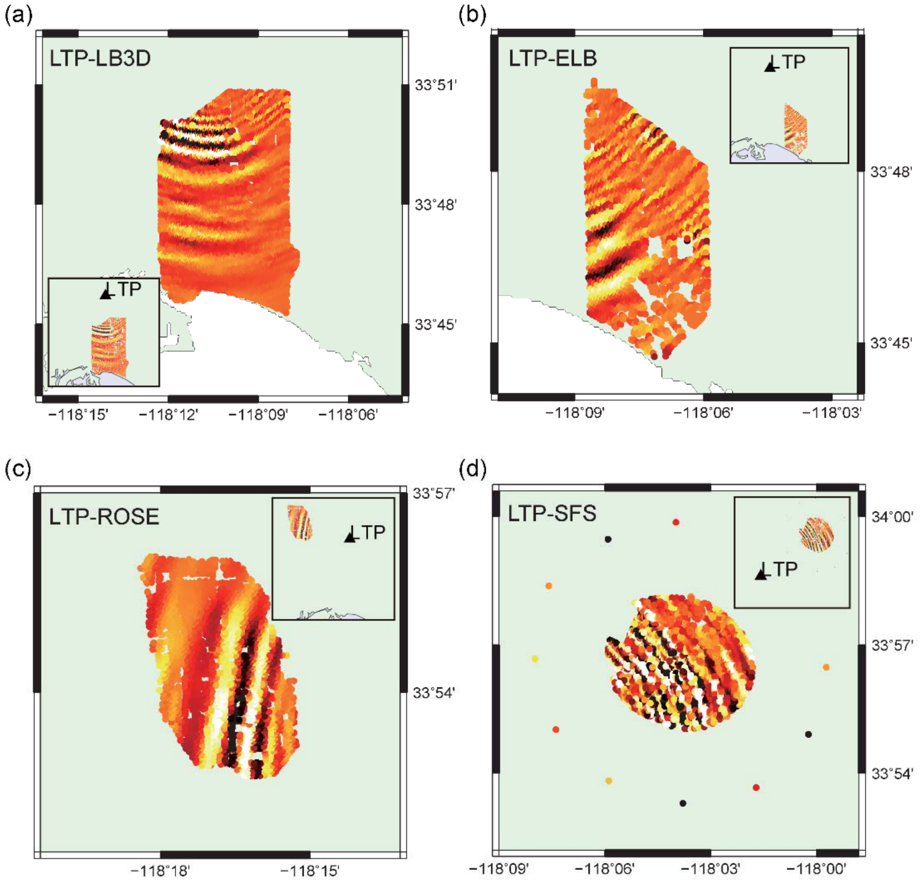

Figure 6.3. Wavefield snapshots of the noise correlation functions from station LTP to dense arrays (a) LB3D, (b) ELB, (c) ROSE, and (d) SFS.

We use a frequency-time analysis (FTAN) method (Levshin et al., 1972; Herrmann, 2013) to retrieve both the fundamental and first overtone modes of Rayleigh wave group velocity dispersions for all SCSN-array pairs. As for the data selection, we empirically set the minimum signal-to-noise ratio to be 5. We filter the waves between 0.2~1.0 Hz before we screen them with SNR. For the NCF with a distance *l*, we define the signal time window between *l*/1.2~*l*/0.3 s, and the noise window to be 0~*l*/1.2 s, where 1.2 and 0.3 km/s are proxies of upper and lower bounds of Rayleigh waves velocities. Both signal and noise are measured by the root mean square value of the waves over time. We only keep the interstation distance of the NCFs greater than 8 km. The distance restriction is to allow adequate separation of the modes. Furthermore, to ensure the robustness of the dispersion measurements, we stack the NCFs for almost identical ray paths defined by dense array bins of 300-meter radius, typically involves tens of stations. There are reasons why we choose the circular distance to be 300 meters. The first is to avoid gaps in the arrays caused by infrastructure. Secondly, our correlation distance in tomography is 1km, and a larger stacking radius is closer to this wavelength limit, which could potentially introduce artificial smoothness. Furthermore, to test the nodal array interstation distance needed in this study, we down sampled the nodal station density to average interstation distances to 0.3, 0.45, and 0.7 km, and we conducted checkerboard tests at period of 2s in these cases. We found that an average interstation distance of less than 0.3km is required for recovering the checkerboard map (Fig. S6.1). In the FTAN approach, we apply a Gaussian filter where we set the filter parameter alpha to 25 as a compromise between the narrow-band assumption and filtering robustness (Zhang et al., 2020). Once we obtained the velocity-time amplitudes, we adopt a hybrid dispersion picking strategy, in which we first automatically pick the dispersion curves within velocity-time corridors, and then manually check the picked curves. The corridors are estimated through stacking the velocity-time amplitudes of NCFs from each SCSN station to all geophones in each dense array, because these NCFs share similar ray paths. Fig. S6.2a shows the example of corridors on the stacked FTAN maps from the virtual source LGB to the different dense arrays. The fundamental mode and first overtone surface wave signals are well covered by the corridors. Moreover, the picked dispersions for LGB against array LB3D (Fig. S6.2a) is consistent with machine learning picked ones (Zhang et al., 2020). Fig. S6.2b presents an overview of all corridors on the stacked velocity-time maps. Within the large number of noise correlations, we manually check one dispersion curve at equal intervals every 50 curves. Because each dense array has thousands of nodal stations, and the ray paths from one virtual source to nodal stations of same array are similar to each other, this sampling inspection approach provide robust way of assessing the quality of corridors and the criteria used for accepting the picks. We accept the picks within the corridor when their spectral amplitudes are larger than all other possible picks at the same frequency, and when their spectral amplitudes are larger than 0.4 cm-s for the fundamental mode and 0.3 cm-s for the first overtone. These thresholds provided good quality picks with a reasonably high acceptance rate. Fig. 6.4 shows an example of the group velocity dispersion picking for the pair of broadband station LTP and dense array geophone 1041-5011. The dispersion curves of the fundamental mode and first overtone Rayleigh waves are clear and well picked.

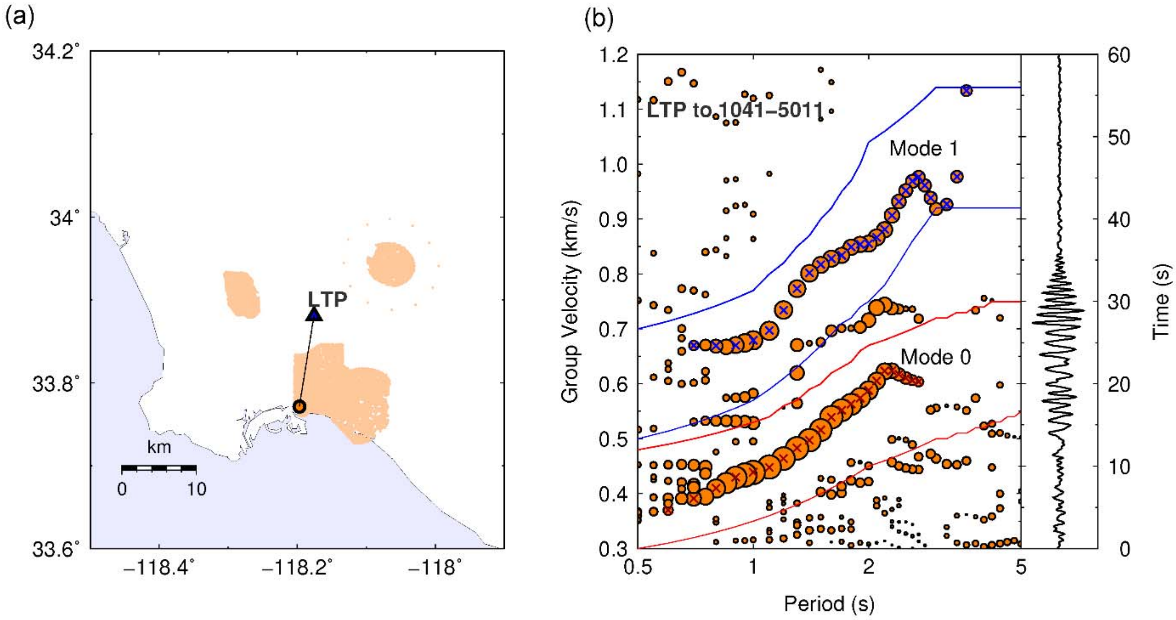

Figure 6.4. Example of labeling of dispersion curves. (a) The ray path from broadband station LTP (black triangle) to a dense array station 1041-5011 (orange circle). (b) The FTAN image (period axis uses a logarithmic scale) of the noise correlation function for the

ray path in (a). The size of each circle is proportional to the wave packet energy at the corresponding period and group velocity. The red and blue crosses are the picked dispersion data for the fundamental mode and first overtone, respectively. The red and blue lines indicate the corridors for these two modes. The waveform to the right indicates the time-domain noise correlation function.

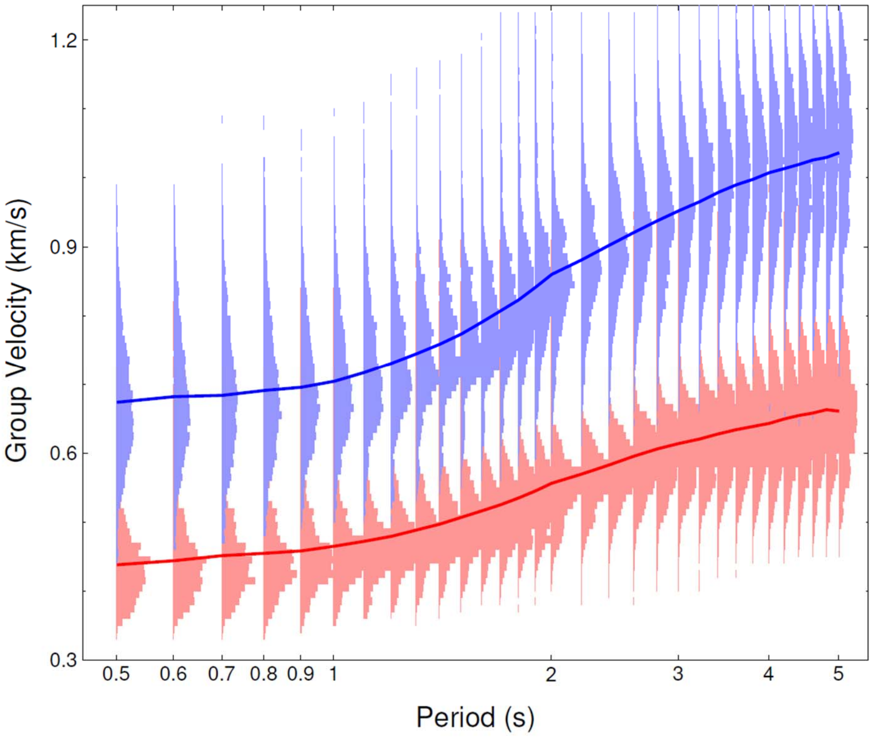

Figure 6.5. Compilation of all used dispersion picks. The histograms indicate distributions of the fundamental mode (in light red) and first overtone (in light blue) group velocity picks for different periods. The period axis uses a logarithmic scale. Lines in red and blue indicate the mean group velocities for fundamental mode and first overtone, respectively.

Due to the uneven data quality between each station-array pair, the numbers of picked dispersion data for different SCSN station and nodal array pairs can be significantly different (Fig. S6.3). If their weights are not balanced, the tomographic inversion will be dominated by those station-array pairs that contribute most dispersion picks. Therefore, we adjust the weightings of different station-array pairs by uniformly resampling so no more than 200 picks for each station-array pair and each period are used. The dispersion counts from different station-array pairs after this reweighting are much more even (Fig. S6.3), indicating that the data are better weighted. A compilation of all dispersion data after reweighting is shown in Fig. 6.5. These curves show an overall increase of group velocity U with period, and hence an increase of Vs with depth. Fig. 6.6 shows the compilation of extracted fundamental mode and first overtone Rayleigh wave group velocities for periods of 1s, 2s, 3s, and 4s.

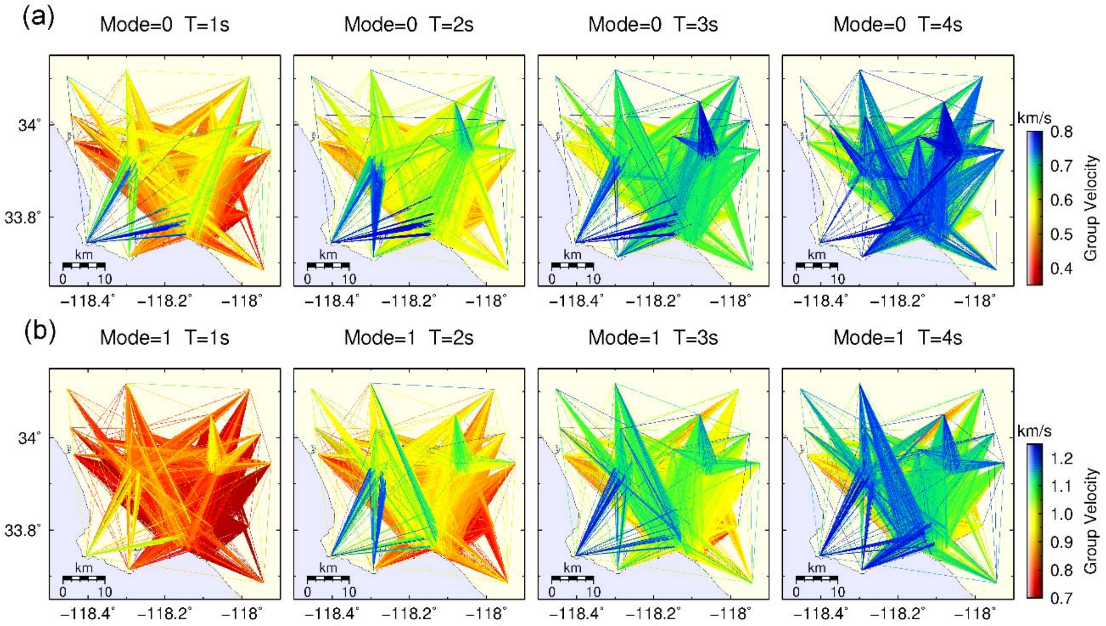

Figure 6.6. Ray coverage of (a) the fundamental mode and (b) the first overtone Rayleigh wave group velocity measurements for periods 1-4 s.

To analyze the inter-station group velocity dispersion measurements, we use the 2D straight-ray tomography adapted from Barmin et al. (2001) to derive the fundamental mode and first overtone Rayleigh wave group velocity maps. The region is discretized into 0.012° × 0.008° grids, and we linearly invert for group velocity maps of each period between 0.5-4.0 s. In the linear inversions, we adopt two penalty terms for regularization, 1) constraint on model smoothness, and 2) damping as a function of the ray coverage density. For the smoothness constraints, we set the correlation length to be 1 km. The ray coverage damping uses the concept of azimuthal coverage proposed by Ekström (2006) to quantitatively indicate the effective ray coverage in each grid. We perform this linear inversion with two iterations. In the first iteration, we weight all the dispersion data equally, and apply a strong regularization for a smooth model which presumably represents the first order structural heterogeneities. We then forward predict the synthetic group arrival times for all ray paths, and approximate the misfit between data and synthetic arrival times as data error. We discard those data with misfits that are larger than three times of standard deviation (Castellanos et al., 2018). In the second iteration, we construct the data covariance matrix which diagonal terms are specified based on the data errors. Thus, the data weightings are inversely proportional to the data error, making the group velocity map inversions less dependent on specific paths with large misfits. To understand the data resolvability in our group velocity map inversions, we generate standard checkerboard resolution maps through the resolution matrix $(G^tC^{-1}G+Q)^{-1}G^tC^{-1}Gm^*$ (Ma and Clayton, 2014), where C is the data covariance matrix, Q is the regularization matrix, G is the forward operator, and m* is the input checkerboards containing up to ±20% contrasting slowness variations. Fig. 6.7 shows the checkerboard resolution maps at periods of 1, 2s, 3s, and 4s for both fundamental mode and first overtone Rayleigh waves. We found that the contrasting checkerboard structures are well recovered in a large portion of the LA Basin for all these periods and wave modes. However, the resolution is lower at the edge of the studied area due to the poor azimuthal coverage of the rays.

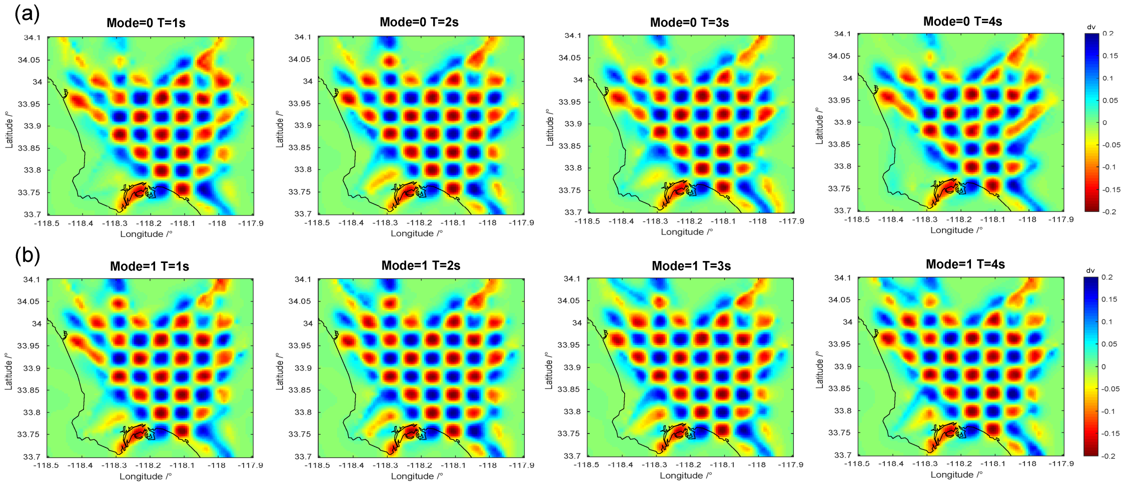

Figure 6.7. Checkerboard resolution maps of (a) the fundamental mode and (b) the first overtone Rayleigh wave group velocity tomography for periods 1-4 s.

We invert for the shear wave velocities as a function of depth, using 1D group velocity profiles at each grid extracted from the tomographic maps. We use the SURF96 program (Herrmann, 2013) for this shear wave velocity inversion. SURF96 is designed for horizontally isotropic layered structure, and involves an iterative least squares inversion procedure. Using the SCEC CVM-S4 profiles embedded with Vs30-derived geotechnical layer (Ely et al., 2010) at all grid points as the initial model, we iteratively perturb the shear wave velocities of all layers while calculating P wave velocities following the empirical relationship introduced by Brocher (2005), until a good fit between observed and synthetic fundamental mode and first overtone Rayleigh wave dispersion curves are achieved. These final 1D shear wave velocity profiles are integrated into a whole 3D Vs model of the study region. We also tested using the 1D model inverted from the mean of all dispersion curves as the initial model, and found no significant change to the shear wave velocity profiles.

6.4 Results

We invert the extracted dispersion curves from the Rayleigh waves group velocity maps for a suite of frequencies between 0.25-2.0 Hz. Fig. 6.8 shows the fundamental mode and first overtone group velocities at periods of 1s, 2s, 3s, and 4s. For both modes and all periods, we observed two high group velocity anomalies in the southwestern and northeastern corners of the study region, which correspond to the Palos Verdes Hills and Puente Hills, respectively. The group velocities are much lower in the area between these high velocity hills, which suggests the decreasing sedimentary layer thickness towards the Palos Verde fault zone to the southwest and towards the Elsinore fault zone to the northeast, consistent with the hard bedrocks beneath these hills that bound the LA Basin in these two directions. Note that the well resolved area is smaller for the short-period and long-period end (period of 1s and 4s in Fig. 6.7). The reason why the areas shrink at these two period ends is that the surface wave energy decreases when period approaches 0.5s and 5s (e.g. Fig. 6.4b). The depleted noise correlation function energy for the short period end is primarily due to the low signal-to-noise ratio of high frequency Rayleigh waves. At the long period end, the lower instrumental responses of the high frequency industrial nodal sensors cause the noise signals less correlated. In the center of the LA Basin, we observe significant group velocity variations of smaller length scales. These variations are far beyond the group velocity errors (Fig. S6.4) estimated from the diagonal term of the model covariance matrix $C=(G^tC^{-1}G+Q)^{-1}$ (Ma and Clayton, 2014). Such small scale variations indicate nontrivial structural heterogeneity of the sedimentary layer, and suggest possible interface roughness within the basin. The effectiveness of data inversion is shown by the significant slowness variance reductions for different modes and periods (Fig. S6.5).

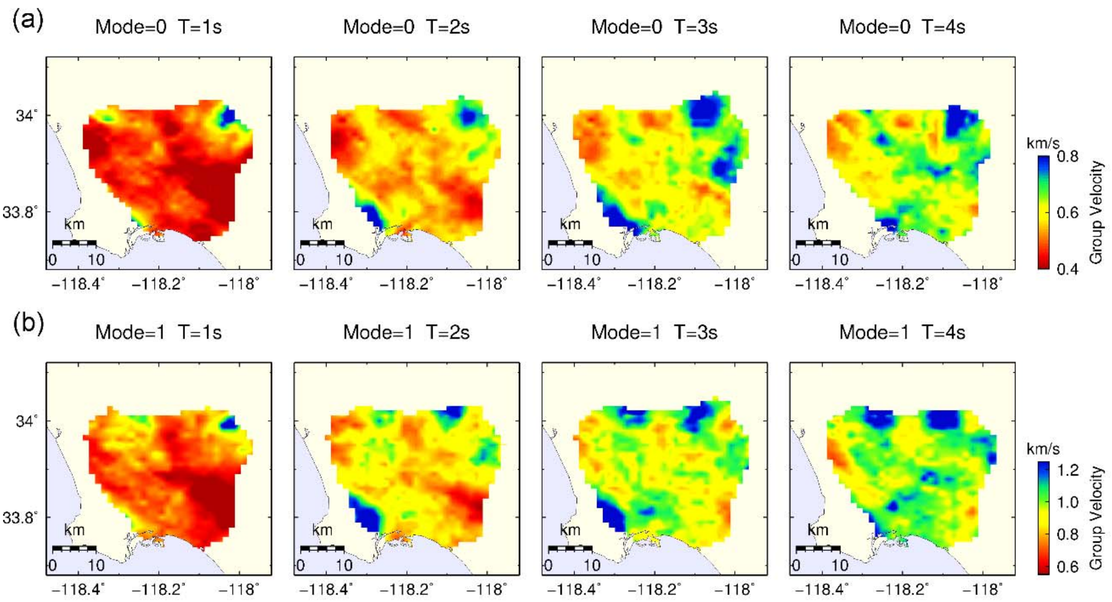

Figure 6.8. Group velocity maps of (a) the fundamental mode and (b) the first overtone Rayleigh wave group velocity tomography for periods 1-4 s.

We show the shear wave velocity inversions in Fig. 6.9. Fig. 6.9a shows horizontal slices of the shear wave velocities at depths of 0.5-2.5 km. At larger depths, the Vs velocity continues to increase and the low velocity area shrinks. We estimate the Vs uncertainties for each grid (e.g. Fig. S6.6) by inverting 50 dispersion curves sampled from group velocity errors. Specifically, for each location grid, we generate 50 randomly perturbed dispersion curves for fundamental mode and first overtone, respectively. At an individual period for each mode, the group velocities are perturbed following a Gaussian distribution with mean of the inverted group velocities (Fig. 6.8) and with standard deviations from the diagonal term of the model covariance matrix in the tomographic inversions (Fig. S6.4). After we obtained the ensemble of dispersion curves (e.g. Fig. S6.6a), we invert them for an ensemble of 1D shear wave velocity models (e.g. Fig. S6.6b). We further measure the standard deviation error of Vs at each depth using the ensemble of 1D Vs models, and combine these 1D Vs errors to Vs error maps (Fig. S6.7). The measured Vs standard deviation error for most of the central LA Basin (Fig. S6.7) is significantly smaller than the observed Vs variations in our model (Fig. 6.9). One pronounced feature of the Vs model is the high velocity belt from NW to SE at the depths of around 1.5 km (Fig. 6.9a). This high velocity strand, accompanied with a sharp horizontal velocity contrast (Fig. 6.9b), appears to be consistent with the trace of the Newport-Inglewood fault system (Fig. 6.9a), which is manifested by a line of hills from Cheviot Hills on the northwestern end to the Signal Hill on the southeastern end (Hauksson, 1987). These hills are the topographic expression of the Newport-Inglewood fault extending to the surface, suggesting that the fault movement transported higher velocity materials from deeper to shallower depths. This explains the observed high shear wave velocity anomalies of the Newport-Inglewood fault zone and is consistent with various dense array studies (Lin et al., 2013; Nakata et al., 2015; Bianco et al., 2019; Castellanos et al., 2020).

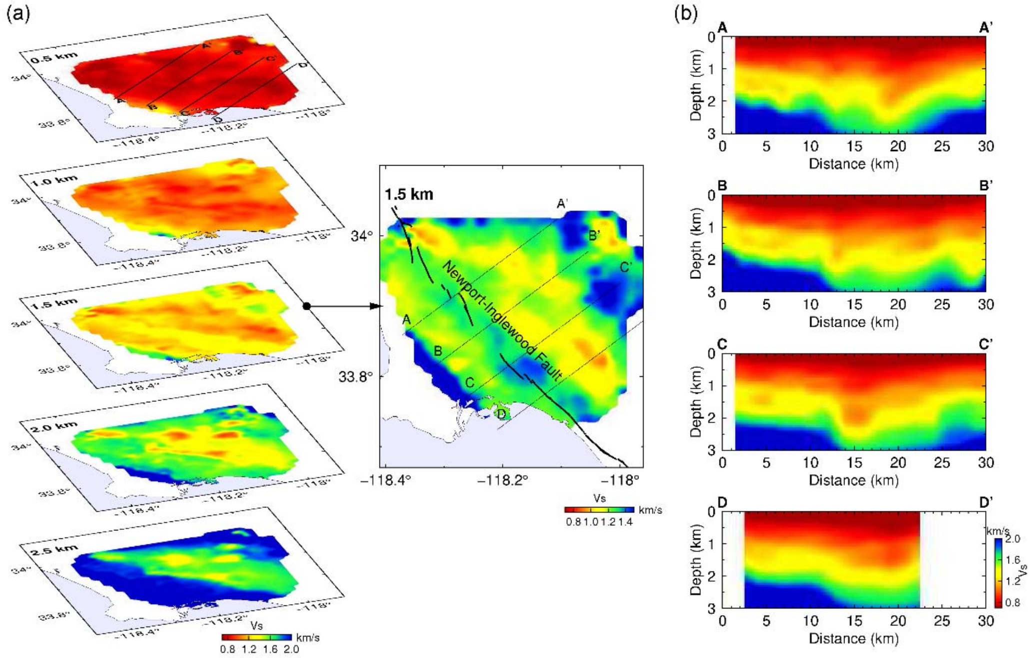

Figure 6.9. The inverted shear wave velocity model of the LA Basin. (a) Horizontal slides of the Vs model at depths of 0.5, 1.0, 1.5, 2.0, and 2.5 km. The center map is a rescaled

version of the 1.5 km depth slice to illuminate the NW-SE trending high velocity zone. Black solid lines indicate the Newport-Inglewood faults. (b) Vertical cross sections of the Vs model along 4 profiles, AA', BB', CC', and DD' in (a).

We note in the Vs slices at a depth of 1-1.5 km (Fig 6.9) that there are low-velocity streaks trending NW to SE, to the northeast of the aforementioned NW-SE high velocity belt. This NW-SE trending low velocity feature corresponds well with the P wave low velocity anomalies obtained with sonic logs and industrial reflection data (Süss and Shaw, 2003). It also agrees with the trend of sedimentary deposits during late Miocene (Redin, 1991), suggesting that they may be due to depositional channels created when the LA Basin was filling with sediments in the Miocene (Süss and Shaw, 2003).

6.5 Discussion

We compare our shear wave velocity model with SCEC CVM-S4 and CVM-H15.1 models as shown in Fig. 6.10. These models generally agree on the large scale structure of the basin [*Taborda et al.*, 2016]. However, their near-surface structures of the LA Basin appear different. The CVM-S model is smoother since it is constructed using full-waveform tomography. On the other hand, since the CVM-H model is largely inferred from geological observations and P wave velocities from oil industry, it has geotechnical layers with sharp artificial boundaries. In the shallow basin, the CVM-S model better characterizes the first-order velocity structure, while the CVM-H model captures finer scale heterogeneities. A comparison of recorded and synthetic waveforms in Southern California confirms that the CVM-S model predicts long period waveforms better, while the CVM-H model better fits the arrival time of scattered waves (Lai et al., 2020). Our Vs model of the LA Basin, named LAS1 (Los Angeles Shallow 1), is in between the CVM-S and CVM-H models, as its overall basin shape and velocity range is closer to the CVM-S model, while rapid lateral variations such as the high velocity anomaly of the Newport-Inglewood fault are similar to the CVM-H model (Fig. 6.10a).

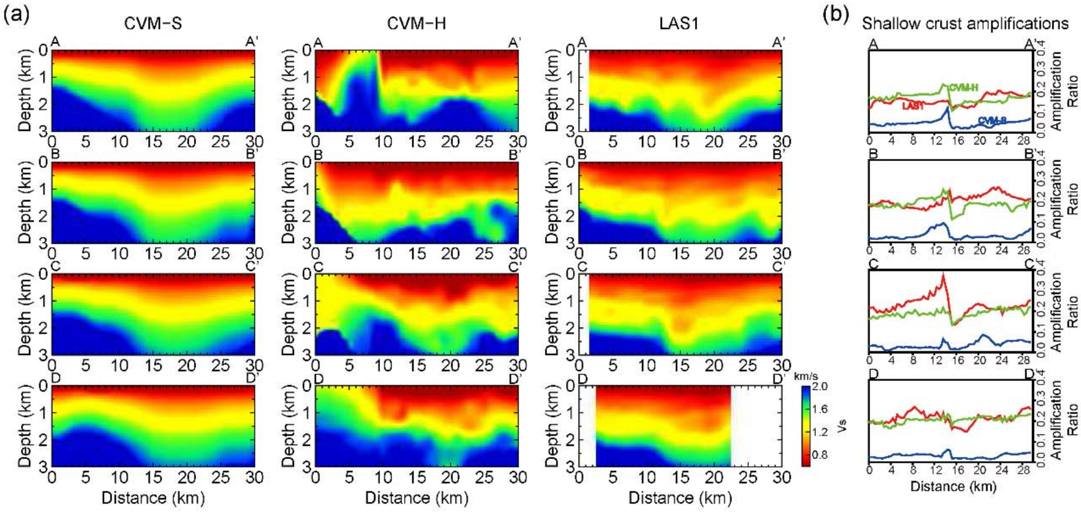

Figure 6.10. Comparison of our inverted LAS1 Vs model with CVM-S and CVM-H models. (a) Model comparisons for 4 cross sections in Fig. 6.9. (b) Prediction of strong motion amplifications along the 4 cross sections using these Vs models. The red, blue, and green lines indicate synthetics from the LAS1, CVM-S, and CVM-H Vs models, respectively. The gapped Vs for the LAS1 cross sections are filled by replicating existing Vs at the edges to the ends of cross sections, where the amplification fluctuations are due to the reflections and scatterings in the 2D simulations.

The small scale shallow structural variation of our LAS1 model appears different from both the SCEC CVM-S and CVM-H models, which may significantly influence the modeling of earthquake ground motion amplitudes for the central LA Basin. To illustrate the effect of the variations in the near surface velocities, we performed 2D simulations of vertically-incidental shear wave pulse using the CVM-S, CVM-H, and our LAS1 models for each cross-section. The calculations are done with a 2D fourth-order staggered-grid finite-difference formulation (Virieux, 1984) that initiated a 1 Hz SH-pulse (in velocity) at a depth of 3 km and propagated it to the surface (Fig. S6.8). The peak acceleration, obtained through numerical differentiation at each horizontal position, is then compared to an equivalent pulse propagated through a medium with a constant shear velocity of 1 km/s (Fig. S6.8). The ratios of the results are displayed in Figure 6.10b and show that the LAS1 and CVM-H models have comparable levels of peak acceleration and lateral variations, but that the CVM-S has significantly lower motions and is laterally smoother. This is likely due to the different wavelengths that these Vs models feature. The CVM-S model comes from a long period (T>5s) full-waveform inversion, while our LAS1 model captures shorter wavelength structural features from short period data (0.5-4s), and the CVM-H model incorporates high-frequency information from geotechnical layers and seismic reflection constraints. The small wavelength heterogeneities can produce larger local lateral and vertical velocity gradient, which could significantly amplify the strong motions (Steidl et al., 1996; Bowden et al., 2015). Additionally, scattering and diffraction due to the existence of structural heterogeneities and rough basin interfaces can cause wave interference, and potentially amplify the motions (Delépine and Semblat, 2012). With the additional constraints from dense array dispersion data, our model can potentially predict the variations of shallow crustal amplifications in the LA Basin which is observed during the 2019 Ridgecrest earthquake sequence [*Filippizitis et al.*, 2021]. The simulations shown here are only intended to illustrate the differences in the models and we present them in lieu of a more complicated 3D simulation.

To better understand the Vs structural difference between our LAS1 model and the CVM-S/CVM-H models, we forward calculate the fundamental model and first overtone Rayleigh wave group velocity dispersions for these models. We used the program sdisp96 (Herrmann, 2013) to calculate dispersion curves for multiple 1D profiles and then combined them to 2D maps at different depths. The comparison of these synthetic dispersion maps against the observed tomographic group velocity maps is shown in Fig. 6.11. Among these models, the LAS1 group velocity maps fit the tomographic observations the best. The CVM-S model over predicts the long period group velocities, while the CVM-H model produces much lower Rayleigh group velocities than the observations. To directly examine the model predictions against the picked dispersion data, we generate synthetic dispersion curves from group velocity maps of our tomographic result and the CVM-S/CVM-H models along the ray paths between SCSN stations and dense arrays. The fittings to directly picked dispersion data for these models are shown in Fig. 6.12. Similar to the group velocity map comparisons, the CVM-S model predicts that long period Rayleigh waves travel faster than observations, and the CVM-H model underestimates the Rayleigh wave group velocities for multiple frequency bands. Our model fits the observations significantly better than CVM-S/CVM-H models, but still generate non-negligible misfits. Possible sources of the misfits are the simple forward modeling used in the problem, in particular the straight ray assumption, and the uneven ray coverage. The diminishing ray density toward the edge of the basin contributes to the data misfit. A possible solution to this is to use machine-learning based tomography to reduce the artifacts (Bianco et al., 2019).

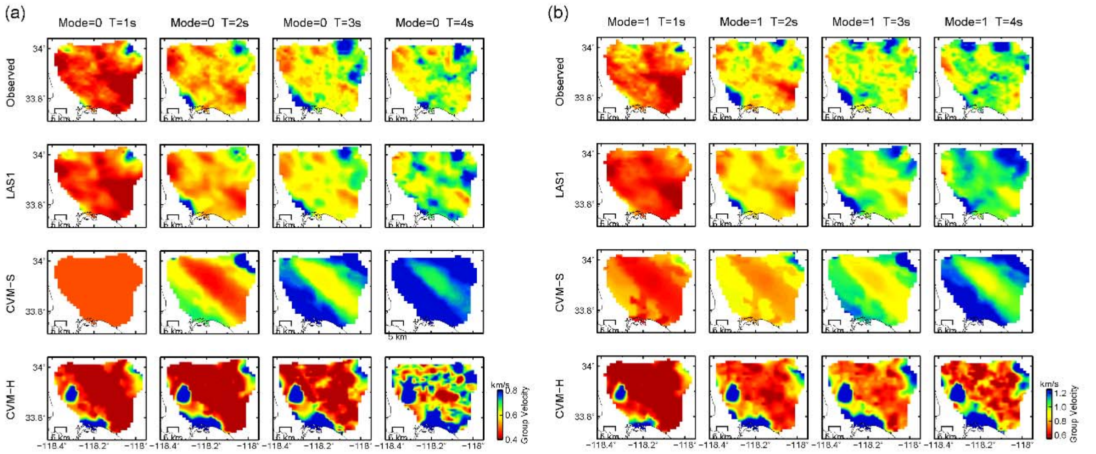

Figure 6.11. Comparison of (a) the fundamental mode and (b) the first overtone group velocity fittings between our Vs model and SCEC CVM Vs models for periods 1-4s. Rows from top to bottom are the observed group velocity maps from tomography, synthetic group velocity maps from the LAS1 Vs model, synthetics from the CVM-S model, and synthetics from the CVM-H model, respectively.

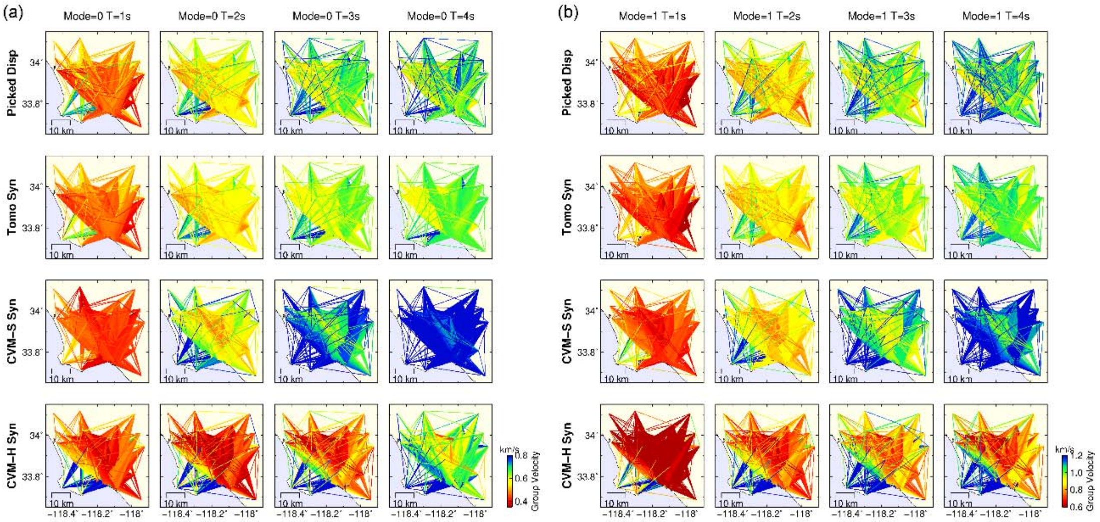

Figure 6.12. Comparison of (a) the fundamental mode and (b) the first overtone dispersion data fittings between our tomographic model and SCEC CVM Vs models for periods 1-4s. Rows from top to bottom are the directly picked dispersion data, synthetic dispersions of rays from our tomographic group velocity model, synthetics from the CVM-S model, and synthetics from the CVM-H model, respectively.

6.6 Conclusions

We use ambient noise correlations between 5 dense oil company nodal networks and 21 broadband Southern California Seismic Network stations to develop a high resolution shallow structural velocity model of the central Los Angeles Basin. We demonstrated that this short period (0.25-2.0 Hz) inter-station noise correlation can produce clear multimodal Rayleigh wavefields, thus can provide very detailed coverage of a large portion of the LA Basin. We extracted group velocity dispersion curves and inverted for the shear wave velocity structure. Our Vs model shows the shrinking circumference of the low velocity sedimentary materials as the basin deepens, and reveals the existence of multiscale structural heterogeneities and interface roughness within the basin. The model also shows evidence of the Newport-Inglewood fault as a high shear-wave velocity belt. The estimated Vs model generally agrees with the SCEC CVM-S and CVM-H models, but better fits the Rayleigh wave dispersion data. It predicts shallow crustal amplification more similar to the CVM-H model than the CVM-S. This model should be able to better predict the variations in the shallow crustal amplification, which will improve strong ground motion simulations.

6.7 Supplementary Materials

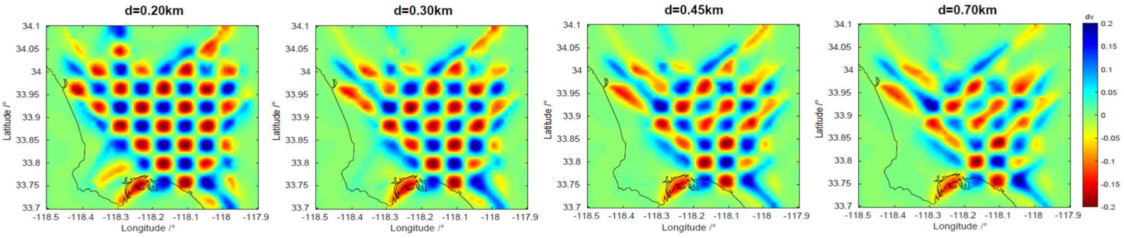

Figure S6.1. Checkerboard test with the average nodal array interstation distances to be approximately 0.2, 0.3, 0.45 and 0.7 km, using fundamental mode Rayleigh wave dispersions at T=2s. The ray coverage used in our tomographic inversions has an average nodal array interstation distance of 0.2 km.

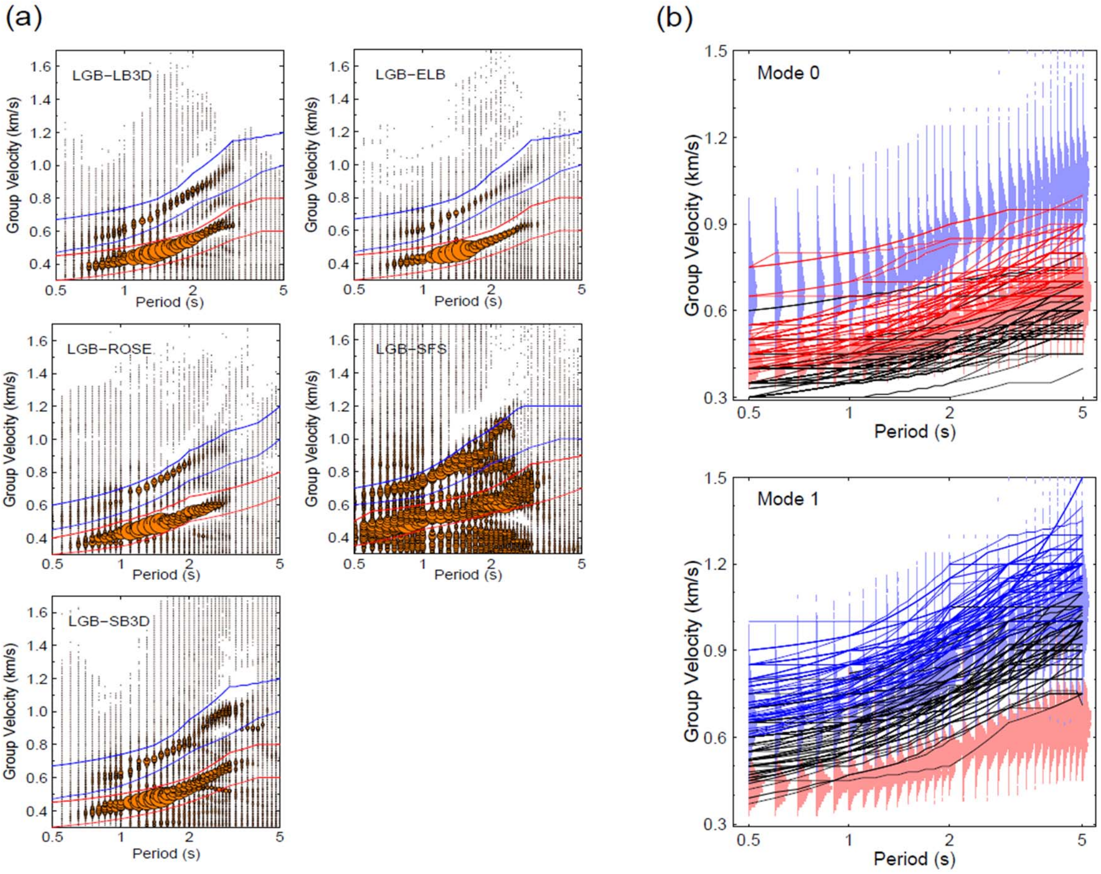

Figure S6.2. Corridors for the dispersion curve picking. (a) Example of fundamental mode (red lines) and first overtone (blue lines) corridors over the stacked velocity-time amplitudes of NCFs from virtual source LGB to each dense array. (b) Overview of all corridors on the stacked velocity-time maps. The lower bounds of corridors are indicated by black lines. The upper bounds of corridors for the fundamental mode and first overtone Rayleigh waves are shown by red and blue lines.

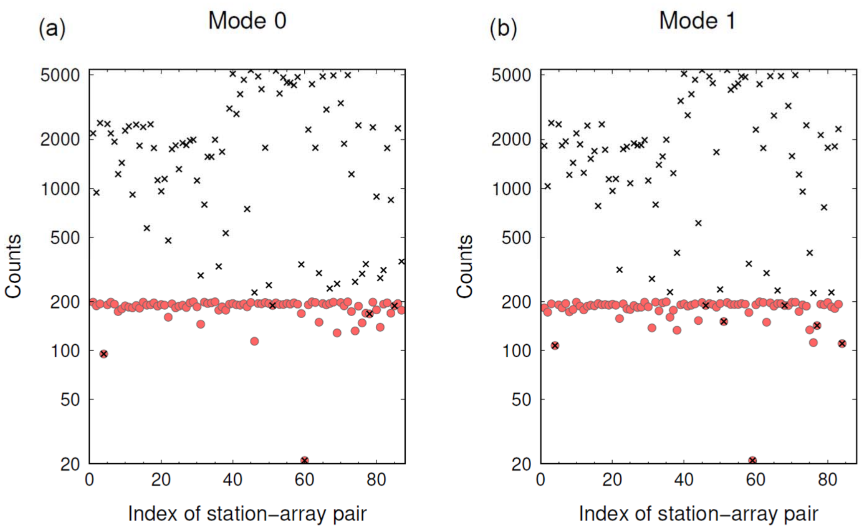

Figure S6.3. Resampling of the picked dispersion datasets for the (a) fundamental mode and (b) first overtone at the period of 2s, respectively. Black crosses and red circles show the picked dispersion data counts of each station-array pair (x axis) before and after resampling.

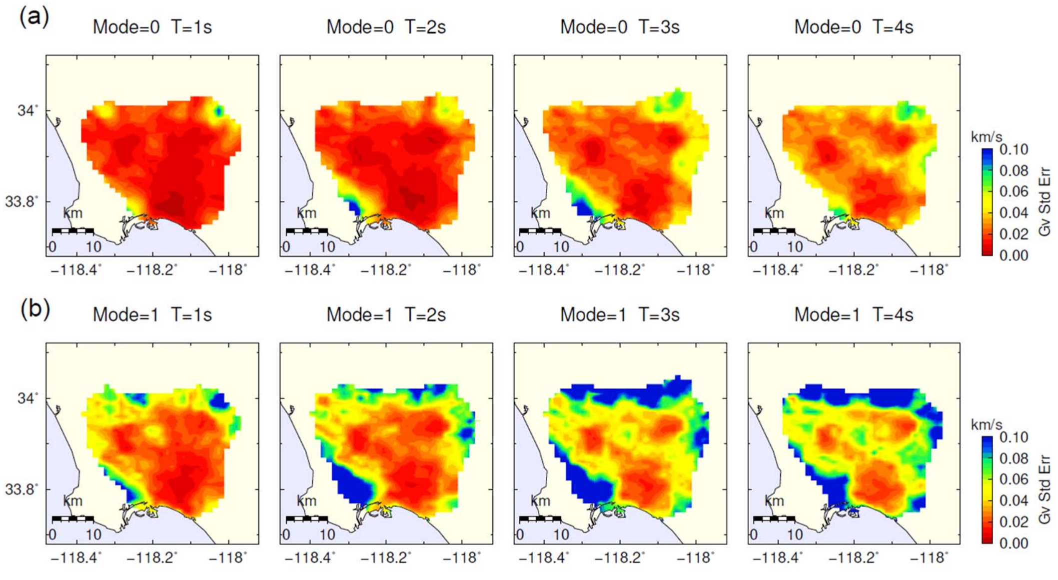

Figure S6.4. Group velocity standard deviation errors of (a) the fundamental mode and (b) the first overtone Rayleigh wave group velocity tomography for periods 1-4 s.

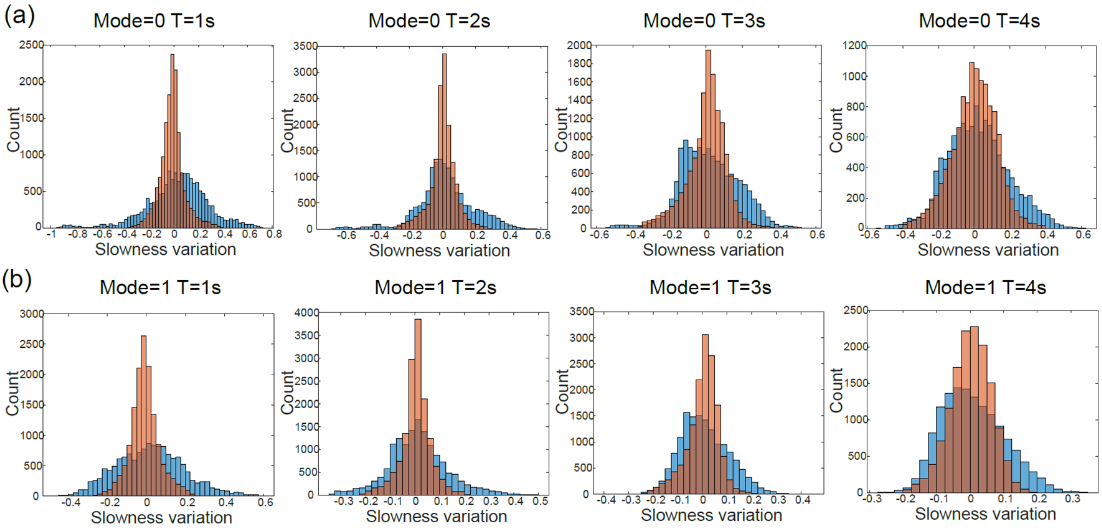

Figure S6.5. Slowness variance reductions of (a) the fundamental mode and (b) the first overtone Rayleigh wave group velocity tomography for periods 1-4 s. Blue and red histograms are the slowness variance distributions for the uniform group velocity model and inverted tomographic model, respectively.

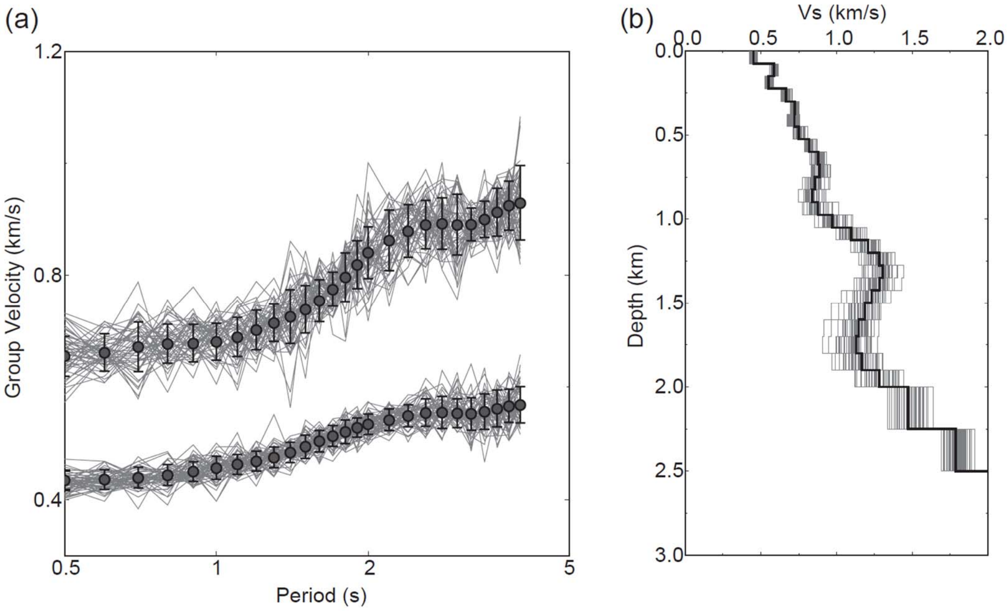

Figure S6.6. An example of the Vs uncertainty estimation. The corresponding grid location is indicated by the black cross in Fig. S6.7. (a) Sampling of the fundamental mode and first overtone group velocities as a function of period. Circles show the inverted group velocities for the two modes. Error bars indicate the group velocity standard deviations. Gray lines denote 50 perturbed dispersion curves from Gaussian distributions. (b) The ensemble of Vs models from perturbed dispersion curves (gray lines). The black line indicated the inverted Vs model from the data.

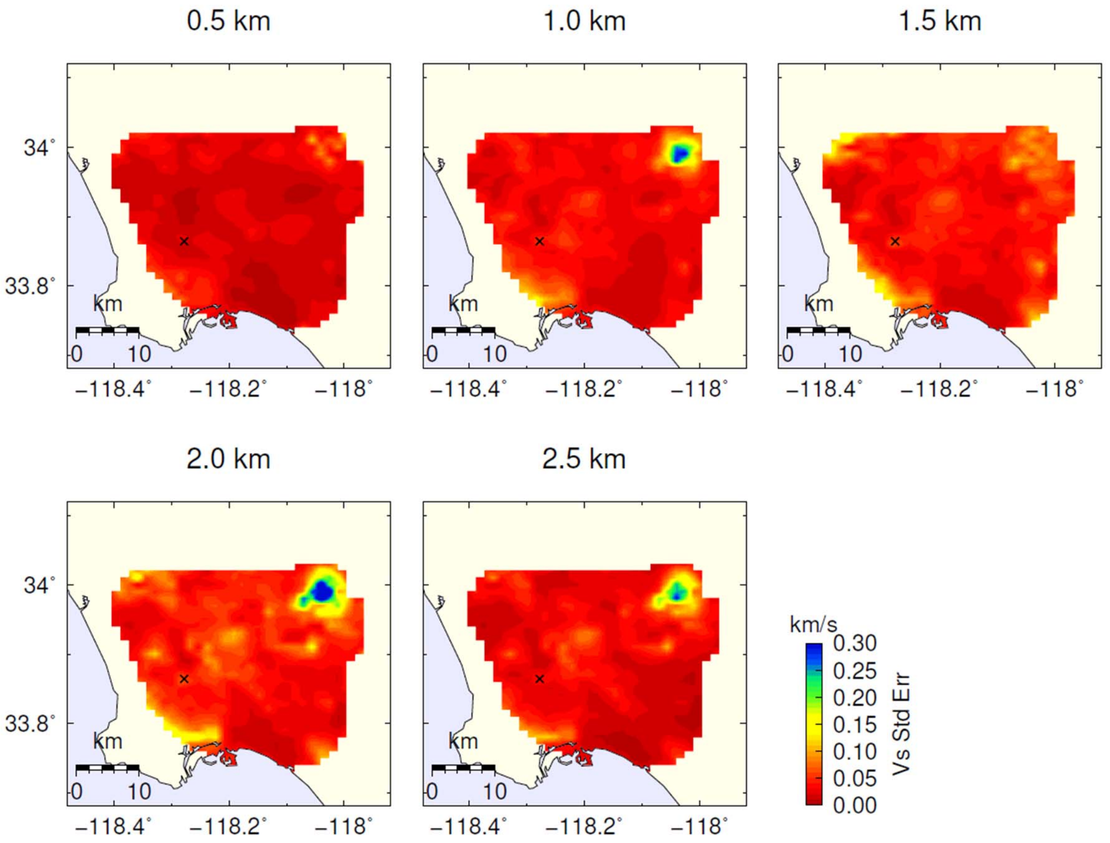

Figure S6.7. Shear wave velocity standard deviation errors of depth slices from 0.5 km to 2.5 km.

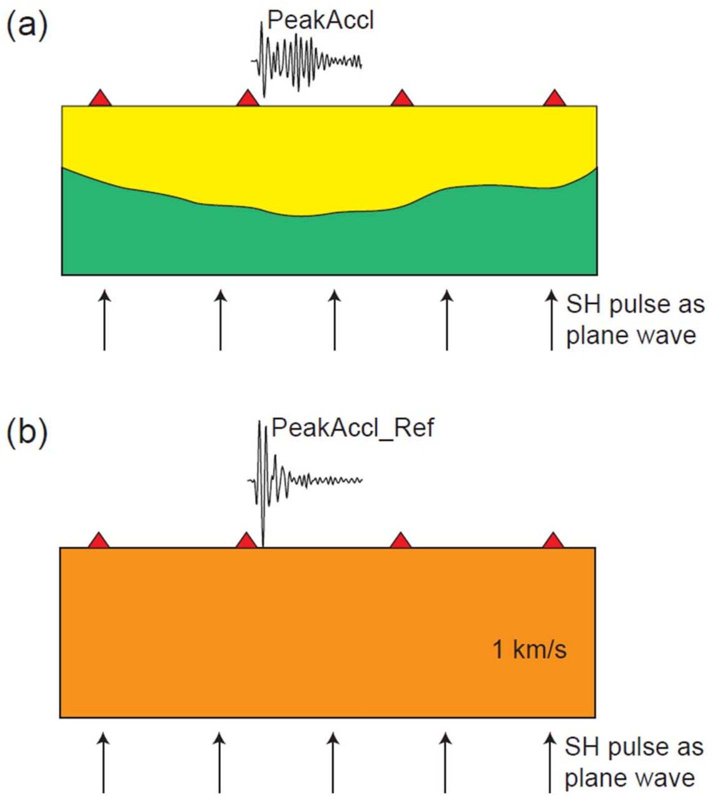

Figure S6.8. Schematic plot of the simulation of strong motion amplification ratio. (a) Strong motion simulation of 2D velocity profile with a 1Hz plane wave SH pulse propagating from bottom to the surface. We measure the peak amplitude of the accelerations. (b) Reference peak acceleration simulated with an equivalent pulse propagated through a medium with a constant shear velocity of 1 km/s.

	Total	**LB3D**	**SB3D**	**SFS**	**ELB**	**ROSE**
Number of NCFs	353006	106800	104811	50660	48840	41895

Table S6.1. Number of noise correlation functions (NCFs) computed in our study. The numbers for individual dense arrays are also displayed.

6.8 References

Barmin, M., Ritzwoller, M., Levshin, A., 2001. A fast and reliable method for surface wave tomography, Monitoring the comprehensive nuclear-test-ban treaty: Surface waves. Springer, pp. 1351-1375.

Ben-Zion, Y., Vernon, F.L., Ozakin, Y., Zigone, D., Ross, Z.E., Meng, H., White, M., Reyes, J., Hollis, D., Barklage, M., 2015. Basic data features and results from a spatially dense seismic array on the San Jacinto fault zone. Geophysical Journal International 202, 370-380.

Bensen, G., Ritzwoller, M., Barmin, M., Levshin, A.L., Lin, F., Moschetti, M., Shapiro, N., Yang, Y., 2007. Processing seismic ambient noise data to obtain reliable broad-band surface wave dispersion measurements. Geophysical Journal International 169, 1239-1260.

Bianco, M.J., Gerstoft, P., Olsen, K.B., Lin, F.-C., 2019. High-resolution seismic tomography of Long Beach, CA using machine learning. Scientific reports 9, 1-11.

Bowden, D., Tsai, V.C., Lin, F.C., 2015. Site amplification, attenuation, and scattering from noise correlation amplitudes across a dense array in Long Beach, CA. Geophys. Res. Lett. 42, 1360-1367.

Brocher, T.M., 2005. Empirical relations between elastic wavespeeds and density in the Earth's crust. Bull. Seismol. Soc. Am. 95, 2081-2092.

Castellanos, J.C., Clayton, R.W., Juarez, A., 2020. Using a Time-based Subarray Method to Extract and Invert Noise-derived Body Waves at Long Beach, California. Journal of Geophysical Research: Solid Earth 125, e2019JB018855.

Castellanos, J.C., Clayton, R.W., Pérez-Campos, X., 2018. Imaging the eastern Trans-Mexican volcanic belt with ambient seismic noise: Evidence for a slab tear. Journal of Geophysical Research: Solid Earth 123, 7741-7759.

Clayton, R., Persaud, P., Denolle, M., Polet, J., 2019. Exposing Los Angeles’s shaky geologic underbelly, Eos, 100.

Delépine, N., Semblat, J.-F., 2012. Site effects in an alpine valley with strong velocity gradient: interest and limitations of the ‘classical’BEM. Soil Dynamics and Earthquake Engineering 38, 15-24.

Ekström, G., 2014. Love and Rayleigh phase-velocity maps, 5–40 s, of the western and central USA from USArray data. Earth and Planetary Science Letters 402, 42-49.

Ekström, G.r., 2006. Global detection and location of seismic sources by using surface waves. Bulletin of the Seismological Society of America 96, 1201-1212.

Ely, G.P., Jordan, T., Small, P., Maechling, P.J., 2010. A VS30-derived nearsurface seismic velocity model, Abstract S51A-1907, Fall Meeting. AGU San Francisco, CA.

Hauksson, E., 1987. Seismotectonics of the Newport-Inglewood fault zone in the Los Angeles basin, southern California. Bulletin of the Seismological Society of America 77, 539-561.

Hauksson, E., 2000. Crustal structure and seismicity distribution adjacent to the Pacific and North America plate boundary in southern California. Journal of Geophysical Research: Solid Earth 105, 13875-13903.

Herrmann, R.B., 2013. Computer programs in seismology: An evolving tool for instruction and research. Seismological Research Letters 84, 1081-1088.

Jia, Z., Wang, X., Zhan, Z., 2020. Multifault Models of the 2019 Ridgecrest Sequence Highlight Complementary Slip and Fault Junction Instability. Geophys. Res. Lett. 47, e2020GL089802.

Lai, V.H., Graves, R.W., Yu, C., Zhan, Z., Helmberger, D.V., 2020. Shallow Basin Structure and Attenuation are Key to Predicting Long Shaking Duration in Los Angeles Basin. Journal of Geophysical Research: Solid Earth, e2020JB019663.

Lee, E.J., Chen, P., Jordan, T.H., 2014a. Testing waveform predictions of 3D velocity models against two recent Los Angeles earthquakes. Seismological Research Letters 85, 1275-1284.

Lee, E.J., Chen, P., Jordan, T.H., Maechling, P.B., Denolle, M.A., Beroza, G.C., 2014b. Full-3-D tomography for crustal structure in southern California based on the scattering-integral and the adjoint-wavefield methods. Journal of Geophysical Research: Solid Earth 119, 6421-6451.

Levshin, A.L., Pisarenko, V., Pogrebinsky, G., 1972. On a frequency-time analysis of oscillations, Annales de geophysique. Centre National de la Recherche Scientifique, pp. 211-218.

Lin, F.-C., Li, D., Clayton, R.W., Hollis, D., 2013. High-resolution 3D shallow crustal structure in Long Beach, California: Application of ambient noise tomography on a dense seismic arrayNoise tomography with a dense array. Geophysics 78, Q45-Q56.

Lin, F.-C., Moschetti, M.P., Ritzwoller, M.H., 2008. Surface wave tomography of the western United States from ambient seismic noise: Rayleigh and Love wave phase velocity maps. Geophysical Journal International 173, 281-298.

Ma, Y., Clayton, R.W., 2014. The crust and uppermost mantle structure of Southern Peru from ambient noise and earthquake surface wave analysis. Earth and Planetary Science Letters 395, 61-70.

Ma, Y., Clayton, R.W., 2016. Structure of the Los Angeles Basin from ambient noise and receiver functions. Geophysical Journal International 206, 1645-1651.

Nakata, N., Chang, J.P., Lawrence, J.F., Boué, P., 2015. Body wave extraction and tomography at Long Beach, California, with ambient-noise interferometry. Journal of Geophysical Research: Solid Earth 120, 1159-1173.

Qiu, H., Lin, F.C., Ben-Zion, Y., 2019. Eikonal tomography of the Southern California plate boundary region. Journal of Geophysical Research: Solid Earth 124, 9755-9779.

Redin, T., 1991. Oil and Gas Production from Submarine Fans of the Los Angeles Basin: Chapter 8.

Roux, P., Moreau, L., Lecointre, A., Hillers, G., Campillo, M., Ben-Zion, Y., Zigone, D., Vernon, F., 2016. A methodological approach towards high-resolution surface wave imaging of the San Jacinto Fault Zone using ambient-noise recordings at a spatially dense array. Geophysical Journal International 206, 980-992.

Shapiro, N.M., Campillo, M., Stehly, L., Ritzwoller, M.H., 2005. High-resolution surface-wave tomography from ambient seismic noise. Science 307, 1615-1618.

Shaw, J.H., Plesch, A., Tape, C., Suess, M.P., Jordan, T.H., Ely, G., Hauksson, E., Tromp, J., Tanimoto, T., Graves, R., 2015. Unified structural representation of the southern California crust and upper mantle. Earth and Planetary Science Letters 415, 1-15.

Small, P., Gill, D., Maechling, P.J., Taborda, R., Callaghan, S., Jordan, T.H., Olsen, K.B., Ely, G.P., Goulet, C., 2017. The SCEC unified community velocity model software framework. Seismological Research Letters 88, 1539-1552.

Snieder, R., 2004. Extracting the Green's function from the correlation of coda waves: A derivation based on stationary phase. Physical Review E 69, 046610.

Steidl, J.H., Tumarkin, A.G., Archuleta, R.J., 1996. What is a reference site? Bull. Seismol. Soc. Am. 86, 1733-1748.

Süss, M.P., Shaw, J.H., 2003. P wave seismic velocity structure derived from sonic logs and industry reflection data in the Los Angeles basin, California. Journal of Geophysical Research: Solid Earth 108.

Taborda, R., Azizzadeh-Roodpish, S., Khoshnevis, N., Cheng, K., 2016. Evaluation of the southern California seismic velocity models through simulation of recorded events. Geophysical Journal International 205, 1342-1364.

Tape, C., Liu, Q., Maggi, A., Tromp, J., 2009. Adjoint tomography of the southern California crust. Science 325, 988-992.

Virieux, J., 1984. SH-wave propagation in heterogeneous media: Velocity-stress finite-difference method. Geop 49, 1933-1942.

Zhang, X., Jia, Z., Ross, Z.E., Clayton, R.W., 2020. Extracting dispersion curves from ambient noise correlations using deep learning. IEEE Transactions on Geoscience and Remote Sensing.

Zhu, L., Kanamori, H., 2000. Moho depth variation in southern California from teleseismic receiver functions. Journal of Geophysical Research: Solid Earth 105, 2969-2980.

Chapter 7

FINDINGS AND CLOSING THOUGHTS

In this thesis, I developed a subevent inversion method in a Bayesian framework, and enhanced this approach with combining multi-geophysical observations and using 3D Earth structure, to fit the need of resolving different rupture complexities. In Chapter 2, I combined rupture process observation and earth interior simulations to unveil how temperature and slabs control the large deep earthquakes at Fiji-Tonga subduction zone. In Chapter 3, I integrated the seismic and geodetic tools to illuminate the complex fault system involved with the 2019 M7 Ridgecrest earthquake sequence. In Chapter 4, I inverted broadband seismic data for the source properties of the 2021 Mw 8.2 South Sandwich Island earthquake, and its complex rupture reveals an extreme integration of the broad spectral behavior of subduction zone earthquakes. I also developed a differential moment tensor (diffMT) inversion algorithm to avoid misinterpreting structural effects as source properties, when a good 3D velocity model is not available. In Chapter 6, application of diffMT on three North Korea nuclear tests leads to reduced errors of isotropic components and double couple focal mechanisms. In Chapter 7, I developed a high-resolution 3D velocity model of the shallow Los Angeles Basin, by combining the aperture of seismic stations and density of industrial arrays. The model's high resolution and broad coverage enables better characterization of the site effects, and may also contribute to earthquake source studies.

These studies show our advancements in resolving earthquake complexities, which intuitively lead to the science question: what controls the diverse complex behaviors of earthquakes? Various factors, such as the macroscopic earth tectonics, thermal environment, pre-existing fault geometries, and frictional properties can play important roles, but a comprehensive understanding is still in its infancy, and requires both detailed and systematic studies of earthquake complexity. For example, I investigated the deep earthquake properties of the Fiji-Tonga region, but for other similar subduction zones, how temperature and slab geometry influence intermediate-depth and deep earthquakes remains to be solved. For the megathrust earthquakes like the 2021 South Sandwich Island earthquake, a synergy of rupture observation and physical simulation is critical to facilitate understanding of how slip deficits and fault geological conditions interact with the rupture heterogeneities. For shallow crustal events like the 2019 Ridgecrest sequence, we need to further explore how the fault geometries control transient slip and long-term earthquake behavior, with accumulative observations and simulations. Enhancing such understandings with novel ideas and multidisciplinary advancements is an important and long-lasting topic.

Occurrence of tectonic earthquakes are generally uncontrollable. However, human activities like injecting fluids into underground formations during oil or geothermal industry can perturb the natural system and generate earthquakes, named “induced seismicity”. The famous examples include the decades-long seismic activities at the Coso and Salton Sea geothermal fields in Southern California. The causality between injection and induced seismicity offers relatively controllable and well characterized stimuli that produce fault reactivations, making induced seismicity a natural laboratory for studying earthquakes. However, understanding their seismogenesis and hazard is very challenging, because the related stress environment requires knowledge of precise earthquake mechanisms, which is difficult to determine at small magnitudes. But instead of traditional direct-inversion methods, there is a chance of building high-quality focal mechanism catalogs of induced earthquakes with differential measurements, which reduces the magnitude limit and mechanism error of the traditional approaches. The anticipated improvements in abundance and precision of earthquake mechanisms could guide the mapping of fault systems and tracking the underground stress field, thus contributing to the assessment of natural or anthropogenic causes of earthquakes at injection sites.